

Magnetic Shear in Two-ribbon Solar Flares

BY

Yingna Su

M.S., Purple Mountain Observatory (2004)

Dissertation

Submitted to the Purple Mountain Observatory
in Partial Fulfillment of
the Requirements for the Degree of

Doctor of Philosophy

in

Astrophysics

December 2007

ALL RIGHTS RESERVED

©2007

Yingna Su

This thesis has been examined and approved.

Thesis director, Guangli Huang
Chief Scientist

Leon Golub
Senior Astrophysicist

A. B. Black
Faculty in Residence in xxx

Date

Acknowledgments

First of all, I would like to thank my advisor Dr. Guangli Huang for introducing and encouraging me to apply for the Smithsonian Astrophysical Observatory (SAO) Predoctoral Fellowship. I am deeply grateful to Dr. Leon Golub for enrolling me to do my thesis research with TRACE and Hinode/XRT data at SAO/CfA (Harvard-Smithsonian Center for Astrophysics). Thank Dr. Leon Golub for his continuous motivations, invaluable support, and various helps through my entire thesis research process. I am deeply appreciative to Dr. Adriaan van Ballegooijen for sharing stimulating and insight views and guiding me through the intricacies of the research. You do not know how much I learned from you through the numerous valuable discussions on both observations and theories of various phenomena on the Sun. Thank you for teaching me on magnetic field modeling. My last-year thesis research was primarily based on the new XRT data. I want to thank everyone who made this possible, especially Dr. Edward Deluca, the Principle Investigator of XRT. Thanks Dr. Deluca for fruitful discussions and various support on my research. I also acknowledge Dr. Jun Lin for valuable discussions on research and generous helps.

I feel very lucky that I can spend three years on my thesis research in the SSXG (Solar and Stellar X-ray Group) group at SAO. I am indebted to everyone in this group for their help in different aspects. Thank Dr. Mark Weber for generous helps especially on programing and English. I will not forget your 'one English word a day' and the numerous delightful conversations. Thank Monica Bobra, Jin-Yi Lee, and Paolo Pagano, my colleagues and good friends, for discussions on research and lunch together, you made my graduate-student life in the US more joyful. Thanks to Jonathan Cirtain for various helps. It is very nice to get to know you and your family, I wish you and your family a great time in Huntsville. I acknowledge Dr. Kathy K. Reeves and Dr. Paolo Grigis for fruitul discussions on flares/CMEs and various helps on my thesis. Thanks Patricia Jibben for helping me

on programming. Thank Dr. Kelly Korreck and Antonia Savcheva for organizing the fun parties. It is great to know you and your twins, Dr. Saar Steven, thank you for various delightful discussions and your fresh home peaches. I acknowledge James McCaughey for his contributions to the research. I also want to thank the other SSXG group members: Dr. Loraine Lundquist, Dr. Jay Bookbinder, Doug Kline, and Samaiyah Farid. Thank all of the people who had helped me at the CfA, such as Dr. Anne Davenport, Ms. Loryane Mohammed, Ms. Christine Crowley, and so on.

I am also grateful to a lot of solar physicists outside of SAO for various helps. I would like to give my special thanks to Dr. Spiro Antiochos for sharing insight views and valuable discussions on my research, and the first work of this thesis was motivated by one of his hypothesis. Thank Dr. Judith Karpen for inviting me to give a seminar talk at the Naval Research Laboratory (NRL) and useful discussions. I also want to thank Drs. Brigitte Schmieder, Arek Berlicki, Pascal Démoulin, and Maurice Gros for fruitful discussions on my research and their hospitality during my visit at Meudon. I am indebted to Drs. Jiong Qiu and Haisheng Ji for their help with BBSO data process. I would like to acknowledge Drs. Sarah Gibson, Ward Manchester, and Mei Zhang for helpful discussions on solar flare and CME models. Thank Rui Liu and Dr. Holly Gilbert for useful discussions on filaments.

The TRACE analysis is supported at SAO by a contract from Lockheed Martin. Hinode is a Japanese mission developed and launched by ISAS/JAXA, with NAOJ as domestic partner and NASA and STFC (UK) as international partners. It is operated by these agencies in co-operation with ESA and the NSC (Norway). US members of the XRT team are supported by NASA contract NNM07AA02C to SAO. I am also supported by the SAO Pre-doctoral Fellowship, the NSFC projects with 10333030 and 10273025, and “973” program with 2006CB806302. I would like to thank all of the team members of TRACE, Hinode/XRT, Hinode/SOT, SOHO/MDI, SOHO/LASCO, SOHO/EIT, NJIT/BBSO, GOES, RHESSI, Yohkoh/HXT, SPI/ACS, MLSO/PICS for providing the valuable data.

At last, I wish to thank my parents Mangui Su and Xiaoling Zhou for their great love and invaluable support over years. This thesis could be barely finished without the loving

support and encouragement from my husband, Xuepeng Chen. To my family, I dedicate this thesis.

Table of Contents

Acknowledgments	iv
Abstract	xv
1 Introduction	1
1.1 Observations of Solar Eruptions	1
1.1.1 Solar Flares	1
1.1.2 Prominence Eruptions	12
1.1.3 Coronal Mass Ejections	16
1.1.4 Relationship between Solar Flares, Prominence Eruptions, and CMEs	20
1.2 Theories of Solar Eruptions	26
1.2.1 Theories of Solar Flares	26
1.2.2 Models of Coronal Mass Ejections	31
1.3 Instruments	36
1.3.1 TRACE	36
1.3.2 <i>Hinode</i> /XRT	37
1.3.3 Other Instruments	39
1.4 Fundamental Questions in Solar Eruptions	42
2 Magnetic Shear in an X17 Solar Flare on 2003 October 28	45
2.1 Introduction	45
2.2 Observations	48
2.3 Comparison of EUV and HXR Emission	51

2.3.1	Correlation between EUV and HXR emission	51
2.3.2	Pre-HXR EUV brightenings	53
2.4	Evolution of the EUV Bright Kernels	61
2.4.1	Identification of the EUV conjugate footpoints	61
2.4.2	Evolution of the shear of the EUV conjugate footpoints	64
2.5	Discussion	68
2.5.1	EUV brightenings generation mechanism	68
2.5.2	Evolution of the magnetic shear	70
2.6	Conclusions	73
3	A Statistical Study of Shear Motion of the Footpoints in Two-ribbon Flares	76
3.1	Introduction	76
3.2	Observational Data	79
3.3	Three Types of Two-ribbon Flares	81
3.3.1	Type I Flares	82
3.3.2	Types II and III Flares	90
3.4	“Ejective” and “Confined” Flares	92
3.4.1	“Ejective or Possibly Ejective” Flares	94
3.4.2	“Confined” Flares	95
3.4.3	An Energy Scale for Two-ribbon Flares	97
3.5	Time Difference Between the Cessation of Shear Motion and the End of Impulsive Phase in Type I Flares	98
3.6	Summary	99
4	What Determines the Intensity of Solar Flare/CME Events?	103
4.1	Introduction	103

4.2	Data Selection and Methods	106
4.2.1	Measurement Uncertainties of the Shear Angles	108
4.2.2	Measurement Methods of the Magnetic Size	109
4.3	Results	112
4.3.1	Peak Flare Flux and CME Speed vs. Magnetic Field Strength	112
4.3.2	Peak Flare Flux and CME Speed vs. Six Magnetic Parameters	116
4.3.3	Peak Flare Flux and CME Speed vs. Multi-parameter Combinations	119
4.4	Summary and Discussion	123
5	Evolution of the Sheared Magnetic Fields of Two X-class Flares Observed by <i>Hinode</i>/XRT	129
5.1	Introduction	129
5.2	Instrumentation and Data	130
5.3	Results	133
5.3.1	Formation of the Sheared Magnetic Fields	133
5.3.2	Evolution of Sheared Magnetic Fields during the Flares	136
5.3.3	Pre-flare vs. Post-flare Sheared Magnetic Fields	140
5.4	Discussions and Conclusions	142
6	Observations and NLFFF Modeling of Active Region 10953	145
6.1	Introduction	145
6.2	Observations	147
6.2.1	Data set and Method	147
6.2.2	Observational Results	148
6.3	Non-Linear Force Free Field Modeling of NOAA 10953	155
6.3.1	Flux -Rope Insertion Method	155

6.3.2	Modeling Results	158
6.4	Summary and Discussion	169
7	Summary and Outlook	173
7.1	Brief Summary	173
7.2	Future Work	176
7.2.1	Further Study on Shear Motion of Footpoints	176
7.2.2	Evolution of Sheared Fields in Solar Flares: Observation	177
7.2.3	Evolution of Sheared Fields in Solar Flares: Modeling	178
	Appendix A Estimate of the Coronal Magnetic Field Strength	180
	Appendix B Multiple Linear Regression Fit	180
	Bibliography	183
	Curriculum Vitae	195
	List of Publications	196

List of Tables

1.1	The X-ray classification of solar flares	6
1.2	TRACE Temperature Response (from Handy et al. 1999)	37
2.1	Timing of HXR peaks and corresponding EUV brightenings.	52
2.2	Summary of the bright kernels occurring in different phases of the 2003 October 28 flare.	63
2.3	Shear angle change rate and the corresponding time.	66
3.1	Type I flares with shear motion and ribbon separation.	86
3.1	Type I flares with shear motion and ribbon separation.	87
3.1	Type I flares with shear motion and ribbon separation.	88
3.2	Type II and Type III flares without shear motion.	91
4.1	Constants, coefficients as well as their 1- σ uncertainties of the multiple linear regression fits for three types of multi-parameter combinations.	120
4.2	The contributions from each parameter in three types of multi-parameter combinations (σ_i^2) and other unknown sources (σ_o^2) to the total vari- ances of the observed $\log_{10}(PFF)$ ($\sigma_{tot}^2 = 0.29$, PFF in unit of Watt m^{-2}) and V_{CME} ($\sigma_{tot}^2 = 3.45 \times 10^5 \text{ km}^2 \text{ s}^{-2}$).	122
6.1	The Average Deviations (dmavg) of the model field lines from the observed X-ray loops for various models of AR 10953	159
6.2	Degree of Convergence for Various Models for AR 10953.	160
6.3	Model parameters for NOAA AR 10953 in 2007.	169

List of Figures

1-1	Sketch of the first reported solar flare.	3
1-2	Time profiles of an average flare at different wavelengths.	7
1-3	Images of different solar flares at different wavelengths.	9
1-4	Filaments and prominences observed in $H\alpha$	13
1-5	Images of filament/prominence eruptions in EUV.	15
1-6	Images of a CME observed by SMM.	18
1-7	Schematic diagram of a disrupted magnetic field that forms in an erup- tive process	28
1-8	Sketch the standard model in 3D by Moore et al. (2001)	30
1-9	The total XRT Temperature Response for all of the X-ray focal-plane filters.	38
2-1	Light curves of the EUV and HXR emission.	49
2-2	SPI/ACS/HXR light curves, TRACE/EUV images and light curves of different brightenings during Phase 1.	54
2-3	Similar to Figure 2-2 but for Phase 2.	55
2-4	Similar to Figure 2-2, but for Phases 3 and 4.	56
2-5	Similar to Figure 2-2, but for Phase 5	57
2-6	Similar to Figure 2-2, but for Phase 6	58
2-7	Similar to Figure 2-2, but for Phase 7	59
2-8	Similar to Figure 2-2, but for Phase 8	60
2-9	EUV brightenings and $H\alpha$ image.	65

2-10	HXR light curve and the temporal evolution of the shear angle and the change rate of this angle.	67
2-11	Cartoon of the evolution of the magnetic field in the standard model of solar flares.	71
3-1	Event on 2001 April 26.	83
3-2	Types II and III flares.	84
3-3	Histograms for the 24 type I flares with measured shear angle.	91
3-4	Schematic representation of the flare energy scale indicating the type of flare footpoint motions.	98
3-5	Histogram of event number in terms of the time difference between the end of the HXR impulsive phase and the cessation of the change of shear angle.	100
4-1	<i>SOHO</i> MDI image overlaid with <i>TRACE</i> contours at 195 Å on 2000 June 10.	107
4-2	Scatter plots of the Peak Flare Flux and CME Speed vs. Magnetic Field Strength.	113
4-3	Peak Flare Flux and CME Speed vs. Six Magnetic Parameters.	115
4-4	Scatter plots of six pairs of magnetic parameters.	116
4-5	Scatter plots of $\log_{10}(PFF)$ and V_{CME} vs. three magnetic parameters representing magnetic size	117
4-6	Similar to Figure 4-5, but scatter plots of $\log_{10}(PFF)$ and V_{CME} vs. three parameters representing magnet shear.	118
4-7	Scatter plots of the Peak Flare Flux and CME Speed vs. Multi-parameter Combinations.	121

5-1	Formation of the sheared magnetic fields observed by XRT aboard <i>Hinode</i>	133
5-2	<i>Hinode</i> /SOT G band images overlaid with SOHO/MDI magnetic contours.	134
5-3	XRT observations of the sheared magnetic field evolution during two X-class flares.	136
5-4	Pre-flare and post-flare XRT and TRACE images of the X3.4 flare on 2006 December 13.	139
5-5	Pre-flare and post-flare XRT and TRACE images for the X1.5 flare on 2006 December 14.	141
6-1	Flux cancellations in Active Region 10953 from April 30 to May 3 in 2007.	149
6-2	The GOES soft X-ray light curve for the C8.5 two-ribbon flare occurred on 2007 May 2.	150
6-3	Evolution of the filament activation associated with the C8.5 flare.	151
6-4	Pre-EUV X-ray footpoint brightenings during the C8.5 flare.	154
6-5	Highly sheared loops before and after the C8.5 flare.	154
6-6	A NLFFF model for NOAA Active Region 10953 on 2007 May 1 at 06:27 UT.	157
6-7	NLFFF models with different axial fluxes for AR 10953 on 2007 May 1 versus the observed X-ray loops.	162
6-8	NLFFF models with different axial fluxes for AR 10953 on 2007 May 2 versus the observed X-ray loops.	165
6-9	NLFFF models with different axial fluxes for AR 10953 on 2007 May 3 versus the observed X-ray loops.	167

ABSTRACT

Magnetic Shear in Two-ribbon Solar Flares

by

Yingna Su

Purple Mountain Observatory, December, 2007

In this thesis, we study the evolution of the highly sheared magnetic fields before, during, and after solar flares, in order to address the fundamental questions in solar flare research: how does the magnetic free energy stored and released? The work primarily focuses on the analysis of multi-wavelength data, while non-linear force free field (NLFFF) modeling of one active region is also explored.

A detailed analysis of the strong-to-weak shear motion of the flare footpoints (TRACE) in an X17 flare (2003 Oct 28) shows that the cessation of this shear change occurs in the middle of the impulsive phase. The observations are interpreted in terms of the splitting of the sheared envelope field of the greatly sheared core rope during the early phase of the flare, based on a 3D version of the standard flare model. This shear motion of the footpoints has been found to be common, i.e., 43 out of 50 of the well-observed (by TRACE) two-ribbon flares we studied show this shear motion, this type of flares are called type I flare. We also found that: for a subset of 24 type I flares, the initial and final shear angles of the footpoints are mainly in the range from 50° to 80° and 15° to 55° , respectively; in 10 of the 14 flares having both measured shear angle and corresponding hard X-ray observations, the cessation of shear change is 0–2 minutes earlier than the end of the impulsive phase, which may suggest that the change from impulsive to gradual phase is related to magnetic shear change. For a sample of 18 Type I flares associated with CMEs, we found that the magnetic flux and the change of shear angle of the footpoints significantly correlated with the intensity of flare/CME events, while the initial shear angle of the footpoints does not. This observation indicates that the intensity of flare/CME events may depend on the *released*

magnetic free energy rather than the *total* free energy stored prior to the flare. We also found that a linear combination of several parameters shows a much better correlation with the intensity of flare/CME events than each parameter itself.

The aforementioned work are mainly based on TRACE observations, in which we infer the sheared field information from the flare footpoints. However, the X-ray telescope (XRT) on board the newly launched *Hinode* spacecraft provides direct observations of highly sheared coronal loops at various stages. XRT observations of two X-class flares occurred last December show that part of the sheared core field erupted, and another part of the sheared core field stayed behind during the flares, which may explain why a large part of the filament is still seen by TRACE after the flare. We also find that the post-flare core field is clearly less sheared than the pre-flare core field, which is consistent with the idea that the energy released during the flares is stored in the highly sheared fields prior to the flare. At last, we explored the NLFFF modeling of a simple bipolar active region (NOAA 10953), which produced several small flares (mostly B class and one C8.5 class) and filament activations from April 30 to May 3 in 2007. These events appear to be associated with the frequent flux cancellations (SOHO/MDI) that occurred in the region close to the polarity inversion line. We constructed a series of NLFFF models for this active region at three times, using the flux-rope insertion method. The models are constructed based on MDI magnetograms, and constrained by H α filaments and highly sheared loops observed by XRT. We find good NLFFF models that fit the observations before the C8.5 flare, but not for the case after the flare. The flux rope contains highly sheared but weakly twisted magnetic fields. Before the C8.5 flare, this active region is close to an eruptive state: the axial flux in the flux rope is close to the upper limit for eruption.

Chapter 1

Introduction

1.1 Observations of Solar Eruptions

1.1.1 Solar Flares

A flare is defined as a sudden, rapid, and intense variation in brightness. A solar flare is an enormous explosion in the solar atmosphere, involving sudden bursts of particle acceleration, plasma heating, and bulk mass motion (for extensive discussions of solar flares see Švestka 1976, 1981; Sturrock 1980; Priest 1981; Tandberg-Hanssen & Emslie 1988; Švestka et al. 1992). Solar flares produce radiation across virtually the entire electromagnetic spectrum, from radio waves at the long wavelength end, through optical emission to x-rays and gamma rays at the short wavelength end (see Figure 9.1 in Golub & Pasachoff 1997). X-rays and UV radiation emitted by solar flares can affect Earth's ionosphere and disrupt long-range radio communications. Direct radio emission at decimetric wavelengths may disturb operation of radars and other devices operating at these frequencies.

Most flares occur in active regions around sunspots, where intense magnetic fields emerge from the Sun's surface into the corona. Flares are powered by the sudden (timescales of minutes to tens of minutes) release of magnetic energy stored in the corona. The amount of energy released is the equivalent of millions of 100-megaton hydrogen bombs exploding at the same time! As the magnetic energy is being released, particles, including electrons, protons, and heavy nuclei, are heated and accelerated

in the solar atmosphere. The energy released during a flare is typically on the order of 10^{27} ergs per second. Large flares can emit up to 10^{32} ergs of energy. This energy is ten million times greater than the energy released from a volcanic explosion. On the other hand, it is less than one-tenth of the total energy emitted by the Sun every second.

The frequency of flares coincides with the Sun's eleven year cycle. When the solar cycle is at a minimum, active regions are small and rare and few solar flares are detected. These increase in number as the Sun approaches the maximum part of its cycle. The Sun will reach its next maximum in the year 2011, give or take one year.

History of Solar Flare Research

The first recorded observation of a solar flare was made by R. C. Carrington in 1859 at his private observatory at Redhill, outside London. Carrington (1859) was engaged in his daily sunspot drawing in the forenoon on 1 September 1859 when he first noticed the flare (Figure 1-1). The white-light emission was initially visible at points A and B and during the courses of five minutes moved about 50000 km to points C and D where it vanished as two rapidly fading dots of white light. Carrington expressed surprise that the 'conflagration' had in no way alerted the appearance of the sunspot group which he had finished drawing before the occurrence. Fortunately, Carrington's observation was confirmed by Hodgson (1859), an amateur astronomer who was observing nearby.

The history of flare research can be divided into three main periods (for a detailed review see Švestka & Cliver 1992). The first period from 1859-1934 spans the careers of Carrington and Hale. This period is notable for the relative lack of progress. The published 'record' of major flares for this 75 year interval encompasses only about 35 events, consisting of fortuitous observations of white-light flares, reports

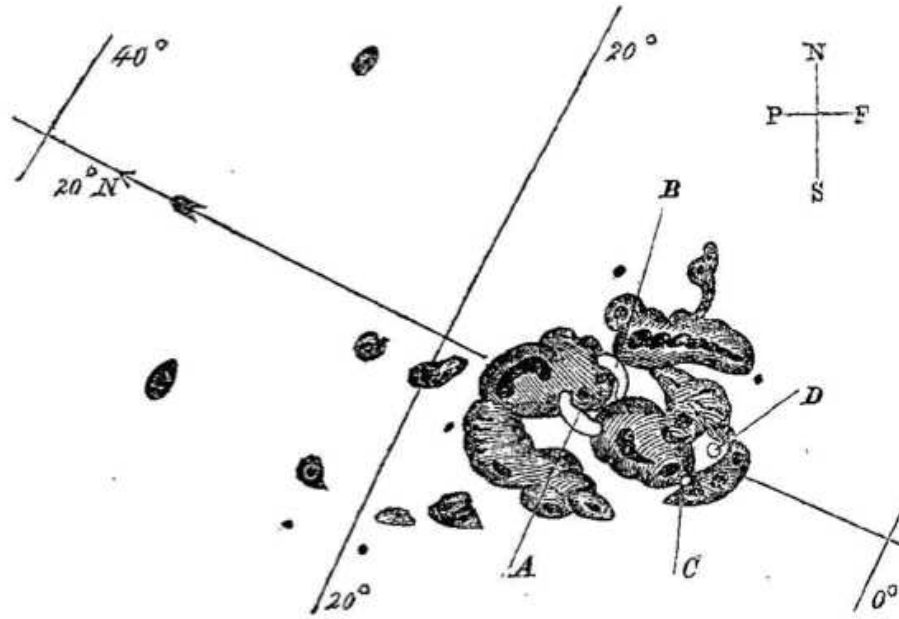


Figure 1-1 Sketch of the first reported solar flare. The flare was observed by Carrington in white light on 1859 September 1 (Carrington 1859). White regions marked as A, B, C, and D are the flaring regions.

by early spectroscopists of reversals of line emission near sunspots, and, after 1892, flares observed with the Hale spectroheliograph. With this spectroheliograph, Hale obtained the first published photographs of a solar flare on 15 July 1892 (Figure 3 in Švestka & Cliver 1992).

The spectrohelioscope (an instrument that allowed the entire Sun to be scanned visually at selected wavelengths) developed by Hale during the 1920s was responsible for the rapid advance in the knowledge of flares that took place in the next era of flare research from 1935-1963. The institution of a world-wide flare patrol brought significant advances in knowledge of flares in the 1930s and 1940s and new ‘window’ were opened to observe flares at short (soft X-ray, which was indicated by the sudden ionospheric disturbances; Kreplin et al. 1962) and long (radio) wavelengths. In the 1950s and 1960s metric radio bursts were related to trapped energetic electrons and shocks, and two-ribbon flares were associated with energetic protons in space.

Radio and X-ray observations gave evidence for two basic types of flare processes: an impulsive phased followed by a long-duration or gradual phase. It was found that flares were often preceded by filament activations, and growing loop prominence systems were recognized as the limb counterpart of two-ribbon disk flares. This ‘middle’ era of flare research has a data survey and classification character that is well-captured by the book ‘Solar Flares’ by Smith and Smith (1963).

The modern era, since 1963, is characterized by space observations and a trend toward synthesis indicated by the development of increasingly sophisticated and comprehensive models of the flare phenomena. The early 1970s brought Skylab observations of coronal mass ejections (CMEs) and arcades of coronal soft X-ray loops above two-ribbon flares. In the mid-1970s, the Kopp-Penuman reconnection model, based on configurations proposed earlier by Carmichael, Sturrock, and Hirayama, provided a framework in which the newly discovered CMEs could be related to the basic characteristic of two-ribbon flares. The 1980s brought key new results from SMM and *Hinotori* including images of hard X-ray flares and large-scale coronal structures associated with eruptive flares. The key new results from *Yohkoh* in the 1990s are: evidence for on-going magnetic reconnection in solar flares, i.e., cusp-shaped soft X-ray arcades in long-duration flares and above-the-loop-top hard X-ray sources in impulsive flares; sigmoidal soft X-ray structures in active regions identified as signatures of the likely onset of flares and CMEs; arcade formation and coronal dimming identified as the soft X-ray counter part of a CMEs (Kosugi & Acton 2002). In the 2000s, RHESSI (Lin et al. 2002) has provided the first capability for gamma-ray imaging as well as high-resolution spectroscopy of ion-produced gamma-ray lines and X-ray imaging spectroscopy of the bremsstrahlung radiation from energetic electrons. One of the key new results of RHESSI is gamma-ray line imaging of solar flares implies spatial differences in acceleration and/or propagation between the flare-accelerated

ions and electron (Hurford et al. 2003, 2006).

Classification of Solar Flares

Solar flares are classified according to their size, duration, morphology or magnetic topology and the composition of their associated energetic particles (Cliver 2000).

We review two types of classifications that used in this thesis.

Size Classification of Solar Flares: Soft X-ray

There are only two widely used classification systems that address flare ‘size’ or ‘importance’. The first of these is the H α classification scheme (see Table 2.1 in Švestka 1981) that was developed during the 1930s. A second size classification that has come into common usage since about 1970 is based on the integrated total output of soft X-rays detected from the Sun in the 1–8 Åband by Earth-orbiting satellites, such as the GOES satellites. The size of the flare is given by the peak intensity (on a logarithmic scale), in $\text{erg cm}^{-2} \text{s}^{-1}$. As shown in Table 1.1, the letters A, B, C, M and X are used to represent increasing intensities in order-of-magnitude increments. Thus a B-flare has a peak intensity of $10^{-4} \text{ erg cm}^{-2} \text{ s}^{-1}$. If the peak intensity happens to be 3×10^{-4} , the flare is designated B3. Generally, flares smaller than C1 can only be detected during a solar cycle minimum when the X-ray background is low. Flares occasionally exceed class X9 in intensity; they are simply referred to as X10, X11 etc events (Cliver 2000).

A second size classification that has come into common usage since about 1970 is based on the integrated total output of soft X-rays detected from the Sun in the 1–8 Åband by Earth-orbiting satellites, such as the Geostationary Operational Environmental Satellite (GOES). The size of the flare is given by the peak intensity (on a logarithmic scale), in $\text{erg cm}^{-2} \text{ s}^{-1}$. As shown in Table 1.1, the letters A, B, C, M and X are used to represent increasing intensities in order-of-magnitude increments. Thus

Table 1.1. The X-ray classification of solar flares

Class	Intensity (erg cm ⁻² s ⁻¹)	I (W m ⁻²)
A	10 ⁻⁵	10 ⁻⁸
B	10 ⁻⁴	10 ⁻⁷
C	10 ⁻³	10 ⁻⁶
M	10 ⁻²	10 ⁻⁵
X	10 ⁻¹	10 ⁻⁴

a B-flare has a peak intensity of 10^{-4} erg cm⁻² s⁻¹. If the peak intensity happens to be 3×10^{-4} , the flare is designated B3. Generally, flares smaller than C1 can only be detected during a solar cycle minimum when the X-ray background is low. Flares occasionally exceed class X9 in intensity; they are simply referred to as X10, X11 etc events (Cliver 2000).

Classification of Solar Flares in Terms of Morphology (Magnetic Topology)

In this classification, there are two main types of flare, which appear to require different physical mechanisms (Priest 1981).

1) *Simple-Loop or Compact Flare (Confined Flare)*

Most flares and subflares are of this type. It is a small flare, in which essentially a single magnetic loop or flux tube brightens in X-rays and remains apparently unchanged in shape and position throughout the event (see Figure 1.2 in Priest 1981). The loop may have a structure consisting of several (or a continuum of) loops and may cause a simple brightening in H α at the feet of the loop. Simple-loop flare vary considerable in size, and we may see brightened arches that comprise a whole fully developed active region, as well as short-lived brightenings of tiny X-ray bright points not detectable at all in the chromosphere. Generally, compact flares are short-duration impulsive flares that not associated with CMEs.

2) *Two-Ribbon or Eruptive Flare (Ejective Flare)*

All major flares are of this type. It is much larger and more dramatic than

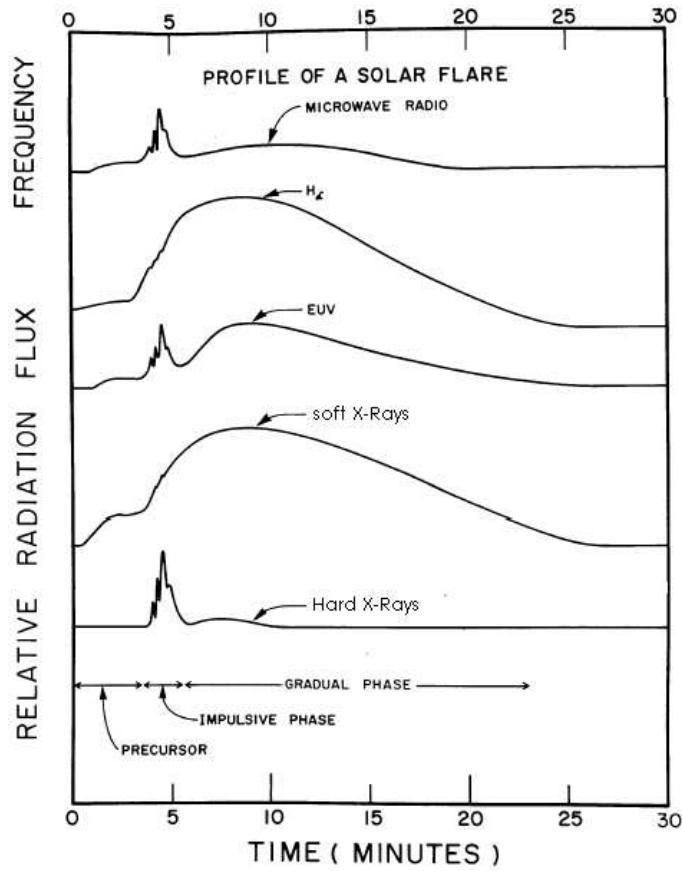


Figure 1-2 A schematic representation of the different phases of a solar flare as observed in the electromagnetic and particle radiation (from Kane 1974).

a compact flare and generally occurs along a polarity inversion line (PIL) in the photospheric magnetic field and is seen in $H\alpha$ on the disc as two bright ribbons expanding outward from the polarity inversion line. Frequently, they are seen to be connected by a rising arcade of so-called “post”-flare loops (see Figure 1.4 in priest 1981 and Figure 1.3 in this thesis). Two-ribbon flares are usually long-duration gradual flares associated with CMEs.

Multi-wavelength Observations of Solar Flares

The flare observed by Carrington (1859) was an example of a relatively rare event – a large white light flare – in which the optical continuum is enhanced sufficiently

over the background photospheric field to be visible in contrast. Most flares are not so conspicuous in visible light; they reserve their strongest enhancements for spectral lines such as $H\alpha$, and they also radiate copious amounts of energy in extreme ultraviolet (EUV) and soft X-ray wavebands (Tandberg-Hanssen & Emslie 1988). Figure 1-2 shows the intensity of emission as a function of time for an average flare – to the extent that such averaging is meaningful, since each flare is different – at a variety of wavelengths which are typically available for flare detection. These range from the radio and optical, which are available from ground-based facilities, through soft and hard X-rays, which are available only from instruments placed on satellites or high-altitude balloons. Images of different flares in each of these wavelengths are shown in Figure 1-3. Figure 1-2 shows that the flare presents a very different appearance in terms of intensity versus time at these different wavelengths. These differences in appearance imply that flares may have several different phases, possibly representing a series of different physical occurrences, or a series of steps through which the flare instability evolves (Golub & Pasachoff 1997). A flare can, in general, be roughly divided into three phases: *preflare phase*, *impulsive phase* and *main (or gradual) phase*.

(1) *Preflare phase*

In the preflare phase, one often see the flare precursors at various wavelengths. Gaizauskas (1989) defines a precursor as “a transient event preceding the impulsive phase, possibly even before the onset and not necessarily at the site of the flare itself”. Such events may include homologous and sympathetic flares, soft X-ray and Ultraviolet (UV) precursors (see Figure 1-2), microwave activity, and filament activations. Homologous flares are earlier flares in the same location with similar emission patterns. Sympathetic flares are earlier flares in different locations, but erupting in near synchronism. Soft X-ray precursors are transient enhancements in soft X-rays. lasting

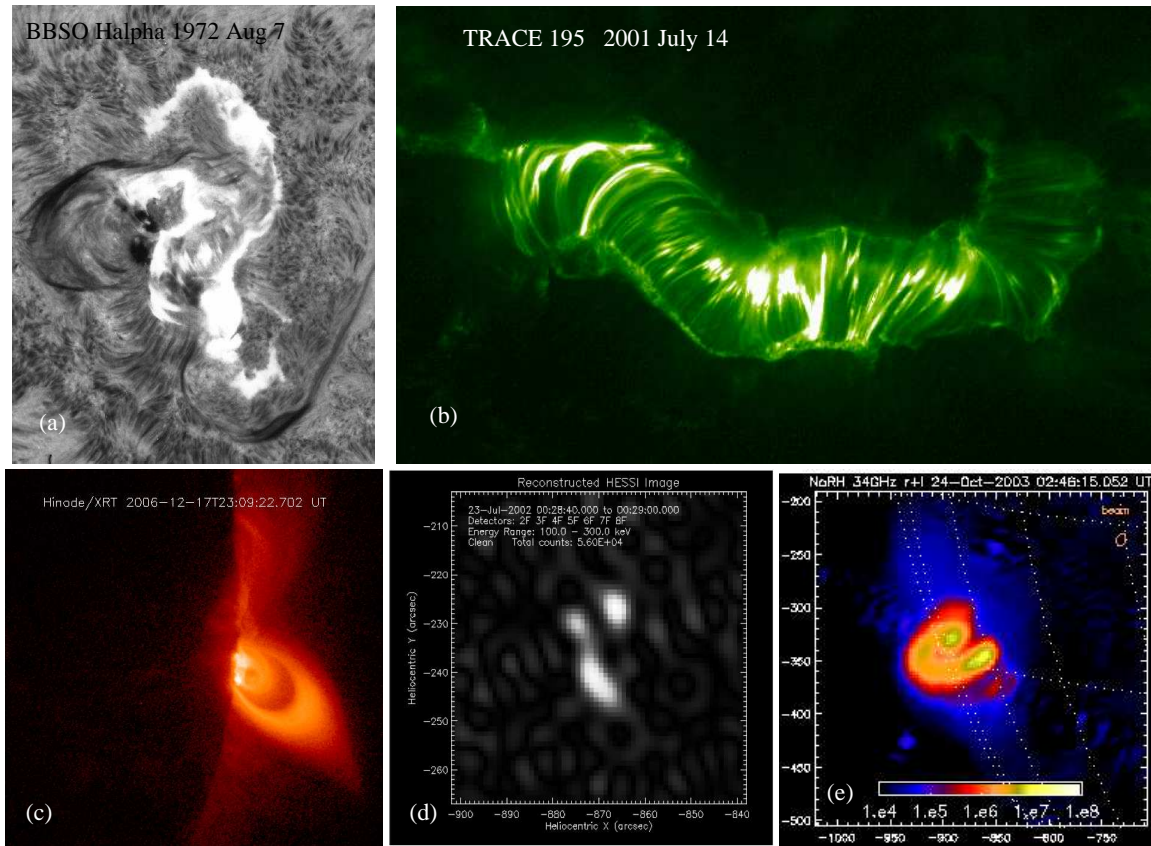


Figure 1-3 Images of different solar flares at different wavelengths. (a) The great ‘Seahorse Flare’ of August 7th, 1972, and this image in the blue wing of H α (BBSO) shows the two-ribbon structure late in the event with bright H-alpha loops connecting the ribbons. (b) TRACE EUV Post-flare loops of the famous ‘Bastille Day Flare’ observed at 194 Å on 2000 July 14. (c) Soft X-ray cusp-shape post-flare loop observed by *Hinode*/XRT on 2006 December 17. (d) and (e) Hard X-ray and Microwave images of different flares observed by RHESSI and Nobeyama Radioheliograph, respectively.

for several minutes, that occur in loops or unresolved kernels at, or close to, flare sites. UV precursors are mostly small-scale transient brightenings above active regions, and they exhibit a broad range of amplitudes. Radio precursors, most often observed in microwave, consists of changes in intensity and/or polarization of radiowaves emitted from an active region, tens of minutes before the onset of a flare. One should note that none of the precursors given above is both *necessary* and *sufficient* for a flare. One of the earliest precursor signatures reported is the activation of filaments and prominences (Martin & Ramsey 1972), consisting of morphological changes and darkening of filaments some minutes to tens of minutes before the first H α brightenings. For a detailed review of the precursors, see Gaizauskas (1989).

(2) *Impulsive phase*

The impulsive phase of a flare is characterized by intense, rapid, and spiky emissions in γ -rays, hard X-rays, and radio. There are also associated emissions at other energies, such as EUV and optical, generated as a result of the thermal response of the atmosphere to the rapid energization associated with this phase (see Figure 1.2). Physically, the impulsive phase corresponds to the sudden release of stored magnetic energy into various forms, including accelerated particles, heating of plasma, bulk acceleration of fluid, and enhanced radiation fields (Tandberg-Hanssen & Emslie 1988).

During the impulsive phase of a two-ribbon flare, two ribbons of H α (UV and EUV) emission form (Figure 1-3a), one on each side of the polarity inversion line and, throughout the main phase, the ribbons move apart at 2–10 km s⁻¹. Frequently, they are seen to be connected by a rising arcade of so-called “post”-flare loops in the main phase. Nonthermal emission in hard X-ray (bremsstrahlung emission) and microwave (gyrosynchrotron emission) appear when strong energy releases occur, and the sites of the radiation sources indicate where the energy is released. In hard X-rays, the dominant morphology is the double footpoint source, although single compact sources

or multiple components are also frequently seen (Figure 1-3d; Sakao 1994). The microwave emission traces out the entire volume accessible to nonthermal electrons (Figure 1-3e). There are two types of microwave sources, i.e., both loop-top source and double-footpoint sources, and footpoint emission dominates at high frequencies (Bastian et al. 1998).

(3) *Main phase*

After its initial abrupt release in the impulsive phase of a flare, the energy is transported to other regions of the atmosphere, often as it changes form. New areas of the atmosphere are affected, mainly due to heating, and it is this interplay of energy transport and atmospheric response that we refer to as the main or gradual phase of the flare (Tandberg-Hanssen & Emslie 1988).

Most flares (compact flare) are short lived and they simply cool during the main phase, decaying within minutes or tens of minutes. However, the other kind of flares, i.e., two-ribbon flares, continue to release energy during their main phase, and in those flares the decay is much longer: in some events it can continue for many hours. “Post”-flare loops are observed during the main phase of two-ribbon flare. These loop systems are observed to rise upward slowly into the corona (see Figure 7.3 in Pneuman 1981). The velocity of ascent decreases with height from about 10–20 km s⁻¹ at the beginning to a fraction of a km s⁻¹ when they are finally observed in soft X-rays at great heights. Hot loops (soft X-ray, Figure 1-3c) are first formed and often show a cusp shaped structure (Figure 1-3c; Tsuneta et al. 1992; Forbes & Acton 1996), then shrink and subsequently cooled to EUV ($\sim 10^5$ K, Figure 1-3b) and H α temperature (10^4 K, Figure 1-3a). The term “post”-flare as applied to these systems is, unfortunately, quite misleading, since it implies that the phenomenon occurs after the flare and is somehow a byproduct of the flare process. This designation probably originated historically, because the loops were firstly clearly seen on the limb in H α

only after the system had risen quite high in the corona; that is, unless the flare occurred exactly on the limb, the loops lower down would not be clearly see against the disk. Nowadays, the comprehensive multi-wavelength observations indicate that the “post”-flare loops are a major aspect of the flare.

1.1.2 Prominence Eruptions

Prominences are relatively cool and dense objects that are embedded in the hotter solar corona and are commonly observed above the solar limb in emission in $H\alpha$, the first spectral line of the Balmer series of neutral hydrogen (Gilbert et al. 2001). When seen projected against the solar disk, prominences appear in $H\alpha$ as dark features called “filaments” (see Figure 1-4). Often a prominence reaches downward towards the chromosphere in a series of regularly spaced feet, which resemble great tree trunks. These feet are often located at supergranule boundaries and are joined by huge arches as shown in Figure 1-4b. Although prominences and filaments are now known to be the same structures, they were originally identified as distinct objects. We use the terms “filament” and “prominence” interchangeably in general context. The term prominence is used to describe a variety of objects, ranging from relatively stable structures with life times of many months, to transient phenomena that last for hours, or less. They have been classified in several different ways, but there appear to be two basic types (Priest 1989) :

(1) A *quiescent prominence* is in its global appearance an exceedingly stable structure and may last for many months. It may begin life as a relatively small active-region (or plage) filament, which is located either along the polarity inversion line between the two main polarity regions of an active region or at the edge of an active region where it meets a surrounding region of opposite polarity. Sometimes it may enter a sunspot from one side. As the active region disperses, the prominence grows thicker

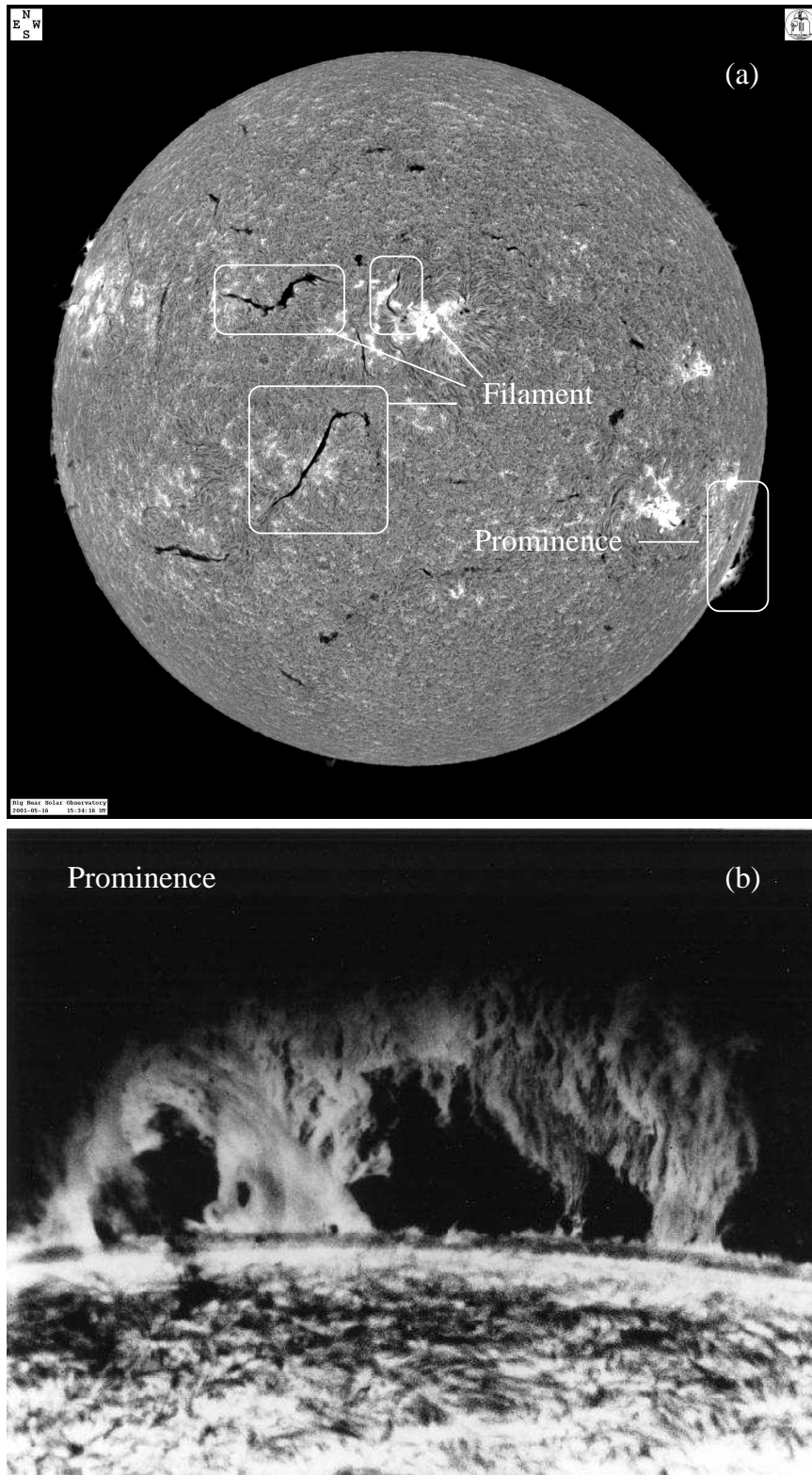


Figure 1-4 Filaments and Prominences observed in H α by BBSO.

and longer to become a quiescent filament. It may continue growing for many months up to 10^6 km in length, and in the process it migrates slowly towards the nearest pole.

(2) *Active prominences* are located in active regions and are usually associated with solar flares. They are dynamic structures with violent motions and have life-times of only minutes or hours. There are various types, such as surges, sprays (probably erupting plage filaments) and loop prominences: both their magnetic field (about 100 G) and average temperature are higher than for quiescent prominences.

Prominences are formed in “channels” where the chromospheric fibrils are aligned with PIL (Foukal 1971; Martin 1990, 1998; Gaizauskas et al. 1997; Gaizauskas 1998). This alignment indicates the presence of a horizontal axial magnetic field directed along the length of the channel. A handedness property known as ‘chirality’ has been discovered for filament channels and filaments (Martin et al. 1994). If we view the filament from the positive polarity side, a filament has an axial magnetic field directed to the right is called ‘dextral’, while a ‘sinistral’ filament has an axial field directed to the left. This so-called chirality of filaments is correlated with latitude on the Sun. Martin et al. (1994) showed that the mid-latitude filaments on the northern hemisphere are predominantly dextral, while those in the south are predominantly sinistral.

Filament activation encompasses a wide array of phenomena, including oscillating, eruption, rising/falling, rotating, and counter-streaming, and so on (Gilbert 2007, private communication). Here we only discuss the eruptive-like dynamic activity (which a portion of a prominence lifts significantly in a short period of time, at least $0.1 R_s$ in less than 1 hour) in filaments. Prominence eruptions (“disparition brusque” in French) were observed by D’Azambuja (1955) using daily spectroheliograms from the Meudon Observatory in Paris. He found that prominences tend to erupt and reform in their original place, and that many erupt more than once. Two images of

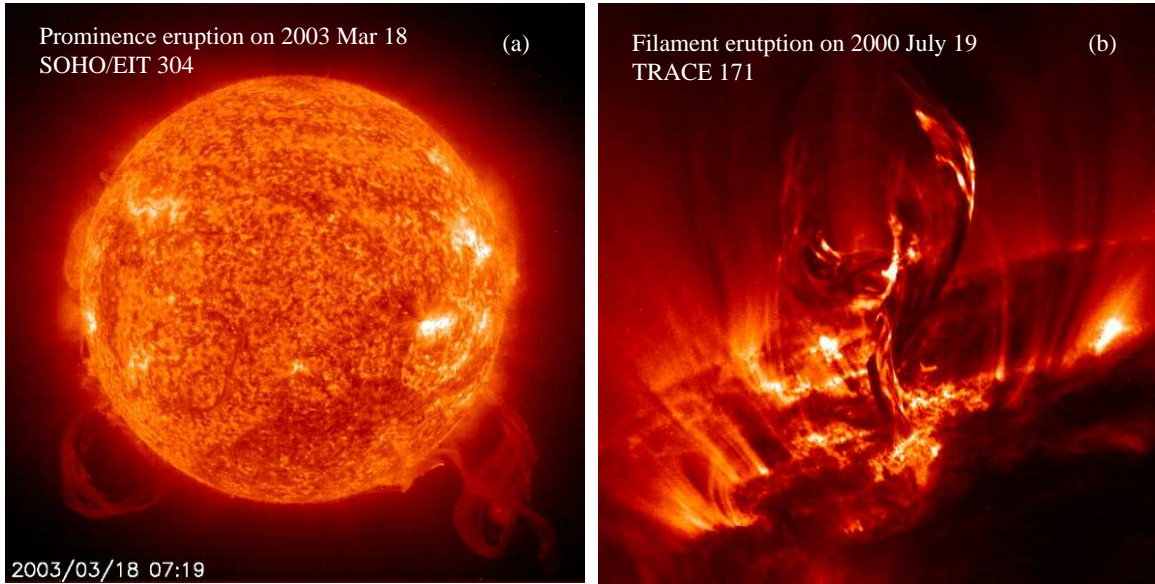


Figure 1-5 Images of filament/prominence eruptions in EUV. (a) Two large eruptive prominences observed by SOHO/EIT at 304 \AA on 2003 March 18. (b) A filament eruption observed by TRACE at 171 \AA on 2000 July 19.

filament/prominence eruptions are shown in Figure 1-5. Modern advanced studies show that prominences exhibit a wide range of eruptive activity behavior including dramatic activation with the filament mass remaining confined to the low corona (e.g. Ji et al. 2003; Alexander et al. 2006), the eruption of part of the observed filament structure (Tang 1986; Gilbert et al. 2000; Pevtsov 2002; Gibson 2002), and the almost complete eruption of all of the prominence mass (e.g. Tang 1986; Plunkett et al. 2000).

To help elucidate the relation between the filament mass and corresponding supporting magnetic structure, Gilbert et al. (2007) developed observational definitions of “full”, “partial”, and “failed” eruptions. A “full eruption” is defined to occur when the entire magnetic structure erupts while containing the bulk (approximately 90% or more) of the pre-eruptive filament mass (i.e., the mass escapes without draining or settling back to the surface). “Failed eruptions” are defined by the dynamical evolution of the filament, which displays an initially eruptive-like acceleration persisting

for a relatively short duration prior to a period in which the filament decelerates, reaching a maximum height as the mass in the filament threads drains back toward the Sun (Alexander et al. 2006). In the other words, in a “failed” eruption none of the lifted filament mass nor the supporting magnetic structure escapes the solar gravitational field, although this does not preclude localized dynamic activity, heating and flare production (see Figure 1 in Alexander et al. 2006). “Partial” eruptions are more complicated to define observationally, since the coupling of the filament mass and its supporting magnetic structure create a couple of different sub-categories in this class. The first type of partial eruption occurs when the entire magnetic structure erupts containing either some or none of its supported pre-eruptive filament mass. The second type of partial eruption occurs when the magnetic structure itself partially escapes containing either some or none of the filament mass.

1.1.3 Coronal Mass Ejections

Coronal mass ejections (CMEs) are transient phenomena in the solar corona that expel a large amount of plasma and magnetic flux into interplanetary space. The concept of mass leaving the Sun was thought possible over 100 years ago from the observations of prominence material that was seen to be moving outward at speeds in excess of the escape velocity (for a historical review see Howard 2006). Mass ejections may be identifiable (in retrospect) on eclipse photographs from 1860 (Eddy 1974) and 1893 (Cliver 1989). However, the first coronagraph observations of CMEs were made by the space-borne coronagraph on board the Orbit Solar Observatory-7 (Tousey 1973) and Skylab (Gosling et al. 1974; MacQueen et al. 1974) in the early 1970s. Typical coronagraphs have an occulting disk to artificially eclipse the bright photosphere, so CME is detected because of photospheric light Thomson-scattered off free electrons in the corona. After Skylab, the most extensive observations of

CMEs were made by the coronagraphs in space such as those in the SOLWIND (1979-1985; Michels et al. 1980), SMM (Solar Maximum Mission; 1980 and 1984-1989; MacQueen et al. 1980), and SOHO (Solar Heliospheric Observatory, 1995-now). CMEs are now routinely observed from the ground with the Mark III (MK3) K-Coronameter at the MLSO (Mauna Loa Solar Observatory; Fisher et al. 1981). The CME observed by the aforementioned instruments is a projection of a three-dimensional object projected onto a flat image, in the plane of the sky. This provides a few very basic questions. Is the CME loop representing the projection of a bubble, a loop or an arcade? The latest mission with a coronagraph is the STEREO (Solar TERrestrial RELations Observatory) mission which was launched in October 2007. The mission objective is to understand the 3D nature of CMEs, their initiation and propagation. To do this, STEREO will send two identically instrumented spacecraft into a heliospheric orbit, one leading Earth and one trailing.

CMEs often display spatial structures, commonly referred to as the ‘three-part-structure’ (a bright frontal loop, a dark cavity, and a bright core; Hundhausen 1999). Figure 1.6 shows a time sequence of SMM coronagraph images showing a typical CME initiation and eruption observed in white light. This CME originates from a helmet streamer that has been slowly rising or swelling outward days before the eruption. A clear three-part structure of the CME is seen. The frontal loop overlies the cavity, which contains the bright core. The core has shown to be the eruptive prominence by comparing coronagraph and $H\alpha$ observations. Eclipse pictures often show the three-part structure in the pre-eruptive stage, where the helmet streamers takes the place of the frontal loop. Not all CMEs show the three-part structure either due to geometrical reasons (Cremades et al. 2004) or due to the nature of the source region (Gopalswamy 2006).

The basic attributes of a CME are its speed, width, acceleration, and central

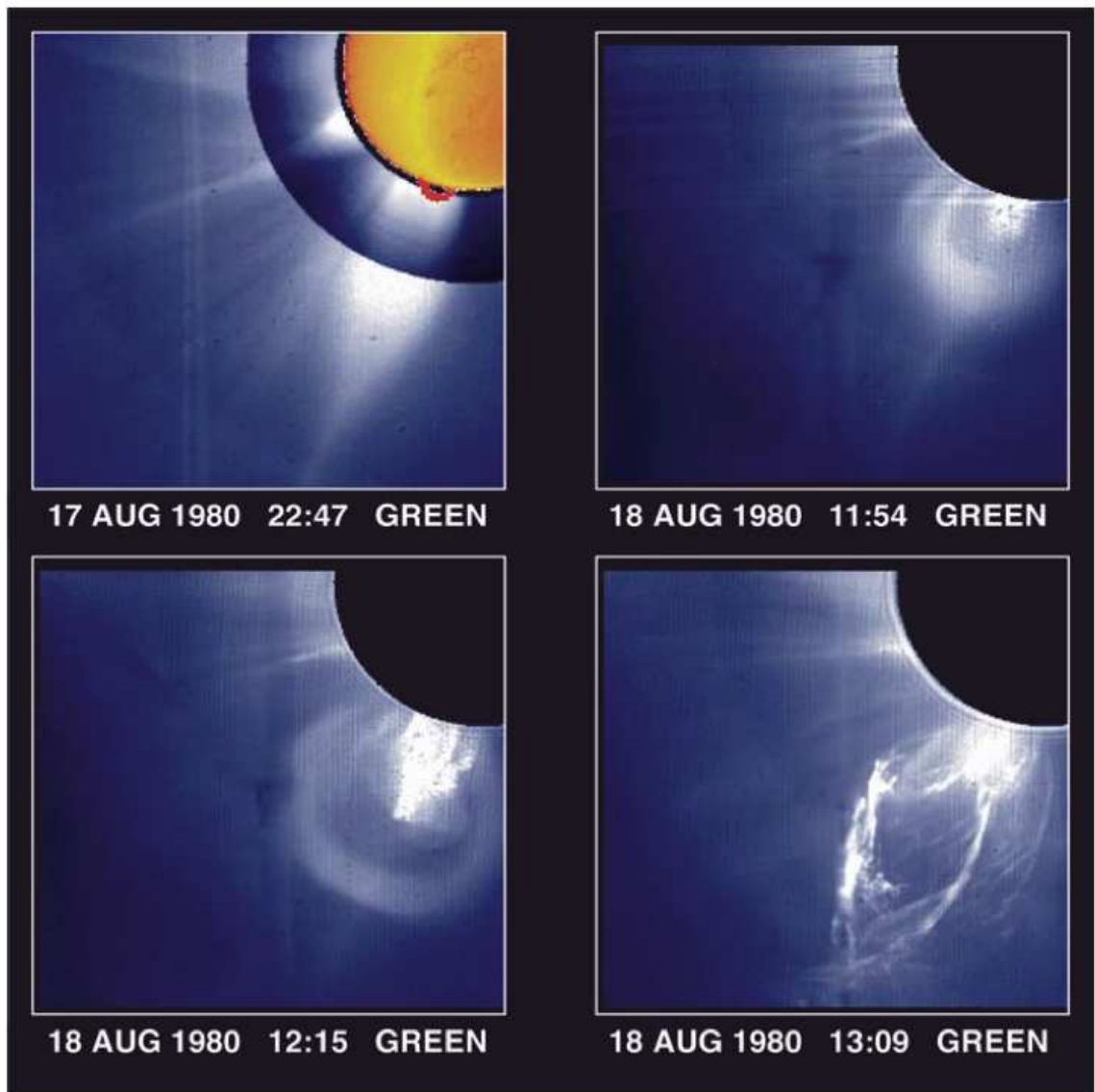


Figure 1-6 Images of a CME observed by SMM. A time sequence of SMM coronagraph images showing a CME on 1980 August 18, from Hunhausen (1999).

position angle (CPA), all with reference to the sky plane (Gopalswamy 2006). These are obtained from a time sequence of coronagraphic images, in which the CME can be recognized as a moving feature occupying a well-defined region. The angular extent of the moving feature defines the width. The central angle of this extent with reference to the solar north is CPA. The speed is normally determined from a linear fit to the height-time (h-t) plots. But CMEs often have finite acceleration, so the linear-fit speed should be understood as the average value within the coronagraphic field of view. Quadratic fit to the h-t plots gives the constant acceleration, which again is an approximation because the acceleration may also change with time.

The measured sky-plane speed ranges from a few km s^{-1} to $\sim 3000 \text{ km s}^{-1}$ (see Gopalswamy 2006; and references therein), with an average value of $\sim 483 \text{ km s}^{-1}$. The CME speed has a lognormal distribution (Yurchyshyn et al. 2005). Most of the height-time plots fall into three types: accelerating, constant speed, and decelerating, indicating different degrees of propelling and retarding forces acting on CMEs (Gopalswamy et al. 2001). The mass of a CME is estimated as the excess mass in the coronagraphic field of view assuming that the entire mass is located in the sky plane (see Vourlidas et al. 2002). The mass changes during the early phase of the CME before stabilizing to a new-constant value, which is used as the representative mass. The mass ranges from a few times 10^{13} g to more than 10^{16} g . The kinetic energy obtained from the measured speed and mass ranges from $\sim 10^{27} \text{ erg}$ to $\sim 10^{32} \text{ erg}$, with an average value of $5 \times 10^{29} \text{ erg}$. Some very fast and wide CMEs have kinetic energies exceeding 10^{33} erg , generally originating from large active regions (Gopalswamy et al. 2005).

The apparent angular width of CMEs ranges from a few degrees to more than 120° , with an average value of $\sim 46^\circ$. The average width was computed for CMEs with width $\leq 120^\circ$. Depending on their width, CMEs are categorized as nonhalo,

partial halo, and full halo to CMEs with width lower than 120° , between 120° and 320° and greater than 320° , respectively (Lara et al. 2006). The true width of halo CMEs (Howard et al. 1982), which appear to surrounding the occulting disk, is unknown.

The CME plasma is multithermal with the prominence core at ~ 8000 K and the outer structure at a few MK. Occasionally, CMEs may consist of flare ejecta with temperature exceeding 10 MK. The magnetic field in CMEs is not directly measurable near the Sun. The magnetic field in prominences is typically up to 30 G, while it can exceed 1000 G in the active region cores. The field strength in the outer corona is typically less than ~ 1 G. The coronal cavity overlying the filament may also have field strengths higher than the overlying corona for pressure balance requirements.

How frequently do CMEs occur? The occurrence of CMEs shows a strong solar cycle dependence. During solar minimum, one CME occurs every other day. The rate goes up to several per day during solar maximum. The daily CME rate averaged over Carrington Rotations (27.3 days) was found to exceed 6/day during solar cycle 23 (See Figure 3 in Gopalswamy 2006).

1.1.4 Relationship between Solar Flares, Prominence Eruptions, and CMEs

Solar flare, filament eruptions, and coronal mass ejections (CMEs) are the most important solar events as far as space weather are concerned, linking solar eruptions, major interplanetary disturbance, and geomagnetic storms (Gosling et al. 1991).

The majority of flare activity arises in active regions which contain sunspots, while CMEs can also originate from decaying active regions and even so-called quiet solar regions which contain a filament. Two classes of CME, namely flare-related CME events and CMEs associated with filament eruption are well reflected in the evolution of active regions, flare related CMEs mainly occur in young active regions containing

sunspots and as the magnetic flux of active region is getting dispersed, the filament-eruption related CMEs will become dominant (Schmieder & van Driel-Geszteli 2005). This is confirmed by statistical analyses.

Flare-CME relationship

The relationship between flares and CMEs remains a topic of active research. As far back as 1979, it was realized that there was an association between flare activity and CMEs by Munro et al. (1979), who found that approximately 40% of CMEs they studied were associated with flares, while about 70% were associated with filament eruptions.

Since not all CMEs are associated with flares, many authors worked to determine the conditions under which the two types of solar phenomena are linked (Reeves 2006). Observations using the coronagraph on Skylab indicated that CMEs associated with flares tend to be fast (averaging 775 km s^{-1}), while those associated with eruptive prominences tend to be slow (averaging 330 km s^{-1}) (Gosling 1976). Observations with the K-Coronameter at MLSO (MacQueen & Fisher 1983) and the SOHO/LASCO (Sheeley et al. 1999; Andrews & Howard 2001; Moon et al. 2002) have also indicated that flares tend to be associated with high-speed CMEs. Combining their results with the results by Gosling et al. (1976), MacQueen & Fisher (1983) put forward the concept of two distinct classes of CMEs: the flare-associated ones, being accelerated impulsively at low heights, and the non-flare CMEs accelerated gradually over a large height range. As many authors tried to find and discuss differences between CMEs associated with flares and those without flares, Svestka (1986) instead pointed out in the first place that in both these cases the cause of the CME is the same: an opening of magnetic field lines, previously closed in the form of arcades or helmet streamers, along the zero line of the longitudinal magnetic

field; the only difference between flare-associated and non-flare-associated CMEs is the strength of the magnetic field in the region where the opening takes place (see also Svestka 1992, 1995, 2001). St. Cyr and Webb (1991) arrived at a similar conclusion when studying 73 CMEs observed by the SMM. Later on, through a large data sample from SOHO/LASCO, Vršnak et al. (2005) found that both of these two types of CMEs show quite similar characteristics, contradicting the concept of two distinct (flare/non-flare) types of CMEs. The non-flare CMEs show characteristics similar to CMEs associated with flares of soft X-ray class B and C, which is indicative of a “continuum” of events rather than supporting the existence of two distinct CME classes. On the other hand, they also found that CMEs associated with major flares are on average faster and broader than non-flare CMEs and small-flare CMEs.

There has also been research investigating which type of flare tends to be associated with a CME. Sheeley et al. (1975) studied spatially resolved Skylab observations obtained during long-duration (>4.5 hr) soft X-ray events (LDEs) seen with the SOLRAD spacecraft. Their observations suggested that all LDEs are accompanied by CMEs and that most LDEs were accompanied by filament eruptions. With observations made by the Solwind coronagraph, Sheeley et al. (1983) found that the longer the duration of an X-ray event, the higher the probability of an associated CME. Webb & Hundhausen (1987) found that most of the soft X-ray events associated with the CMEs observed by SMM in 1980 were LDEs. Harrison (1995) reviewed the previously published studies relating CMEs and X-ray flares and concluded: flares associated with CMEs tend to have longer durations than average flares. However, flares of any duration can be associated with CMEs; Brighter flares are more likely to be associated with CMEs. With GOES and SOHO/LASCO observations, Andrews (2003) found that thresholds of 6.0×10^{-5} W m⁻² in peak flux, 0.07 J m⁻² in total flux, and 4 hours in duration independently allow a 95% confidence in predicting

that a CME will be observed. For flares with peak flux and duration below these thresholds, the fraction of flares with CME candidates is independent of the observed value of peak flux or duration.

There are also several studies regarding the timing relationship between flares and CMEs. The CME onset time, which has to be extrapolated using the observations above the occulting disk, is found to be randomly located within windows tens of minutes wide around the flare onset time (Harrison 1995). Prior to the SOHO observations, the ground-based MK3 K-Coronameter of the High Altitude Observatory (occulter from 1.3 to 2.2 R_{\odot} ; Fisher & Poland 1981) provides a viable tool to observe CMEs at low coronal heights. By examining individual events based on combined MK3 and SMM observations, it has been demonstrated that CMEs start almost simultaneously with the accompanying flares (Maxwell, Dryer, & McIntosh 1985; Dryer 1994), or CMEs onset a few minutes earlier than the flare onset time (Hundhausen 1999). Using observations made by LASCO and EIT (the Extreme Ultraviolet Imaging Telescope) onboard SOHO, Zhang et al. (2001) found that for all of the events studies, the initiation phase of the CME comes before the onset of the corresponding flare. In general, the CME onset appears to lead the flare onset, but there are also cases that flares appear to lead the CME onsets (Harrison 1991, 1995).

Overall, the flare-CME relationship can be summarized as follows: (1) There is a strong statistical association between flares and CMEs, but there is NOT a one to one association between flares and CMEs; (2) There is a “continuum” of events rather than two distinct (i.e., flare/non-flare) types of CMEs. On the other hand, CMEs associated with major flares are on average faster and broader than non-flare CMEs and small-flare CMEs; (3) Longer Duration Flares (LDE) have a greater chance of association with a CME, but a CME can be associated with a flare of any duration, or can be associated with no flare at all; (4) The onset of a CME associated with a

flare appears to occur at any time within several tens of minutes of the flare onset; i.e. either can appear to lead the other; (5) The scale sizes of CMEs and flares are very different; the average CME spans some 45 degrees whereas active regions are typically much smaller than 10 degrees in size; (6) The flare tends to lie anywhere within the span of an associated CME, and often lie to one side.

Most of these points except point 2 are from Harrison (1995), who gave a thorough review of numerous pre-SOHO studies and also presented a statistical study of the flare-CME relationship. These pre-SOHO conclusions are consistent with many recent SOHO studies, for a recent review on the flare-CME relationship please refer to Harrison (2006). These observations led Harrison (1995, 1996) to conclude : “The flare and CME are both consequences of the same magnetic ‘disease’. They do not cause one another but are closely related. Their characteristics are the results of local conditions, and thus, we may witness a spectrum of flare and CME properties which are apparently unrelated, even resulting in events without the flare or CME component.” The idea that the flare and CME do not cause one another but are different responses to the same driver has become a common conclusion with a few exceptions (e.g., Khan & Hudson 2000).

Filament Eruption-CME relationship

The majority of previous statistical studies regarding the connection between filament (or prominence) eruptions and CMEs have focused on prominences because they could easily be detected, observed, and measured against the dark sky background. Moreover, CMEs, associated with the prominences, are not difficult to detect. Many prominence classifications have been proposed in the past. For example, Gilbert et al. (2000) developed definitions of active prominences (APs) and eruptive prominences (EPs) and studied the relationship between APs, EPs, and CMEs for 54 events. They

found that 94% of the EPs had an associated CME compared to only 46% for APs. Gopalswamy et al. (2003) defined a prominence as a radial or a transverse event. Authors showed that the radial events have a strong correlation to the CMEs: 83% of the radial events were associated with CMEs compared to 24% for transverse events. Jing et al. (2004) defined a “filament eruption” as a solar activity event with significant upward motion and with at least 50% of the material vanishing during the course of a day. Through a statistical study of 106 filament eruptions observed by BBSO, they found that: (1) excluding eight events with no corresponding LASCO data, 55% or 56% of 98 events were associated with coronal mass ejections (CMEs); (2) active region filament eruptions have a considerably higher flare association rate of 95% compared to quiescent filament eruptions with 27%, but a comparable CME association rate, namely, 43% for active region filament eruptions and 54% for quiescent filament eruptions.

In summary, the correlation between a CME and a solar flare depends on the energy that is stored in the relevant magnetic structure, which is available to drive the eruption: the more energy that is stored, the better the correlation is; otherwise, the correlation is poor (Svestka 1986; Lin 2004). The correlation between solar flares and CMEs depends on the strength of the magnetic field in the source region – strong fields obviously can store more flare energy. The correlation between a CME and eruptive prominence, on the other hand, depends on the plasma mass concentration in the configuration prior to the eruption. If the mass concentration in the source region is significant, CME will be associated with filament eruptions, otherwise, a CME develops without an apparent associated eruptive prominence.

1.2 Theories of Solar Eruptions

Solar flares, prominence eruptions, and CMEs are believed to be different manifestations of a single physical process that involves a disruption of the coronal magnetic field (Harrison 1996, Forbes 2000). Any attempt to explain solar eruptions has to account for two basic aspects of eruptive processes (Priest & Forbes 2002). The first aspect is the fundamental cause of the eruption itself, and the second is the nature of the morphological features that form and develop during the eruptive process. Such features include the rapid ejections of large amount of magnetic flux and plasma into interplanetary space, separating two bright $H\alpha$ ribbons on the solar disk, and rising soft X-ray and $H\alpha$ loop systems in the corona.

1.2.1 Theories of Solar Flares

As mentioned previously, the most conspicuous features of a two-ribbon flare are the two long flare ribbons which expanded laterally away from a polarity inversion line in the photospheric magnetic field of the active region. When the separation of the ribbons became obvious, loops connecting the flare ribbons became visible. An upward expansion of these loops is apparent, with the expansion speeds being about $5\text{--}10\text{ km s}^{-1}$. A classical description of flare loops, as seen in $H\alpha$ image, was first given by Bruzek (1964) who noted that the ribbons essentially lie at the footpoints of the loop system, which forms an arcade of loop. Doppler-shift measurements show that the apparent motions of the loops and ribbons are not caused by mass motions of the plasma, but rather by the continual propagation or mapping of an energy source onto new field lines (Schmieder et al. 1987). High resolution observations also show that cooler loops are nested below hotter ones, with the coolest loop, seen in $H\alpha$, rooted at the inside edges of the ribbons (Roy 1972; Rust & Bar 1973). By contrast, the hottest loops, seen in X-rays, are rooted in the outer portions of the ribbons (Moore

et al. 1980).

The standard model for two-ribbon flares has been developed by the following pioneering researchers: Carmichael (1964), Sturrock (1968), Hirayama (1974), and Kopp-Pneuman (1976). Svestka & CLiver (1992) gave a detailed review of this standard model, which was also called as CSHKP model by Sturrock (1992) in the same proceedings book. At first, Carmichael (1964) presciently proposed the general magnetic configuration and the relationship of eruptive flares with the yet-to-be-discovered CMEs. Sturrock (1968) proposed the first quantitative model of such flares, invoking reconnection to account for particle acceleration, ejected plasma, and the formation of the two bright footpoints in the chromosphere. Later on, Hirayama (1974) modeled the flare-associated dynamic events, including evaporation of chromospheric gas into coronal loops. His pioneering work was followed two years later by the widely accepted Kopp & Pneuman (1976) model of field opening and sequentially reconnecting field lines. The modern version (Figure 1-7) of the standard model is based on the CSHKP model and advanced by many later studies (see Forbes & Acton 1996; Lin & Forbes 2000, and references therein). For reviews of the current flare and CME models, please refer to Forbes (2000), Priest & Forbes (2002), Lin et al. (2003), and Zhang & Low (2005).

The preflare magnetic field in the CSHKP configuration becomes unstable (due to instability or an outer trigger), opens, and the open field lines subsequently reconnect. A dark filament, if present, manifests the field opening by its eruption and an associated CME may propagate into interplanetary space (Figure 1-7, top). Thermal conduction from the reconnected field lines, or particles bombardment from the reconnection site, then provides energy source for the ribbon emissions at chromospheric (e.g., $H\alpha$) and transition-region wavelengths (UV, EUV). This reconnection process also causes ‘chromospheric evaporation’ (i.e., the expansion of chromospheric

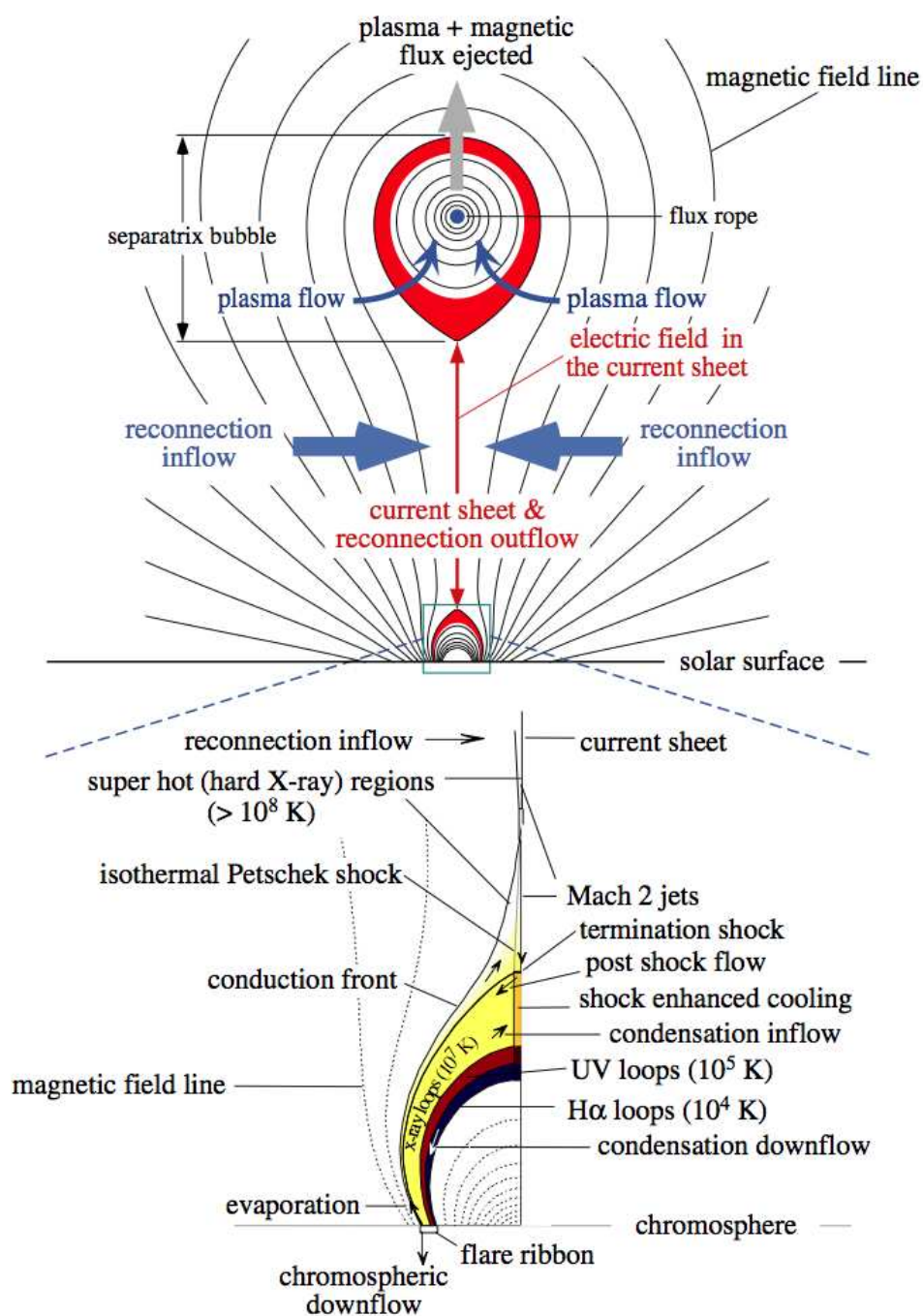


Figure 1-7 Schematic diagram of a disrupted magnetic field that forms in an eruptive process. Catastrophic loss of equilibrium, occurring in a magnetic configuration including a flux rope, stretches the closed magnetic field and creates a Kopp-Pneuman-type structure. This diagram is created by incorporating the traditional two-ribbon flare model (*bottom*, from Forbes & Acton 1996) with the CME model (top) of Lin & Forbes (2000). Colors denote the different hierarchies of plasma in the configurations.

plasma up into the corona), through energetic particle beams (Sturrock 1973; Lin & Hudson 1976) and/or conduction fronts (Hirayama 1974; Antiochos & Sturrock 1978; Forbes & Acton 1996), which fills up the postflare loops with hot and dense plasma (see, e.g., Kopp & Pneuman 1976; Cargill & Priest 1983; Forbes, Malherbe, & Priest 1989). The rise of the loop system is explained by the fact that the reconnection site continually move upward as more and more magnetic field lines reconnect. This picture automatically accounts for the apparent motion of flare ribbons without the existence of any actual plasma flow in the ribbons. It also explains why the hottest X-ray loops are at the top of the loop system, since the hottest loops should be the ones that are higher in altitude and closer to the reconnection site and the loops at lower altitude are the ones that have had time to cool down (Figure 1-7 bottom).

The aforementioned work provide a good interpretation for the two-ribbon (ejective) flares, which are only one type of solar flares as mentioned earlier. The other type, i.e., simple-loop or confined flare was first thought to require a different physical mechanism (Priest 1981). But more recent observations (e.g., Yohkoh) lead more researchers to believe both eruptive and compact flares can be interpreted by one unified model based on the CSHKP model. After a review of various evidence of magnetic reconnection revealed by Yohkoh SXT/HXRT observations, Shibata (1999) proposed a unified model, '*plasma-induced-reconnection model*', to explain not only LDE flares (eruptive flares) and impulsive flares (compact flares) but also microflares and X-ray jets. Through MHD simulations, Török & Kliem (2005) found that the helical kink instability of a twisted magnetic flux rope can produce both ejective and confined flares. The decrease of the overlying field with height is a main factor in deciding whether the instability leads to a confined event or to a CME. Based on the similarity of the onsets of ejective and confined flares observed by Yohkoh/SXT, Moore et al. (2001) concluded that both ejective and confined flares were unleashed

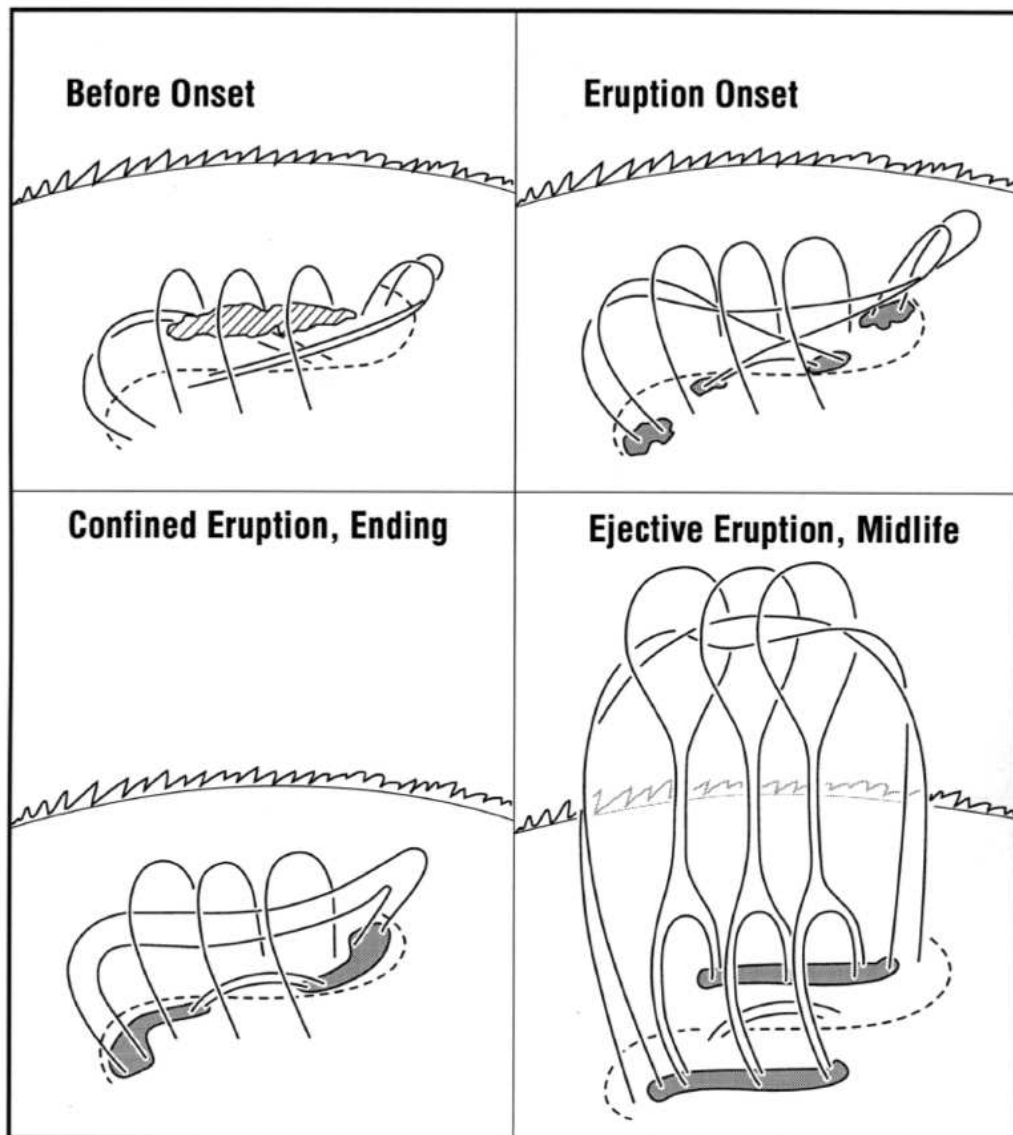


Figure 1-8 A 3D version of the standard model for the magnetic field explosion in single-bipole eruptive solar events (from Moore et al. 2001). This version is tailored to bipoles having sigmoidally sheared and twisted core fields and accommodates confined explosions as well as ejective explosions. The rudiments of the field configuration are shown before, during, and after the onset of an explosion that is unleashed by internal tether-cutting reconnection. The dashed curve is the photospheric neutral line, the dividing line between the two opposite-polarity domains of the bipole's magnetic roots. The ragged arc in the background is the chromospheric limb. The gray areas are bright patches or ribbons of flare emission in the lower atmosphere at the feet of reconnected field lines, field lines that we would expect to see illuminating in soft X-ray images. The diagonally lined features above the neutral line in the top left panel is the filament that is often present in sheared core fields.

by runaway tether-cutting via explosive reconnection in the middle of the sigmoid, as in the standard model. A three-dimensional (3D) version of the standard model made by Moore et al. (2001) is shown in Figure 1-8.

1.2.2 Models of Coronal Mass Ejections

There are two broad classes of models for CMEs (Lin et al. 2003). The first category requires the magnetic energy to be quickly injected into the corona magnetic field leading the latter to expand explosively during the eruption. The other category requires the energy to be slowly stored in the corona magnetic field prior to the eruption. The former mechanism is known as the dynamo or injection models and the latter corresponds to the energy storage model.

The dynamo model was initially proposed by Sen and White (1972), Heyvaerts (1974), Kan et al. (1983), and Hénoux (1986). In these models, the actual energy source of the eruption comes from a dynamo region hidden in the convection zone, and an eruption occurs when a field aligned current is produced in a loop by the sudden motion of the plasma in the dynamo region (see Figure 4a in Lin et al. 2003). The existing form of the current dynamo model does not address the cause of the sudden motions of the plasma in the convection zone, and thus it really fails to explain the eruptive mechanism (Lin et al. 2003). Melrose & McClymont (1987) have shown that the concept of a photospheric dynamo of this type is grossly inconsistent with the observed properties of the photosphere and the way it coupled to the regions above and below it. Similar to the situation of an injection current via a convection dynamo, a flux injection model was proposed by Chen (1989, 2001). In this model, the poloidal magnetic flux and the power is impulsively injected to the corona to cause an eruption. This model is also problematic since the predicted displacement of the photospheric material during the flux injection has ever been observed (Lin et

al. 2003).

The most commonly accepted solar eruption models now assume that the energy released during eruptions is stored in the coronal magnetic field prior to the eruption. These models transfer energy from the convection zone over long time scale (i.e., tens of hours or even a couple of days). The continual emergence of new flux from the convection zone and the movement of the footpoints of closed coronal field lines causes stresses to build up in the coronal field. Eventually, these stresses exceed a threshold beyond which a stable equilibrium can no longer be maintained, so the coronal field erupts. The models are based on the mechanism of accumulating energy in the coronal magnetic field, so they are thought of as the storage model.

According to Zhang & Low (2005), we will discuss various CME models by dividing them into two groups, i.e., analytical models and numerical models. These two types of models are different approaches, taken in order to mathematically understand the same physical process of the CMEs. The numerical techniques allow solution of the whole set of MHD equations that govern the evolution of a magnetized plasma system and to investigate various parameters that are used to describe the evolution in detail. In contrast, the analytical method cannot incorporate too many details, and considers only a few essential parameters that fundamentally govern the system in order to find the solutions in closed form. Advantageously, the analytical models allow a thorough investigation of the response of the system to variation of basic parameters that specify the background field (Lin et al. 2003).

Analytical models

One example of the analytical models is the “mass-loading model” developed by Low and his collaborators (Low & Hundhausen 1995; Low 1996, 2001). In this model, the weight of a prominence and a coronal helmet plays a central role in anchoring

a levitating flux rope of twisted magnetic fields containing the prominence. This model captures the three-part structure of the CMEs. The bright front of the CME is interpreted to be the disrupted coronal streamer. The existence of the flux rope, as the central driver of the CME, can explain the cavity structure commonly observed around a quiescent prominence (Zhang & Low 2005). In this model, the weight of the prominence could act as a (rigid) lid that allows the magnetic energy to increase above the open limit, and when the lid is suddenly removed, the field springs outward. However, many CMEs do not appear to contain any prominence material, so it seems unlikely that such a mechanism could explain all CMEs (Lin et al. 2003).

Another example is the “catastrophe model” developed by Forbes and his collaborators (Forbes 1990; Forbes & Isenberg 1991; Isenberg et al. 1993; Lin & Forbes 2000, Lin et al. 2001). In this model, CMEs are initiated by a catastrophic loss of equilibrium. By constructing a series of magnetic equilibria to represent a quasi-static evolution, they find that a dynamical catastrophe can be triggered by various mechanisms controlled, for example, by the parametric variations of the flux rope or the background. The catastrophe can also be triggered by new-flux emergence and again the strengths and the positions of the emerging flux can influence when the catastrophe will happen. The key point is that, although in most cases magnetic properties such as the heights of the prominence (represented by a detached flux rope) evolve smoothly along a quasi-static evolution curve (see Figures 3a–3e in Forbes & Isenberg 1991), beyond a critical point and an abrupt jump in the equilibrium height can appear (Figure 3f). With this jump, a vertical current sheet will form behind the flux rope. If magnetic reconnection sets in to dissipate the current sheet, the flux rope may completely fail to find equilibrium and rise through the solar atmosphere as a CME.

Numerical models

One representative numerical model is the “break-out model”, which is developed by Antiochos et al. (1999). It is a 2.5D numerical simulation carried out using an ideal MHD code in spherical geometry. Recently, a 3D version of the break-out model has been developed (Lynch et al. 2005). This model requires a multipolar magnetic configuration and identifies magnetic reconnection as a key signature of a CME. By shearing the footpoints of a magnetic arcade to a critical point, they find that magnetic reconnection between the sheared arcade flux and the neighboring flux will set in to trigger an eruption. Reconnection will remove the unsheared field lying over the sheared arcade to allow the latter, very-low-lying magnetic field line, to open up to infinity.

Sheared arcades also play an important role in the CME initiation model by Linker and collaborators (Linker & Mikić 1995; Linker et al. 2001). In this numerical model, flux cancellation in a sheared arcade causes a flux rope to erupt. This model is closely related to the loss-of equilibrium models discussed previously, and was inspired by an analytical model that includes the forces due to a curved flux rope (Lin et al. 1998).

Amari and coworkers (1996, 1999, 2000, 2003a, 2003b) presented a series of ideal and resistive numerical calculations using a 3D resistive MHD code in Cartesian geometry. In their calculations, the magnetic energy is built up by twisting the footpoints of an initial bipolar potential field (Figure 1 in Amari et al. 2003a). After building up a certain amount of magnetic energy and magnetic helicity in this way (Figure 5 in Amari et al. 2003a), the footpoint twisting is stopped and the field is allowed to relax to a nearly force-free equilibrium. The flux rope can be made to erupt by one of several ways: by flux cancellation at the boundary (Amari et al. 2000), by further imposing footpoint converging motions (Amari et al 2003a), or by imposing the diffusion of the boundary normal field beyond a certain threshold (Amari et al.

2003b). When these eruptions occur, the rising flux rope resembles a three-part CME as indicated by Figure 11 in Amari et al. (2003a).

Other CME-related numerical simulations include the flux emergence trigger model (Chen & Shibata 2000; Chen et al. 2002); the repeated ejections model (Choe & Lee 1996; Cheng et al. 2003); the numerical catastrophe model (Hu & Jiang 2001; Hu 2001; Hu, Li, & Xing 2003); the flux rope-streamer interaction model (Guo, Wu, & Tandberg-Hanssen 1996; Wu et al. 1995, 1997, 1999). In Chen & Shibata's model, the emerging flux can trigger magnetic reconnection and cause a preexisting flux rope to have a CME-like expulsion. In Choe and Cheng's model, an anomalous nonuniform resistivity is applied to reproduce reconnection and repeated plasma ejections. Hu and coworkers' models demonstrate the catastrophe effect numerically, both in Cartesian plane and in spherical geometry. In Wu and coworker's model, CMEs are triggered by the interaction between a preexisting flux rope and its overlying helmet-streamer or by the interaction between an emerging flux rope and the preexisting flux rope.

In summary, none of the existing CME models can answer all of the common questions (e.g., why an eruption should occur by naming an instability or a catastrophe and why the development following from it should be the particular kind? How the CME is accelerated out of the corona and what its fate is in interplanetary space? Zhang & Low 2005) and explain all the observations related to CMEs. Each addresses one or a few of them. Put together, the CME models have two common features. One is a sheared or twisted magnetic field as an initial state to store the energy required for the CME. The other is the occurrence of magnetic reconnection.

1.3 Instruments

In this thesis we used observations at various wavelengths obtained both with ground-based and with space-based instruments. The multi-wavelength observations from various instruments provide information of different layers of the solar atmosphere, i.e., from the photosphere, chromosphere, transition region, inner corona, to the outer corona. The primary data sources in this thesis are from the *Transition Region and Coronal Explorer* (TRACE) and the X-ray Telescope (XRT) onboard *Hinode*.

1.3.1 TRACE

The TRACE satellite, launched on 2 April 1998 in Universal Time (UT), is a NASA (National Aeronautics and Space Administration) Small Explorer (SMEX) mission to image the solar photosphere, transition region and corona with high spatial and temporal resolution (Handy et al. 1999). TRACE enables solar physicists to study the connections between fine-scale magnetic fields at the solar surface and the associated plasma structures in the solar outer atmosphere in a quantitative way. The instrument features a 30 cm Cassegrain telescope with a field of view (FOV) of 8.5×8.5 arc minutes and a spatial resolution of $1''$ ($0.''5/\text{pixel}$). Normal incidence multilayer optics capable of observing from the photosphere to the corona enable TRACE to follow the evolution and dynamics of the solar atmosphere at selected temperatures over the range of 6000 K – 10 MK. The TRACE temperature response at different wavelengths is listed in Table 1.2. The TRACE observatory is a spacecraft in a sun-synchronous polar orbit. This allows for continuous uninterrupted solar observing for approximately 9 months each year. For the remaining 3 month eclipse season, the view from part of the TRACE orbit is occulted by the Earth. The instrument is described in detail by Handy et al. (1999). The initial-flight performance is reviewed by Golub et al. (1999) and Schrijver et al. (1999).

Table 1.2. TRACE Temperature Response (from Handy et al. 1999)

Wavelength (Å)	Emission	Bandwidth (Å)	Temperature (K)
171	Fe IX/X	6.4	$1.6\text{--}2.0 \times 10^5$
195	Fe XII/XXIV	6.5	$5.0\text{--}20 \times 10^5$, $1.1\text{--}2.6 \times 10^7$
284	Fe XV	10.7	$1.25\text{--}4.0 \times 10^6$
1216	H I Ly α	84	$1.0\text{--}3.0 \times 10^4$
1550	C IV	30	$6.0\text{--}25 \times 10^4$
1600	UV Cont, C I, Fe II	275	$4.0\text{--}10 \times 10^3$
1700	Continuum	200	$4.0\text{--}10 \times 10^3$
5000	White Light	broad	$4.0\text{--}6.4 \times 10^3$

1.3.2 *Hinode*/XRT

The *Hinode* satellite (previously called Solar-B) is a Japanese mission developed and launched by ISAS (Institute of Space and Astronautical Science)/ JAXA (Japan Aerospace Exploration Agency), with NAOJ (National Astronomical Observatory of Japan) as domestic partner and NASA and STFC (Science and Technology Facilities Council, UK) as international partners. It is operated by these agencies in co-operation with ESA (European Space Agency) and NSC (Norwegian Space Centre, Norway). *Hinode* is designed to study the interaction of surface magnetic fields with the solar atmosphere, including the generation of small-scale fields through the surface dynamo action, the transport and dissipation of magnetic field in the atmosphere, and associated energetic events. *Hinode* (Kosugi et al. 2007) is equipped with three advanced solar telescopes, i.e., the X-ray Telescope (XRT), the Solar Optical Telescope (SOT), and the EUV Imaging Spectrometer (EIS). It was launched on 22 September 2006 UT.

The XRT is a high-resolution grazing-incidence telescope, which provides unprecedented high resolution and high cadence observations of the X-ray corona through a wide range of filters. XRT can “see” emission for a range of temperatures $6.1 < \log T < 7.5$, with a temperature resolution of $\Delta(\log T) = 0.2$. Temperature discrim-

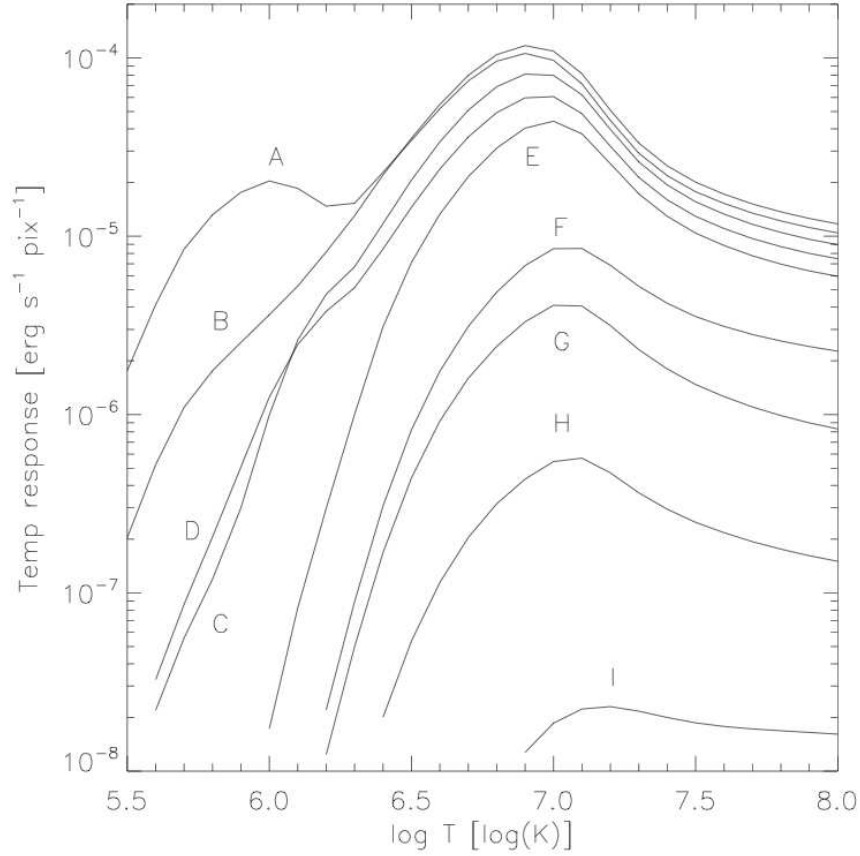


Figure 1-9 The total XRT temperature response for all of the X-ray focal-plane filters (from Golub et al. 2007). Each curve plots the combination of the total instrument response (as $f(\text{wavelength})$) with a coronal plasma emission model (ATOMDB/APEC) for a columnar emission measure of 10^{30} cm^{-5} . The labels indicate which filter is in the path, as follows: A=Al-mesh, B=Al-poly, C=C-poly, D=Ti-poly, E=Be-thin, F=Be-med, G=Al-med, H=Al-thick, and I=Be-thick.

ination is achieved with a set of diagnostic filters (nine X-ray filters in total) in the focal plane. The XRT temperature response by filter is shown in Figure 1-9. The XRT also contains visible light optics. The focal plane detector of XRT is a $2\text{k} \times 2\text{k}$ back-illuminated CCD with $1.''0$ per pixel, giving a $2000''$ field of view (FOV) which can see the entire solar disk. Details of the XRT instrumentation and performance can be found in DeLuca et al. (2005), Golub et al. (2007), and Kano et al. (2007).

1.3.3 Other Instruments

SOHO

The *Solar and Heliospheric Observatory* (SOHO; Domingo et al. 1995) is a cooperative mission between ESA and NASA (National Aeronautics and Space Administration) to study the Sun, from its deep core to the outer corona, and the solar wind. SOHO was launched on December 2, 1995, and placed in a halo orbit around the Sun-Earth L1 Lagrangian point. Twelve main instruments are equipped on SOHO, and six of them are for the observation of the solar atmosphere. Observations from two instruments, i.e., MDI (Michelson Doppler Imager) and LASCO (Large Angle and Spectroscopic Coronagraph) are used in this thesis.

MDI– With MDI (Scherrer et al. 1995) we can obtain the line-of-sight component of the photospheric magnetic field. The temporal resolution is 96 min in routine observation, but 1 min in campaign observations. In full-disk mode each magnetogram consists of $1024'' \times 1024''$ with a pixel size of about $2''$, while in high-resolution mode each magnetogram consists of $1024'' \times 1024''$ with a pixel size of about $0.''6$.

LASCO– LASCO (Brueckner et al. 1995) comprises three coronagraph, C1, C2, and C3, that together image the solar corona from 1.1 to $30 R_{\odot}$ (C1: $1.1-3 R_{\odot}$, C2: $1.5-6 R_{\odot}$, C3: $3.7-30 R_{\odot}$). A coronagraph is a telescope that is designed to block light coming from the solar disk, in order to see the extremely faint emission from the corona. The C1 coronagraph is a newly developed mirror version of the classic internally-occulted Lyot coronagraph, while the C2 and C3 coronagraphs are externally occulted instruments.

GOES

The *Geosynchronous Operational Environmental Satellites* (GOES) are a series of meteorology observing satellites operated by NASA. GOES monitors space weather via

its onboard Space Environment Monitor (SEM) system. The three main components of space weather monitored by GOES at 35,000 Km altitude are: X-rays (X-ray Sensor), energetic particles (Particle Sensor), and magnetic field (Magnetometer). The data used in this thesis are from the X-ray Sensor (XRS), which provides the whole-sun X-ray fluxes for the 0.5-to-3 (0.5-to-4 prior to GOES-8) Å and 1-to-8 Å wavelength bands. The National Geophysical Data Center (NGDC) of the United States provides both high (three-second average) and low (one-minute average) temporal resolution data from GOES/XRS.

Yohkoh

The *Yohkoh* (Ogawara et al. 1999) satellite, an observatory for studying X-rays and γ -rays from the Sun, was launched in 1991 August. *Yohkoh* is a project of the ISAS (the Institute for Space and Astronautical Sciences, Japan). It was built in Japan and completed as an international collaboration with the United States and the United Kingdom. The *Yohkoh* spacecraft has four instruments, i.e., Bragg Crystal Spectrometer (BCS), Hard X-ray Telescope (HXT), Soft X-ray Telescope (SXT), and Wide Band Spectrometer (WBS). The light curves of solar flares from HXT are used in this thesis.

RHESSI

The *Ramaty High Energy Solar Spectroscopic Imager* (RHESSI, Lin et al. 2002) satellite is a NASA Small Explorer mission designed to explore the basic physics of particle acceleration and explosive energy release in solar flares, through imaging and spectroscopy of hard X-ray/ γ -ray continua emitted by energetic electrons, and of γ -ray lines produced by energetic ions. RHESSI was launched on February 5, 2002 and has been operated smoothly since then. The spatial resolution is as fine as $\sim 2.''3$

with a full-sun ($\geq 1^\circ$) field of view, and the spectral resolution is $\sim 1\text{--}10$ keV FWHM over the energy range from soft X-rays (3 keV) to γ -rays (17 MeV).

***Hinode*/SOT**

The Solar Optical Telescope (SOT; Tsuneta et al. 2007) on board *Hinode* is the largest aperture, most advanced solar telescope flown in space. The G band and Ca II H data used in this thesis are from the Broadband Filter Imager (BFI) of SOT. The BFI produces photometric images with broad spectral resolution in 6 bands (CN band, Ca II H line, G band, and 3 Continuum bands) at the highest spatial resolution available from the SOT ($0.0541''/\text{pixel}$) and at rapid cadence (<10 s typical) over a $218'' \times 109''$ FOV. The scientific capabilities of SOT are described in detail by Shimizu (2004).

BBSO, KSO, and MLSO

Full disk $H\alpha$ observations made by Big Bear Solar Observatory (BBSO, California) and the Kanzelhöhe Solar Observatory (KSO, Austria) are used in this thesis. Each of these two stations has a $2K \times 2K$ pixel CCD detector available to monitor the Sun with a spatial resolution of $1''/\text{pixel}$ and a cadence of at least 1 image per minute (Steinegger et al. 2000). We also used $H\alpha$ observations made by the *Polarimeter for Inner Coronal Studies* (PICS) which have been operated by the High Altitude Observatory at the Mauna Loa Solar Observatory (MLSO) since 1994 (Gilbert et al. 2000). The full disk $H\alpha$ images taken by PICS with 3 minutes temporal cadence have a spatial resolution of $2.''9$.

1.4 Fundamental Questions in Solar Eruptions

In this section, we summarize the current status of the solar flare/CME research (focus on the magnetic nature) based on the following fundamental key questions: How and where is the flare/CME energy stored? What is the trigger of the energy release? How and where is the energy released?

How and where is the flare energy stored?

It is well accepted that solar flare, prominence eruption, and coronal mass ejection are different manifestation of a single physical process that is related to the release of the magnetic free energy stored in the corona prior to the eruption. The magnetic free energy is stored by a change in photospheric boundary conditions, such as emerging flux (Zirin 1983; Heyvaerts et al. 1977), flux cancellation (Martin et al. 1985), or sunspot motions (Gesztelyi et al. 1986). Storage of free energy requires a nonpotential magnetic field, and it is therefore associated with a shear or twist in the corona away from the potential, current-free state (Priest & Forbes 2002). Shear before flares is often observed in the chromosphere, as shown in $H\alpha$ fibrils (Tanaka & Nakagawa 1973) and also in the photosphere, as shown in vector magnetograms near the polarity inversion line (Hagyard et al. 1984). These are suggestive of shear in the overlying corona (but sometimes there are significant differences in orientation between $H\alpha$ structures and photospheric magnetic fields (Gary et al. 1987). An indication of a stressed magnetic field in the corona is the presence of a prominence and another important one discovered by Canfield et al. (1999) with *Yohkoh* is the presence of sigmoidal structures.

Despite all the progress, there are still questions yet to be answered, such as, are there reliable precursors of flare/CME events? Can we predict flares/CMEs? What is the coronal magnetic configuration prior to the flare? From plasma structures ob-

served at various wavelengths, it appears that the field is in the form of a sheared arcade or half-emerging flux rope. The two possibilities are essentially indistinguishable unless the axis of the flux rope rises above the surface (Forbes 2000). This leads to the two competing models for the pre-CME magnetic configuration. Some models (e.g., Forbes & Isenberg 1991; Gibson & Low 1998; Wu et al. 1999; Krall et al. 2000; Roussev et al. 2003) assume that a magnetic flux rope exists prior to the solar eruption. However, the other models (e.g., Mikić et al. 1988; Mikić & Linker 1994; Antiochos et al. 1999; Amari et al. 2003a; Manchester 2003) relies on the existence of sheared magnetic arcades. The later models may create a flux rope by reconnection between the sides of the arcade during the eruption process.

What is the trigger of the energy release?

The trigger of energy release is model-dependent and must be inferred retrospectively, by comparing observations with the prediction of a model. In various CME models, eruption usually results from variations in the boundary, such as flux emergence, loss of the loaded mass, converging motion, or flux cancellation at the boundary (Zhang & Low 2005). Eruption may also result from the variations of source drivers themselves, such as twisting the field beyond a critical point. Moore & Sterling (2006) discussed three different mechanism that singly or in combination can trigger the CME: (1) runaway internal tether-cutting reconnection, (2) runaway external tether-cutting reconnection, and (3) ideal MHD instability or loss of equilibrium. For most eruptions, sorting out from observations which of these various possibilities is the trigger apparently requires (at least) high-cadence, high-resolution movies in chromospheric, transition-region, and coronal emission, such as are provided by TRACE and *Hinode*, along with high-cadence, high-resolution magnetograms.

How and where is the energy released?

It is generally believed that magnetic reconnection occurred somewhere in the corona is responsible for the ribbons and the set of rising post-flare loops, and such a process is well supported by numerical experiments and detailed observations from *Yohkoh*. The magnetic energy released via reconnection is then converted to thermal (plasma heating) and kinetic energy (particle acceleration) causing solar flare and CME. However, there are still a lot of important questions remain to be answered. Such as, what is the relative amount of energy contained in the flare vs. the CME? What is the relative amount of energy injected directly into plasma heating vs. particle acceleration? How did the reconnection lead to particle acceleration is even less understood. Particle acceleration in flares may in principle occur in a variety of ways, such as stochastic acceleration by MHD turbulence, acceleration by direct electric fields at the reconnection site, or diffusive shock acceleration at the different kinds of magnetohydrodynamics (MHD) shock waves that are produced during the flare (Priest & Forbes 2002). However, which of these processes is most important for producing the energetic particles that strike the solar surface remains a mystery.

Magnetic energy conversion by reconnection in two dimensions is relatively well understood, but in three dimensions we are only starting to understand the complexity of the magnetic topology and the MHD dynamics which are involved (Priest & Forbes 2002). The flare observations and NLFFF models in this thesis are aimed to address the magnetic nature of the solar eruption in the third dimension (along the direction parallel to the polarity inversion line). We try to address the first and third fundamental questions, through multi-wavelengths investigations of the evolution of the highly sheared magnetic fields before, during, and after the flares. Observations and model focused on these questions are presented in Chapters 2, 3, 4, 5, 6, based on, respectively, Su et al. (2006, 2007a, 2007b, 2007c, and 2007d).

Chapter 2

Magnetic Shear in an X17 Solar Flare on 2003 October 28

2.1 Introduction

A two-ribbon structure in the chromosphere and transition region (e.g., in $H\alpha$, UV, and EUV) is often seen during a solar flare, especially for those long-duration events associated with coronal mass ejections (CMEs). The magnetic reconnection model proposed by Carmichael (1964), Sturrock (1966), Hirayama (1974), and Kopp & Pneuman (1976) (the CSHKP model) suggests that for an eruptive flare or CME, field lines open and then merge and reconnect at progressively higher altitudes in the corona. The EUV ribbons are the footprints in the transition region of the closed, reconnected field lines which are typically filled with hot coronal plasma in the form of post-flare loops.

There are two proposed mechanisms for producing the EUV ribbon emission: thermal conduction from the reconnected loops, and direct bombardment of the lower atmosphere by accelerated particles from the reconnection site (Fletcher & Hudson 2001). A close temporal relationship between the hard X-ray (HXR) and UV emission during the impulsive phase in solar flares was reported by Kane & Donnelly (1971) and Kane, Frost, & Donnelly (1979) using data from OGO and OSO satellites and was also found by SMM, when HXR and UV light curves were seen to be simultaneous

to within 1 second (Woodgate *et al.* 1983; for a review, see Fletcher 2002).

Cheng *et al.* (1981) and Cheng, Tandberg-Hanssen, & Orwig (1984) made the first attempt to study the spatial structure of UV bursts using the UV observations with spatial resolution of a few seconds of arc obtained by UVSP. Their study showed that: (a) there was considerable pre-flare activity with UV transient brightenings occurring in many small point-like kernels; and (b) individual peaks in the HXR bursts can be identified with individual peaks in the UV bursts of individual flaring kernels. The recent observations from TRACE, Yohkoh and BATSE reported by Warren and Warshall (2001) showed that the initial HXR burst was positively correlated only with footpoints that showed no pre-HXR activity, which indicated that energy release during the preflare and impulsive phase of the flare was occurring on different loops. A comparison of HXR emission and EUV emission measured at the locations of the HXR sources was reported by Fletcher and Hudson (2001), who found that the light curves map to one another quite well. However, due to the TRACE time resolution of the event they reported, they could only establish that the two peaks are within 20 s of each other.

It is well known that during a two-ribbon flare the two footpoint ribbons, residing in opposite magnetic polarities, expand outward and away from each other (Svestka and Cliver, 1992). Some recent papers even reported an anticorrelation between the time profile of the separation distance of the conjugate footpoints and that of the HXR emission in a flare on 2002 September 9 (Ji *et al.* 2004a, 2004b; Huang & Ji 2005). In addition to the ribbon separation in the direction perpendicular to the magnetic inversion line (MIL) which is predicted generically by the two dimensional magnetic reconnection model, motions of the footpoints parallel to the direction of the MIL during flares have also been found by several authors. Masuda, Kosugi, and Hudson (2001) reported observations of the evolution of the HXR (*Yohkoh*/HXT)

footpoints from a strong to a weak sheared structure, which was also found in H α (Sartorius Refractor at Kwasan Observatory; Asai *et al.* 2003) observations. A shear change of the footpoints observed at HXR (RHESSI) and microwave (Nobeyama Radioheliograph) was also reported by Kundu, Schmahl, & Garaimov (2004). This strong-to-weak shear change of the footpoints reflects a decrease in the shear of the newly reconnected loops during the course of the flare. It should be noted that this decrease of the magnetic shear means that the outer magnetic field has weaker magnetic shear, and it does not mean that the magnetic shear is reducing during a flare.

In this chapter we focus on the question of what changes occur when a flare goes from the impulsive phase to the main phase. What cause this change, and how? The magnetic shear may show abrupt changes during a flare as reported in the above papers. The question we address here is: could the change from the impulsive to gradual phase be related to the magnetic shear change? For example, does the transition from the impulsive phase to the gradual phase occur as the initial flare brightenings evolve out of the filament channel into the larger surrounding volume?

To answer this question, we have selected a particularly well-observed X17 solar flare on 2003 October 28 which shows obvious shear change via the evolution of the EUV footpoints observed by TRACE, and examined the temporal evolution of the shear and the rate of change of the shear. The main observational data are summarized in Section 2.2. In Section 2.3.1 we present the comparison of EUV and HXR emission, and in Section 2.3.2 we study the pre-HXR EUV brightenings. The identification of the conjugate footpoints is described in Section 2.4.1. In Section 2.4.2 we focus on describing the decrease of the shear of the EUV footpoints, which is an apparent motion of the footpoints during the flare. The EUV emission mechanism of the brightenings is discussed in Section 2.5.1. Our interpretation of the evolution

of the shear of the EUV footpoints is discussed in detail in Section 2.5.2. Conclusions are given in Section 2.6.

2.2 Observations

An X17 (GOES soft X-ray class) two-ribbon solar flare occurred in NOAA active region 10486 on 2003 October 28, at $\approx 11:00$ UT. The main observational data used in this investigation were obtained simultaneously by the *Transition Region and Coronal Explorer* (TRACE) (Handy *et al.* 1999) and the anticoincidence system (ACS) of the SPI spectrometer on board the ESA INTEGRAL satellite (Attié *et al.*, 2003; Vedrenne *et al.* 2003). In addition to this large event, a filament eruption was seen in EUV (TRACE) and in $H\alpha$ images (Figure 4 in Schmieder *et al.* 2006 and Figure 2 in Wang *et al.* 2005) about 40 minutes before the X17 solar flare and following a soft X-ray/EUV event which occurred about 10 minutes earlier ($\approx 9:50$ – $10:10$ UT). Even though this filament eruption and the large flare that we studied involved the same magnetic inversion line, it is not clear whether they were related to each other, because of the large time difference. In this chapter we focus only on the X17 event.

During this event, SPI was observing the IC443 supernova remnant. Technical constraints fixed the satellite attitude in such a way that solar photons arrived at 122° from the telescope axis. At this incidence angle, the photons have to cross the satellite platform and the anticoincidence system (ACS) of SPI. While the satellite platform practically is transparent to the photons at such energies, the SPI/ACS system, composed of 5 cm thick BGO blocks, provides efficient shielding to photons arriving at the Germanium camera. On the other hand, the cross-section of this SPI/ACS, viewed under this 122° incidence angle, is ≈ 5200 cm². With a $\approx 100\%$ efficiency from 150 keV up to some hundreds of keV, SPI/ACS is a very efficient detector for solar HXR in this energy range. As a result count rates with 50 ms

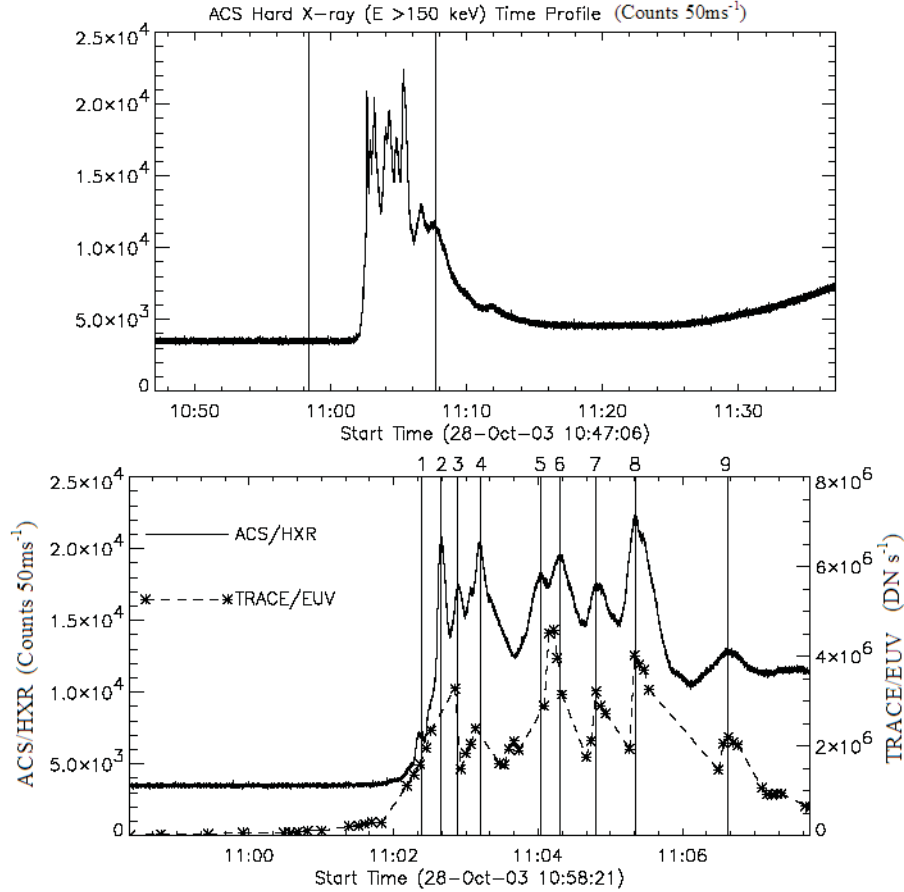


Figure 2-1 Light curves of the EUV and HXR emission. The SPI/ACS HXR light curve of the solar flare on 2003 October 28 is displayed in the top panel; the two lines mark the time range of the enlarged HXR light curve in the bottom panel, and 9 spikes are marked by 9 vertical lines. The summed TRACE/EUV light curve from all the brightenings is displayed via the dashed line with asterisk signs in the bottom panel.

integration have been recorded with significant statistics, allowing a comparison of EUV and HXR intensity time profiles with very high precision. The SPI/ACS time profile of photons with energy $E > 150$ keV, in steps of 50 ms, is displayed Figure 2-1. During the time period that we are interested in (bottom panel in Figure 2-1) nine peaks are seen and shown by the vertical lines, Peak 1, and Peaks 2–9 occurred during the rise phase and impulsive phase of the flare, respectively.

Given the high intensity of the flare, the number of photons detected in the SPI Ge

detector matrix was sufficient to perform spectral analysis with one minute integration time. The time profiles obtained for different energy bands suggest that during Peaks 1 to 4, photons with energies up to 10 MeV were emitted. The spectra integrated over these peaks show a clear power law bremsstrahlung spectrum (Gros *et al.* 2004). Data from *Koronas*/SONG (Kuznetsov *et al.* 2005) show that this spectrum extends up to 40 MeV. For the later peaks, it seems that this bremsstrahlung emission is mixed with nuclear (4–7 MeV) and pion (60–100 MeV) emissions.

TRACE observed AR 10486 from several hours before the flare until 12:56:46 UT on 2003 October 28, yielding data at 195 Å (Fe XII/XXIV), 284 Å (Fe XV), and 1600 Å (C IV plus UV continuum). Details of the TRACE instrumentation and performance can be found in Handy *et al.* (1999) and Golub *et al.* (1999). Observations at 195 Å and 1600 Å were recorded using an array size of 768×768 pixels, with a pixel size of 0.5 arcsec, while the 284 Å observations used a 2×2 summed array of 512×512 pixels. Apart from the few 284 Å images taken, the observing mode was designed to alternate data acquisition between 195 Å and 1600 Å, with the time cadence at 195 Å higher than that at 1600 Å. To compare with HXR spikes, the TRACE data with high time cadence (typically ≈ 4 s) from 10:58:21 UT to 11:07:46 UT at 195 Å was selected. Due to the motion of the field of view (FOV), a small part of the north ribbon was sometimes not observed at 195 Å, but the ribbons in their entirety could be seen at 1600 Å and 284 Å at all times. TRACE observations show us that in the UV and EUV the two flare ribbons are composed of discrete bright kernels (e.g., Figures 2-2-2-8). Our analysis focuses primarily on the observed evolution of these kernels during the course of the flare.

We note that some pixels in some of the EUV bright kernels saturated the Analog to Digital Converter (ADC) during the impulsive phase. We investigated the degree of saturation in the EUV images of this flare and found that (1) very few pixels (3%)

saturated the ADC even for the brightest flare kernel, (2) the CCD itself did not reach saturation level (full well is 5 times greater than the ADC conversion limit), and (3) the saturated pixels were only slightly stronger than the other pixels in the kernels, as determined from analysis of the first-order images. This saturation will have some effect on the accuracy of the actual intensity of the flare kernel, but produces a negligible change in the shape of the summed light curves. Details of the method for investigating these effects are presented by Lin, Nightingale, and Tarbell (2001).

2.3 Comparison of EUV and HXR Emission

2.3.1 Correlation between EUV and HXR emission

The SPI/ACS HXR data have excellent temporal resolution, but essentially no spatial resolution, while the TRACE data have both temporal and spatial resolution. RHESSI was behind the Earth at the start of this flare and began observations at 11:06:26 UT, which only caught the last HXR peak (Peak 9) in the impulsive phase. Our basic method of comparison to determine whether the EUV and HXR emissions are correlated is therefore based mainly on the timing of the EUV brightenings vs. the timing of the HXR peaks.

In order to compare the EUV emission from the bright kernels and the HXR emission, boxes are defined in the EUV images that enclose the bright kernels. Because the bright kernels are continuously evolving (viz. Fletcher, Pollock, and Potts, 2004), in order to track them we divide the rising and impulsive phases of this flare into 8 time bins. Different boxes are chosen at the different time bins (see Figures 2-2-2-8) and the relevant kernels located in the boxes are labelled A, B, etc.

The bottom panel in Figure 2-1 shows us the comparison of the hard X-ray light curve and the summed light curve of all the EUV bright kernels (for example, during Phase 1 it is the summed light curve of brightenings “S”/“S1” and “T”/“T1”). We

Peak	SPI/ACS HXR	TRACE/EUV	Time lag		Corresponding TRACE/EUV bright kernels
	(E > 150 keV) t_{HXR} (UT)	(195 Å) t_{EUV} (UT)	$\Delta t = t_{\text{EUV}} - t_{\text{HXR}}$ (Seconds)		
Peak 1	11:02:23.373	11:02:22			B1
Peak 2	11:02:39.573	11:02:31			
Peak 3	11:02:53.773	11:02:51			A1, B
Peak 4	11:03:11.923	11:03:08	-2.8	± 1.2	C, D
Peak 5	11:04:02.323	11:04:05			I, G
Peak 6	11:04:18.423	11:04:13			I1
Peak 7	11:04:47.923	11:04:48	1.8	± 1.0	J1
Peak 8	11:05:20.823	11:05:20	2.9	± 1.0	O, N1
Peak 9	11:06:37.323	11:06:38	1.1	± 2.4	P1, Q/Q1
Total			-1.25	± 2.15	

Table 2.1 Timing of HXR peaks and corresponding EUV brightenings.

can obtain a timing comparison which is better than the cadence of the individual TRACE images by cross-correlating this summed EUV light curve as a whole against the HXR light curve. From Figure 2-1 we can see that the correlation between the HXR and EUV emission is very good, especially for HXR Peaks 3, 4, 7, 8, and 9. In order to quantify the temporal relationship between the HXR and EUV emission, we have done a cross correlation between these two emissions for the individual HXR Peaks 4, 7, 8 and 9, and also a correlation of the full light curves from 10:58:21 UT to 11:07:46 UT. The time lags ($t_{\text{EUV}} - t_{\text{HXR}}$) obtained for the individual peaks are displayed in Table 2.1, and the average time lag for these four peaks taken as an aggregate is 0.75 ± 1.4 s. The cross correlation between the two complete light curves shown in the bottom panel in Figure 2-1 gives a time lag ($t_{\text{EUV}} - t_{\text{HXR}}$) of -1.25 ± 2.15 s (last line in Table 2.1). From these results we see that these two types of emission are effectively simultaneous to our measurement accuracy, which is in the range $\approx 1-3$ seconds.

With the high spatial resolution of TRACE, we also examined the light curves of individual bright kernels (Figures 2-2–2-8) in order to find the EUV bright kernels

corresponding to each HXR peak, and the resulting identifications are listed in Table 2.1. Table 2.1 presents the times of the HXR peaks, time lags between the EUV and HXR emission, and the EUV bright kernels corresponding to each HXR peak. The second column in Table 2.1 refers to the time of the HXR peak, and the third column shows the time of the EUV observations closest in time to each HXR peak. The fourth column shows the time lags between the HXR and EUV emission determined from a cross-correlation analysis of the respective peaks, and the error bar (1-sigma) is given in the same column. The last column identifies the EUV bright kernels which we believe are corresponding to the HXR peak. From Table 2.1 we can see that in the EUV observations closest in time to nearly each HXR peak we find a peak in the EUV light curves from one or more bright kernels. These bright kernels are therefore possibly related to the HXR peak. We do not find the corresponding EUV bright kernels for HXR Peak 2, but we note the lack of EUV observations near the time of that peak.

2.3.2 Pre-HXR EUV brightenings

From the light curves in Figures 2-1 and 2-2 we can see that the EUV emission from the bright kernels starts to rise at 10:58:21 UT, which is more than 3 minutes before the onset of the first HXR burst (11:02:00 UT). We also see some small peaks in the EUV light curves (e.g. Peak 0 in Figure 2-3d) before HXR onset.

EUV brightenings before the HXR onset appear within two slender ribbons, as can be seen in Figures 2-2b and 2-2c. The comparison of the morphology of the pre-HXR brightenings and the later flare ones (viz. Figure 2-3a) shows us that the flare brightenings result from an outward expansion of the pre-HXR EUV brightenings in a direction perpendicular to the ribbons and an extension of the pre-HXR brightenings along the direction of the ribbons (Figures 2-9a–2-9e). Some of the flare brightenings

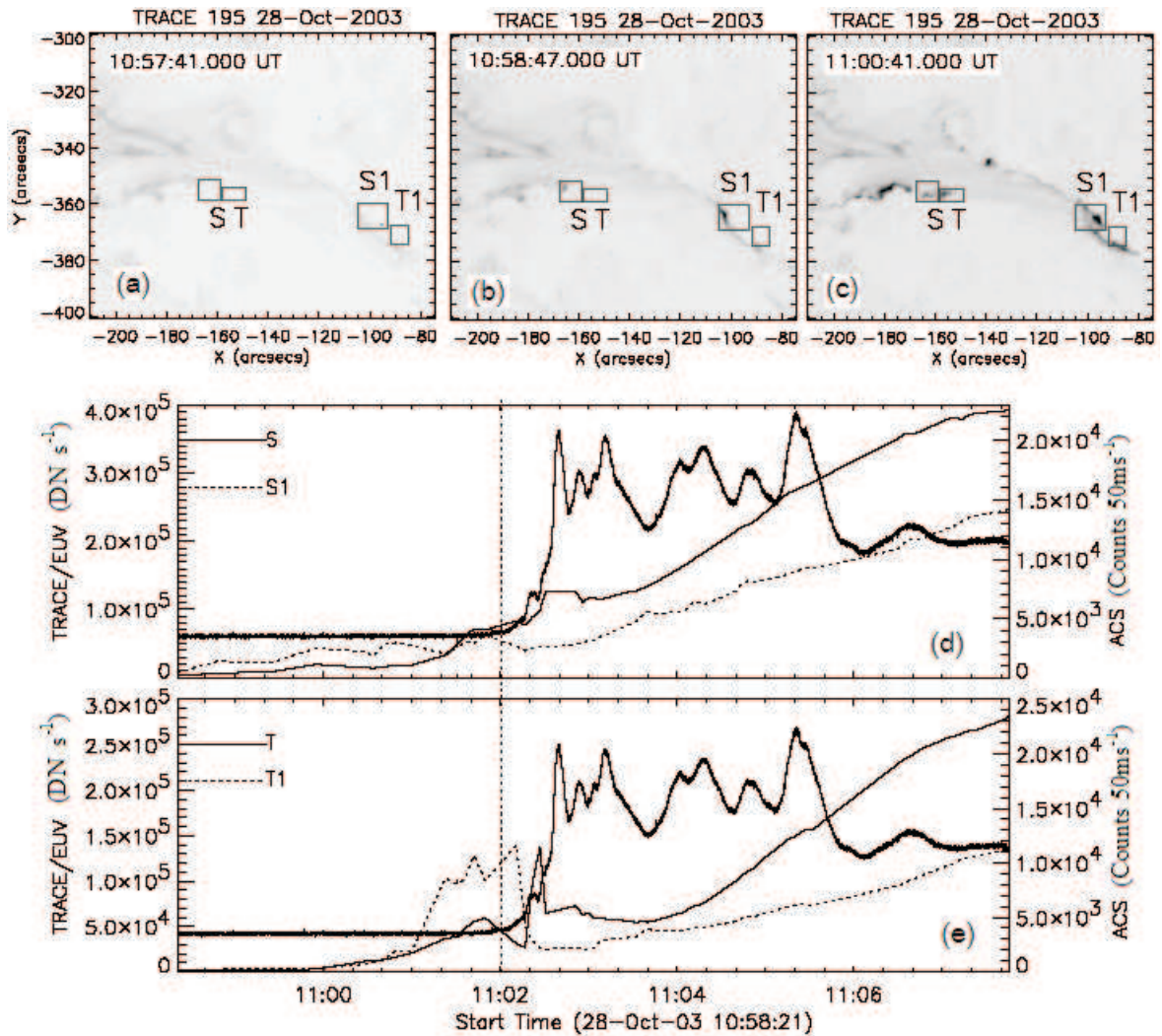


Figure 2-2 SPI/ACS/HXR light curves, TRACE/EUV images and light curves of different brightenings during Phase 1. Phase 1 is the time period before HXR onset which is represented by the vertical dashed line. (a) Gray boxes representing EUV brightenings “S”/“S1” and “T”/“T1” during Phase 1 are overlaid on an EUV image before Phase 1. (b), (c) EUV images are overlaid with gray boxes representing the EUV brightenings during Phase 1. (d), (e) EUV light curves of the two pairs of brightenings “S”/“S1” and “T”/“T1” during Phase 1. The ACS/HXR light curve is represented by the thick solid line.

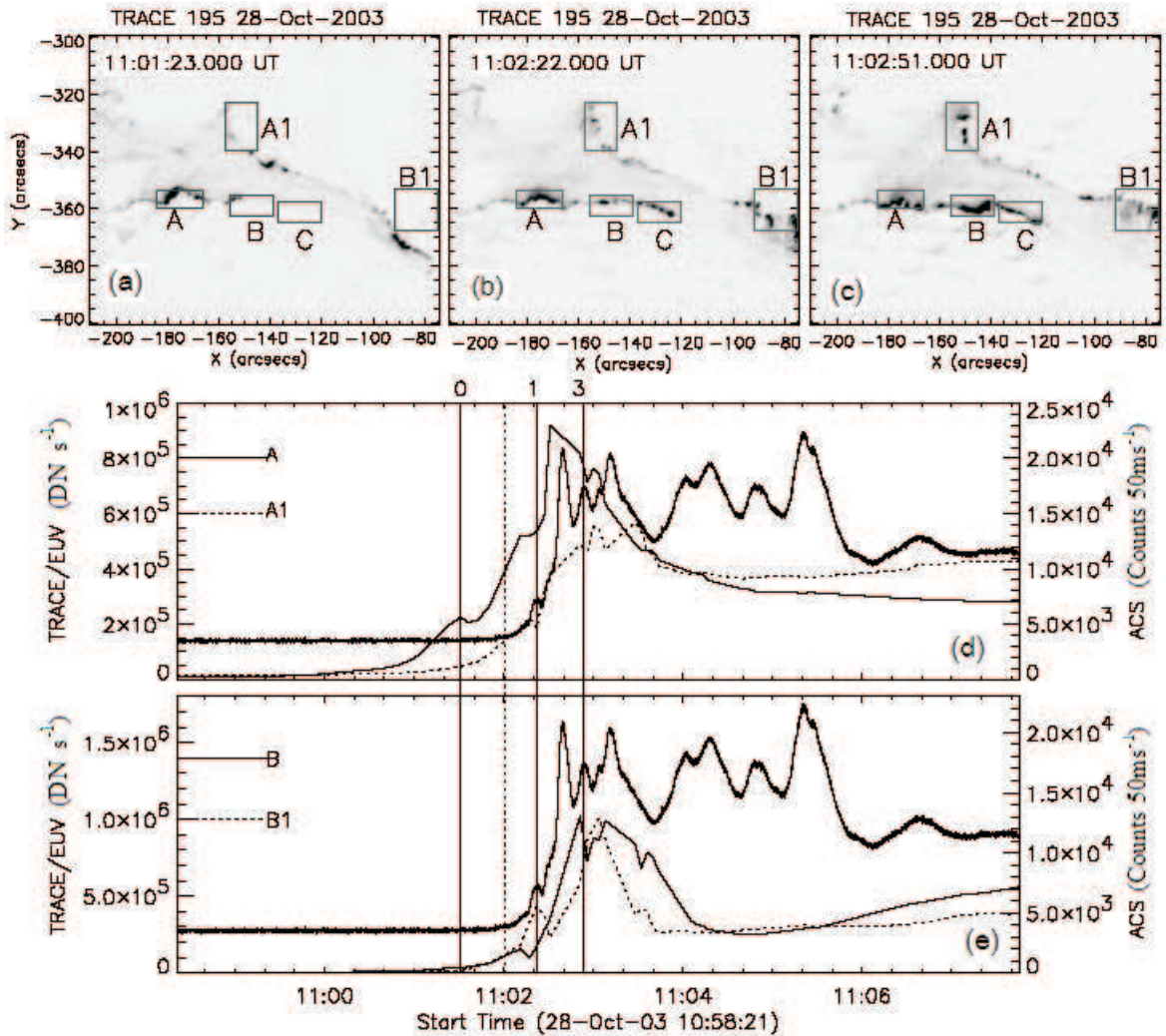


Figure 2-3 Similar to Figure 2-2 but for Phase 2. Phase 2 is the time period between the vertical dashed line representing HXR onset and the solid line representing Peak 3. (a) EUV image at EUV peak 0 before HXR onset is overlaid with gray boxes representing the EUV brightenings “A”/“A1”, “B”/“B1”, and “C” during Phase 2. (b), (c) Gray boxes representing EUV brightenings during Phase 2 are overlaid on EUV images closest in time to HXR Peaks 1 and 3. (d), (e) Similar to Figures 2-2d and 2-2e, but for EUV brightenings “A”/“A1”, “B”/“B1” and “C” during Phase 2. The peaks are marked as vertical line.

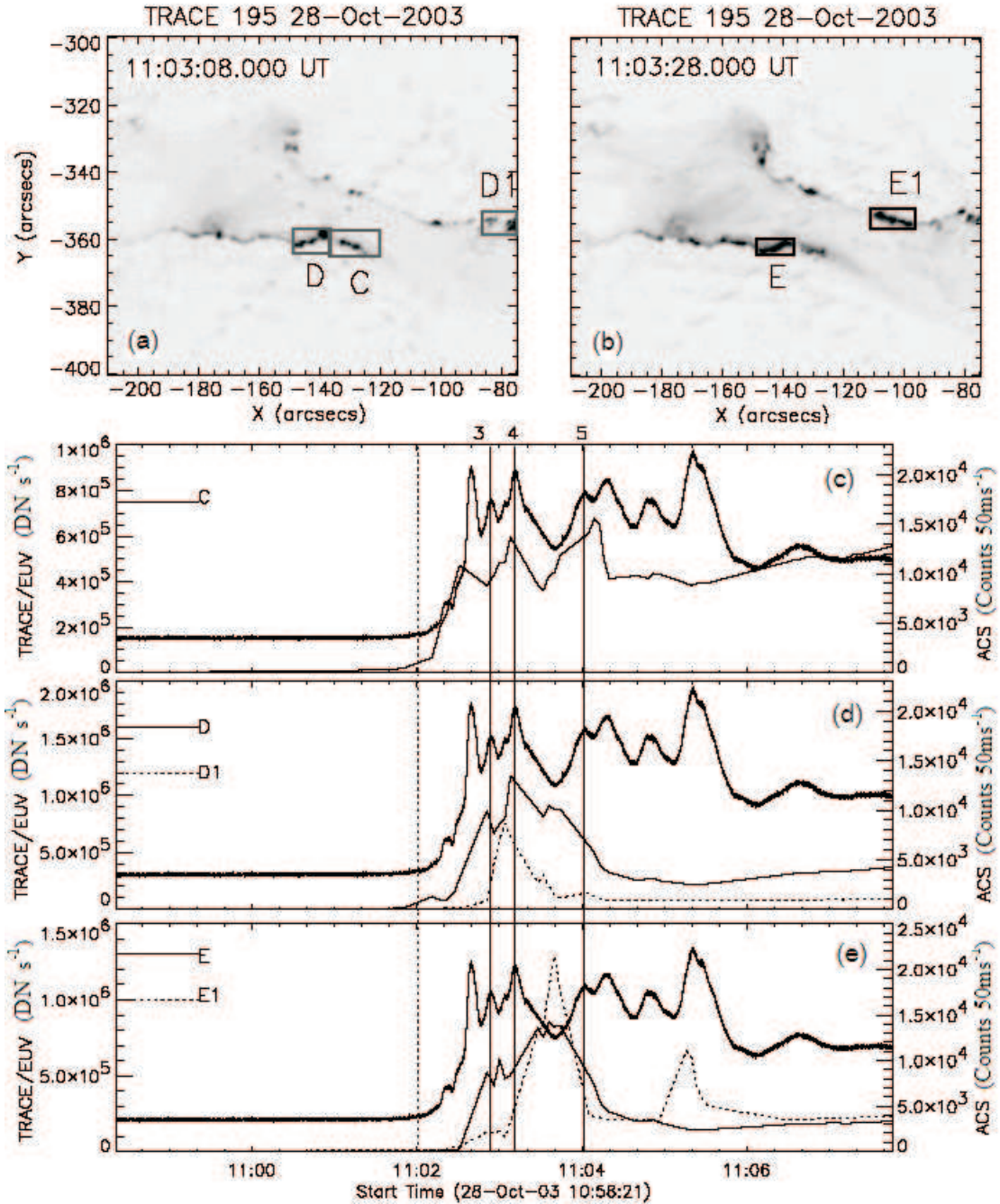


Figure 2-4 Similar to Figure 2-2, but for Phases 3 and 4. The time period between Peaks 3 and 4 is Phase 3, and Phase 4 is the time period between Peaks 4 and 5. (a) EUV image closest in time to HXR Peak 4 is overlaid with gray boxes representing the EUV bright kernels “C” and “D”/“D1” during Phase 3. (b) EUV image is overlaid with gray boxes representing the bright kernels E/E1 during Phase 4. (c), (d), and (e) Similar to Figures 2-2d and 2-2e, but for EUV brightenings during Phases 3 and 4, respectively.

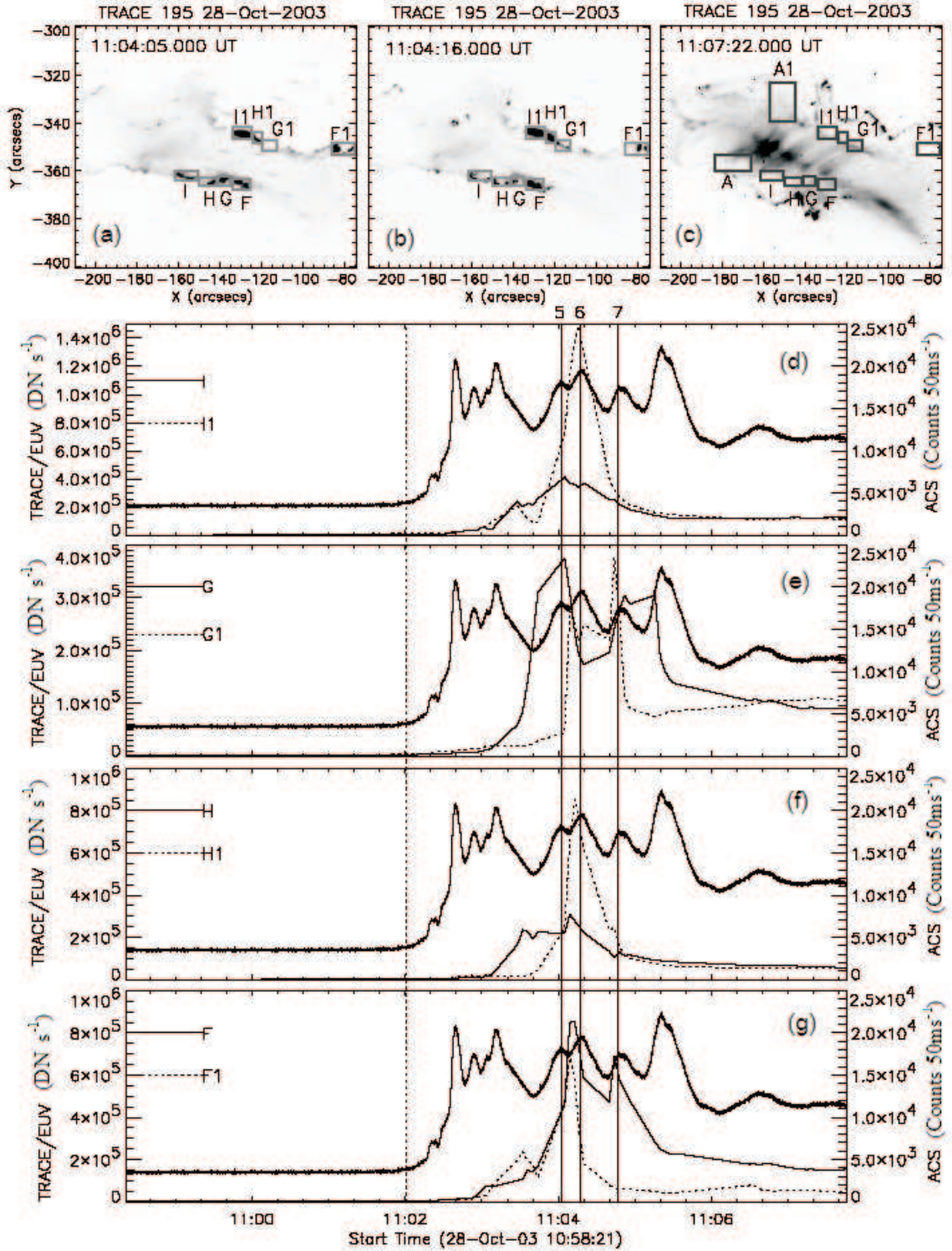


Figure 2-5 Similar to Figure 2-2, but for Phase 5 (the time period between Peaks 5 and 7). (a), (b) Gray boxes representing EUV brightenings during Phase 5 are overlaid on the EUV images closest in time to HXR Peaks 5 and 6, respectively. (c) Gray boxes representing EUV brightenings are overlaid on an EUV image of the post-flare loops. (d), (e), (f), and (g) Similar to Figures 2-2d and 2-2e, but for EUV brightenings during Phase 5.

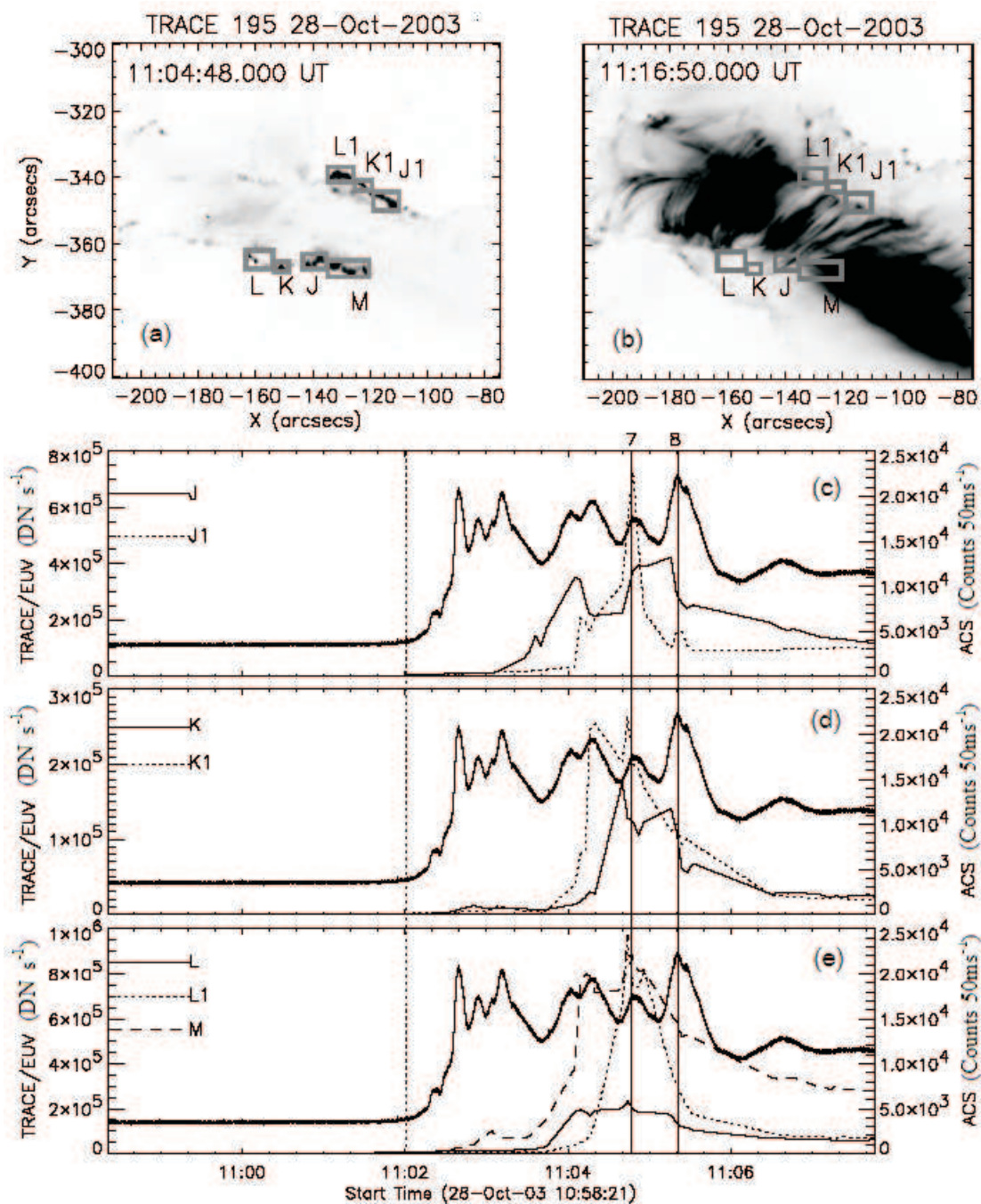


Figure 2-6 Similar to Figure 2-2, but for Phase 6 (the time period between Peaks 7 and 8). (a) Gray boxes representing EUV brightenings during Phase 6 are overlaid on the EUV image closest in time to HXR Peak 7. (b) Gray boxes representing EUV brightenings during Phase 6 are overlaid on an EUV image of the post-flare loops. (c), (d), and (e) Similar to Figures 2-2d and 2-2e, but for EUV brightenings during Phase 6.

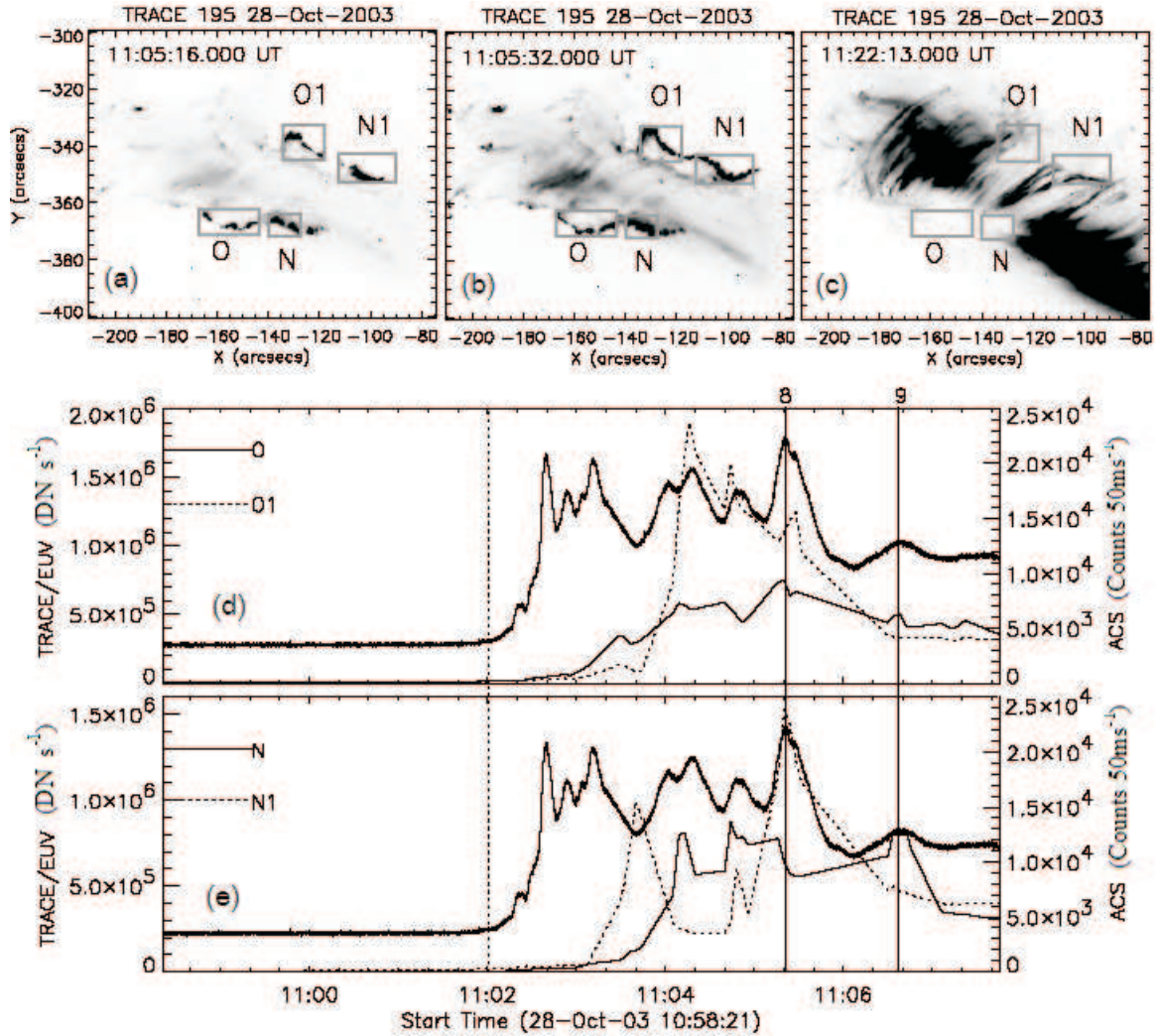


Figure 2-7 Similar to Figure 2-2, but for Phase 7 (the time period between Peaks 8 and 9). (a), (b) Gray boxes representing EUV brightenings during Phase 7 are overlaid on the EUV image closest in time to HXR Peak 8 and another EUV image during Phase 7, respectively. (c) Gray boxes representing EUV brightenings during Phase 7 are overlaid on an EUV image of the post-flare loops. (d), (e) Similar to Figures 2-2d and 2-2e, but for EUV brightenings during Phase 7.

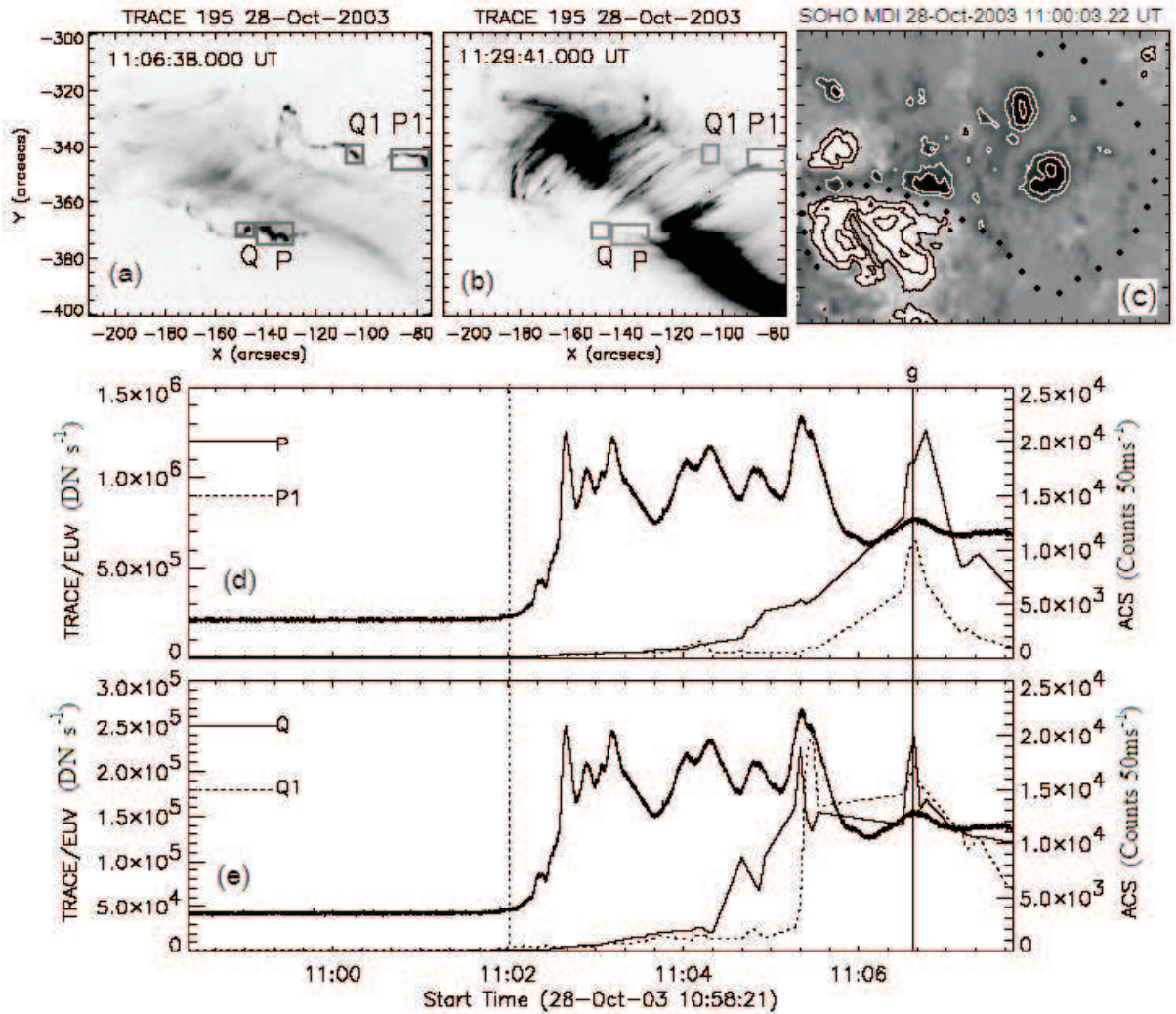


Figure 2-8 Similar to Figure 2-2, but for Phase 8 (the time period after Peak 9). (a) Gray boxes representing EUV brightenings during Phase 8 are overlaid on the EUV image closest in time to HXR Peak 9. (b) Gray boxes representing EUV brightenings during Phase 8 are overlaid on a later EUV image of the post-flare loops. (c) SOHO/MDI photospheric magnetogram overlaid with MDI contours, where white and black contours refer to negative and positive magnetic field, respectively. The black dotted line represents the locus of the filament. The field of view is $240'' \times 160''$. (d), (e) Similar to Figures 2-2d and 2-2e, but for EUV brightenings during Phase 8.

are also seen before the HXR onset, such as brightening “A”. These observations show that the pre-flare EUV brightenings are very similar to the flare ones, differing mainly in intensity but similar to the later flare brightenings in most other respects.

2.4 Evolution of the EUV Bright Kernels

2.4.1 Identification of the EUV conjugate footpoints

The most prominent conjugate footpoints have been identified manually by studying the evolution of the EUV bright kernels. There are three factors that we considered in identifying brightenings as conjugate footpoints: (1) the two brightenings appear simultaneously, (2) the light curves of the two brightenings are very similar, (3) the two brightenings are connected by post-flare loops. In this section we focus on describing in detail several examples of the method to show how we track and identify the conjugate footpoints in this flare.

Most of the EUV conjugate footpoints before Phase 5 have similar light curves, and some of the pairs can also be identified as appearing at the same time. These early brightenings are close to the neutral line and any possible post flare loops connecting them would be hidden under the larger post flare loops connecting the outer brightenings (see below for a discussion of the relative timing). Since no corresponding post-flare loops can be seen, we identify the conjugate footpoints mainly by the first two factors.

For example, at 10:58:21 UT, the first EUV brightening “S1” appears in the western part of the north ribbon and spreads from east to west. The next brightening, “S”, located in the eastern part of the south ribbon appears at 10:58:47 UT and spreads from east to west (Figure 2-2b). Because (i) only these two brightenings can be seen at this time, (ii) the time of their appearance is quite close, and (iii) the two light curves are also similar, we speculate that brightening “S” may be associated

with brightening “S1”.

With the extension of the two ribbons from east to west, brightenings “T” and “T1” appear at 11:00:41 UT (Figure 2-2c). Brightenings “T” and “T1” may be conjugate footpoints, because they appear at the same time and have similar time profiles during Phase 1 (Figure 2-2e).

After Phase 4, we identify the EUV conjugate footpoints mainly by factors (2) and (3), since many brightenings appear simultaneously, and post-flare loops are seen for these kernels. Although the correlation between the light curves of some of these conjugate footpoints is not clear, they can be confirmed by the corresponding post-flare loops. For example, many EUV brightening pairs appear at HXR Peak 5, but the conjugate nature of footpoints “T”/“T1”, “H”/“H1”, “G”/“G1”, and “F”/“F1” may be confirmed from the appearance of post-flare loops (Figure 2-5c) connecting them.

For some conjugate brightening pairs before 11:04:05 UT, we do not see the expected post-flare loops, but this does not mean that they are not conjugate footpoints. Cargill, Mariska, and Antiochos (1995) derived a simple formula for the cooling time of high-temperature flare plasma, which is $\tau_{cool} \approx 2.35 \times 10^{-2} L^{5/6} / T_0^{1/6} n_0^{1/6}$ s. The parameters L , T_0 , and n_0 in the formula are the loop half-length, electron temperature, and electron density, respectively. From the formula we can see that the most sensitive parameter is the loop length. The distance between the earlier brightening pairs before Phase 5 is much longer than that between the later brightening pairs (Figures 2-2-2-8). Because of their large separation along the neutral line, these early loops are 2-3 times longer than the later loops, so it should take substantially longer for the earlier loops to cool down to the TRACE/EUV observational temperature range than the later ones. By the time they cool down to the TRACE temperature range, the shielding by the overlying loops makes them unobservable.

Phase	TRACE (195 Å)			Ribbon	Angle θ (°)
	Brightening Kernels				
Phase 1 (Fig. 2) 10:58:21–11:02:10		T T1	S S1	S N	73, 71
Phase 2 (Fig. 3) 11:02:11–11:02:55	C	B B1		A A1 S N	54
Phase 3 (Fig. 4) 11:02:56–11:03:27	C	D D1		S N	50
Phase 4 (Fig. 4) 11:03:28–11:04:04		E E1		S N	41
Phase 5 (Fig. 5) 11:04:05–11:04:47	F F1	H H1	G G1	I I1 N	18
Phase 6 (Fig. 6) 11:04:48–11:05:19	M	K K1	J J1	L L1 S N	19
Phase 7 (Fig. 7) 11:05:20–11:06:29		N N1	O O1	S N	9, 23
Phase 8 (Fig. 8) 11:06:30–11:07:46	P P1	Q Q1		S N	20

Table 2.2 Summary of the bright kernels occurring in different phases of the 2003 October 28 flare.

Table 2.2 gives a summary of the brightenings occurring in the different phases of the flare. Note that the different phases in this table just refer to the different time bins and they do not have physical implication. The start and end times of the phases are displayed in the first column. The middle columns give the identifying labels of the different bright kernels in each ribbon. The grouping of the identifying letters into different vertical columns (e.g., “T”/“T1”, “B”/“B1”, “D”/“D1”, “E”/“E1”) indicates the evolution of a pair of conjugate footpoints through the stages of its evolution. The middle column marked between the two vertical lines represents the strongest brightening pairs, and the positions of these brightening pairs appear to evolve continuously during the evolution of the flare (especially for the brightenings in the south ribbon). The next Column indicates which ribbon (North (N) or South (S)) the bright kernels occurred in. These identifications are then used to define an

angle θ , listed in the last column and discussed in the next section.

2.4.2 Evolution of the shear of the EUV conjugate footpoints

It is well known that filaments typically lie on inversion lines in the longitudinal magnetic field when viewed near the center of the disk (McIntosh, 1972), which also can be seen in Figure 2-8c. In order to get information about the ribbon's underlying magnetic inversion line, we use the solar filament which can be seen in $H\alpha$ image obtained at Big Bear Solar Observatory (BBSO). Because there are no $H\alpha$ observations at BBSO close in time to the pre-flare phase, we choose an image late in the day on 2003 October 27, which is about 15 hours before this flare.

To get good co-alignment of the TRACE/EUV and BBSO/ $H\alpha$ images, we proceeded in three steps: (i) we derotated the $H\alpha$ image to the same time as the EUV image, and found the SOHO/MDI magnetogram closest in time to the EUV image; (ii) we overlaid the $H\alpha$ image with the SOHO/MDI magnetogram, using the dark sunspots; (iii) we selected the two images in 195 Å closest in time from SOHO/EIT and TRACE/EUV, and obtained the offset of the TRACE/EUV image by cross-correlation.

In order to examine the evolution of the shear of the EUV conjugate footpoints, we select one image from each time bin; the EUV contours in the different time bins overlaid on the $H\alpha$ image can be seen in Figures 2-9a–2-9g, and the conjugate footpoints obtained from our analysis are marked as black lines connecting the bright kernels. The different group of brightening pairs shown in Table 2.2 are indicated by different line types in the figure. The evolution of the shear is clearly seen in this sequence of images.

In order to calculate a shear angle, the conjugate brightening pairs during each of the phases connected by the solid, dot-dashed, and dashed lines as shown in the

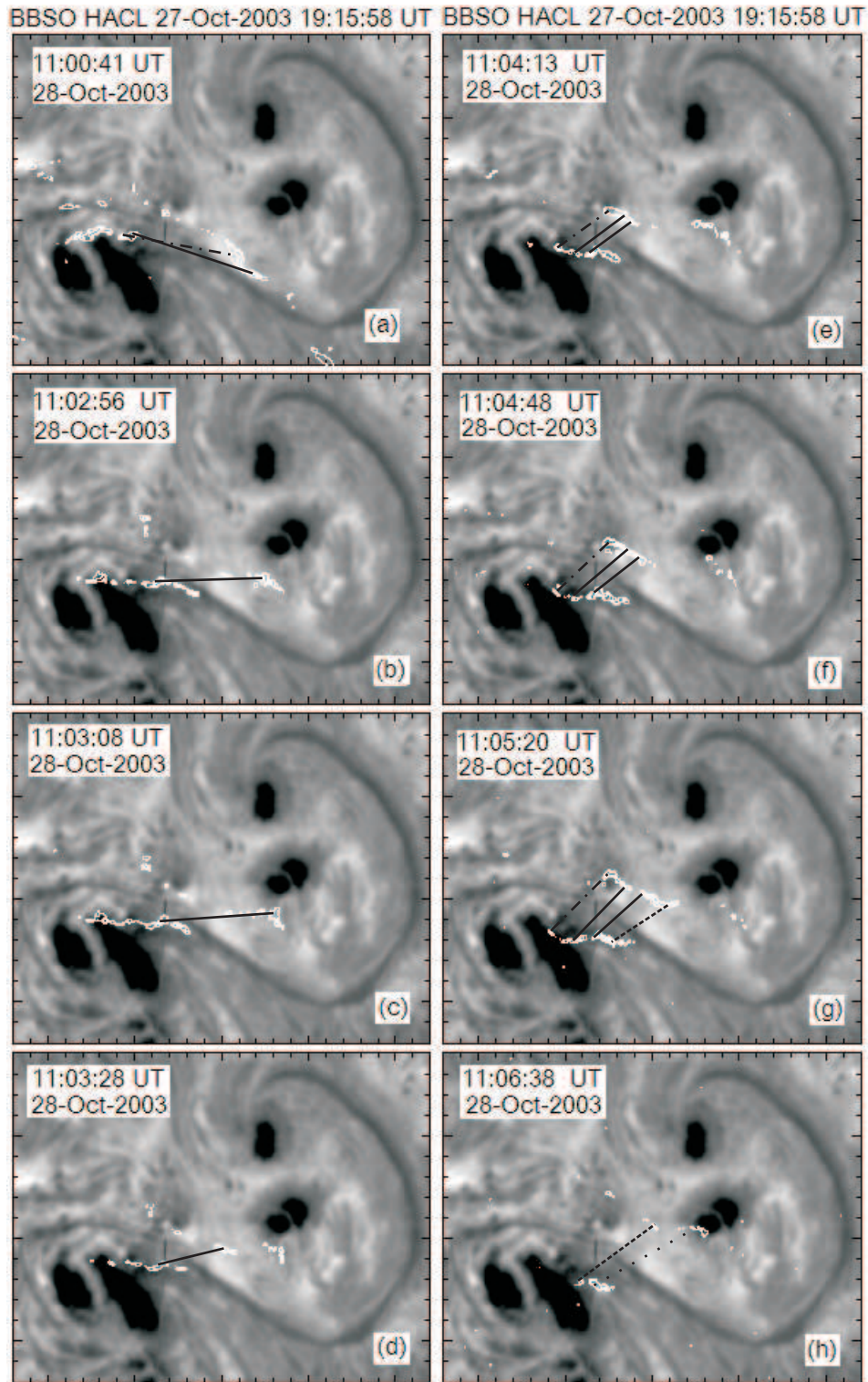


Figure 2-9 EUV brightenings and H α image. TRACE/EUV contours at different times are overlaid on an earlier H α image from BBSO. The times of the EUV contours are marked on each image, and the black lines connecting to the EUV bright kernels represent the possible conjugate EUV footpoints. Different kind of line refer to different group of brightening pairs. The field of view is 240'' \times 160'' for each image.

Time(UT)	11:01:48	11:03:02	11:03:18	11:03:48	11:04:30	11:05:04	11:05:59
$d\theta/dT(^{\circ}/s)$	0.14	0.33	0.45	0.51	0.03	0.03	-0.07

Table 2.3 Shear angle change rate and the corresponding time.

middle column marked between the two vertical lines in Table 2.2 are regarded as a group and the angles are averaged. The angles (shear angle) between the lines connected these conjugate footpoints and the line perpendicular to the filament have been measured and displayed in the last column in Table 2.2. The angles between the lines connected different brightenings pairs in this group are very similar at each phase (time bin) during the early phases (time bins), but become more dispersed after Phase 6. For example, the angle between the line connecting brightening pair “N”/“N1” and the line perpendicular to the filament is very different (23° vs. 9°) from the angles measured for the other brightening pairs seen in Phase 7. All values, however, are retained when taking the average.

Because most of the strongest brightening pairs predominating at the earlier phases (time bins) disappeared by Phase 8, the angle θ is measured using brightening pair “Q”/“Q1”, which appears to be related to the brightening pair “N”/“N1” in position. Because the brightening pairs which are associated with the strongest brightening pair “P”/“P1” at Phase 8 are outside of the FOV most of the time, the evolution of this group of brightening pairs is not discussed here.

Furthermore, we have also examined the rate of change of these angles ($-d\theta/dt$; we use the average value of θ , if we have more than one value in a given time bin), which is shown in the first column in Table 2.3, and the corresponding time (we use the mid point between the two times at which we measured the two angles) is displayed in the second column.

The ACS/HXR time profile is displayed in Figure 2-10a. The temporal evolution

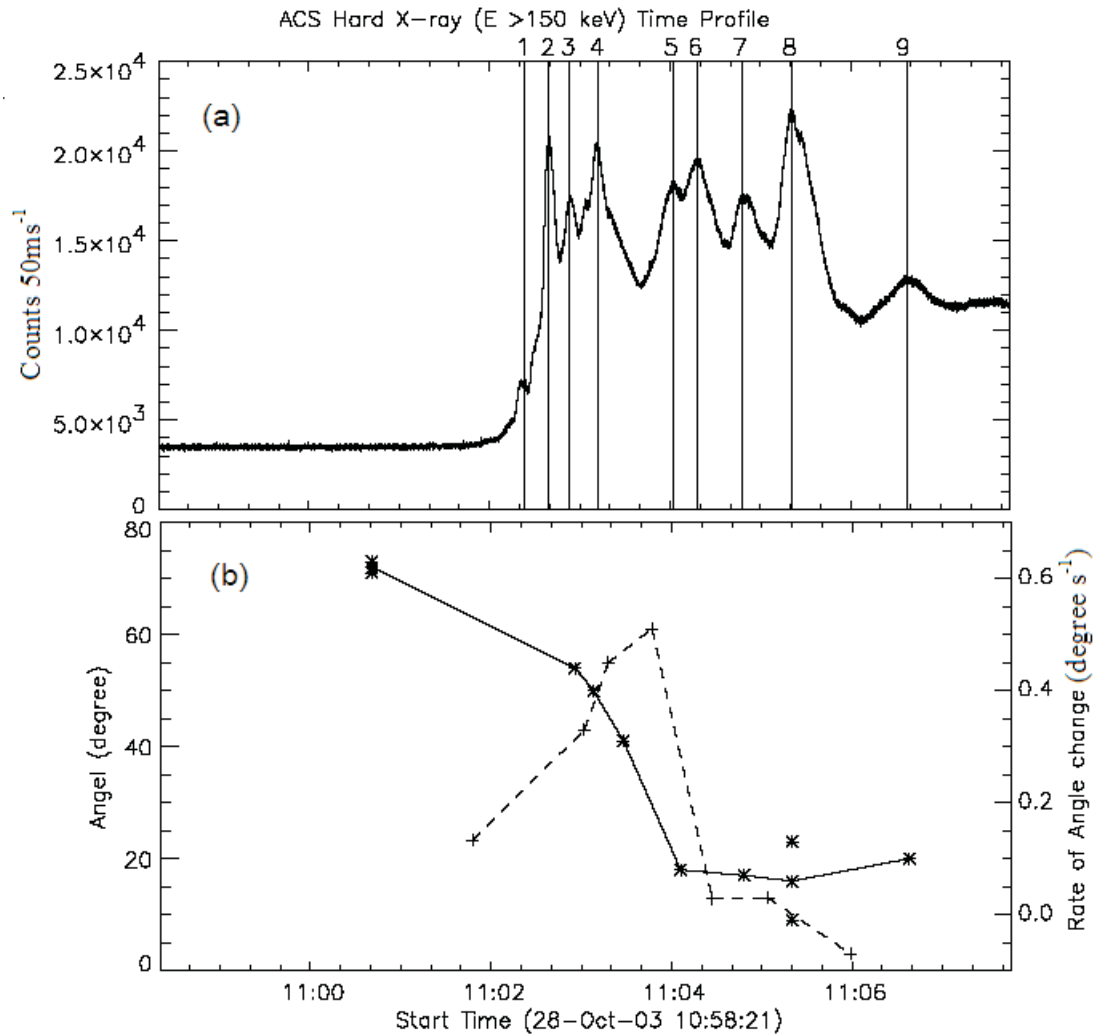


Figure 2-10 HXR light curve and the temporal evolution of the shear angle and the change rate of this angle. (a) The ACS/HXR light curve of the solar flare on 2003 October 28. (b) The evolution of the shear angle θ (solid line with asterisk sign), and the evolution of the change rate of this angle (dashed line with plus sign).

of the average shear angle θ and the change rate of this angle $d\theta/dt$ are displayed as a solid line with asterisk signs and a dashed line with plus signs, respectively in Figure 2-10b. The real measured angles are shown as individual asterisk signs around the average angle.

From Figure 2-10b we see that the shear angle θ of the strongest brightening pairs is decreasing all the time during the early impulsive phase, which indicates that the shear of the conjugate footpoints is decreasing during the early impulsive phase (before Peak 6). The change rate of the shear angle peaks during the early impulsive phase, as can be seen in Figure 2-10b, and the shear change becomes very slow after Peak 5. It seems, therefore, that the change in shear angle of the EUV brightenings does not correlate in a straightforward way with the impulsive phase HXR bursts.

2.5 Discussion

2.5.1 EUV brightenings generation mechanism

As mentioned previously, there are mainly two generation mechanisms for the EUV brightenings: thermal conduction from the reconnected loops, and direct bombardment of the lower atmosphere by accelerated particles from the reconnection site. By the comparison of the EUV and HXR emission, we are able to discuss the EUV brightenings generation mechanism in this event.

Thermal conduction models have been proposed where the initial instability occurs at the loop top where the gas is heated and produces hard X-rays. A thermal conduction front proceeds down the loop to heat the chromosphere to at least transition region temperatures (Smith & Lilliequist 1979; Smith & Auer 1980; Nagai 1980).

TRACE/EUV image overlaid with RHESSI HXR ($E = 100\text{--}200$ keV) image at the time period of the HXR Spike 9 has been shown in Figure 2-9 in Krucker & Hudson (2004). From that figure we can see, the HXR sources are located within the

two EUV ribbons rather than at the loop top, and we also can see the strongest HXR sources are corresponding to the strongest EUV brightening pair “P”/“P1”. These observations suggest that the EUV brightenings during HXR Spike 9 may not be due to thermal conduction.

Unfortunately, we do not have HXR image before HXR spike 9 to check the viability of the thermal conduction model for the other EUV brightenings. However, the travelling time of the thermal conduction front can be estimated as $t = L^2 n_e k_B / \kappa_0 T^{5/2}$ (Yokoyama and Shibata, 1997), where k_B is Boltzmann constant, κ_0 is a physical constant (about 10^{-6} in cgs). Here, L , n_e , and T are the half length of the loop, electron number density, and the temperature of the hot plasma, respectively. Our event is located close to disk center, so we can’t measure the length of the loops directly because of the viewing angle. However, we can measure the distance between the EUV conjugate footpoints. The shortest distance between the EUV conjugate footpoints for Peaks 4, 7, 8, and 9 is approximately 28800 km, thus the half-length of the shortest loop should be approximately 23000 km, if we assume a semicircular loop. If we assume that the electron number density and the temperature of the hot plasma are $2 \times 10^9 \text{ cm}^{-3}$ and 20 MK, respectively, the travelling time will be 0.94 sec, which is comparable to the observed time delay (less than 3 sec) between the EUV and HXR emission. This means that we cannot rule out thermal conduction as the cause of the EUV brightenings. However, we should note that the temperature is the most sensitive parameter in this equation: the higher the temperature is, the shorter the travelling time is. The temperature that we used above is within the range of Fe XXIV emission, which starts to appear after Peak 9, as can be seen in Figure 2-5c, so this travelling time may be only appropriate for the later brightenings after Peak 9. However, due to the lack of HXR observations with spatial resolution, we cannot rule out the possibility that the HXR emission is from a hot ($T > 20$ MK) loop-top

source; therefore, we cannot rule out the possibility of the thermal conduction.

As mentioned in Section 2.3.2, the observations show that the pre-flare EUV brightenings are similar to the later flare ones in most respects, differing mainly in intensity. Therefore, we speculate that the pre-HXR EUV brightenings have the same generation mechanism as the flare ones. Why can we see EUV brightenings before the HXR onset in this event? The EUV observations show that the pre-HXR EUV bursts are much weaker than the later ones, as can be seen from the summed EUV light curves in the bottom panel of Figure 2-1. Given the high count rates and good statistics seen in the HXR for all of the flare peaks, the HXR sensitivity does not seem to be an issue. We therefore suggest that the energy released from the reconnection site may be relatively low during the rising phase, so that there is less contribution to the HXR emission in the SPI/ACS energy band ($E > 150$ keV).

2.5.2 Evolution of the magnetic shear

The EUV bright kernels are argued to represent the chromospheric footpoints of the newly reconnected flare loops. Therefore, we can to some extent infer the magnetic field connectivity by observation of the evolution of the EUV footpoints.

In order to study the shear change, the strongest brightening pairs of EUV footpoints which represent the major energy release site are selected. A strong to weak shear change is observed during the impulsive phase, which confirms the earlier results found at other wavelengths (Masuda et al. 2001; Asai et al. 2003; Kundu et al. 2004). The decrease of the shear of the EUV footpoints implies that the newly reconnected loops have a lesser magnetic shear.

However, we also would like to know what these observations can tell us about the flare magnetic topology. The observed shear change can be understood in terms of the standard model for solar flares (e.g., Moore et al. 1995; Moore et al. 2001). According

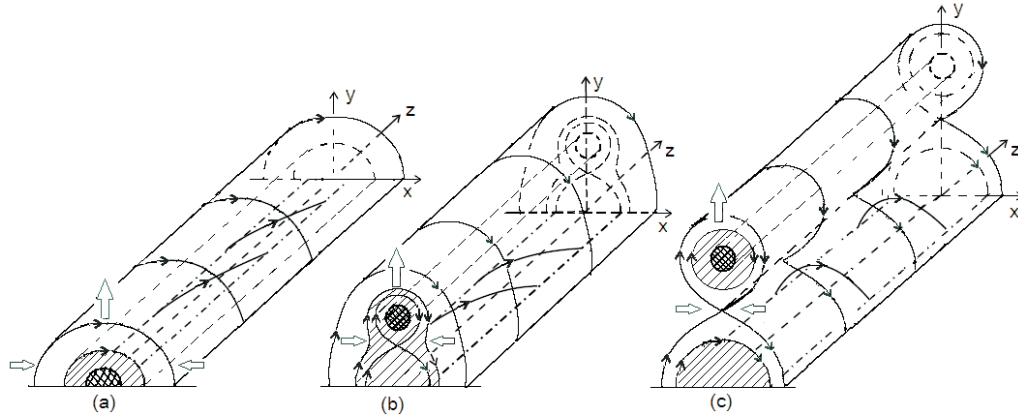


Figure 2-11 Cartoon of the evolution of the magnetic field in the standard model of solar flares. (a) Pre-flare magnetic field configuration with greatly sheared core field region (double hatched) surrounded by relatively less but still highly sheared envelope field (single hatched), which is underlying the unsheared envelope field. (b) Magnetic reconnection occurs in the highly sheared envelope field region. (c) The sheared envelope field splits completely, and magnetic reconnection occurs in the region where the field is unsheared. The direction of the magnetic field is represented by the arrows on the field lines. Note that the double hatched shadings indicate magnetic shear, not the presence of cool plasma ($H\alpha$ filament).

to this model the pre-flare magnetic field contains a highly sheared core field overlying the magnetic inversion line (MIL) on the photosphere. It is assumed that the pre-flare configuration evolves appropriately for the sheared core field to become eruptively unstable, and that the flare begins with the onset of the core eruption. Magnetic field begins to reconnect just below the rising core field, producing newly reconnected loops that, though less sheared than the pre-flare core field, retain some obvious shear (see Figure 1 in Moore et al. 1995). This indicates that, soon after the start of the eruption, the reconnection site is located at some height above the photosphere, inside the sheared envelope field. This reconnection causes the sheared envelope to split into two parts during the early phase of the flare. The upper part is ejected into the heliosphere, while the lower part stays behind on the sun.

Figure 2-11 illustrates the evolution of the magnetic field in the early phase of the

flare according to the standard model, but focusing on the evolution of the shear of the magnetic field. We use a Cartesian coordinate system (x, y, z) with the origin lying on the MIL in the photosphere; x is the horizontal coordinate perpendicular to the MIL, y is the height above the photosphere ($y \geq 0$), and z is the distance along the MIL. Figure 2-11a shows the magnetic configuration well before the flare at a time when flare-related reconnection has not yet occurred. Figure 2-11b shows the configuration in the early phase of the flare when the main reconnection has already started. The transition from Figure 2-11a to Figure 2-11b may take 1 hour or even longer. It is unclear exactly how this transition occurs. A detailed model of the magnetic field evolution during this period is beyond the scope of this chapter.

It is useful to divide the initial magnetic field configuration into three parts: (1) the inner part is a bundle of greatly sheared core field (double hatched) located just above the MIL; (2) the envelope field immediately coating the sheared core bundle is relatively less but still highly sheared (single hatched); (3) the outermost part is unshaped magnetic field overlying the immediate sheared envelope (Figure 2-11a). Note that the shear of the magnetic field transitions gradually between these regions.

The observed high shear during the early impulsive phase indicates that magnetic reconnection occurred in the region where the magnetic field (highly sheared, within the immediate sheared envelope region of Figure 2-11b) has a strong component along the direction of the magnetic inversion line. With the expansion of the sheared core flux bundle, the reconnection line moves upward, and the reconnection region moves out progressively. Therefore, the shear of the newly reconnected loops decreases progressively, which can explain the progressive decrease of the shear of the footpoints with the ribbon separation (Figures 2-9a-2-9d).

The sheared envelope soon splits into two separate parts: an upper part that moves away from the sun and a lower part that stays behind in the low corona (Figure 2-

11c). Magnetic reconnection occurs at an X-line located between the upper and lower parts of the sheared envelope field. As the eruption proceeds, the upper and lower parts of the sheared envelope field become more and more clearly separated, and the B_z component of magnetic field at the X-line decreases. Therefore, during the later phase the newly reconnected loops are weakly sheared, as shown in Figure 2-11c. This model provides a natural explanation for the observed shear change.

At 11:04 UT, the shear angle is about 20° , and little change in shear angle occurs after that time (Figure 2-10). This suggests that the splitting of the sheared envelope field is nearly complete at 11:04 UT, in the middle of the impulsive phase. Hence, there is no obvious relationship between the splitting of the sheared envelope field and the end of the impulsive phase.

2.6 Conclusions

An X17 class (GOES soft X-ray) two-ribbon solar flare which occurred on 2003 October 28 is studied in this chapter. Comparison of the light curves of the EUV emission from the brightenings within the two ribbons observed by TRACE and the HXR ($E > 150$ keV, SPI/ACS) emission show very good correlation, and we have also found that most of the individual peaks in the HXR bursts can be identified with EUV peaks from one or more bright kernels. The cross correlation between the light curves of the two types of emission shows that the typical time delay between the EUV and HXR emission is less than 3 seconds in this event. The comparison of the HXR ($E = 100\text{--}200$ keV, RHESSI) and EUV image at Phase 8 shows that the HXR sources are located at the EUV bright points. Although all of these observations seem to be favorable to the explanation that the EUV brightenings are mainly caused by direct bombardment at the lower atmosphere of the energetic particles accelerated at the reconnection site, we cannot rule out the possibility of thermal conduction, since the

travelling time of the thermal conduction front can be comparable to the observed time delay between the EUV and HXR emission, if the HXR emission is from a very high temperature ($T > 20$ MK) loop-top source. Good data sets observed simultaneously by TRACE, RHESSI, and the Solar-B/XRT which will be launched in 2006 will be helpful in obtaining a more conclusive result in this topic.

The onset of the EUV brightenings is about 3 min earlier than the HXR emission. These pre-HXR EUV brightenings appear to be associated with the flare ones in position, and these two kinds of brightenings do not have any obvious major difference. Some of the flare brightenings are also seen before the HXR onset, such as brightening “A”. All of these observations may suggest that the pre-HXR EUV brightenings have the same generation mechanism as the flare ones.

The EUV conjugate footpoints start at a position close to the magnetic inversion line but widely separated along the inversion line (highly sheared), and change into far from and straight across the inversion line (less sheared) gradually during the impulsive phase. This evolution of the EUV footpoints from strong to weak shear confirms the earlier results reported at other wavelengths. This suggests that the observed evolution in shear during the initial stages of a flare may be a frequent occurrence. We propose an interpretation in terms of the splitting of the sheared envelope field of the greatly sheared core rope overlying the magnetic inversion line during the early phase of the event. It is clear now, there must be some sheared field left behind on the sun, but what is the fraction of this kind of sheared field, or how much sheared field has been erupted? A lot of work need to be done in order to answer this question.

Our most significant new result is that the shear (between the strongest EUV footpoints) change was very fast during the early impulsive phase, but stopped in the middle of the impulsive phase. This result may indicate that the sheared envelope

field is split completely in the middle of the impulsive phase. This observation also gives a negative answer to our initial question: the magnetic shear change *per se* does not seem to be the reason for the transition from the impulsive phase to the main phase. More detailed studies of magnetic reconnection and particle acceleration in flares are needed in order to answer this question.

Chapter 3

A Statistical Study of Shear Motion of the Footpoints in Two-ribbon Flares

3.1 Introduction

Solar flares can be grouped according to the number of ribbons, from unresolved compact point-like flares to four-ribbon flares. The most commonly seen chromospheric flare morphology is the two-ribbon flare, according to Tang (1985). It is well known that ribbons of large two-ribbon flares separate as a function of time. This ribbon separation is interpreted as the chromospheric signature of the progressive magnetic reconnection in the corona, in which new magnetic field lines reconnect at higher and higher altitudes, according to the two-dimensional classical “CSHKP” model for two-ribbon flares (Svestka & Cliver 1992).

After analyzing 31 flares observed by the Hard X-ray telescope (HXT) on aboard *Yohkoh*, Bogachev et al. (2005) classified the footpoint motions into three types: 1) motion away from and nearly perpendicular to the magnetic inversion line (MIL) (ribbon separation); 2) motion mainly along the MIL and in antiparallel directions (shear motion); 3) parallel motion in the same direction along the MIL. Furthermore, they found that 14 out of their 31 flares show the second type motion, which often

appears as strong-to-weak shear change of the footpoints during a flare. This shear motion was also found in several individual two-ribbon flares (Ji et al. 2006; Su et al. 2006, hereafter Paper I, and references therein). This motion cannot be explained by a simplified two-dimensional flaring model, but it is instead consistent with a three-dimensional magnetic field configuration having highly sheared inner and less sheared outer magnetic field lines in the pre-flare phase (Moore et al. 1995, and references therein). The cessation of shear change during the impulsive phase can be interpreted as a splitting of the envelope of the highly sheared core field, according to Paper I.

So far, this change from strong to weak shear of the footpoints during the flare has been reported in almost 20 solar flares, which suggests that this motion may be a common feature in solar flares. In this chapter we have made a detailed statistical study of the shear motion of the footpoints in 50 two-ribbon flares using high spatial resolution extreme-ultraviolet (EUV)/ultraviolet (UV) images obtained with the Transition Region and Corona Explorer (TRACE, Handy et al. 1999), in order to make a conclusive statement about the prevalence of shear motion of footpoints in such flares. Our flares are classified into three groups: type I flares which show both ribbon separation and shear motion; type II flares show only ribbon separation; type III flares show no footpoint motion.

It is often considered that, to a first approximation, the life history of a flare consists of an impulsive phase, characterized by mainly nonthermal emissions (hard X-rays, γ -rays, radio waves, and neutrons) and a gradual (main) phase characterized by predominantly thermal emissions (soft X-rays, UV, and optical radiation) (Tandberg-Hanssen & Emslie, 1988). The impulsive and gradual phases can also be recognized on the basis of hard X-ray and microwave time profiles. The impulsive emissions have a short timescale, of order several tens of seconds to a few minutes, and gradual emissions evolve over a longer timescale of tens of minutes. The distinction between

the two turns out to be more than superficial and is not limited to temporal properties. Statistical and case studies in the last two decades revealed other respects in which the impulsive and gradual emissions show contrasting properties (for a detailed review, see Qiu et al. 2004 and references therein).

The physical differences between the flare impulsive phase and gradual phase are pronounced, and the transition from impulsive phase to main phase is typically abrupt. What is the nature of the change that occurs when a flare goes from the impulsive phase to the gradual phase? The magnetic field strength *per se* is unlikely to change abruptly, but the magnetic shear may show abrupt temporal gradients. Therefore, Lynch et al. (2004) suggested that the observed cessation of hard X-ray bursts with the start of the main phase can be understood in terms of the difference between reconnection in a strongly sheared versus an unsheared field. This hypothesis has been examined in detail for one flare in our previous paper (Paper I). The observations showed that the cessation of shear change of footpoints occurs in the middle of the impulsive phase. However, it is difficult to draw a conclusive statement on this question from this one case study. In this chapter, we examine the time difference between the cessation of the shear motion and the end of the impulsive phase in a sample of 14 events having both measurable shear angle and corresponding hard X-ray observations.

The observational data are summarized in Section 3.2. In Section 3.3.1 we present the study of type I flares. The observational results of types II and III flares are described in Section 3.3.2. In Sections 3.4.1 and 3.4.2, we compare our classification scheme (types I, II, and III flares) with that of Svestka (1986) (“ejective” and “confined” flares), and an energy scale for two-ribbon flares is described in Section 3.4.3. The time difference between the cessation of shear motion and the end of impulsive phase in type I flares is presented in Section 3.5. Summary is given in Section 3.6.

3.2 Observational Data

We construct our data sets based on the TRACE Flare Catalog¹, provided by the Solar and Stellar X-ray Group at Smithsonian Astrophysical Observatory, that lists all those X- and M- class (GOES soft X-ray) from May 1998 to the present time (and those C-class flares from 1998 to 2002, and they are not cataloged after this) observed by TRACE . The TRACE Flare Catalog is formed by selecting those flare events having TRACE observations around the flare peak time reported by GOES. The information of the class and peak time of the flares listed in the TRACE Flare Catalog is taken from the GOES Flare Catalog². We have selected 50 well observed two-ribbon solar flares from 1998 to 2005, according to the following criteria:

- (1). We only consider flares in which two long and roughly parallel ribbons are seen during the flare.
- (2). Most parts of the two ribbons are visible within the field of view (FOV) of TRACE.
- (3). TRACE obtained several good images during the rise and impulsive phase, from which we can see the two ribbons and their evolution clearly.
- (4). Flares near the limb for which the two ribbons and their evolution cannot be seen are not considered.

All of the flares we included in this study are listed in Tables 3.1 and 3.2.

The TRACE mission explores the dynamics and evolution of the solar atmosphere from the photosphere to the corona with high spatial and temporal resolution (Handy et al. 1999). It observes the white-light photosphere, the transition region at the wavelengths of 1216, 1550, and 1600 Å and the 1–2 MK corona at 171, 195, and 284 Å. However, because of its limited field of view (FOV), TRACE may miss observing

¹See http://hea-www.harvard.edu/trace/flare_catalog/

²See http://www.lmsal.com/SXT/plot_goes.html

some flares, if these flares happen outside the FOV (Zhang et al. 2002). We have used the TRACE catalog, understanding that it will not be a complete sample of all flares occurring during the studied period, because the TRACE observations of flares provide high spatial and temporal resolution images, which make possible the study of shear motion of the footpoints.

The hard X-ray time profiles used in this study from 1998 to 2001 are taken from the *Yohkoh* Flare Catalog³. *Yohkoh* HXT (Kosugi et al. 1991) used a Fourier synthesis technique to take images in four energy bands (L: 13–23 keV, M1: 23–33 keV, M2: 33–53 keV, and H: 53–93 keV) with a collimator response (FWHM) of about 8". For those flares that occurred after 2001, the hard X-ray data are obtained from RHESSI. RHESSI provides unprecedented high-resolution imaging and spectroscopy capability for solar flares (Lin et al. 2002). For the analysis, we use the energy band 33–53 keV for both HXT/*Yohkoh* and RHESSI, since lower energy bands may have a considerable contribution from the superhot plasma emission. We could also use a higher energy band, but the HXR emission are usually too weak in those bands to define the end of the impulsive phase with proper accuracy.

The magnetic inversion line information in most events used in this study is from the line of sight photospheric magnetograms observed by the Michelson Doppler Imager (MDI) onboard SOHO. For those events which do not have corresponding MDI observations, or if the MIL on the MDI magnetograms is too complicated, the MIL is identified by the corresponding filament on the H α images observed by Big Bear Solar Observatory (BBSO). Information about related coronal mass ejections (CMEs) is obtained from the SOHO LASCO CME Catalog⁴.

³See <http://gedas22.stelab.nagoya-u.ac.jp/HXT/catalogue/index.html>

⁴See http://cdaw.gsfc.nasa.gov/CME_list/index.html

3.3 Three Types of Two-ribbon Flares

Of the available TRACE passbands, more than half of the events we studied were mainly observed only in the EUV (171/195 Å) or UV (1600/1700 Å), and less than half of them were observed with a sequence that took a combination of EUV (171/195/284 Å) and UV (1600/1216/1550 Å) images. In order to study shear motion of the footpoints, our first step is to look through all the movies at the wavelength in the main observing sequence for each event, i.e. the wavelength that has the best coverage of the event. The motion of the brightenings can be seen clearly from the movies, and is visible in either UV or EUV channels. To make a detailed study, we first synthesized a set of TRACE images at the wavelength in main observing sequence for each event. In order to distinguish the motions of footpoints with respect to the magnetic field, the next step is to co-align the TRACE images with the corresponding magnetic field or H α images. To get good co-alignment of the EUV/UV (TRACE) and SOHO/MDI magnetograms or BBSO/H α image, we proceeded in three steps: (i) aligned the EUV/UV images with the white light (WL) images observed by TRACE using the “trace_prep.pro” program provided as part of the TRACE analysis software; (ii) aligned the WL images with the SOHO/MDI magnetograms or BBSO/H α images, using the dark sunspots; (iii) aligned the EUV/UV images with the SOHO/MDI images or BBSO/H α images using the offsets obtained from the first two steps.

After studying the motions of the brightenings observed by TRACE with respect to the magnetic field, we found that our events could be categorized into three groups:

Type I flares— The common characteristic among all flares in this group is that the EUV conjugate footpoints start at a position close to the magnetic inversion line but widely separated along the MIL (highly sheared), and change into a configuration far from and straight across the inversion line (less sheared) during the impulsive phase. In other words, this type of flare shows strong-to-weak shear motion of the footpoints

and also ribbon separation.

An example of a type I flare on 2001 April 26 is shown in Figure 3-1. Figure 3-1a represents the hard X-ray time profiles obtained from *Yohkoh*/HXT. The TRACE EUV initial brightenings (white contours) at the flare onset overlaid on the EUV image having the final brightenings at the time when the shear change stops is shown in Figure 3-1b. Figures 3-1c and 3-1d show the initial and final brightenings (white contours) overlaid on the later post-flare loop images showing the post-flare loops connecting these brightenings, respectively. The TRACE image at the time when the shear change stops overlaid with photospheric magnetic field contours observed by SOHO/MDI is shown in Figure 3-1e. Figures 3-1f and 3-1g show how we measure the initial and final shear angle.

Type II flares— We do not see measurable shear motion of the conjugate brightenings, but we see very small ribbon separation in this type of flares (e.g., Figures 3-2a and 3-2b).

Type III flares— We do not see shear motion of the conjugate brightenings, nor ribbon separation in these flares. Two examples of type III flares are shown in Figures 3-2c–3-2f.

3.3.1 Type I Flares

Footpoint Motion in Type I Flares

In all, 86% (43 out of 50) of the two-ribbon flares we studied show shear motion of the EUV/UV footpoints during the flare, which indicates that this motion is a common feature in two-ribbon flares. This 86% fraction is much larger than the 45% (14 out of 31) fraction reported by Bogachev et al. (2005). They found that 8 of these 14 flares with shear motion show mainly this shear motion, while the other 6 flares show a combination of ribbon separation and shear motion. However, all of our 86% flares

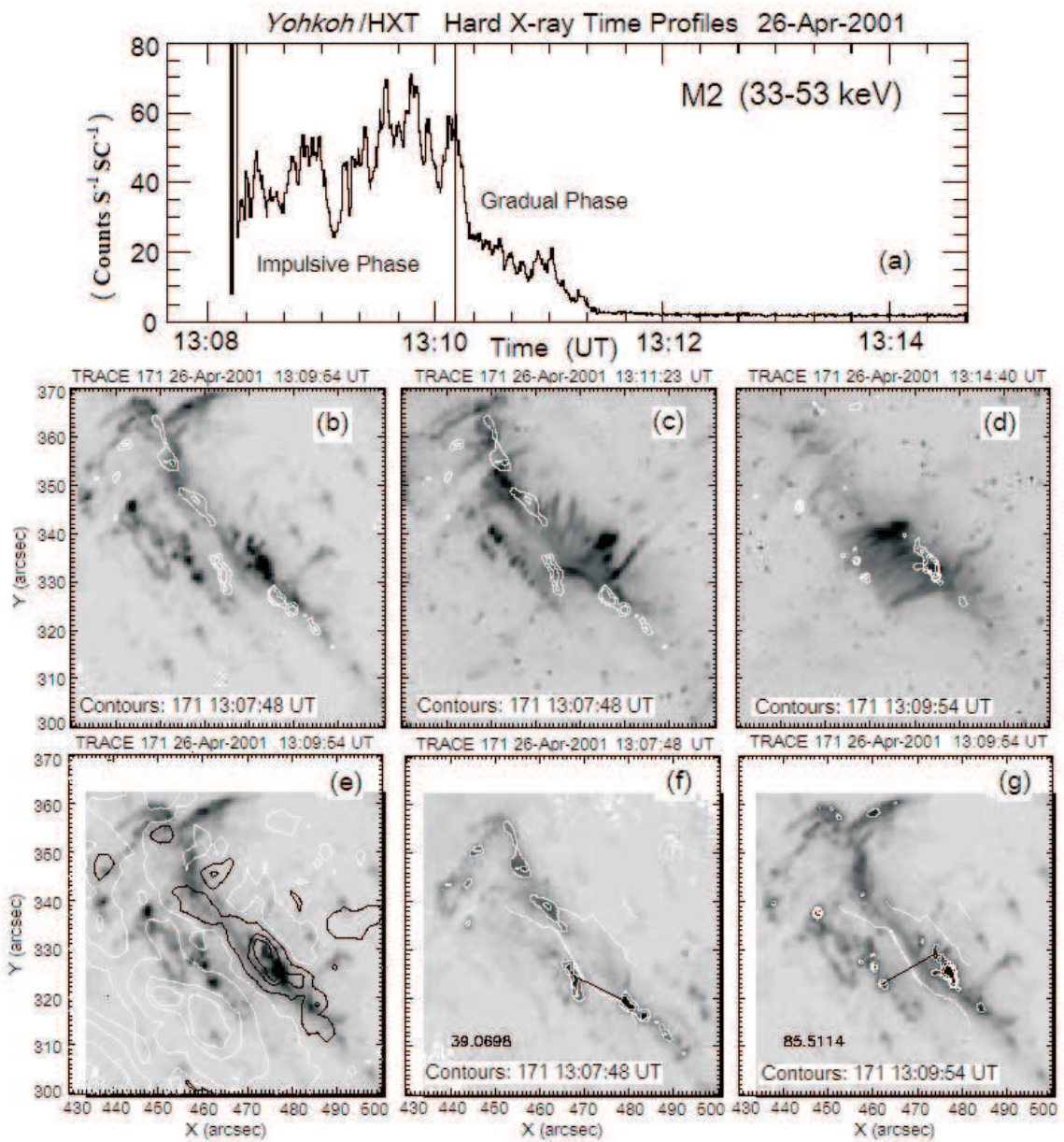


Figure 3-1 Event on 2001 April 26. (a) Hard X-ray ($E=33\text{--}53$ keV) time profile observed by HXT on board *Yohkoh*. The end of the impulsive phase is marked as a vertical line on the figure. (b–d) EUV images at 171 \AA observed by TRACE at different times. (e) TRACE EUV image overlaid with corresponding photospheric magnetic field (SOHO/MDI) contours. The black and white contours represent the positive and negative magnetic polarities, respectively. (f, g) TRACE EUV images at different times overlaid with white contours which represent the brightenings. The white lines refer to the magnetic inversion line (MIL, SOHO/MDI), and the thick white lines represent the simplified MIL. The brightenings connected by the black lines are conjugate footpoints.

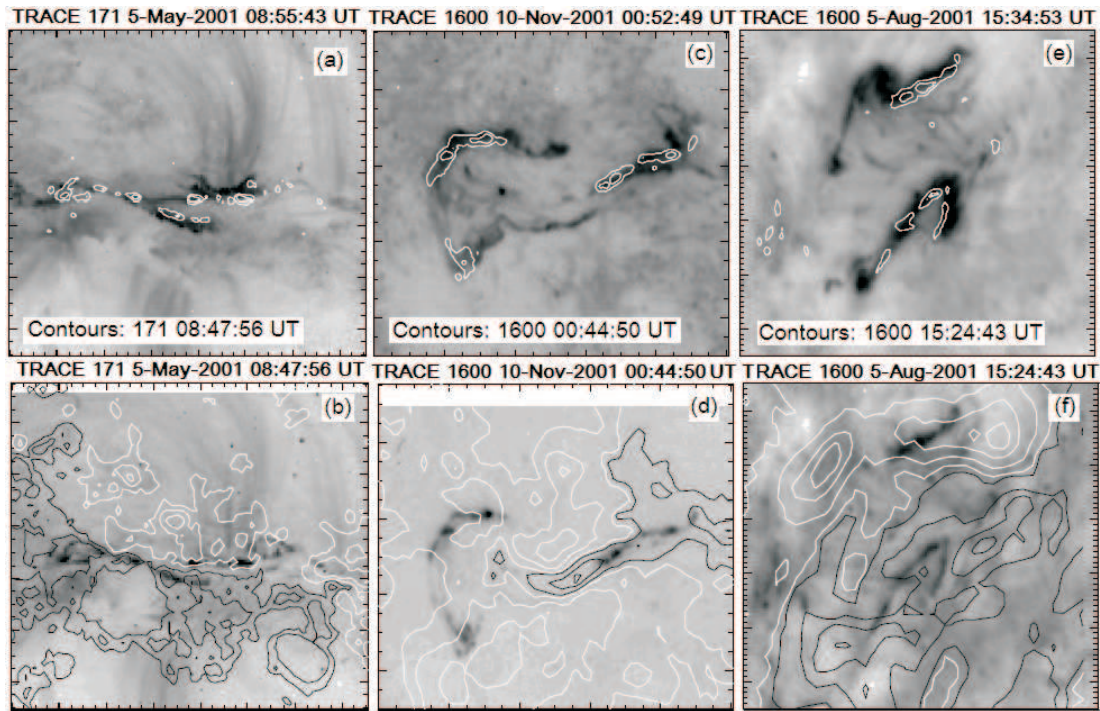


Figure 3-2 Types II and III flares. *Left:* Images for event 2001 May 5, and the field of view (FOV) is $150'' \times 125''$ (a) TRACE image at around the GOES flare peak time overlaid with white contours representing the bright kernels at the flare onset. (b) TRACE image at the flare onset overlaid with photospheric magnetic contours. The black and white contours refer to the positive and negative magnetic polarities (SOHO/MDI), respectively. *Middle:* Similar to the left panel, but for event 2001 November 10, and the FOV is $100'' \times 85''$. *Right:* Similar to the left panel, but for event 2001 August 5, and the FOV is $70'' \times 60''$.

show a combination of ribbon separation and shear motion. Two reasons which may explain this difference are: (1) Data selection criteria are different. All the flares we selected must have two long and nearly parallel ribbons observed by TRACE, which is not required by Bogachev et al. (2005). (2) Bogachev et al. (2005) used hard X-ray data observed by Yohkoh HXT (2."47 per pixel), while we are measuring the EUV/UV footpoints using the much higher spatial resolution (0."5 per pixel) data observed by TRACE.

As mentioned in Section 1, there are mainly three types of HXR footpoint motions: ribbon separation, shear motion, and motion in the same direction (Bogachev et al. 2005). In this chapter, although we focus our study on the shear motion of EUV/UV footpoints, we have also checked for the other two types of motions, i.e., ribbon separation and motion in the same direction. We have found that all the 43 type I flares show both ribbon separation and shear motion, and the brightest footpoints in 22 out of the 43 type I flares show “same direction” motion along with the shear motion and ribbon separation. This indicates that a mixture of these three types of motion often exists in two-ribbon eruptive flares.

Shear Angles of the Footpoints in Type I Flares

In order to get a quantitative determination of the shear motion of conjugate footpoints, we have selected 24 events out of the 43 type I flares, representing those events for which the MIL information and TRACE observations are good enough to (1) represent the magnetic inversion line using a straight line, and (2) identify the initial and final conjugate footpoints. The initial and final shear angles of these events have been measured and listed in Table 3.1. The shear angle is defined as the angle between the line connecting the conjugate footpoints and the line perpendicular to the magnetic inversion line.

Table 3.1. Type I flares with shear motion and ribbon separation.

Date	GOES Class	TRACE Observed Band(s) (Å)	TRACE Shear Angle			Time				GOES Peak (UT)	CME onset (UT)
			θ_1^a (°)	θ_2^a (°)	$\theta_1-\theta_2$ (°)	t_{EUV1}^b (UT)	t_{EUV2}^b (UT)	t_{HXR}^c (UT)	$t_{HXR}-t_{EUV2}$ (Seconds)		
1998 Sep 23	M7.1	1550,195	07:13	No data
1999 Jun 22	M1.7	1216,195,171	52±2	31±2	21	18:20:26	18:24:51	18:23	-111	18:29	18:54
1999 Jun 23	M1.7	1216,195,171	56±2	32±2	24	06:50:42	06:57:02	07:09	07:31
2000 Feb 08	M1.3	171,1600	65±2	19±2	46	08:44:05	08:49:32	08:51:55	143	09:00	09:30
2000 Apr 12	M1.3	171	03:35	No
2000 Jun 04	M3.2	171,1600	67±2	49±2	16	22:06	22:09:27	22:10	23:54
2000 Jun 06	X2.3	171,1600	15:25	15:30
2000 Jun 10	M5.2	195,1600	51±2	19±2	32	16:47:12	16:53:30	17:02	17:08
2000 Jul 14	X5.7	195	65±2	23±2	42	10:24:23	10:26:51	10:27	9	10:24	10:54
2000 Nov 08	M7.4	171	23:28	23:06
2000 Nov 24	X2.3	1600	15:13	15:30
2000 Nov 24	X1.8	1600	57±2	15±2	42	21:49:14	21:52:51	21:54:07	76	21:59	22:06
2001 Jan 20	M1.2	1600	18:47	19:31
2001 Jan 20	M7.7	1600	21:20	21:30
2001 Mar 24	M1.7	171,1600	80±2	50±2	30	19:37:53	19:55:05	19:55	20:50

Table 3.1 (cont'd)

Date	GOES Class	TRACE Observed Band(s) (Å)	TRACE Shear Angle			Time				GOES Peak (UT)	CME onset (UT)
			θ_1^a (°)	θ_2^a (°)	$\theta_1-\theta_2$ (°)	t_{EUV1}^b (UT)	t_{EUV2}^b (UT)	t_{HXR}^c (UT)	$t_{HXR}-t_{EUV2}$ (Seconds)		
2001 Apr 09	M7.9	171,1600	63±2	35±2	28	15:25:02	15:31:27	15:34	15:54
2001 Apr 10	X2.3	171	53±2	2±2	51	05:08:39	05:17:25	05:19	95	05:26	05:30
2001 Apr 11	M2.3	171	76±2	46±2	30	12:58:27	13:07:46			13:26	13:31
2001 Apr 26	M7.8	171,1600	51±2	5±2	46	13:07:48	13:09:54	13:10:10	16	13:12	13:31
2001 Jun 15	M6.3	195	10:13	10:31
2001 Aug 25	X5.3	284	16:45	16:50
2001 Oct 19	X1.6	171	16:30	16:50
2001 Dec 26	M7.14	1600	05:40	05:30
2002 Mar 14	M5.7	171	61±2	26±2	35	01:42:02	01:47:22	01:46	-82	01:50	23:54
2002 Apr 10	M1.6	195	52±2	27±2	25	19:01:55	19:04:03	19:04:15	12	19:07	20:26
2002 Jul 29	M4.7	171,1600	10:44	No
2002 Jul 31	M1.2	171	50±2	1±2	49	19:37:53	01:51:10	01:51:40	30	01:53	No
2002 Oct 22	M1.0	195	85±2	50±2	35	15:32:18	15:33:25	15:35	No
2002 Oct 25	M1.5	195	17:47	18:06
2003 May 29	X1.2	195,1600	01:05	01:27

Table 3.1 (cont'd)

Date	GOES	TRACE	TRACE Shear Angle			Time				GOES Peak (UT)	CME onset (UT)
	Class	Observed Band(s) (Å)	θ_1^a (°)	θ_2^a (°)	$\theta_1-\theta_2$ (°)	t_{EUV1}^b (UT)	t_{EUV2}^b (UT)	t_{HXR}^c (UT)	$t_{\text{HXR}}-t_{\text{EUV2}}$ (Seconds)		
2003 May 31	M9.3	195	52±2	29±2	23	02:19:03	02:21:54	02:24	02:30
2003 Jun 11	X1.6	1700	20:14	No data
2003 Aug 19	M2.7	171,195,1600	70±2	48±2	22	09:49:45	10:00:24	10:02:22	118	10:06	10:30
2003 Oct 24	M7.6	195,1600	72±2	41±2	31	02:27:56	02:44:58	02:52:20	440	02:54	02:54
2003 Oct 28	X17.2	195,1600,284	78±2	22±2	56	11:00:41	11:04:05	11:05	55	11:10	11:30
2004 Nov 10	X2.5	1600	02:13	02:26
2004 Dec 30	M2.2	1600	10:47	10:57
2005 Jan 15	X2.6	1600	23:02	23:06
2005 May 17	M1.8	171	75±2	36±2	39	02:33:37	02:42:46	02:42:50	4	02:39	03:06
2005 Jul 07	M4.9	171,1600	61±2	18±2	43	16:07:21	16:20:50	16:29	17:06
2005 Jul 09	M2.8	171,1600	48±2	19±2	29	21:55:55	22:05:27	22:06	22:30
2005 Jul 30	X1.3	171	06:35	06:50
2005 Sep 17	M9.8	171,1600	67±2	46±2	21	06:02:15	06:04:53	06:05:40	47	06:05	No

^a θ_1 and θ_2 refer to the initial and final shear angles, respectively.

^b t_{EUV1} and t_{EUV2} refer to the time when the initial and final shear angles are measured, respectively.

^cThe time when the impulsive phase stops.

We have developed a semi-automatic program to measure the shear angles of these events. The projection effects of events close to the limb have been corrected by moving the source region to the solar disk center in software. The process of measuring the shear angles is described below:

1. Inspect and compare all of the EUV/UV images overlaid with magnetic field contours during the flare to select two EUV/UV images. The first image is the one when the initial brightenings (e.g., white contours on Figure 3-1b) appear, and the second image is the one when the shear change of footpoints stops (e.g., Figure 3-1b). For those flares without SOHO/MDI observations, all the EUV/UV images are shown as contours overlaid on the BBSO/H α image closest in time, and the MIL is indicated by the filament.

2. Select the initial and final conjugate footpoints from the two images. Most events start as two bright kernels appearing on both sides of the MIL. These two bright kernels will be identified as the initial conjugate footpoints if they are subsequently connected by corresponding post-flare loops (e.g., Figure 3-1c). Two long ribbons composed of many bright kernels have been formed by the time the shear motion of the footpoints stops. We choose the brightest brightening pair at the end of shear change as the final conjugate footpoints. Furthermore, the corresponding post-flare loops for most of these brightening pairs at this time are roughly parallel to each other (e.g., Figure 3-1d), which means the shear angles of most of the brightening pairs are similar.

3. The angle between the line connecting the two conjugate footpoints (e.g., black line on Figures 3-1f and 3-1g) and the simplified magnetic inversion line (thick white line on Figures 3-1f and 3-1g) is measured using our semi-automatic program. This angle can be measured by clicking the start and end points of the MIL and the two conjugate footpoints on the image. Note that the shear angle is complementary to

the angle thus measured.

The various parameters of all type I flares are listed in Table 3.1. The histogram of event number in terms of the initial and final shear angles (Figure 3-3a) shows that the initial and final angles in most events are in the range from 50° to 80° and 15° to 55° , respectively. The distribution of the final shear angle may suggest that the magnetic field does not generally relax fully to a potential state (Gibson & Fan 2006b). This is because reconnection under high electrical conductivity approximately conserves the global magnetic helicity, according to Berger and Field (1984). Thus, coronal fields will naturally produce a flux rope, rather than a potential field, as a metastable state (Zhang & Low 2005). It is worth noting here, due to the uncertainties in our method of measuring shear angle (e.g., we use a simplified straight line to represent the magnetic inversion line), we cannot exclude the possibility that the magnetic field does relax to a fully potential state after the flare for some events, especially those events having final shear angle less than 15° . In order to make sure if the magnetic field relax to a fully potential state or not, we should make detailed calculation using the potential magnetic field model, which is beyond the scope of this chapter.

Figure 3-3b is the histogram of event number in terms of the change of shear angle, which shows that the change of shear angle is distributed in the range between 15° and 60° .

3.3.2 Types II and III Flares

These types of flares have no obvious shear change of the footpoints. All these flares have relatively low soft X-ray flux (GOES class $< M5$).

Type II flares (marked as “a” in Table 3.2) show very small ribbon separation during the flare (e.g., Figure 3-2a). We found two such events. In both cases, a filament is seen before the flare in both TRACE and the $H\alpha$ images (BBSO). The

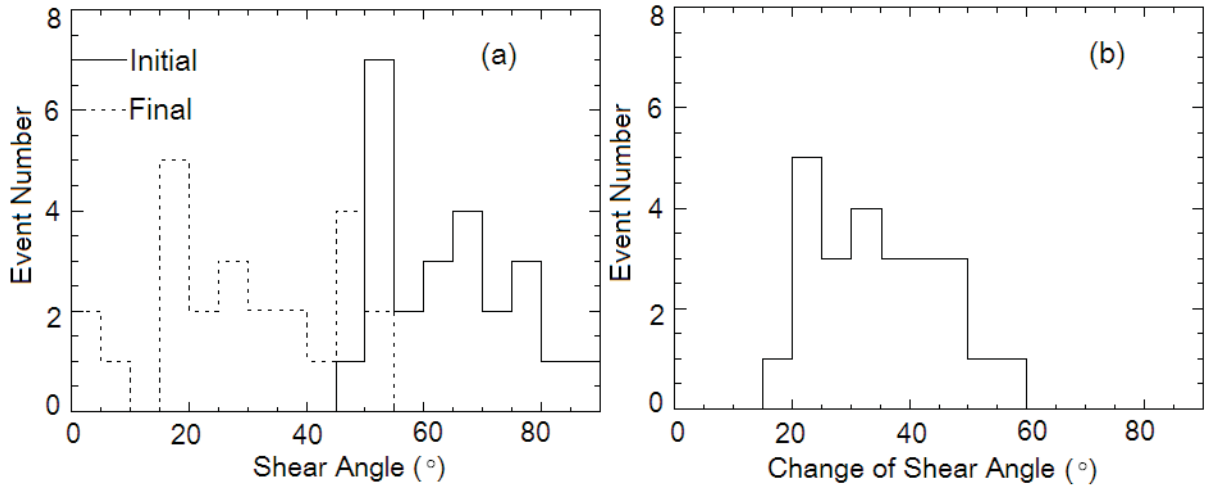


Figure 3-3 Histograms for the 24 type I flares with measured shear angle. (a) Histogram of event number in terms of the initial and final shear angles. (b) Histogram of event number in terms of the change of shear angle. The bin size in these two histograms is 5° .

Table 3.2. Type II and Type III flares without shear motion.

Date	GOES Class	Observed Band(s) (\AA)	GOES Peak Time (UT)	Ribbon Separation	CME Onset Time (UT)
2001 May 05 ^a	M1.0	171,1600	08:56	Small	No
2001 Aug 05 ^b	M1.7	171,1600	15:31	No	No
2001 Aug 05 ^b	M4.9	171,1600	22:24	No	No
2001 Oct 31 ^c	M3.2	171	08:09	No	No
2001 Nov 10 ^c	M1.0	1600	00:50	No	No
2001 Dec 29 ^c	M1.1	1600	05:45	No	No
2003 Jan 22 ^a	M1.2	171	04:44	Small	05:06

^aType II flares.

^bType IIIA flares.

^cType IIIB flares.

two ribbons initially appear close to the magnetic inversion line, then move outward very slightly away from the MIL. There is no observable filament activation associated with event 2001 May 5, but a filament eruption is seen to be associated with event 2003 January 22. Both type II flares have single-bipole magnetic field configuration (Figure 3-2b).

We found 5 type III events (marked as “b” and “c” in Table 3.2), in which there is no observed ribbon separation. The brightenings of all type III flares appear at a position far from the magnetic inversion line, and the shear of the conjugate brightenings is very weak at the flare onset. As the flare progresses, the two ribbons may show some expansion along the direction parallel to the inversion line, but there is no motion along the direction perpendicular to the MIL at all throughout the entire flare process (i.e., Figures 3-2c and 3-2e). Type III flares are divided into two subgroups (i.e., type IIIA and type IIIB marked as “b” and “c” in Table 3.2, respectively) based on the photospheric magnetic field configuration. The difference between type IIIA and type IIIB flares is that: type IIIA flares have a complicated magnetic field configuration (e.g., Figure 3-2d), whereas type IIIB flares have a simple single-bipole magnetic field configuration (e.g., Figure 3-2f).

3.4 “Ejective” and “Confined” Flares

Flares have been categorized in many different ways, but two particular types, the simple-loop (compact or confined) flare and the two-ribbon (dynamic or ejected) flare may be particularly significant (Pallavicini et al. 1977; Moore et al. 1980; Priest 1981). In compact flares we see brightenings of loops that do not show any apparent expansion, rise, or other kinds of motion. In $H\alpha$, the brightened footpoints of the flare stay in the same position until they decay. They do not appear to be associated with filament disruption (which is a characteristic feature of the two-ribbon

flares), nor with white-light coronal transients (which are consequences of the filament disruptions, Priest 1981). The two-ribbon flares are much larger and more dramatic than a compact flare and take place near a solar prominence or filament. During the flash phase, two ribbons of $H\alpha$ emission form, one on each side of the filament (or filament channel) and, throughout the main phase, the ribbons move apart at 2–10 km s⁻¹. Occasionally, the filament remains intact, though slightly disturbed, but usually it rises and disappears completely (Priest 1981). Following Svestka (1986), the first class of flares are called “confined” flares to emphasize their essential difference from the other classes, and the other class are called “ejective” flares (Machado et al. 1988).

In this section we compare our classification scheme (Section 3.3) with that of Svestka (1986), and introduce some available models for these flares. We classify those flares having both ribbon separation and corresponding CMEs into the “ejective” flare category. For some flares we do not find corresponding CMEs from the SOHO LASCO CME Catalog, and we call these flares “possibly ejective”. Flares having no ribbon separation nor corresponding CMEs are classified into the “confined” flare category. We regard the flare and CME as associated if the CME onset time (first appearance time at LASCO/C2) is within a ± 2 hour time window of the flare peak time and the position of the flare lies in the range of the CME span, defined as the position of the CME \pm half of the CME width $\pm 15^\circ$ (Zhang & Golub 2003). If the CME candidate is a halo CME, then the center of the TRACE field must lie within 45° of disk center in both longitude and latitude, otherwise the latitude of the center position of the TRACE field must lie in the range of the CME span, according to Zhang et al. (2002).

3.4.1 “Ejective or Possibly Ejective” Flares

From Tables 3.1 and 3.2 we can see that 36 type I flares plus one type II flare belong to the “ejective” flare category. For this type of flare, there is now a generally accepted picture for the overall three-dimensional magnetic field and its change during the flare. This standard picture is basically the one proposed by Hirayama (1974), which (with various modifications, refinements, and changes in emphasis) has been adopted by many flare modelers (Moore et al. 1995 and references therein). In this scheme, the flare energy release is driven by the eruption of a magnetic flux rope from the sheared core of a closed bipolar magnetic field (Moore 1988; Forbes 1992). The strong-to-weak shear motion of the footpoints is interpreted as magnetic reconnection progressing from a highly sheared to a less sheared region (Figure 11 in Paper I). This strong-to-weak shear motion of the footpoints or of the post-flare loops is seen in a magnetohydrodynamic (MHD) simulation of the nonlinear development of instabilities of magnetically sheared arcades made by Manchester (2003) (see his Figure 2). An MHD simulation of the eruption of a 3D flux rope done by Gibson & Fan (2006b) also shows this motion (see their Figures 5g–5i).

For the other 7 type I flares and one type II flare, the corresponding CME information is uncertain. The CME onset times for all the flares we studied are listed in the last column of Tables 3.1 and 3.2. For two flares the CME information is uncertain because there is a gap in LASCO observations (marked as “No data”). For the other 6 flares, we do not find corresponding CMEs fitting our criteria. Note that, although we do not find corresponding CMEs from the LASCO C2 observations, we cannot say these flares are not associated with CMEs, because the associated CME may be too weak to be detected by the SOHO LASCO C2. We call these flares “possibly ejective” flares, because they show ribbon separation, but there is no certain corresponding CMEs’ information.

For 2 out of these 8 “possibly ejective” flares, we see obvious filament eruptions in EUV observations made by TRACE. Although the corresponding CME information is uncertain, we suggest that these two “possibly ejective” flares, similar to “ejective” flares, may also be caused by the ejective eruption of the sheared core field (Moore et al. 2001). It is worth noting that in this scheme, all or part of the filament (sheared core field) is often seen to erupt in association with a flare. However, according to Gibson & Fan (2006a, 2006b), the degree to which the initially dipped field was filled with filament mass, and the location of this mass relative to where the flux rope breaks in two, would then determine whether all, some, or none of the filament would actually be observed to erupt and escape with the CME. If only the lower dips were filled with filament mass, the filament might not show any sign of eruption at all, which may explain why we do not see filament eruption in the other 6 “possibly ejective” flares (e.g., event 2001 May 5). Since the flux rope or the envelope of the sheared core field can break in two (Gibson & Fan 2006a, 2006b; Paper I), a weak CME may happen if only a smaller upper part of the flux rope (CME) is ejected, and the larger lower part of the flux rope is left behind. Therefore, these 6 “possibly ejective” flares may be caused by partial eruption of the flux rope (or sheared core field).

3.4.2 “Confined” Flares

It is known that ribbons of large two-ribbon flares separate as a function of time, which can be interpreted by the classical two-dimensional magnetic reconnection model discussed in Section 1. However, the separation of ribbons is not universal, and we observed several small two-ribbon flares (i.e., type III flares) that have no ribbon separation at all throughout the entire flare process. The ribbons of these flares are not close together at the flare onset and no strong shear of the footpoints is

observed either, which is consistent with the earlier results reported by Tang (1985) and Kurokawa (1989).

We find that all 5 type III flares belong in the “confined” category for which no corresponding CMEs have been found from the SOHO/LASCO observations, and all these 5 flares have low soft X-ray peak flux (GOES class < M5). These observations suggest that only a small amount of energy is released in these flares, therefore there might be very little free energy stored prior to the flare.

In the following we discuss our observations in the context of models for “confined” flares:

1) *Emerging (or evolving) flux model*: According to this model, a (small) confined flare occurs if the new flux appears in a region where no great amount of magnetic energy in excess of potential is stored (Heyvaerts et al. 1977; Shibata et al. 1992). All the three type IIIA flares have complicated magnetic field configuration, such as in the flare on 2001 November 10 (e.g., Figure 3-2d), the negative polarity is surrounded by the positive polarities and the magnetic inversion line is strongly contorted, therefore this MIL can be treated as two magnetic inversion lines. However, the two type IIIB flares have a single bipolar configuration, and the magnetic inversion line is nearly straight. More than one magnetic inversion line are needed to make this model work. Therefore, this model seems possible for the type IIIA flares, but may not fit the type IIIB flares.

2) *(Resistive) kink instability*: When a loop is twisted by more than a critical amount it becomes kink or resistive kink unstable. If ideal kink occurs, the loop may become contorted and develop current sheets in the nonlinear development. If the resistive kink takes place, one or several current sheets form at which the magnetic energy is dissipated (Sakurai 1976; Priest 1981; Gerrard & Hood 2003). A recent simulation done by Török & Kliem (2005) shows that the kink instability of coronal

magnetic flux ropes could drive a confined eruptions if the decrease of the magnetic field above the flux rope is not steep enough. For our “confined” flares, we do not see any observational evidence which supports this model, but we also do not have enough observational evidence to rule out this possibility.

3) *Confined explosion of a sheared core bipole*: The sheared core field and filament undergo an eruption that is soon arrested within the confines of the closed bipole, and the flare has a correspondingly short duration (Moore et al. 2001). This model predicts that the brightenings at the flare onset are highly sheared and close to the inversion line, while our observations show that the brightenings in the 5 “confined” (i.e., type III) flares at the flare onset are weakly sheared and far away from the inversion line (e.g., Figure 3-2).

3.4.3 An Energy Scale for Two-ribbon Flares

Table 3.3 shows the relationship between the two types of classification for all the flares we studied using different criteria. From Table 3.3 we can see that “ejective” flares almost always show shear change of the footpoints (only 1 counter example out of 37). There are two flares that show ribbon separation but no shear motion. However, shear motion of the footpoints is always accompanied by ribbon separation.

The eruptive or non-eruptive behavior of flares is likely determined by the *relative* amount of free energy ε , i.e., the ratio of the magnetic free energy ΔE released in the flare and the energy ΔE_{open} required to open up the field. For $\varepsilon \geq 1$, sufficient energy is available to produce an eruption, whereas for $\varepsilon \ll 1$ only confined flares are energetically possible. We suggest that this ratio ε also determines the type of footpoint motions that occur within the flare. Figure 3-4 shows a schematic representation of the flare energy scale sequence of the three types (types I, II, and III) of flares. Type I flares are the most powerful eruptions, which show both shear motion

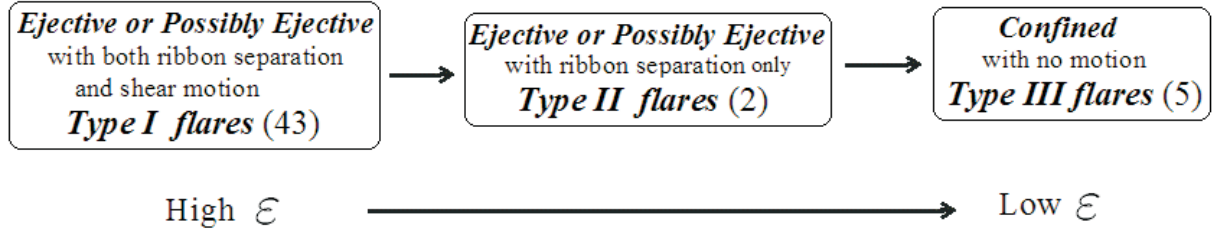


Figure 3-4 Schematic representation of the flare energy scale indicating the type of flare footpoint motions. “ ε ” refers to the relative amount of magnetic free energy in the corona prior to the flare.

of the footpoints and ribbon separation, and most of these flares are associated with coronal mass ejections. This suggests that a large amount of free energy is stored in the corona prior to this type of flare, $\varepsilon \geq 1$. Type II flares are relatively smaller flares, and they only show very small ribbon separation, but no measurable shear change of the footpoints, and only one of the observed type II flares is associated with a CME. These observations may indicate that the free energy stored in the magnetic field in these flares is relatively small, i.e. $\varepsilon < 1$, which causes very small ribbon separation and no obvious shear change of the footpoints. Type III flares show no shear change of the footpoints nor ribbon separation, and no corresponding CMEs. There is for such flares only minor nonpotentiality and thus the energy in the corona prior to eruption is small (Priest & Forbes 2002).

3.5 Time Difference Between the Cessation of Shear Motion and the End of Impulsive Phase in Type I Flares

We have selected 14 events with good corresponding HXR (*Yohkoh*/HXT or RHESSI) observations out of the 24 type I flares with measured shear angle, in order to answer the question: could the transition from impulsive to gradual phase be related to the magnetic shear change?

In the impulsive phase of these flares, the hard X-ray and gamma-ray emission rises impulsively, often with many short but intense spikes of emission, each lasting a few seconds to tens of seconds. The end of the impulsive phase in this study is defined as the last peak of the impulsive phase (e.g., the vertical line in Figure 3-1a). We note that in most events, the time of the end of the impulsive phase is earlier than the GOES soft X-ray peak time which is listed in Table 3.1. In the gradual phase, the hard X-ray and gamma-ray fluxes start to decay away more or less exponentially with a time constant of minutes (e.g., Figure 3-1a).

The histogram of the time difference between the end of the HXR impulsive phase and the cessation of the shear change shows that in most events, the cessation of shear change is 0–2 minutes earlier than the time when the impulsive phase stops (Figure 3-5).

This observation indicates that during the impulsive phase magnetic reconnection occurs mainly in the highly sheared region (within the filament channel), but reconnection progresses out to the weakly sheared region (outside the filament channel) during the gradual phase. This result implies that the change from impulsive phase to gradual phase may be related to the magnetic shear change as suggested by Lynch et al. (2004), although the two changes do not happen at exactly the same time. The observation also indicates that the splitting of the sheared envelope of the highly sheared core field happens near the end of the impulsive phase in most cases, since the cessation of shear change may be interpreted as this splitting of the sheared envelope (Paper I).

3.6 Summary

We have, for the first time, carried out a statistical study of shear motion of the UV/EUV footpoints in a large sample (50) of well-observed X- and M- class two-

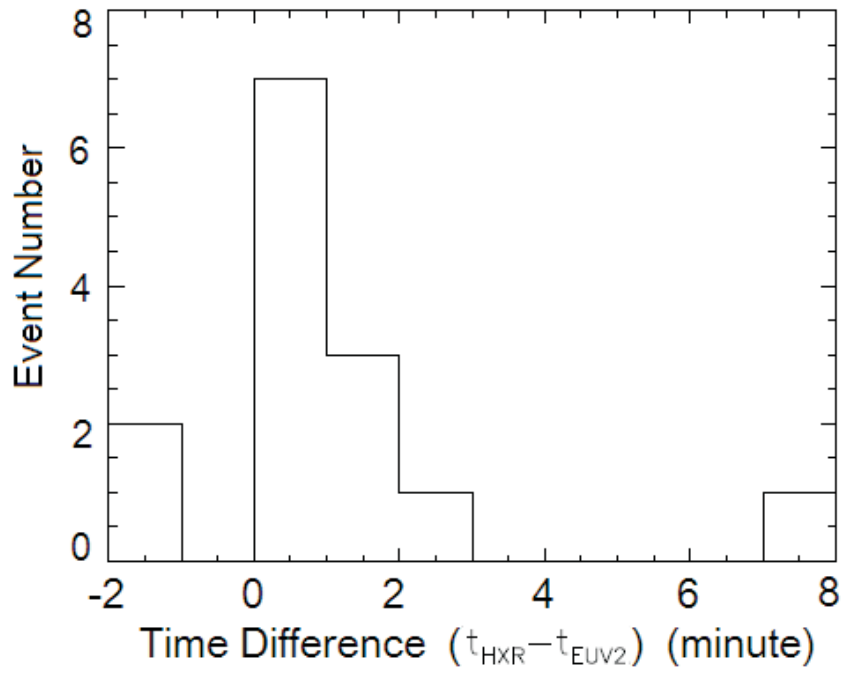


Figure 3-5 Histogram of event number in terms of the time difference between the end of the HXR impulsive phase and the cessation of the change of shear angle in the 14 type I flares with both measured shear angles and corresponding hard X-ray observations. The time bin size is 1 min.

ribbon flares, observed by TRACE in 1998–2005. These flares are classified into three groups: type I flares, which show shear motion of footpoints and ribbon separation; type II flares which show ribbon separation, but no measurable shear motion of footpoints, type III flares show no shear motion of the footpoints nor ribbon separation. We also compared our classification with the traditional classification of “ejective” and “confined” flares (Svestka 1986). Our results can be summarized as follows:

1. Our study shows that 86% (43 out of 50) of the flares belong to type I, and all type I flares (“ejective or possibly ejective”) show obvious ribbon separation during the flare. This 86% fraction is much larger than the 45% (14 out of 31) fraction reported by Bogachev et al. (2005). Our observations indicate that both shear motion of conjugate footpoints and ribbon separation are common features in two-ribbon flares. These flares may be interpreted with the well-accepted standard picture of two-ribbon eruptive flares, which is the (whole or partial) eruption of a magnetic flux rope from the sheared core of a closed bipolar magnetic field (Moore, LaRosa, & Owing 1995, and references therein). A detailed description of this standard model and the interpretation of shear motion of footpoints are given in our previous paper (Paper I).

2. “Ejective” flares (which have ribbon separation and corresponding CMEs) almost always show shear change of the footpoints (only 1 counter example out of 37). There are two flares that show ribbon separation but no shear motion. However, shear motion of the footpoints is always accompanied by ribbon separation, which is not consistent with the result reported by Bogachev et al. (2005), who found that 8 out of the 31 flares show mainly shear motion.

3. The initial and final angles of the footpoints in 24 type I flares have been measured, and they are mainly distributed in the range from 50° to 80° and 15° to 55° in most events, respectively. This result may indicate that the magnetic field

relaxes toward, but does not generally reach, a fully potential state. However, we cannot exclude the possibility that the magnetic field does relax to a fully potential state after the flare for some events, especially those events having final shear angle less than 15° , due to the uncertainties in our measurements of the shear angle. The *change* of shear angle is in the range between 15° and 60° . This measurement of the distributions of the initial and final shear angles may provide some constraints on three-dimensional magnetic reconnection models for solar eruptions.

4. Some flares show no shear change of the conjugate footpoints during the flare. These flares have either no obvious ribbon separation (5 type III flares) or very small ribbon separation (2 type II flares). Similar to type I flares, type II flares may also be driven by the (whole or partial) eruption of a magnetic flux rope from the sheared core of a closed bipolar magnetic field, but we speculate that these are partial eruptions involving a relatively small amount of axial magnetic flux. The brightenings of type III flares appear at a position far from the magnetic inversion line at the flare onset, and no ribbon separation is observed during the flare. These flares belong to the “confined” flares category. Our observations in the context of several models for “confined” flares are discussed in Section 4.2.

5. The cessation of shear change is 0–2 minutes earlier than the end of the impulsive phase in 10 out of the 14 events with measured shear angle and corresponding HXR observations. This provides a positive answer to our hypothesis, namely that the change from impulsive to gradual phase appears to be related to the magnetic shear change.

Chapter 4

What Determines the Intensity of Solar Flare/CME Events?

4.1 Introduction

Solar flares, prominence eruptions, and coronal mass ejections (CMEs) are magnetic phenomena thought to be powered by the magnetic free energy (i.e., the difference between the observed total magnetic energy and the potential field magnetic energy) stored in the corona prior to the eruption. Storage of free energy requires a non-potential magnetic field, and it is therefore associated with a shear or twist in the coronal field away from the potential, current-free state (Priest & Forbes 2002). One indication of such a stressed magnetic field is the presence of a prominence. Another important indicator of a stress magnetic field is the presence of sigmoid signatures discovered by Rust & Kumar (1997) and Canfield et al. (1999) with *Yohkoh*. Indeed, they have found that active regions that are sigmoidal to be the most likely to erupt. Lin (2004) pointed out that the free energy stored in a stressed magnetic structure prior to the eruption depends on the strength of the background field, so the stronger the background field, the more free energy can be stored, and thus the more energetic the eruptive process. The results obtained by Falconer et al. (2006) agree with the total nonpotentiality (total free energy) of an active region being roughly the product of the overall twist and the flux content of its magnetic field.

A positive correlation between the potential field magnetic energy of the active region and the CME speed have been found by Venkatakrisnan & Ravindra (2003). Guo et al. (2006, 2007) have found a weak correlation between the total magnetic flux of an active region and the CME speed. However, a statistical study of 49 filament eruption-associated CMEs by Chen et al. (2006) showed that the CME speeds are strongly correlated with both the average magnetic field and the total magnetic flux in the filament channel, and the corresponding linear correlation coefficients (LCCs) are 0.7 and 0.68, respectively. Using the catastrophic loss of equilibrium model, Lin (2002, 2004) found that the cases with higher background fields correspond to fast CMEs and lower fields corresponds to slow CMEs. Reeves & Forbes (2005) also found that when the background magnetic field is weak, the radiation emitted by the reconnected X-ray loops beneath a CME (i.e., flare intensity) is faint for an extended version of the Lin & Forbes (2000) model.

Good correlations have been found between different parameters representing the magnetic shear (or twist) or the nonpotentiality of the active region and the flare/CME productivity (Falconer et al. 2006, and Jing et al. 2006 and references therein). As mentioned previously, several authors have found a positive correlation between the background magnetic field strength, magnetic flux, or potential magnetic field energy and the CME speed. However, to our knowledge, few studies have been made of the relationship between the magnetic shear or nonpotentiality of the background field and the intensity of flare/CME events (i.e., peak flare flux and CME speed). Our previous study (Su et al. 2007a, hereafter Paper I) shows that 86% of the 50 events we examined show a strong-to-weak shear motion of the footpoints during the flare, which indicates that it is a common feature in two-ribbon flares. In Paper I, we have also measured the initial shear angle (θ_1 , measured at the flare onset) and final shear angle (θ_2 , measured at the time when the shear change stops)

of the flare footpoints for 24 events having shear motion of the footpoints and good observations. A detailed interpretation of this shear motion is given by Su et al. (2006), according to a three-dimensional magnetic field configuration having highly sheared inner and less sheared outer magnetic field lines in the pre-flare phase (Moore et al. 2001, and references therein). Some detailed studies of both the shear motion and the contracting motion of the footpoints in some individual flares are carried out by Ji et al. (2006, 2007).

Solar flares can be classified as A, B, C, M or X class according to the soft X-ray peak flux measured by *GOES*, and CME speed can also vary from less than 100 km s⁻¹ to several thousand km s⁻¹. An important question is: What determines the magnitude of these quantities? In this paper we address this question by examining how does the peak flare flux (*PPF*, Watt m⁻²) and CME speed (V_{CME} , km s⁻¹) correlate with six magnetic parameters using a subset of two-ribbon flares selected from Paper I. Three of the parameters are measures of the magnetic size: the average background magnetic field strength (B , Gauss), the area of the region where B is counted (S , cm²), and the magnetic flux of this region (Φ , Mx). The other three parameters are measures of the magnetic shear: the initial shear angle (θ_1 , °), the final shear angle (θ_2 , °), and the change of shear angle ($\theta_{12} = \theta_1 - \theta_2$, °) of the footpoints during the flare. We examine the correlations between the intensity of flare/CME events and each of these six parameters as well as three types of multi-parameter combinations. We also study the fraction of the contribution to the total variance of the observed $\log_{10}(\text{PPF})$ and V_{CME} from each parameter for these three types of combinations.

This Chapter is arranged as follows. The data sets and the measurement methods are described in § 4.2. Our results are presented in § 4.3, and summary and discussion are given in § 4.4. The detailed formulae for calculating the coronal magnetic field

strength and the multiple linear regress fit are listed in the Appendix.

4.2 Data Selection and Methods

In paper I, we have found that 43 out of the 50 selected two-ribbon flares show both strong-to-weak shear motion of the footpoints and ribbon separation. All of these 43 flares (which are listed in Table 1 in Paper I) have two long and parallel ribbons located on the two opposite magnetic polarities, as can be seen from a combination of the *TRACE* EUV/UV and *SOHO* MDI observations, and an example is shown in Figure 4-1. In this study, we first select a subset of 31 flares from the 43 flares, to examine the correlations between the $\log_{10}(PFF)$, V_{CME} , and the background field strength. All of these 31 flares are associated with CMEs and have good corresponding MDI observations. Among these 31 events, 26 events are close to the disk center (longitude $< 45^\circ$), while the other 5 events are close to the solar limb (longitude $> 45^\circ$). The associated CME for each flare is identified based on both temporal (*GOES* flare peak time ± 2 hours) and spatial windows. A detailed description of the criteria can be found in Paper I. From the 31-flare sample, we then select 18 flares with measured shear angles of the footpoints, to examine the correlations between six magnetic parameters and the intensity of these flare/CME events.

The peak flare flux is derived from the *GOES* soft X-ray classification which is listed in Table 1 in Paper I. In addition to the peak flare flux, we also considered the *GOES* integrated X-ray flare flux (IFF, J m^{-2}), which is taken from the National Geophysical Data Center¹. The CME speed is the linear speed taken from the *SOHO* LASCO CME catalog². Since most of our events originated near the solar disk center, they probably involve projection effect for the CME speed. In order to correct the

¹<http://www.ngdc.noaa.gov/stp/SOLAR/ftpsolarflares.html>

²http://cdaw.gsfc.nasa.gov/CME_list/

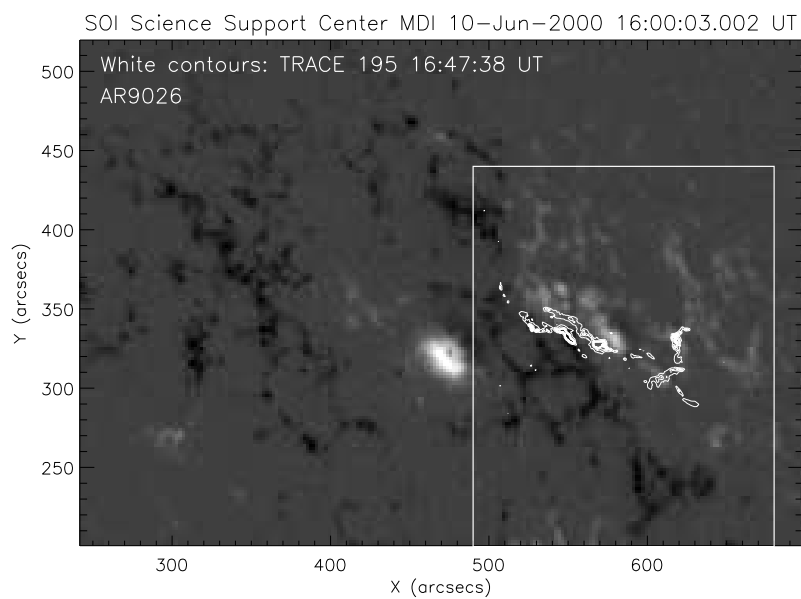


Figure 4-1 *SOHO* MDI image overlaid with *TRACE* contours (in white) at 195 Å on 2000 June 10. The white and black spots in MDI image show the positive and negative polarities, respectively. The area enclosed in the white box is the region where the three parameters representing the magnetic size are measured.

projection effect of the CME speed, we adopt a formula by Leblanc et al. (2001), which assumes radial propagation of CMEs. In this formula, the radial speed (V_{rad}) is given by

$$V_{\text{rad}} = V_{\text{sky}} \frac{1 + \sin\alpha}{\sin\phi + \sin\alpha}, \quad (4.1)$$

in which α is the half angular width of the CME and ϕ is the angle between the radial passing through the solar origin and the Earth direction given by $\cos\phi = \cos\lambda\cos\psi$, where λ and ψ are heliolatitude and heliolongitude, respectively. Unfortunately, it is very difficult to measure the angular width of halo CME, which is the dominating type of CMEs that we studied and also subject to projection effects. Therefore, we have taken the average angular width value (i.e., $\alpha = 36^\circ$) listed in St. Cyr et al. (2001) for all the 31 events, as suggested by Leblanc et al. (2001). Using the above formula and the coordinate information of all the events, we have estimated their radial speed as the corrected CME speed. The estimated correction factor ranges from 1.09 to 3.8. In this Chapter, we call the CME speed obtained directly from the catalog V_{CME} , and the radial speed after the correction of projection effect $V_{\text{C-CME}}$, respectively.

4.2.1 Measurement Uncertainties of the Shear Angles

Within our 31-flare sample, the shear angles ($\theta_1, \theta_2, \theta_{12}$) of 20 flares have been measured and listed in Table 1 in Paper I. The shear angle is defined as the angle between the normal to the magnetic inversion line and the line connecting the conjugate footpoints. The detailed measurement method of these shear angles is illustrated in Figure 1 in Paper I. There are three types of uncertainties in the measurement of the shear angles. First, there are some uncertainties in defining conjugate footpoints, especially for the initial footpoints, which are defined as the first two brightenings that

appeared at the flare onset. The difficulty arises because the corresponding post-flare loops do not always show up in TRACE data for the initial conjugate footpoints. To minimize this uncertainty, we select 18 flares from the 20 flares having measured shear angles, because we do not see the corresponding post-flare loops for the initial conjugate footpoints in the other two flares (i.e., flares on 2000 Nov 24 and 2003 May 31). Second, the inversion line is often difficult to define due to the separation of magnetic polarities and complex shape of the inversion line. Therefore, as described in Paper I, to measure both θ_1 and θ_2 we replaced the real complicated magnetic inversion line with a simplified straight line, which causes some uncertainty in these two angles. However, the change of shear angle θ_{12} is unaffected by such uncertainty. Third, the footpoints always extend over multiple pixels, therefore, for each footpoint we measure an average position with some uncertainty. The uncertainty of the footpoint positions results in an uncertainty of the shear angle, which is listed in Table 1 in Paper I. Despite these uncertainties, the shear angle is a useful proxy for the non-potential fields involved in these flares.

4.2.2 Measurement Methods of the Magnetic Size

The other three parameters (i.e., B , S , and Φ) are measured from the line of sight *SOHO* MDI magnetograms (at a cadence of 96 min) immediately before each flare. To measure these parameters, we first align the *TRACE* EUV/UV images with the corresponding *SOHO* MDI magnetograms. To do the alignment, we first determine the offset between the *TRACE* white light (WL) image and the corresponding MDI magnetogram. We then apply this offset to the *TRACE* EUV/UV images. Figure 4-1 shows a magnetogram of active region 9062 overlaid with the white contours, which refer to the two flare ribbons observed at 195 Å at 16:47:38 UT on 2000 June 10. By comparison of the MDI magnetogram with the corresponding *TRACE* EUV

image, we then select a subarea (the area enclosed in the white box in Figure 4-1) of the magnetogram that includes the magnetic elements immediately surrounding the flare ribbons, since these elements are expected to be the dominating magnetic fields that provide energy to the solar flares and CMEs. This selected subarea of the magnetogram is used to measure the three parameters representing the magnetic size.

MDI magnetograms systematically underestimate magnetic field strength and saturate at high magnetic field strength values (Berger & Lites 2003). Following Green et al. (2003) we first multiply the raw MDI data by 1.45 for values below 1200 G and by 1.9 for values above 1200 G to obtain the corrected flux density (B_{MDI}). Since most of our events are not located exactly at the solar disk center, the correction for the angle between the magnetic field direction and the observer's line of sight is needed. To do this correction, we assume a purely radial magnetic field and apply the following cosine corrections to each pixel following McAteer et al. (2005):

$$B_{\text{corrected}} = \frac{B_{\text{MDI}}}{\sin(\arccos(d/r))}, \quad (4.2)$$

where d is the distance from disk center, and r is the heliocentric radius of the solar disk, which is set to a typical value of 960 arcsec. After these corrections, we have applied two methods to measure the background magnetic field strength.

The first method (*method 1*) is calculating the average photospheric magnetic field strength. In each selected subarea of the magnetogram and for each magnetic polarity, we average the magnetic field strength of all pixels within a contour at 20% of the maximum magnetic field value. We select the 20% contour because it best defines the areas of the positive and negative polarities most closely associated with the flare for our data sample. For example, if there are sunspots involved, the 20% contour will enclose the sunspots. We refer to the average magnetic field strength for the positive and negative polarities as B_{pos} and B_{neg} . B is defined as the average of the absolute value of B_{pos} and B_{neg} , i.e., $(|B_{\text{pos}}| + |B_{\text{neg}}|)/2$. The area ($S = \sum S_i$) and magnetic

flux ($\Phi = \sum B_i S_i$) are the sum taken over all the pixels within this 20% contour, and B_i , S_i are the magnetic field strength and the area corresponding to each pixel, respectively. Similar to B_i , the projection effect of S_i is also corrected by applying the cosine corrections. One may argue that this method is highly arbitrary because it depends heavily on the maximum magnetic field strength value at a single pixel. But we should note that the measurements are also controlled by the distribution of values within the 20% maximum value contour. We also tried a fixed threshold of 200 G, which includes more disconnected and weaker background fields. This method produces worse correlations with the peak flare flux and CME speed than the 20% contour method. Therefore, we will use the 20% contour method in this paper.

The second method (*method 2*) for measuring the background field is estimating the coronal field strength at a point “P” above the magnetic inversion line (MIL). The pre-flare magnetic field in active regions is expected to be strongly sheared, so a potential-field model cannot accurately describe the direction of the coronal field. However, to estimate the field strength, a potential-field model may be adequate. The point “P” is located at a height h above the photosphere. For all of the events, we set h to 7250 km ($10''$), which is a typical value of the half distance between the two flare ribbons at the *GOES* flare peak time for most of the events we studied. The projection of “P” in the photosphere “P₀” is on the magnetic inversion line (MIL) involved in the flare/CME events. The formulae we used to estimate the magnetic field strength at “P” are shown in Appendix A. From these formulae we find that the field strength B_{cor} is heavily dependent on the photospheric field at the points close to the point “P₀”. In order to minimize the random errors, for each event we make 10 measurements of B_{cor} , by moving the point “P₀” along the magnetic inversion line between the two flare ribbons. B_{cor} used below is the average of these 10 values.

4.3 Results

4.3.1 Peak Flare Flux and CME Speed vs. Magnetic Field Strength

The left four panels in Figure 4-2, from the top to the bottom, show scatter plots of $\log_{10}(PFF)$, $\log_{10}(IFF)$, V_{CME} , and $V_{\text{C-CME}}$ versus B (method 1) for all of the 31 events, respectively, and the right four panels show how the relationships change when B is replaced with B_{cor} (method 2). The solid lines show the linear fits to the data points, and the LCC of each plot is also presented in each panel.

Figure 4-2 shows that both B and B_{cor} are positively correlated with the intensity of flare/CME events represented by $\log_{10}(PFF)$, $\log_{10}(IFF)$, V_{CME} , and $V_{\text{C-CME}}$. The distribution of the points in the lower four panels of Figure 4-2 are more scattered and the correlations are slightly worse in comparison to the corresponding upper four panels, which may be due to larger observational uncertainties in the CME speed measurements. We also see that B has slightly worse correlations with $\log_{10}(PFF)$ and $\log_{10}(IFF)$, but slightly better correlations with both V_{CME} and $V_{\text{C-CME}}$ than B_{cor} . But overall, there is no significant difference between these two parameters. Therefore, we choose B to represent the background magnetic field strength in the following detailed studies.

The upper four panels of Figure 4-2 show that the IFF has better correlations with both B and B_{cor} , in comparison to the PFF, but only slightly. Since there is not much difference between the scatter plots corresponding to IFF and PFF, and PFF is more widely used to represent the flare class, we choose PFF to represent the flare intensity in the following detailed study. In comparison to V_{CME} , the $V_{\text{C-CME}}$ shows slightly better correlations with B and B_{cor} (see lower four panels in Figure 4-2), which indicates that the correction of the CME speed has only slightly improved the correlations. Moreover, some overcorrection may exist in this correction method as suggested by Gopalswamy et al. (2001). Therefore, the original CME speed (V_{CME})

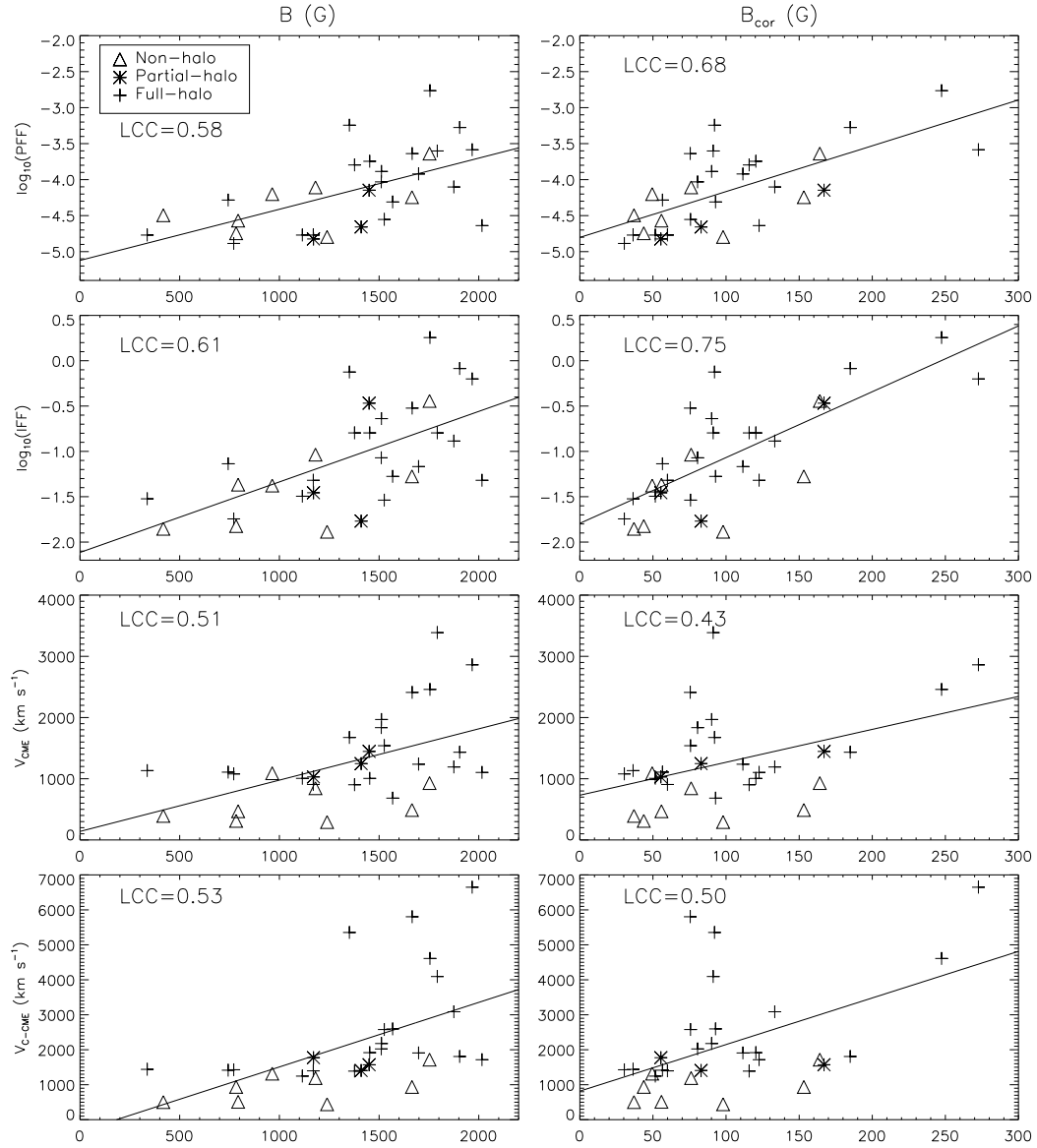


Figure 4-2 Scatter plots of the logarithm of the peak flare flux ($\log_{10}(PFF)$, *first row*), the integrated flare flux ($\log_{10}(IFF)$, *second row*), the CME speed (V_{CME} , *third row*), and the corrected CME speed (V_{C-CME} , *last row*) vs. the background magnetic field strength for all of the 31 events included in this paper. The magnetic field strengths in the left (B) and right (B_{cor}) columns are calculated using methods 1 and 2, respectively. The solid lines in each panel are the linear fits to the data points, and the linear correlation coefficient (LCC) of the data points is presented in each panel. The flares associated with non-halo, partial-halo, and full-halo CMEs are marked using different symbols, i.e., triangle, asterisk, and plus sign, respectively.

is used to represent the CME speed in the following detailed analysis.

CMEs are categorized as non-halo, partial-halo, and full-halo CMEs for those having angular width lower than 120° , between 120° and 320° , and greater than 320° , respectively (Lara et al. 2006). The lower four panels of Figure 4-2 show that most of the non-halo CMEs (*triangle*) have slower speed than the partial-halo (*asterisk*) and full-halo CMEs (*plus sign*), which is consistent with the result reported by Lara et al. (2006), who propose that the observed “halo” is the manifestation (compressed material) of the shock wave driven by fast CMEs. But we do not see obvious difference between the speeds of partial-halo and full-halo CMEs as reported by Lara et al. (2006), which may be due to our smaller data sample. We also see no obvious differences in the PFF and IFF between the flares associated with these three types of CMEs as shown in the upper four panels of Figure 4-2.

Figure 4-3a presents the scatter plot of the coronal field strength (B_{cor}) versus the CME speed (V_{CME}) for the 31 events included in this study. Different symbols represent the events with different ranges of CME mass, and those CMEs with unknown mass are marked with diamonds. The CME mass is taken from the *SOHO* LASCO CME catalog. One should note that there are generally large uncertainties in these numbers, because the estimation of the CME mass involves a number of assumptions (Vourlidas et al. 2000). Figure 4-3a shows that the CMEs with larger mass tend to have faster speed in our sample. If the magnetic forces driving the CME were roughly the same in all cases, we would expect that the CME speed is inversely related to CME mass, contrary to our finding in Figure 4-3a. This indicates that the scatter in this plot is not simply due to the different CME mass.

We calculate CME speed as a function of the background field strength at $10''$ height above the photosphere (B_{th}), using the extended Lin & Forbes model (2000) by Reeves & Forbes (2005). The result is shown in Figure 4-3b. The plots with

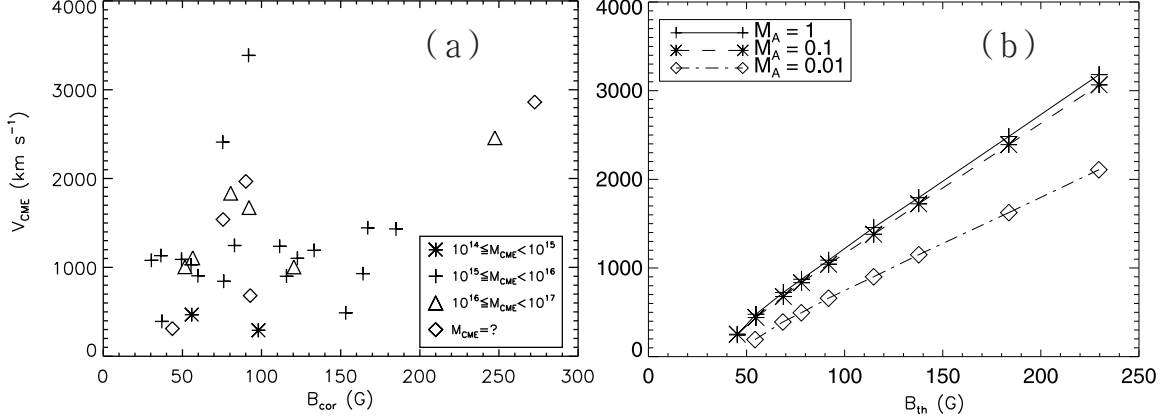


Figure 4-3 (a) Scatter plots of the CME speed vs. B_{cor} for all of the 31 events. B_{cor} is the magnetic field strength at a $10''$ height above the photosphere, which is calculated from the observations using method 2. The CMEs with different ranges of mass (in unit of g) are marked with different symbols, and those CMEs with unknown mass are marked as diamonds. (b) Theoretical correlation plots of CME speed and the background magnetic field strength at a $10''$ height above the photosphere calculated from a catastrophic loss of equilibrium model (Reeves & Forbes 2005). The different types of lines correspond to different values of Alfvén Mach number M_A .

different inflow Alfvén Mach number (M_A) are marked with different symbols. In the model, the CME accelerates in the early stages of the event and then asymptotically approaches a constant velocity. This constant velocity is reported in the plot, and refers to a height of about three solar radii, which is similar to that of the LASCO observations. The model predicts that the CME speed increases with the background field strength, and for events with the same background field strength, the CME speed also increases with the Mach number (i.e., reconnection rate), but saturates for $M_A \geq 0.1$. This saturation occurs because the force on the flux rope due to the current sheet becomes small when $M_A \geq 0.1$ is large (see Reeves 2006). Consistent with the theoretical model, our observations show that the events with stronger background fields tend to have faster CME speeds. A comparison of Figures 4-3a and 4-3b suggests that much of the scatter in the plot of Figure 4-3a may be caused by different reconnection rates. However, there may be other contributions to the scatter in Figure 4-3a, such as the measurement uncertainties for the CME speed.

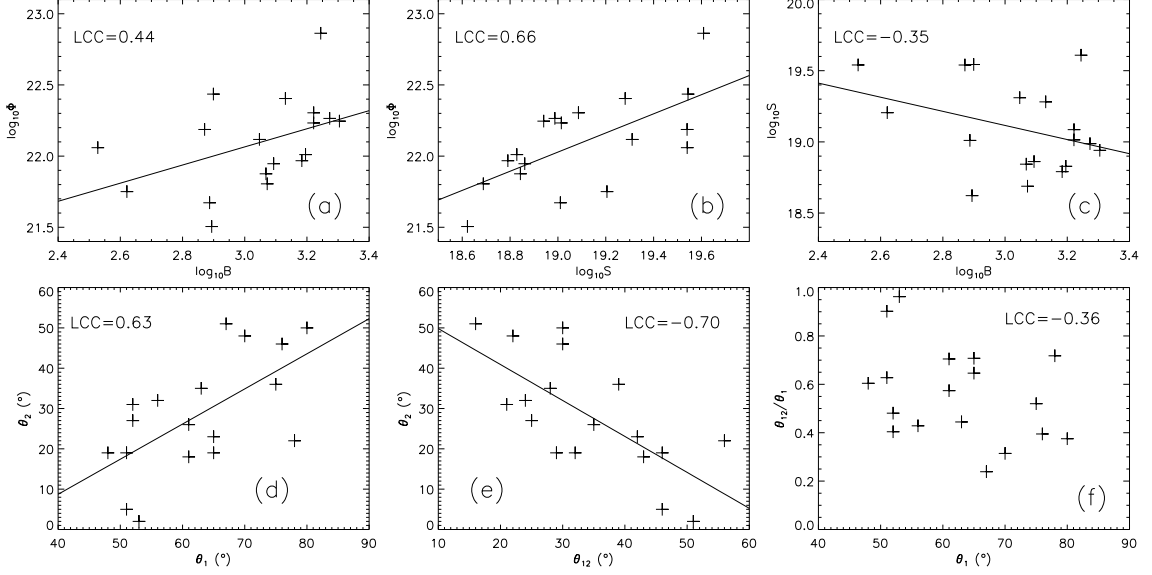


Figure 4-4 Scatter plots of six pairs of magnetic parameters measured from the 18 events with measured shear angles. (a) $\log_{10}B$ vs. $\log_{10}\Phi$, (b) $\log_{10}S$ vs. $\log_{10}\Phi$, (c) $\log_{10}B$ vs. $\log_{10}S$, (d) θ_1 vs. θ_2 , (e) θ_{12} vs. θ_2 , and (f) θ_1 vs. θ_{12}/θ_1 . The solid lines in the figure refer to the linear fits to the data points.

4.3.2 Peak Flare Flux and CME Speed vs. Six Magnetic Parameters

In the last section, we examined the relationship between the intensity of the 31 flare/CME events and the background field strength. In this section, we carry out a further detailed study for a subset of 18 events with measured shear angles of the footpoints. The magnetic parameters in these 18 events we considered can be classified into two categories: parameters representing the magnetic size ($\log_{10}B$, $\log_{10}S$, and $\log_{10}\Phi$), and parameters representing the magnetic shear (θ_1 , θ_2 , and θ_{12}).

At first, we examine the correlations between each parameter. To do this study, we first check the correlations between the parameters in the same category. The correlation plots between each pair of parameters representing magnetic size are shown in Figures 4-4a–4-4c. We find that both $\log_{10}B$ and $\log_{10}S$ are positively correlated with $\log_{10}\Phi$. This is not surprising, because Φ is the product of B and S . We also find a weak anti-correlation between $\log_{10}B$ and $\log_{10}S$. For the other category with

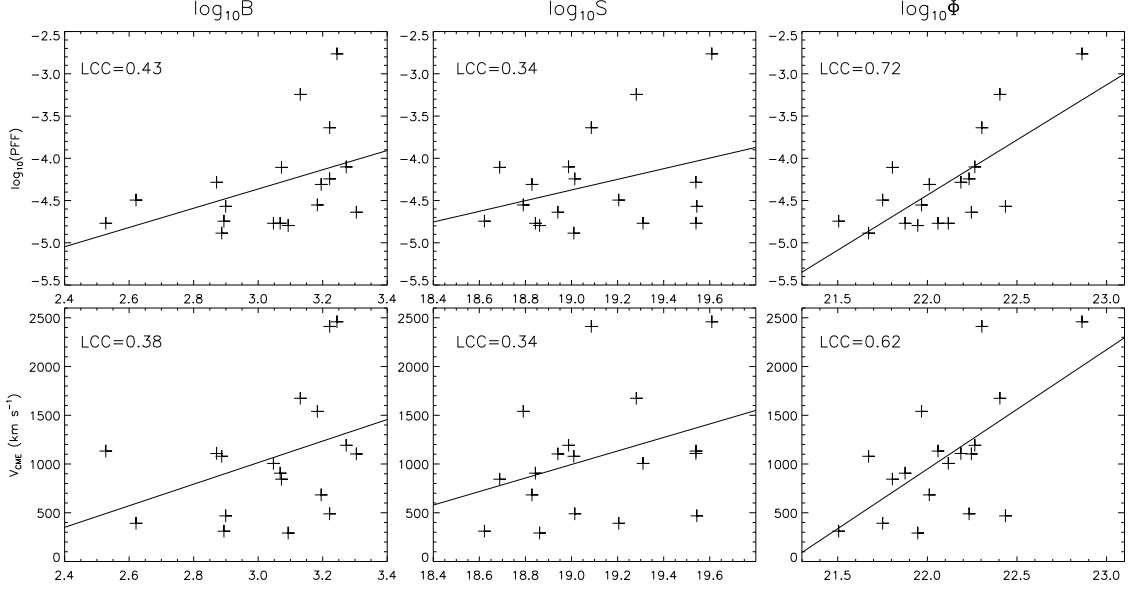


Figure 4-5 Scatter plots of $\log_{10}(PFF)$ (*top panels*) and V_{CME} (*bottom panels*) vs. three magnetic parameters for the 18 events with measured shear angles out of our 31-event sample. The parameters, from the left to the right panels, are the logarithms of the average magnetic field strength ($\log_{10}B$), the area ($\log_{10}S$) and the magnetic flux ($\log_{10}\Phi$) of the region where B is counted, respectively. The solid lines in each figure refer to the linear fits to the data points.

parameters representing magnetic shear, we find that θ_2 is highly correlated with both θ_1 and θ_{12} , as shown in Figures 4-4d–4-4e. But we find no correlation between θ_1 and θ_{12} . This result indicates that θ_2 is not an independent parameter. We then check the correlations between the parameters in different categories. We find a weak correlation between $\log_{10}B$ and θ_{12} (LCC=0.48), while all of the other parameters in different categories are not correlated with each other (LCC \leq 0.3). Figure 4-4f shows the correlation plot of θ_1 vs. θ_{12}/θ_1 , so it is not surprising to see a weak correlation in this plot. Figure 4-4f also shows that for the same initial shear angle, the change of shear angle can vary in a very large range in different events ($0.24 \leq \theta_{12}/\theta_1 \leq 0.96$).

For these 18 events, the correlation plots of the three parameters representing magnetic size versus $\log_{10}(PFF)$ and V_{CME} are shown in the top and bottom panels of Figure 4-5, respectively. These parameters are $\log_{10}B$ (*left panels*), $\log_{10}S$ (*mid-*

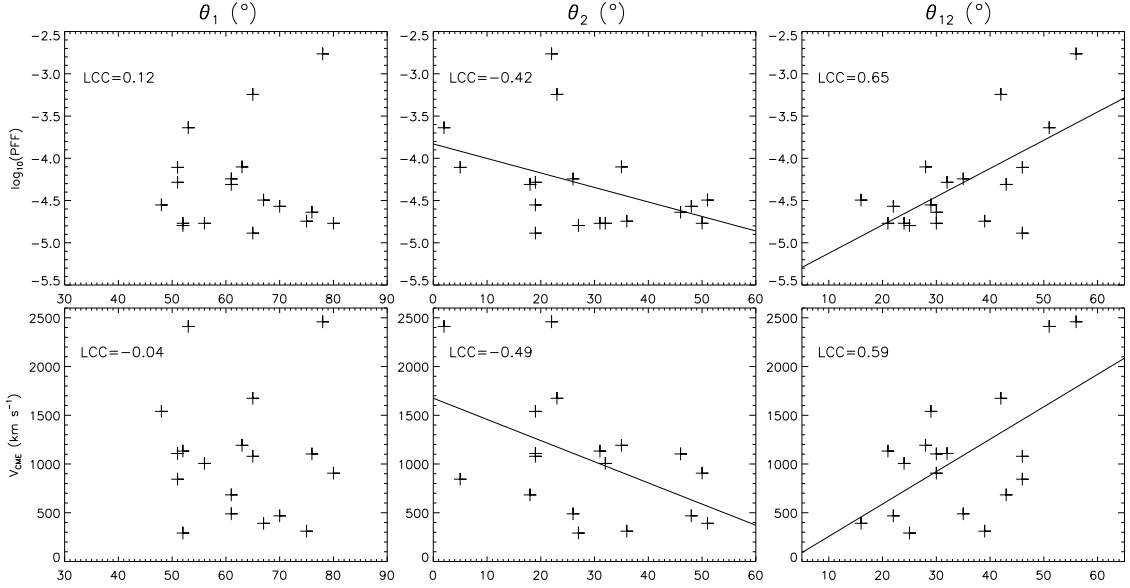


Figure 4-6 Similar to Figure 4-5, but scatter plots of $\log_{10}(PFF)$ (*top panels*) and V_{CME} (*bottom panels*) vs. the other three parameters for the 18 events with measured shear angle. These parameters are the initial shear angle (θ_1 , *left panels*), the final shear angle (θ_2 , *middle panels*), and the change of shear angle (θ_{12} , *right panels*) of the footpoints, respectively.

dle panels), and $\log_{10}\Phi$ (*right panels*). Each of these three parameters is positively correlated with both $\log_{10}(PFF)$ and V_{CME} . Of these parameters, $\log_{10}S$ shows relatively weak correlation with the intensity of flare/CME events, and the corresponding LCCs are 0.34. The correlation between $\log_{10}B$ and the intensity of flare/CME events appears to be slightly better but still weak (LCCs=0.43, 0.38). Among these three parameters, $\log_{10}\Phi$ is the parameter which shows the best correlations with both $\log_{10}(PFF)$ (LCC=0.72) and V_{CME} (LCC=0.62).

Similar to Figure 4-5, the top and bottom panels in Figure 4-6 show the correlation plots of the three parameters representing magnetic shear versus $\log_{10}(PFF)$ and V_{CME} . These parameters are θ_1 (*left panels*), θ_2 (*middle panels*), and θ_{12} (*right panels*). θ_1 is neither correlated with $\log_{10}(PFF)$ nor with V_{CME} , while θ_2 is negatively correlated with the intensity of flare/CME events (LCCs=-0.42, -0.49). θ_{12} shows good positive correlations with both $\log_{10}(PFF)$ (LCC=0.65) and V_{CME} (LCC=0.59).

To summarize, five of these six parameters except the initial shear angle (θ_1) show either positive or negative correlations with both $\log_{10}(PFF)$ and V_{CME} . Among these five parameters, the total magnetic flux of the region where the magnetic field is counted ($\log_{10}\Phi$) and the change of shear angle (θ_{12}) of the footpoints during the flare are the two parameters which show the strongest correlations with the intensity of flare/CME events.

4.3.3 Peak Flare Flux and CME Speed vs. Multi-parameter Combinations

In the previous section, we have found that $\log_{10}\Phi$ and θ_{12} are the two parameters which show the best correlations with the intensity of the 18 flare/CME events. One of the alternative interpretations is that Φ is a combination of B and S , while θ_{12} is a combination of θ_1 and θ_2 . In the other words, only four (i.e., $\log_{10}B$, $\log_{10}S$, θ_1 , and θ_2) of our six parameters are single parameter measured from observations. This result indicates that a combination of two parameters shows much better correlation with the intensity of the flare/CME events than the individual parameter. Therefore, we consider three multi-parameter combinations in this section. In order to study the correlations between each of these three combinations and the intensity of the flare/CME events, we have done multiple linear regression fits to the observed $\log_{10}(PFF)$ and V_{CME} for each combination, using the “regress” function in IDL. Appendix B shows the expression for the fitting function (Y_{fit}), which is a linear combination of all the parameters in each combination.

At first, we create a combination of four parameters (combination 1), i.e., $\log_{10}B$, $\log_{10}S$, θ_1 , and θ_{12} . The first three parameters in this combination are three single parameters measured from the observations. We choose θ_{12} instead of the other single parameter θ_2 in this combination, because θ_2 appears not to be an independent parameter as shown in the last section. The detailed information of the fitting functions

Table 4.1. Constants, coefficients as well as their $1\text{-}\sigma$ uncertainties of the multiple linear regression fits for three types of multi-parameter combinations.

Para. ^a	Coefficients		Para.	Coefficients		Para.	Coefficients	
	$\log_{10}(PFF)$	V_{CME}		$\log_{10}(PFF)$	V_{CME}		$\log_{10}(PFF)$	V_{CME}
$\log_{10}B$	0.93 ± 0.49	$(0.97\pm 0.60)e3$	$\log_{10}\Phi$	1.10 ± 0.24	$(1.04\pm 0.34)e3$	$\log_{10}\Phi$	1.10 ± 0.23	$(1.01\pm 0.34)e3$
$\log_{10}S$	1.00 ± 0.30	$(1.08\pm 0.37)e3$	θ_1	$(-0.13\pm 0.74)e(-2)$	$(-0.10\pm 0.10)e2$	θ_1	$(-0.13\pm 0.74)e(-2)$	$(-0.10\pm 0.10)e2$
θ_{12}	$(2.86\pm 0.90)e(-2)$	$(0.29\pm 0.11)e2$	θ_{12}	$(2.63\pm 0.69)e(-2)$	$(0.27\pm 0.10)e2$	θ_{12}	$(2.62\pm 0.67)e(-2)$	$(0.27\pm 0.10)e2$
Constant	$-2.73e1$	$-2.30e4$		$-2.93e1$	$-2.23e4$		$-2.93e1$	$-2.21e4$

^aPara. is the abbreviation of Parameters in this table.

for combination 1 is listed in the left three columns of Table 4.1. The first column lists all the parameters in combination 1, and the constant and coefficients (as well as $1\text{-}\sigma$ uncertainty) of each parameter in the fitting functions corresponding to $\log_{10}(PFF)$ and V_{CME} are shown in the second and the third columns, respectively.

From the left three columns of Table 4.1 we can see that the coefficients of $\log_{10}B$ and $\log_{10}S$ are equal within the errors of the linear regression fit, and we also note that these two parameters may not be independent from each other (see Figure 4-4c). Therefore, we replace $\log_{10}B$ and $\log_{10}S$ in combination 1 with a combination of them ($\log_{10}\Phi$) to create combination 2 (i.e., $\log_{10}\Phi$, θ_1 , and θ_{12}). The detailed information of the fitting functions for combination 2 is listed in the middle three columns of Table 4.1, from which we see that the coefficient of $\log_{10}\Phi$ has smaller $1\text{-}\sigma$ uncertainty than the coefficients of both $\log_{10}B$ and $\log_{10}S$. The left panels in Figure 4-7, from the top to the bottom, show the scatter plots of Y_{obs} (the observed $\log_{10}(PFF)$ and V_{CME}) vs. Y_{fit} (the fitted $\log_{10}(PFF)$ and V_{CME}) for combination 1; the plot for $\log_{10}(PFF)$ is shown in the upper left panel, and the plot for V_{CME} is shown in the lower left panel. Similar to the left panels, the middle panels in Figure 4-7 show the scatter plots for combinations 2. A comparison of the left and middle panels of Figure 4-7 shows that combination 2 has better correlation between the observed and fitted

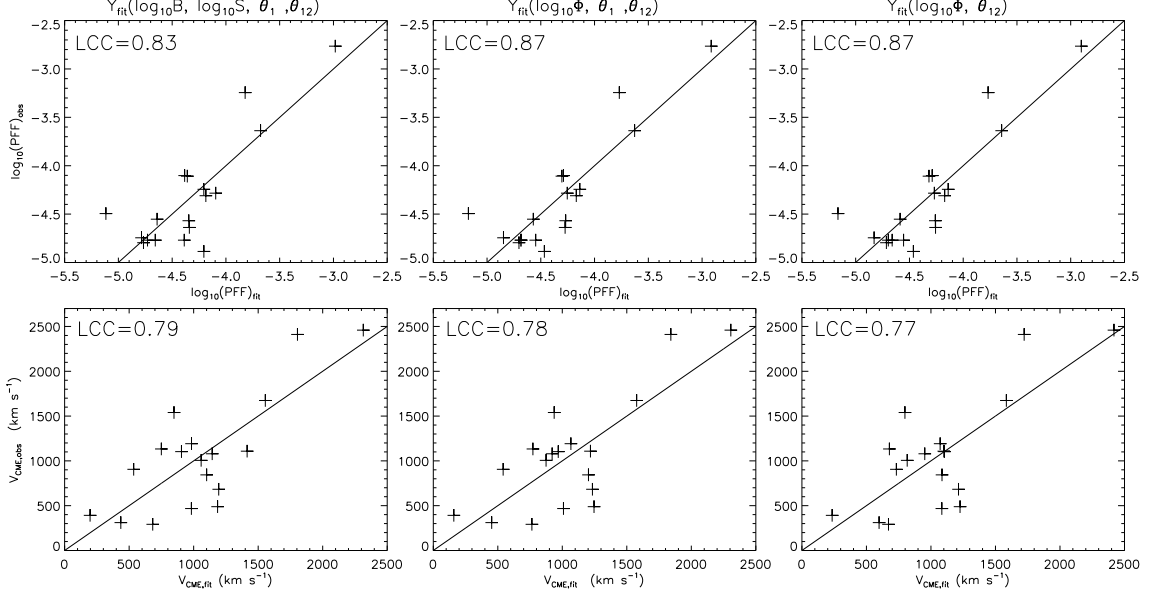


Figure 4-7 Scatter plots of the observed $\log_{10}(PFF)$ (*top panels*) and V_{CME} (*bottom panels*) vs. the fitted $\log_{10}(PFF)$ and V_{CME} (Y_{fit}) corresponding to three types of multi-parameter combinations for the 18 events with measured shear angles. *Left*: combination 1 ($\log_{10}B$, $\log_{10}S$, θ_1 , θ_{12}); *middle*: combination 2 ($\log_{10}\Phi$, θ_1 , and θ_{12}); *right*: combination 3 ($\log_{10}\Phi$ and θ_{12}). The solid lines in each figure refer to the linear fits to the data points.

$\log_{10}(PFF)$ (LCC=0.87) than combination 1 (LCC=0.83). Although combination 2 has slightly worse correlation for V_{CME} (LCC=0.79) than combination 1 (LCC=0.78), overall, combination 2 appears to be better than combination 1.

The left and middle three columns of Table 4.1 shows that the coefficient of θ_1 are very small, and the $1-\sigma$ uncertainty in this coefficient is greater than its value. This indicates that this parameter does not play an important role in the fitting functions corresponding to both combinations 1 and 2. Therefore, we create combination 3 (i.e., $\log_{10}\Phi$, θ_{12}) by removing the parameter θ_1 from combination 2. The detailed information of the fitting functions for combination 3 is listed in the right three columns of Table 4.1. The right panels of Figure 4-7 show the scatter plots for combination 3, and the LCCs in these plots are only slightly worse than those in the corresponding middle panels. This further confirms that θ_1 plays only a minor role

Table 4.2. The contributions from each parameter in three types of multi-parameter combinations (σ_i^2) and other unknown sources (σ_o^2) to the total variances of the observed $\log_{10}(PFF)$ ($\sigma_{tot}^2 = 0.29$, PFF in unit of Watt m⁻²) and V_{CME} ($\sigma_{tot}^2 = 3.45 \times 10^5$ km² s⁻²).

Parameters	$\frac{\sigma_{i/o}^2}{\sigma_{tot}^2} * 100\%$		Parameters	$\frac{\sigma_{i/o}^2}{\sigma_{tot}^2} * 100\%$		Parameters	$\frac{\sigma_{i/o}^2}{\sigma_{tot}^2} * 100\%$	
	$\log_{10}(PFF)$	V_{CME}		$\log_{10}(PFF)$	V_{CME}		$\log_{10}(PFF)$	V_{CME}
$\log_{10}B$	12.5 %	11.2 %	$\log_{10}\Phi$	36.7 %	27.6 %	$\log_{10}\Phi$	36.4 %	25.7 %
$\log_{10}S$	29.3 %	28.3 %	θ_1	0.1 %	2.7 %	θ_{12}	25.8 %	21.9 %
θ_1	0.0 %	2.1 %	θ_{12}	26.0 %	23.4 %	Others	23.6 %	41.3 %
θ_{12}	30.7 %	26.8 %	Others	23.5 %	38.6 %			
Others	30.3 %	38.1 %						

in combination 2. This result is also consistent with the fact that the coefficients and 1- σ uncertainties for $\log_{10}\Phi$ and θ_{12} in combinations 2 and 3 are very similar to each other (see Table 4.1).

The top panels of Figure 4-7 show strong and linear correlation between the observed and fitted values of $\log_{10}(PFF)$ for each parameter combination, with LCCs equal or larger than 0.83. This implies that the observed magnetic parameters that we measured play an important role in determining the peak flare flux. The bottom three panels also show strong linear correlations between V_{CME} and the parameter combinations, but worse ($0.77 \leq LCC \leq 0.79$), and the distributions of the plots are more scattered than the corresponding top panels. Consistent with the earlier result found in Figure 4-2, this result may be caused by the larger measurement uncertainties in the CME speed as compared to the peak flare flux.

In this subsection, we have mainly addressed the question of how well the fitting function reproduces the observed intensity of flare/CME events. Now we study the contributions of the various magnetic parameters to the total variances of both $\log_{10}(PFF)$ and V_{CME} . Table 4.2 shows the fraction (σ_i^2) of each parameter's contribution to the total variances (σ_{tot}^2) of $\log_{10}(PFF)$ and V_{CME} for the three combinations.

The calculation methods of σ_i^2 and σ_{tot}^2 are presented in Appendix B. For combination 1, the largest fractional contribution to the total variances comes from $\log_{10}S$, and the second largest contribution comes from θ_{12} . The contribution from $\log_{10}B$ is slightly less than θ_{12} , while θ_1 shows significantly less contribution than the other three parameters. For both combinations 2 and 3, $\log_{10}\Phi$ is the top-ranked parameter which shows the strongest contribution to the total variance of the intensity of flare/CME events, while θ_{12} is the second-ranked parameter. Similar to combination 1, θ_1 in combination 2 again has a very small contribution to the total variances of $\log_{10}(PFF)$ and V_{CME} . The fraction ($\sigma_o^2/\sigma_{tot}^2$) of the total variances due to unknown sources and/or measurement errors is also calculated and listed in Table 4.2 (see Appendix B for a detailed description of the method). The sum of all the fractions in each column is not 100% because of some approximations that have been made in calculating these fractions (Appendix B). For a large enough data sample, and when there is no correlation at all between magnetic parameters, this sum should be 100%. We find that the observed magnetic parameters account for a large fraction of the observed total variance; less than one third of the variance of $\log_{10}(PFF)$ is due to unknown sources or measurement errors. The total variances of $\log_{10}(PFF)$ and V_{CME} are 0.29 (PFF in unit of Watt m⁻²) and 3.45×10^5 km² s⁻², respectively.

4.4 Summary and Discussion

For a sample of 31 two-ribbon flares associated with CMEs, we have measured the magnetic field strength (from *SOHO* MDI magnetograms) of the magnetic polarities involved in the flares using two methods: the average photospheric magnetic field strength (B) within a contour of 20% of the maximum field strength, and the magnetic field strength at a single point located at 10'' height above the photosphere (B_{cor}). We have found that both measures show that for events with larger magnetic field

strength, the corresponding peak flare flux tends to be larger and the corresponding CME speed tends to be faster. This result is consistent with previous theoretical studies by Lin (2002, 2004) and Reeves & Forbes (2005) who found that the cases with higher background fields correspond to fast CMEs and strong flares, whereas lower fields correspond to slow CMEs and weak flares. This result is found through some calculations under the framework of a catastrophic loss of equilibrium model. Similar results have also been found by Chen et al. (2006) for a sample of CMEs associated solely with filament eruptions.

We have selected 18 events with measured shear angles out of the 31-event sample for further detailed study. For these 18 events, we have measured six parameters using both *SOHO* MDI magnetograms and corresponding *TRACE* observations of the flare footpoints. Three of these six parameters are measures of the magnetic size, and they are the average photospheric magnetic field strength (B), the area of the region where B is counted (S), and the magnetic flux of this region (Φ). The other three parameters represent the magnetic shear as determined from flare observations. These are the initial shear angle (θ_1 , measured at the flare onset), the final shear angle (θ_2 , measured at the time when the shear change stops), and the change of shear angle ($\theta_{12} = \theta_1 - \theta_2$) of the footpoints, respectively. With our six measures, we address the question what determines the intensity of the flare/CME events by examining three sets of correlations: (1) the correlations of the parameters with each other; (2) the correlations of the logarithm of the peak flare flux ($\log_{10}(PFF)$) as well as CME speed (V_{CME}) vs. each of the six parameters; (3) the correlations of the observed $\log_{10}(PFF)$ and V_{CME} vs. three types of multi-parameter combinations, which are: $\log_{10}B$, $\log_{10}S$, θ_1 , and θ_{12} (*combination 1*); $\log_{10}\Phi$, θ_1 , and θ_{12} (*combination 2*); and $\log_{10}\Phi$ and θ_{12} (*combination 3*).

The logarithms of all three parameters representing magnetic size show positive

correlations with both $\log_{10}(PFF)$ and V_{CME} . More specifically, $\log_{10}\Phi$ shows much better correlations (LCCs = 0.72, 0.62) with both $\log_{10}(PFF)$ and V_{CME} than the other two parameters (LCCs ≤ 0.43), i.e., $\log_{10}B$ and $\log_{10}S$, probably because the magnetic flux Φ is the product of the other two parameters. This result differs from the result reported by Chen et al. (2006) who found that the average field strength is better correlated with CME speed than the magnetic flux in the filament channel for the CMEs associated with filament eruptions.

We have, for the first time, found that there are no correlations between θ_1 and $\log_{10}(PFF)$ as well as V_{CME} , while θ_{12} shows a strong positive correlation with the intensity of flare/CME events. The initial shear angle (θ_1) of the footpoints measured at the flare onset may represent the pre-flare magnetic free energy to some extent, according to our cartoon in Figure 11 in Su et al. (2006), while the change of shear angle (i.e., $\theta_{12} = \theta_1 - \theta_2$) may serve as a proxy of the released magnetic free energy during the flare, but one should keep in mind that the shear angle is not the only parameter that determines the magnetic free energy. Therefore, our result indicate that the intensity of flare/CME events may depend on the *released* magnetic free energy rather than the *total* magnetic free energy stored prior to the flare. This may make it very difficult to predict the magnitude of the flare/CME events. Emslie et al. (2004) suggested that not all of the “free” energy may be available on short timescales to power flares and CMEs, owing to the constraints imposed by helicity conservation. An alternative interpretation of the lack of correlation with θ_1 is that this result is due to the large uncertainties in our measurements of the shear angles, which are fully discussed in Section 4.2.1. More specifically, the uncertainty in the definition of magnetic inversion line may cause large uncertainties in measuring both θ_1 and θ_2 , while the change of shear angle is unaffected by such uncertainty. The fact that for the same initial shear angle (θ_1), the change of shear angle (θ_{12}) can vary greatly

in different events (Figure 4-4f) may indicate that the released free magnetic energy could be different in the active regions with the same stored total free energy prior to the eruptions.

For each of the three types of multi-parameter combinations, we have done multiple linear regression fits to the observed $\log_{10}(PFF)$ and V_{CME} . For each combination, the corresponding fitting functions are a linear combination of all the parameters in this combination. We have also calculated the fraction of each parameter's contribution to the total variances of $\log_{10}(PFF)$ and V_{CME} . For all of the three combinations, we see strong linear correlations between the observed and fitted values of $\log_{10}(PFF)$ and V_{CME} . This implies that the observed magnetic parameters play an important role in determining the intensity of the flare/CME events. Furthermore, all three combinations show better correlation with the intensity of flare/CME events than any individual magnetic parameter. Among these three combinations, combination 2 ($\log_{10}\Phi$, θ_1 , and θ_{12}) shows the strongest linear correlation between the observed and fitted values of both $\log_{10}(PFF)$ and V_{CME} . This result indicates that it is very useful to combine B and S into a single magnetic parameter, the flux Φ . Combination 3 ($\log_{10}\Phi$ and θ_{12}) shows only slightly worse correlation with the intensity of flare/CME events than combination 2. Moreover, in combination 2, the fractions of the contribution to the total variances of $\log_{10}(PFF)$ and V_{CME} from both $\log_{10}\Phi$ (36.7% and 27.6%) and θ_{12} (26.0% and 23.4%) are significantly greater than θ_1 (0.1% and 2.7%). These results imply that the initial shear angle θ_1 only plays a minor role in determining the peak flare flux and CME speed, which is consistent with the result reported in the last paragraph. These results also suggest that the magnetic flux of the region where the magnetic field is counted (Φ) and the change of shear angle of the footpoints during the flare (θ_{12}) are two separate but comparably important parameters in determining the intensity of flare/CME events. In other words, large

released free energy (a combination of Φ and θ_{12}) tends to produce large flares and fast CMEs.

Although the fitting functions corresponding to the three multi-parameter combinations show very strong and linear correlations with the intensity of flare/CME events, we still can see some scatter in these plots (Figure 4-7). Some of this scatter may result from different reconnection rates, different durations of reconnection and CME acceleration, different configurations of the ambient magnetic field, and measurement uncertainties. First of all, as shown in Figure 4-3b different reconnection rates may cause the scatter of CME speed, if the background field strength is fixed. Accordingly, different reconnection rates may also cause the scatter of the peak flare flux, if the other parameters are fixed. This is because the fraction of the released energy that is converted into flare or CME energy depends on the reconnection rate as reported by Reeves & Forbes (2005), who also found that greater than 50% of the released energy becomes flare energy when $M_A < 0.006$. Secondly, although many events with larger CME speed and greater peak flare flux tend to originate from strong magnetic field regions, the weak magnetic fields could also produce large CME speed if the durations of reconnection and acceleration are very long as illustrated in Qiu & Yurchyshyn (2005). Thirdly, Liu (2007) found that CMEs under heliospheric current sheet are significantly slower than CMEs under unidirectional open field structures. This implies that the ambient magnetic field structure plays a role in determining the speed of halo CMEs. Therefore, different ambient magnetic structure may make some contributions to the scatter of the plots in the bottom panels of Figure 4-7. Finally, many uncertainties existed in our measurements of the six parameters and the measurements of CME speed. This may also add some contributions to the scatter of the plots in Figure 4-7.

In summary, the magnetic flux (Φ) and the change of shear angle (θ_{12}) of the

footpoints during the flare show the most significant correlations with the intensity of flare/CME events ($\log_{10}(PFF)$, V_{CME}). The fact that both $\log_{10}(PFF)$ and V_{CME} are highly correlated with the change of shear angle (θ_{12}) rather than with the initial shear angle (θ_1) indicates that the intensity of flare/CME events may depend on the *released* magnetic free energy rather than the *total* free energy stored prior to the flare. We also found that a linear combination of a subset of our six parameters shows a much better correlation with the intensity of flare/CME events than each parameter itself, and the combination of $\log_{10}\Phi$, θ_1 , and θ_{12} is the top-ranked combination. Moreover, in this combination, the fractions of the contribution to the total variances of $\log_{10}(PFF)$ and V_{CME} from both $\log_{10}\Phi$ and θ_{12} are significantly greater than θ_1 .

Chapter 5

Evolution of the Sheared Magnetic Fields of Two X-class Flares Observed by *Hinode*/XRT

5.1 Introduction

Solar flares, prominence eruptions, and coronal mass ejections (CMEs) are magnetic phenomena thought to be powered by the magnetic free energy (i.e., the difference between the total magnetic energy and the potential field magnetic energy) stored in the corona prior to the eruption. Storage of free energy requires a nonpotential magnetic field, and it is therefore associated with a shear or twist in the coronal field away from the potential, current-free state (Priest & Forbes 2002). One indication of such a stressed magnetic field is the presence of a prominence. Another important indicator of a stressed magnetic field is the presence of sigmoid signatures discovered by Rust & Kumar (1997) and Canfield et al. (1999) with *Yohkoh*/SXT. Indeed, they have found that sigmoidal active regions to be the most likely to erupt.

A strong-to-weak shear motion of the hard X-ray footpoints during the flare was firstly reported by Masuda et al. (2001). This motion was claimed as a common feature in two-ribbon flares by Su et al. (2007a), who identified this motion in 86% of 50 two-ribbon flares observed by TRACE. A further detailed study by Su et al.

(2007b) shows that the change of shear angle of the footpoints during the flare is positively correlated with the intensity of solar flare/CME events for an 18-event sample. Studies of both shear motion and contracting motion of the footpoints in several individual flares were carried out by Ji et al. (2006, 2007). A detailed interpretation of this shear motion is given by Su et al. (2006), based on a three-dimensional model for eruptive flares (Moore et al. 2001, and references therein). According to this model, the pre-flare configuration contains a highly sheared core field inside and a less sheared envelope field outside in the pre-flare magnetic configuration. Does this configuration really exist? If so, how do the sheared fields build up? How do the sheared fields evolve during the flares? The continuous observations of NOAA Active Region 10930 by *Hinode* (Kosugi et al. 2007) provide an opportunity for us to address these questions. AR 10930 is a complex active region, which produced four X-class flares in 2006 December, and two of them were observed by both the X-ray Telescope (XRT) and the Solar Optical Telescope (SOT) aboard *Hinode*. In this chapter, we study the evolution of the highly sheared coronal fields prior to, during, and after the flares, in order to get some insights into the physics of coronal storage and release of magnetic energy.

5.2 Instrumentation and Data

The *Hinode* satellite (previously called Solar-B) is equipped with three advanced solar telescopes, i.e., XRT, SOT, and the EUV Imaging Spectrometer (EIS). It was launched on 22 September 2006 UT. The XRT is a high-resolution grazing-incidence telescope, which provides unprecedented high resolution and high cadence observations of the X-ray corona through a wide range of filters. XRT can “see” emission for a range of temperatures $6.1 < \log T < 7.5$, with a temperature resolution of $\Delta(\log T) = 0.2$. Temperature discrimination is achieved with a set of diagnostic fil-

ters (nine X-ray filters in total) in the focal plane. The XRT also contains visible light optics. The focal plane detector of XRT is a $2k \times 2k$ back-illuminated CCD with $1.0''$ per pixel, giving a $2000''$ field of view (FOV) which can see the entire solar disk. Details of the XRT instrumentation and performance can be found in DeLuca et al. (2005) and Golub et al. (2007).

The G band and Ca II H data used in this study are from the Broadband Filter Imager (BFI) of SOT (Tsuneta et al. 2007). The BFI produces photometric images with broad spectral resolution in 6 bands (CN band, Ca II H line, G band, and 3 Continuum bands) at the highest spatial resolution available from the SOT ($0.0541''/\text{pixel}$) and at rapid cadence (<10 s typical) over a $218'' \times 109''$ FOV. The scientific capabilities of SOT are described in detail by Shimizu (2004). The EUV (195 \AA) images used in this study are taken by TRACE, which is a high-resolution imaging telescope (Handy et al. 1999). The photospheric magnetograms are taken by SOHO/MDI. The X-ray time profiles of the two X-class flares are obtained by GOES.

Two X-class flares occurred in AR 10930 on 2006 December 13 and 14, and were observed simultaneously by the XRT and SOT onboard *Hinode*. These two flares are the first X-class flares observed by XRT of the *Hinode* mission since its launch. XRT started to observe this active region at 08:52 UT on 2006 December 9, and tracked this region continuously for the remainder of its disk passage. The XRT observations of this region were obtained with the Be-thin filter from Dec 9 to Dec 14, and the temperature response curve of this filter can be found in Golub et al. (2007). Most of the XRT images were taken with a $512'' \times 512''$ FOV and a cadence of 60 s or less. Some full FOV X-ray images were also taken occasionally as context or synoptic images. Similar to XRT, SOT was also observing this active region at the same time. The SOT G band and Ca II H images were taken with a $218'' \times 109''$ FOV and a cadence of 120 s. TRACE was observing this region at 1600 \AA and white light (WL)

most of the time, and some EUV (195 Å) images were also taken from time to time.

All of the XRT data used in this study were calibrated using the standard Solar Soft IDL routines. We then normalized the calibrated XRT data to its maximum value (Dmax). The logarithm of the normalized XRT data is plotted in Figures 5-1–5-5 (except Figure 5-2), and the maximum and minimum values of the data are 0 and -1.8 for most of the XRT images, except for Figures 5-3b–5-3d which have a minimum value of -1.2. All of the XRT images in this chapter are presented in a reversed color scale, but the TRACE and SOT images are in a normal color scale. To increase the signal to noise ratio of some of the XRT images, we first summed a series of XRT data within 10 minutes, then divided by the number of images. This method was adopted for Figures 5-3b, 5-4c, and 5-5c, and the time presented in the corresponding figures refers to the time of the first XRT image. This technique was used only for images that are very similar to each other.

The TRACE, XRT, and SOT images are co-aligned with the MDI images by application of the following procedure. For the Dec 13 flare, we first determined the offset of the TRACE coordinates by aligning the TRACE WL images with the corresponding WL images taken by MDI using the location of the sunspots. We then applied this offset to the TRACE EUV images used in this study. We applied the same method to determine the offset between the SOT and MDI images. The offset between the XRT and SOT images with corrected coordinates are determined by aligning the brightenings (i.e., flare footpoints) in the SOT Ca II H line images and the corresponding XRT images. We then applied the same procedure to do the alignment of the images for the Dec 14 flare. We applied the same offset of the XRT images obtained from the Dec 13 flare to the XRT images on Dec 10 and 12, and the misalignment of the XRT, SOT, and MDI images on Dec 10 and 12 is estimated to be less than 3".

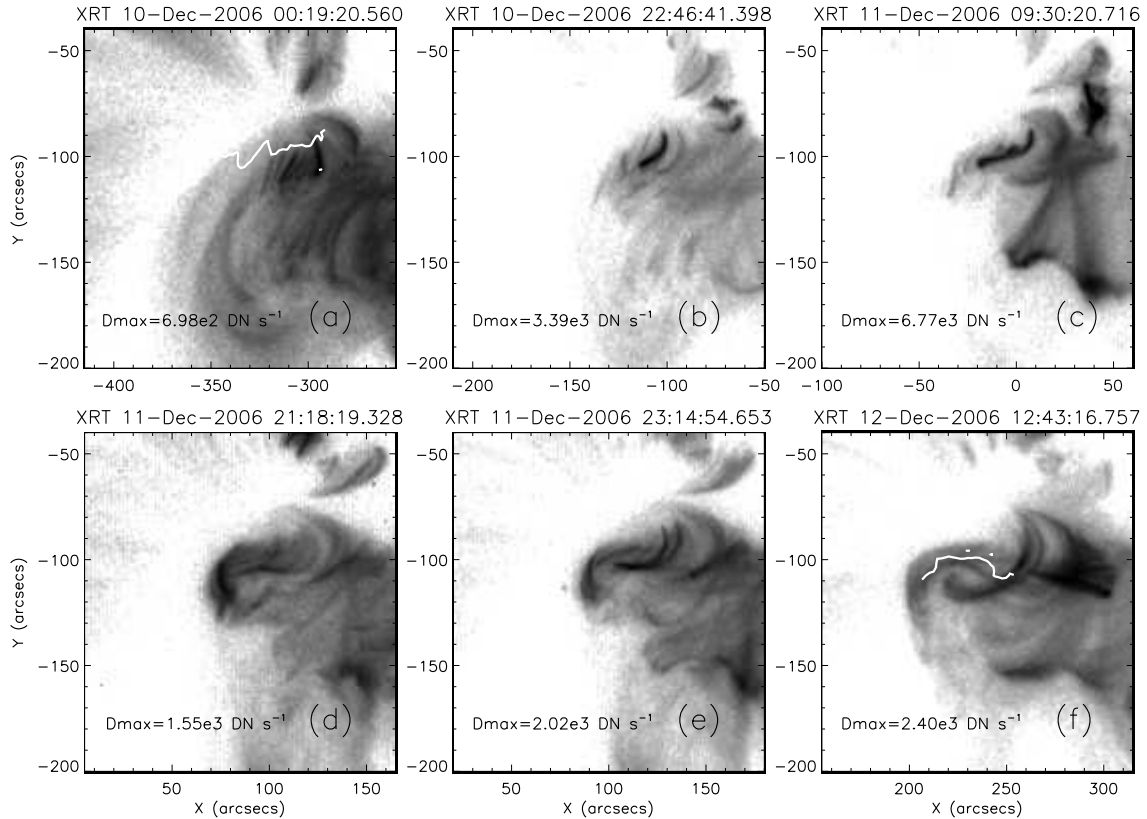


Figure 5-1 Formation of the sheared magnetic fields observed by XRT aboard *Hinode*. (a)–(f) A series of X-ray images observed with Be-thin filter by XRT from 2006 December 10 to December 12. The maximum intensity (D_{\max}) of the XRT image is shown in the lower left corner of each panel. The SOHO/MDI photospheric magnetic inversion line is represented as a thick white line.

5.3 Results

5.3.1 Formation of the Sheared Magnetic Fields

The formation process of the sheared magnetic fields observed by XRT aboard *Hinode* and SOHO/MDI is shown in Figure 5-1. Corresponding to the X-ray images in Figures 5-1a and 5-1f, the *Hinode*/SOT G band images overlaid without and with MDI photospheric magnetic field contours are displayed in the top and bottom panels of Figure 5-2. Figure 5-1a shows that most of the X-ray loops overlying the magnetic inversion line (MIL, marked as a thick white line) are nearly perpendicular to the

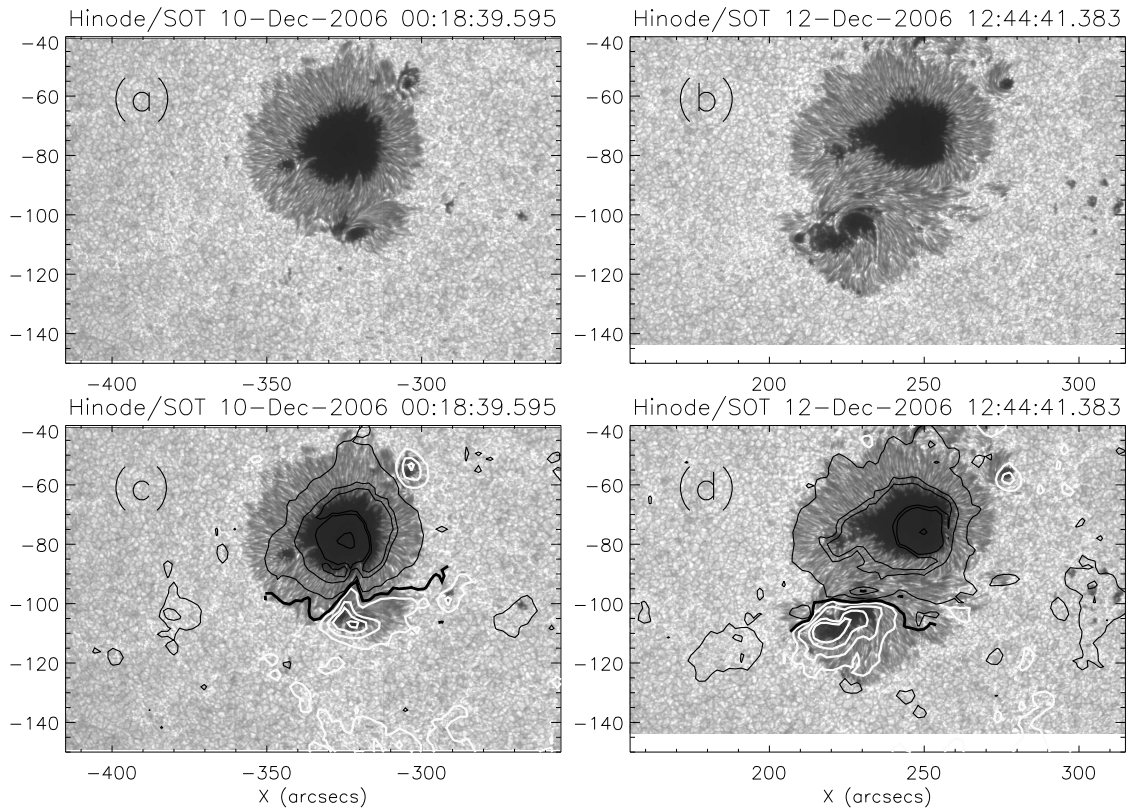


Figure 5-2 *Hinode*/SOT G band images overlaid with SOHO/MDI magnetic contours. (a) and (b) The G band images closest in time to the X-ray images in Figs. 5-1a and 5-1f, respectively. (c) and (d) The same G band images as in (a) and (b) overlaid with MDI magnetic contours. The black and white contours represent the positive and negative line of sight photospheric magnetic fields observed by MDI, and the thick black line represent the magnetic inversion line.

MIL, which indicates that the core field is close to a potential state at 00:18 UT on 2006 Dec 10. The corresponding G band images in Figures 5-2a and 5-2c shows that AR 10930 is composed of a bipole which contains one big sunspot with negative magnetic fields (black contours) and a small spot with positive magnetic fields (white contours). The two spots share a common penumbra. Following Moore et al. (2001), we define the core field as the fields that are rooted close to the MIL through the middle of the bipole. This core field is visible in XRT observations most of the time. Around 22:46 UT on Dec 10, one bright loop with obvious higher shear shows up on the right-hand side of the core field, while there are no obvious changes in the other loops (Figure 5-1b). About 11 hours later, two highly sheared loops are visible in the XRT observations (Figure 5-1c), while we still see no shear increase in the rest of the loops. Figure 5-1d shows an X-ray image taken 12 hours later than that presented in Figure 5-1c. Most of the X-ray loops in the core field region in Figure 5-1d have higher shear than those in Figure 5-1c. The core field in Figure 5-1d shows an S-shaped structure (i.e., Sigmoid) composed of two sets of disconnected loops, and a clearer S-shaped structure can be seen in Figure 5-1e. Most of the magnetic loops in the core field region become nearly parallel to the MIL by 12:43 UT on 2006 Dec 12 (Figure 5-1f), which indicates that the coronal core field has become highly non-potential. The corresponding SOT image (Figures 5-2b and 5-2d) shows that the penumbral fibrils between the two sunspots is also nearly parallel to the MIL, which indicates that the photospheric core field is also highly non-potential at this time.

Figure 5-1 shows that it took about two and a half days for the formation of the sheared coronal core field in AR 10930. The SOT G band and MDI movies in this time period show that the lower positive polarity spot was rotating in a counter clockwise direction, while there is no evidence of rotation in the upper sunspot. A large amount of magnetic flux emerged to the west of the positive polarity spot, and

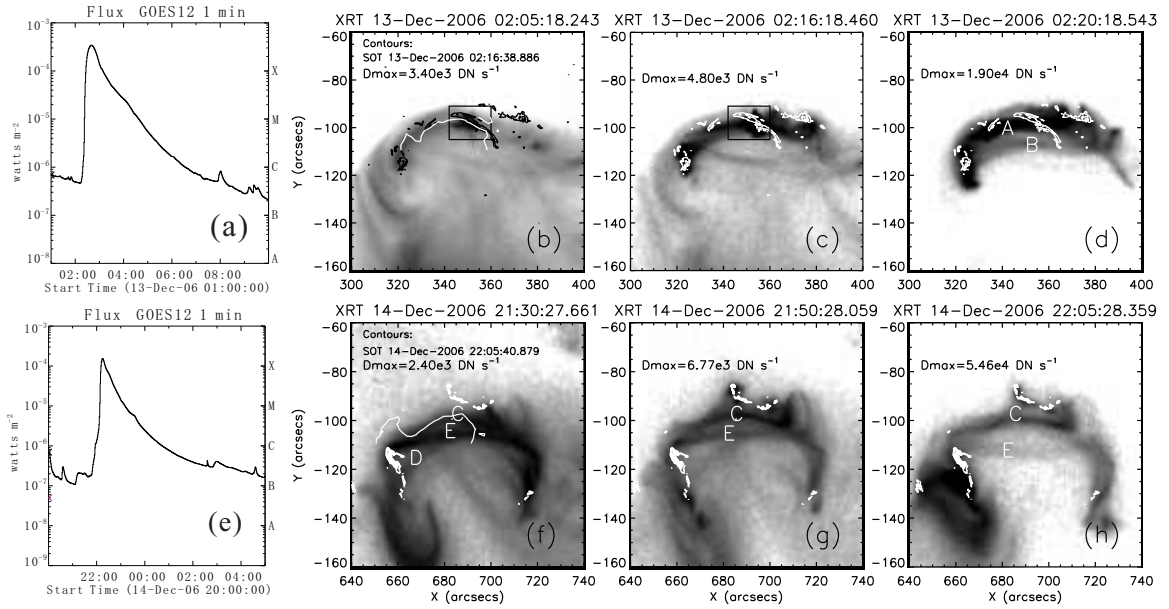


Figure 5-3 XRT observations of the sheared magnetic field evolution during two X-class flares. (a) and (e) GOES X-ray time profiles for the 2006 December 13 and December 14 flares. (b) shows an XRT image prior to the Dec 13 flare, and two XRT images during this flare are presented in (c) and (d). The contours in (b)–(d) refer to the brightenings at 02:16 UT observed by SOT in Ca II H. (f)–(h) The XRT images at the early phase of the Dec 14 flare. The white contours overlaid on these images represent the brightenings at 22:05 UT on Dec 14 observed by SOT in Ca II H. The long-lasting brightening prior to the flare is enclosed by the black box in (b) and (c). The maximum intensity (D_{\max}) of the XRT image is shown in the upper left corner of each panel.

newly emerged follower flux accumulated in the spot as it rotated. A clear west-to-east motion of the lower spot can also be seen in a comparison of Figures 5-2a and 5-2b. All of these observations appear to indicate that the highly sheared core field in AR 10930 is formed by this flux emergence and the accompanying rotation and west-to-east motion of the lower positive polarity sunspot.

5.3.2 Evolution of Sheared Magnetic Fields during the Flares

The evolution of the sheared X-ray loops observed by XRT during the Dec 13 and Dec 14 flares are presented in the top and bottom panels of Figure 5-3, respectively. The

GOES soft X-ray time profile of the Dec 13 flare (Figure 5-3a) shows that it is an X3.4 flare, and it started at 02:14 UT, peaked at 02:40 UT, and ended around 09:00 UT. An X-ray image prior to the flare is displayed in Figure 5-3b, and two X-ray images from the early phase of the flare are shown in Figures 5-3c and 5-3d. The black or white contours overlaid on these three X-ray images refer to the first brightenings seen in the SOT Ca II H line observations at 02:16 UT. At about 10 minutes prior to the flare, two compact brightenings in the highly sheared core field region started to appear, and the long-lasting one is enclosed by a black box in Figures 3b and 3c. After the flare onset, several brightenings showed up in the footpoints of the highly sheared loops (Figure 5-3c), and the pre-flare compact brightening still exists, which is located between the two flare footpoints. An X-ray image taken four minutes later is shown in Figure 5-3d, which shows two highly sheared and nearly parallel loops. The fainter loop (i.e., loop B) erupted, while the brighter loop (i.e., loop A) was left behind. Later on, the flare propagated to the less sheared envelope field region which is located outside of the core field. We see a strong-to-weak shear motion of the footpoints in the SOT Ca II H line observations during this flare, meaning that the footpoints start far apart but close to the MIL, then move toward each other and away from the MIL.

Figure 5-3e shows that the Dec 14 flare is an X1.5 flare, and it started at 21:07 UT, peaked at 22:15 UT, and ended around 04:00 UT on Dec 15. Figures 5-3f–5-3h show three X-ray images at the early phase of the flare. The white contours overlaid on these three X-ray images refer to the brightenings seen in the SOT Ca II H line observations at 22:05 UT, after which the flare ribbons started to extend along the MIL and move away from the MIL rapidly. In the early phase, we identified three X-ray loops, i.e., loop C, loop D, and loop E, as shown in Figure 5-3f. Loop D started to erupt around 21:26 UT, after which we see some brightenings (SOT Ca II H line) and

post-flare loops (XRT) in the lower left corner of Figure 5-3f, and some brightenings also appeared at the same position as the white contours close to loop C, which can be seen in Figure 5-3g. From Figure 5-3g we also see that loop E shows a continuous S-shaped structure. This S-shaped loop E started to erupt around 22:01 UT, which can be seen by a comparison of Figures 5-3g and 5-3h. However, loop C showed no obvious motion during the entire flare process seen in the XRT observations. We also see a strong-to-weak shear motion of the footpoints in the SOT Ca II H line observations in this flare.

Both the Dec 13 and Dec 14 flares started from the highly sheared core field. In both of these flares, we see that some of the highly sheared loops erupted, and other highly sheared loops were left behind. However, the initiation of the two flares appears to be different. In the Dec 13 flare, a compact brightening appeared first, then we see some brightenings (i.e., flare footpoints) located on the two opposite sides of the compact brightening. These observations indicate that magnetic reconnections may occur in the highly sheared core field, which leads to the eruption of the flare (or loop B). The loop that is left behind (i.e., loop A) appears to be a newly reconnected loop, because we see corresponding brightenings in the two ends of this loop after the flare onset. However, we did not see any evidence of magnetic reconnection before the eruption of loop D in the Dec 14 flare. After the eruption of loop D, we see some brightenings that appear to be the footpoints of the newly reconnected loops, after which loop E erupted too. The XRT movie of this flare shows that loop C that is left behind appears not to be involved in the flare process, which can also be seen in a comparison of Figures 5-3f–5-3h.

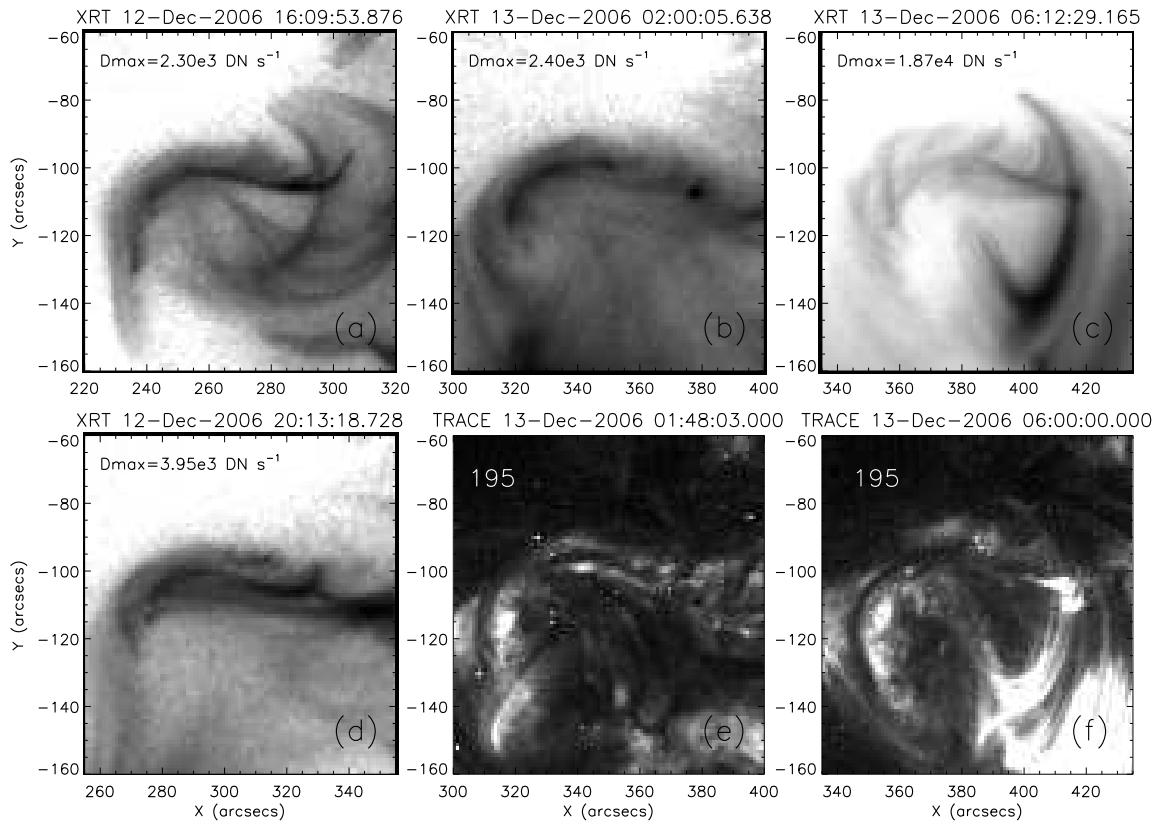


Figure 5-4 Pre-flare and post-flare XRT and TRACE images of the X3.4 flare on 2006 December 13. (a), (b) and (d) Three X-ray images observed by XRT prior to the flare. (c) An XRT image after the flare. (e) and (f) Two EUV images observed by TRACE prior to and after the flare for comparison with (b) and (c). The maximum intensity (D_{max}) of the XRT image is shown in the upper left corner of each panel.

5.3.3 Pre-flare vs. Post-flare Sheared Magnetic Fields

The continuous observations of AR 10930 by XRT with high spatial and temporal resolution provides us an excellent opportunity to compare the pre-flare and post-flare magnetic configurations. Figures 5-4a–5-4d shows the XRT observations of the core field before and after the X3.4 flare on 2006 December 13. The corresponding filaments before and after the flare observed by TRACE are displayed in Figures 5-4e–5-4f. Prior to the Dec 13 flare, XRT has detected two loop eruptions (likely filament eruptions), which started around 16:28 and 21:58 UT on Dec 12, respectively. Figures 5-4a and 5-4d show the core field before and after the first loop eruption, respectively. Both of these figures show that most of the X-ray loops in the core field region are highly sheared and nearly parallel to each other, and the brightest loops give an appearance of a continuous S-shaped structure. The magnetic configuration after the second loop eruption and 14 minutes prior to the Dec 13 flare is displayed in Figure 5-4b. After the Dec 13 flare onset, the post-flare loops propagated gradually from the highly sheared core field region to the outer and less sheared envelope field region, and during this time the less bright core field becomes invisible. Around 05:23 UT, the core field appears again, and a clear picture of the post-flare core field is displayed in Figure 5-4c. Figures 5-4b and 5-4c show that both the pre-flare and post-flare core fields show a highly sheared inner and less sheared outer structure. However, the post-flare core field is much less sheared than the pre-flare core field. Corresponding to the sheared core field observed by XRT, a filament is seen in TRACE prior to the Dec 13 flare (Figure 5-4e). We still see most parts of the filament after the flare, as can be seen in Figure 5-4f.

The XRT images prior to and after the X1.5 flare on 2006 December 14 are shown in Figures 5-5a–5-5c. The corresponding observations taken by TRACE are displayed in Figures 5-5d–5-5f. A filament eruption occurred around 16:40 UT on Dec 14. One

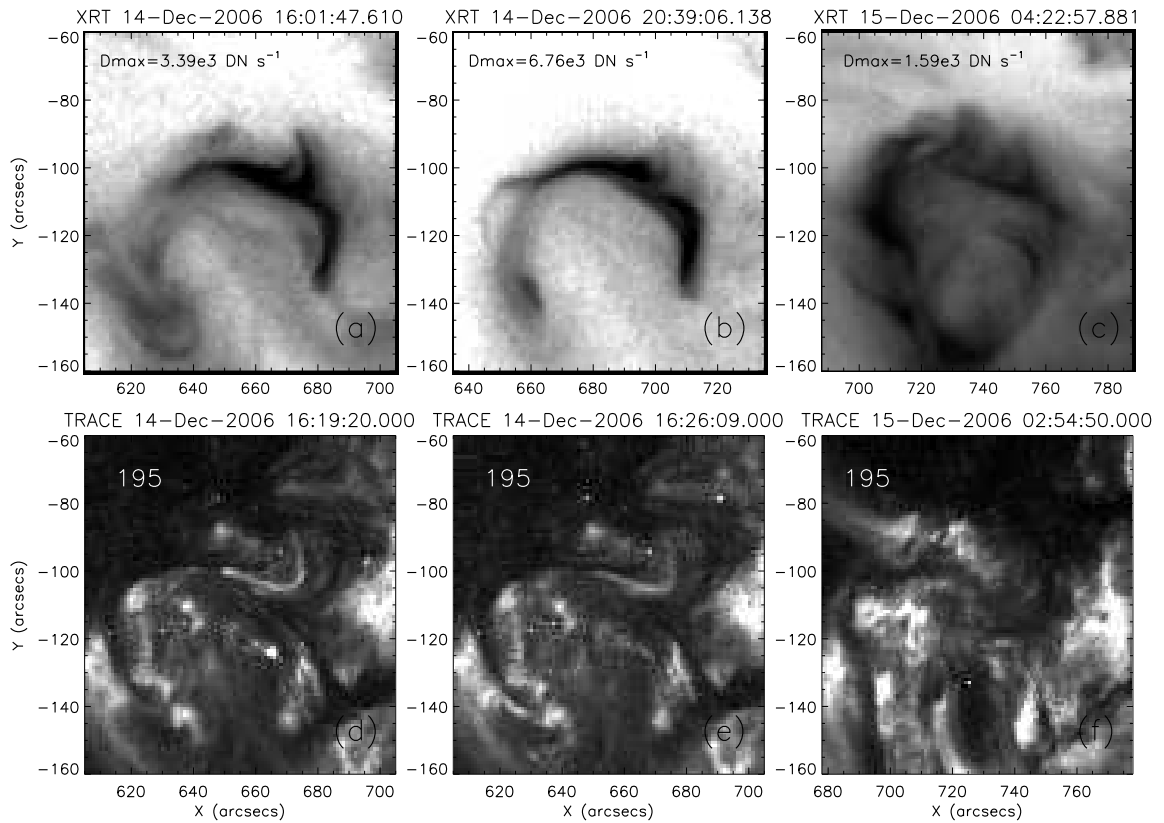


Figure 5-5 Pre-flare and post-flare XRT and TRACE images for the X1.5 flare on 2006 December 14. (a) and (b) Two X-ray images observed by XRT prior to the flare. (c) An XRT image after the flare. (d) and (e) Two EUV images observed by TRACE prior to the flare. (f) A TRACE EUV image after the flare. The maximum intensity (D_{\max}) of the XRT image is shown in the upper left corner of each panel.

X-ray image prior to this eruption is shown in Figure 5-5a, from which we see several highly sheared loops. A good TRACE image taken closest in time to Figure 5-5a is shown Figure 5-5d. A comparison of the figures shows that the filament corresponds to a highly sheared X-ray loop. Figure 5-5b shows an X-ray image after the filament eruption and 30 minutes before the Dec 14 flare. We see no significant changes in the magnetic configuration before and after the filament eruption. Similar to the Dec 13 flare, the post-flare magnetic configuration of the Dec 14 flare shows a highly sheared inside and less sheared outside structure (Figure 5-5c), and the post-flare core field is significantly less sheared than the pre-flare core field. Figure 5e shows the last good EUV image taken by TRACE prior to the Dec 14 flare, and a TRACE image after the flare is displayed in Figure 5f. A comparison of Figures 5-5e and 5-5f shows that a large part of the filament is still present after the flare.

5.4 Discussions and Conclusions

NOAA Active Region 10930 is a complex region, where four X-class flares occurred in December 2006, and two of them (i.e., flares on Dec 13 and Dec 14) were observed by both XRT and SOT aboard *Hinode*. The continuous observations of this region by XRT and SOT provide us an opportunity to study the long-term evolution of the sheared core field. In this chapter, we addressed three questions: How do the non-potential magnetic fields build up? How do they evolve during the flares? What is the difference between the pre-flare and post-flare magnetic configuration?

The XRT observations show that the coronal magnetic fields are close to a potential state at 00:19 UT on 2006 December 10. About 22 hours later, the shear increase started from one X-ray loop on the right-hand side of the core field rooted close to the MIL between the two main magnetic polarities. After that more and more loops gradually become highly sheared. Most of the loops in the core field region become

highly sheared and nearly parallel to the MIL around 12:43 UT on 2006 December 12. The formation of the sheared magnetic fields are caused by the counter clockwise rotation and west-to-east motion of the lower emerging sunspot, which can be seen in the SOT G band and Ca II H line observations as well as the SOHO/MDI observations.

Both of the X-class flares on Dec 13 and Dec 14 started from a highly sheared core field. At the early phase of each flare, we see that some highly sheared loops erupted, and some highly sheared loops are left behind. The highly sheared loop that is left behind in the Dec 13 flare seems to be a newly reconnected post-flare loop. However, the one that is left behind in the Dec 14 flare appears not to be involved in any reconnection as can be seen in the XRT observations. Corresponding to the highly sheared core field, a filament was seen in the EUV observations by TRACE prior to the two flares. A large part of the filament is still present after these two flares, which may be caused by the fact that only part of the sheared magnetic fields erupted during the flares. The initiation of these two flares seems to be different. The X3.4 flare on Dec 13 appears to be initiated by magnetic reconnection in the highly sheared core field, which agrees with the cartoon of the three dimension model for eruptive flares in Moore et al. (2001). However, the X1.5 flare on Dec 14 started from a sheared loop eruption, before which we see no evidence of magnetic reconnection.

Two loop eruptions (likely filament eruptions) were seen by XRT prior to the Dec 13 flare. Most of the loops in the core field are highly sheared and nearly parallel to each other before and after the first loop eruption. The core field shows a highly sheared inside and less sheared outside structure, after the second loop eruption and 16 minutes before the flare. The core field before the Dec 14 flare is composed of several highly sheared loops. About 2–3 hours after the peak of each flare, the core field is visible again in the XRT observations. The post-flare core field shows a highly

sheared inside and less sheared outside structure, but contains significantly less shear in comparison to the pre-flare core field. This observation is in agreement with the idea that the flare is caused by the release of magnetic energy stored in the highly sheared magnetic fields, but apparently only a fraction of the available energy is released.

A strong-to-weak shear motion of the footpoints is observed in both of the two flares on Dec 13 and 14. This motion suggests that the pre-flare magnetic field configuration is composed of a highly sheared core field and overlying less sheared envelope field. We did not see these overlying less sheared envelope fields in the XRT observations prior to the two flares, which is in agreement with the *Yohkoh*/SXT observations (Sterling et al. 2000). Moreover, a long-term XRT observation of AR 10930 shows that the core field is visible most of the time, while the overlying loops can only be seen temporarily after the flares or loop eruptions. The heating mechanism for the core field is apparently different from the post-flare loops. We are left with two open questions: Why do we not see the overlying unsheared loops in the pre-flare phase? What is the heating mechanism of the core field?

Chapter 6

Observations and NLFFF

Modeling of Active Region 10953

6.1 Introduction

It is well accepted that solar flares, prominence eruptions, and coronal mass ejections (CMEs) are different manifestations of a single physical process thought to be powered by the magnetic free energy stored in the corona prior to the eruption. Storage of free energy requires a nonpotential magnetic field, and it is therefore associated with a shear or twist in the coronal field away from the potential, current-free state (Priest & Forbes 2002). Twisted or sheared magnetic fields are often visible in the solar corona before solar eruptions (Rust & Kumar 1996; Canfield et al. 1999; Moore et al. 2001; & Su et al. 2007a), but it is unclear exactly what triggers the eruption. To determine what caused such eruptions and how the energy was released, we need to understand the three dimensional (3D) structure of the pre-flare and post-flare coronal magnetic field configuration.

Within the inner regions of the solar corona ($r < 2.5 R_{\odot}$) the magnetic pressure is generally much greater than the gas pressure ($\beta = 2\mu p/B^2 \ll 1$), so the magnetic force is dominant. Therefore, a commonly used approximation to an equilibrium magnetic field is that of the force-free field ($\mathbf{j} \times \mathbf{B} = 0$), where the electric currents flow parallel or antiparallel to the magnetic field lines (Priest 1982). This equation

may be written as $\nabla \times \mathbf{B} = \alpha \mathbf{B}$, where the torsion parameter $\alpha(r)$ is constant along a field line, but may vary from one field line to the next. Many authors in the past have used the force-free approximation along with different assumptions about the form of α to extrapolate coronal magnetic fields from observed surface distributions.

Two possible choices for α are $\alpha = 0$, which is called a potential magnetic field, and $\alpha = \text{constant}$, which is called the linear force-free field (LFFF). Potential fields have been commonly used to model the open magnetic flux of the Sun (Lockwood et al. 1999; Wang et al. 2000), through potential field source surface model (Altschuler & Newkirk 1969; Schatten et al. 1969; Wang & Sheeley 1992; Wang et al. 2000; Mackay & Lockwood 2002), where it is assumed that open field lines will be untwisted ($\alpha = 0$). Although the potential fields are simple to construct, they are limited by the fact that there is no electric current present, and therefore they cannot describe the corona during periods of highly solar activity (Mackay & Lockwood 2002). More realistic field configurations, which do contain electric currents, are LFFFs (Nakagawa & Raadu 1972; Nakagawa et al. 1978). Such LFFFs have also been shown to explain many of the observed features of filaments (Aulanier & Démoulin 1998; Aulanier et al. 2000). However, a limitation of these models is that they can only be used to describe a very localized area.

The more realistic situation is that $\alpha(\mathbf{r})$ varies with position in the corona, but α is constant along field lines. This is called a nonlinear force-free field (NLFFF). In a NLFFF α may vary from one field line to the next, so such fields can describe highly sheared or twisted regions next to relatively untwisted regions ($\alpha = 0$) such as a large coronal arcade or open flux. Several authors have developed methods for reconstructing NLFFFs by extrapolating observed photospheric vector fields into the corona (Mikić & McClymont 1994; Bleybel et al. 2002; Régnier et al. 2002; Wheatland 2006; Wheatland et al. 2000; Wiegelmann 2004; Wiegelmann et al. 2006).

Measurements of photospheric vector fields and their use in extrapolation are subject to a number of uncertainties (see McClymont et al. 1997). For a review of these various methods please refer to Schrijver et al. (2006), who performed various tests of such extrapolation methods.

In this chapter we focus on another method that does not require observed vector fields, i.e., the flux rope insertion method (van Ballegoijen 2004; van Ballegoijen et al. 2007), which only requires the line-of-sight magnetograms. Using an improved version of this method, Bobra et al. (2007) constructed NLFFF models for two active regions based on magnetograms from SOHO/MDI. The models are constrained by non-potential structures seen in BBSO $H\alpha$ images and TRACE EUV images. They found that the axial fluxes of the flux ropes are well constrained by the observations and the magnetic fields in these active regions are close to an eruptive state: the axial flux in the flux ropes is close to the upper limit for eruption.

In this study, we constructed NLFFF models for a simple bipolar active region (NOAA 10953) at three different times. This active region produced several filament activations and small flares ($< M$ class) in 2007 May. The models are constrained by the *Hinode*/XRT observations of the highly sheared X-ray loops. The purpose of this modeling is to understand the 3D structure of the magnetic field and its evolution associated with flares. This chapter is organized as follows. Section 6.2 describes the observations, and section 6.3 describe how the NLFFF models are constructed and the modeling results. The summary and discussion are given in section 6.4.

6.2 Observations

6.2.1 Data set and Method

A C8.5 (GOES soft X-ray class) two-ribbon flare associated with a filament activation occurred in NOAA Active Region (AR) 10953 around 23:20 UT on 2007 May

02. This event is well observed at multi-wavelengths, i.e., soft X-rays by the *X-ray Telescope* (XRT; Golub et al. 2007) onboard *Hinode* (Kosugi et al. 2007), EUV by the *Transition Region and Coronal Explorer* (TRACE; Handy et al. 1999), and H α by the *Polarimeter for Inner Coronal Studies* (PICS) which have been operated by the High Altitude Observatory at the Mauna Loa Solar Observatory (MLSO) since 1994. The full disk H α images ($\sim 1.09''/\text{pixel}$) taken at the Kanzelhöhe Solar Observatory (KSO) are also used. The XRT images presented in this study are taken at Ti-poly with $512'' \times 512''$ field of view (FOV). The spatial resolution is around $2''$ (i.e., $1.032''/\text{pixel}$). The TRACE EUV images are taken at 171 \AA with a FOV of $1024'' \times 1024''$, and the spatial resolution is $1''$. The full disk H α images taken by PICS with 3-minute temporal cadence have a spatial resolution of $2.9''$. The magnetic field information is obtained from the line of sight photospheric magnetograms from SOHO/MDI. The X-ray light curve of this event is provided by GOES.

The TRACE and XRT images are co-aligned with the MDI magnetograms by application of the following procedure. We first determined the offset of the TRACE coordinates by aligning the TRACE WL images with the corresponding WL images taken by MDI using the location of the sunspots. The offset between the XRT and TRACE images with corrected coordinates is determined by aligning the brightenings (i.e., flare footpoints) in the TRACE EUV images and the corresponding XRT images. We aligned the H α images from the PICS and KSO with the MDI magnetograms by eye.

6.2.2 Observational Results

Flux Cancellations in NOAA 10953

Figures 6-1a and 6-1b show two magnetograms of AR 10953 observed by SOHO/MDI on Apr 30 and May 3 in 2007. From a movie of the 96-min cadence magnetograms

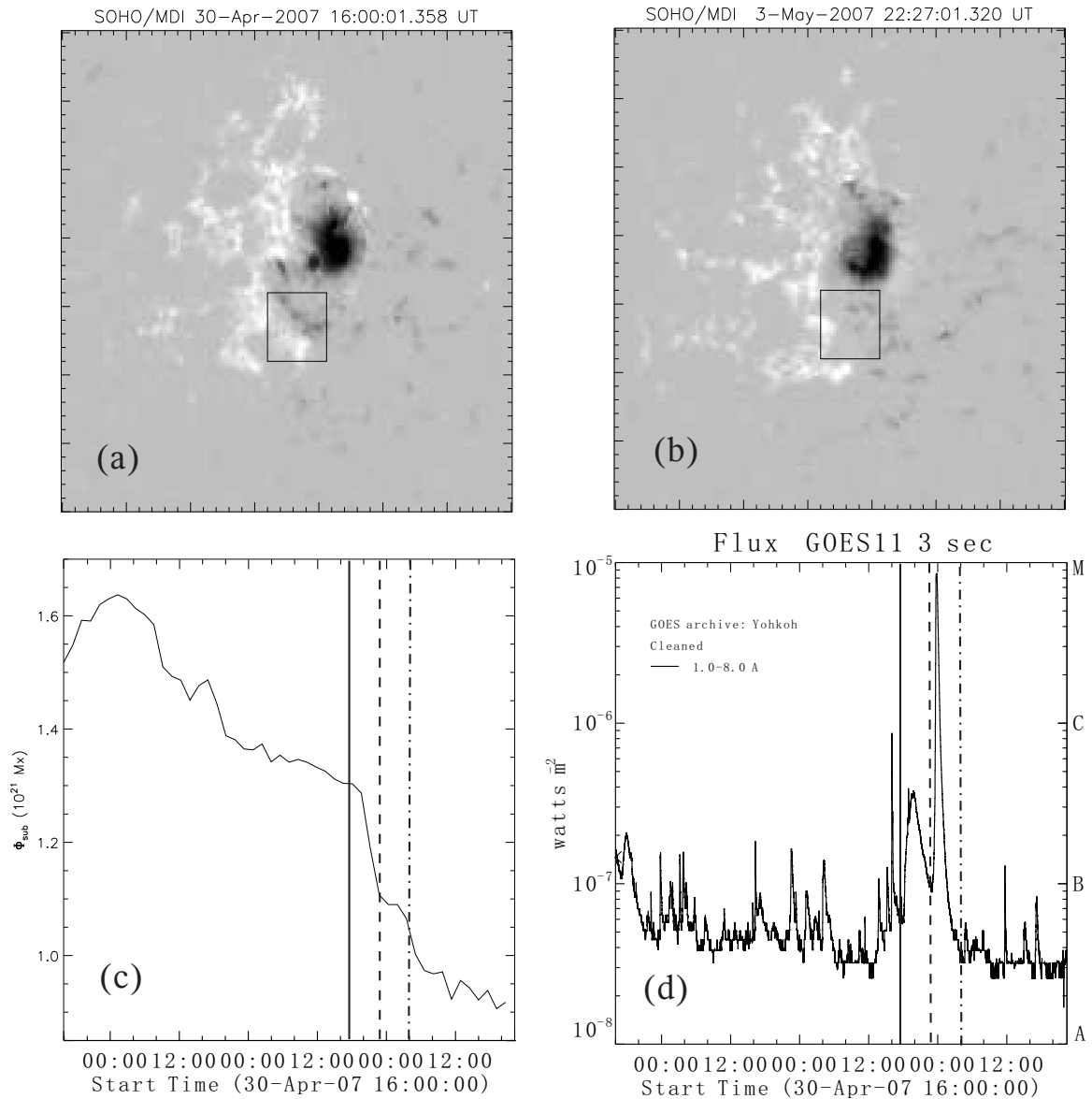


Figure 6-1 Flux cancellations in Active Region 10953 from April 30 to May 3 in 2007. (a) and (b) show the line of sight photospheric magnetograms observed by SOHO/MDI on Apr 30 and May 3. The field of view of these two images are $350'' \times 350''$. The temporal evolution of the total unsigned magnetic flux in the region enclosed by the black box (Φ_{sub}) in the top panels and the corresponding GOES soft X-ray light curve are shown in (c) and (d). The vertical lines refer to the time before and after the B3.8 and C8.5 flares.

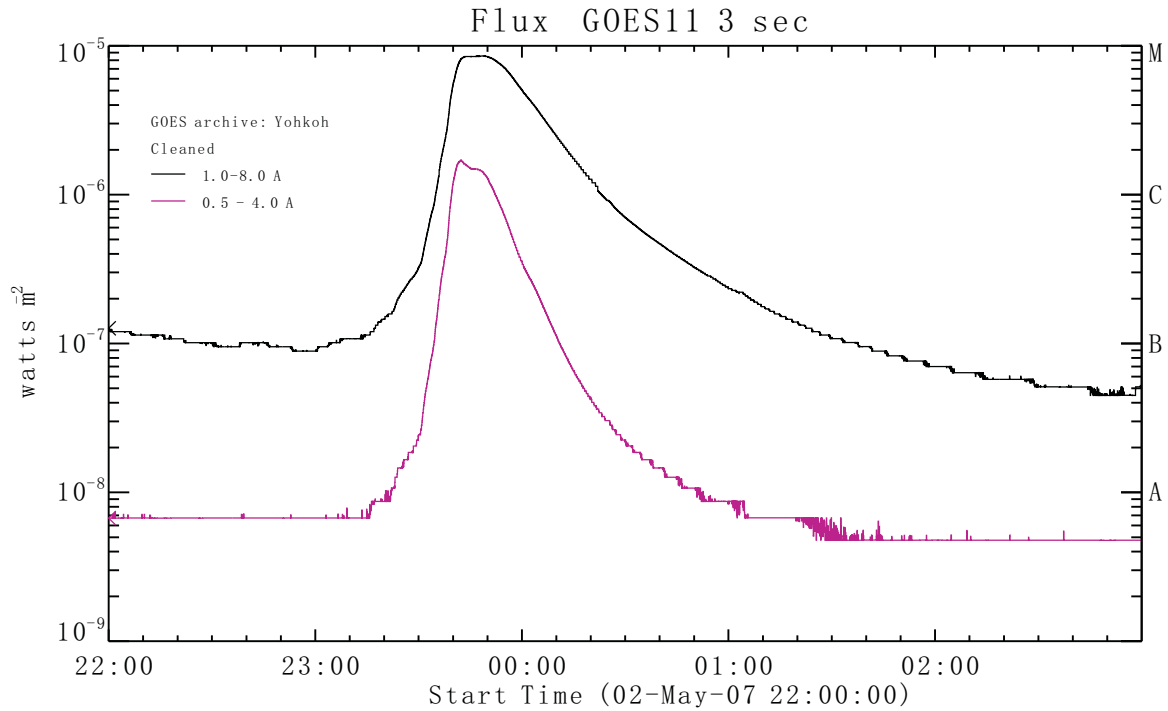


Figure 6-2 The GOES soft X-ray light curves for the C8.5 two-ribbon flare occurred on 2007 May 2.

within this time period, we find that flux cancellations frequently occurred in the region (enclosed in the black box) close to the polarity inversion line (PIL). A better presentation of the flux cancellation is shown in Figure 6-1c, which presents the temporal evolution of the total unsigned flux in the region enclosed in the black box. To calculate this flux we aligned the MDI magnetograms by rotating all of the images to the solar disk center. Figure 6-1d shows the GOES light curve. The three vertical lines in Figures 6-1c and 6-1d refer to the times before and after the B3.8 flare and C8.5 flare. Flux decrease is observed before both of the two flares. Figure 6-1d shows that the B3.8 Flare is a long-duration flare, which started at 18:00 UT and ended around 23:00 UT on May 2. A detailed analysis of the shrinkage of the post-flare loops for this event was reported by Reeves et al. (2007). In the present study, we focus on the C8.5 flare.

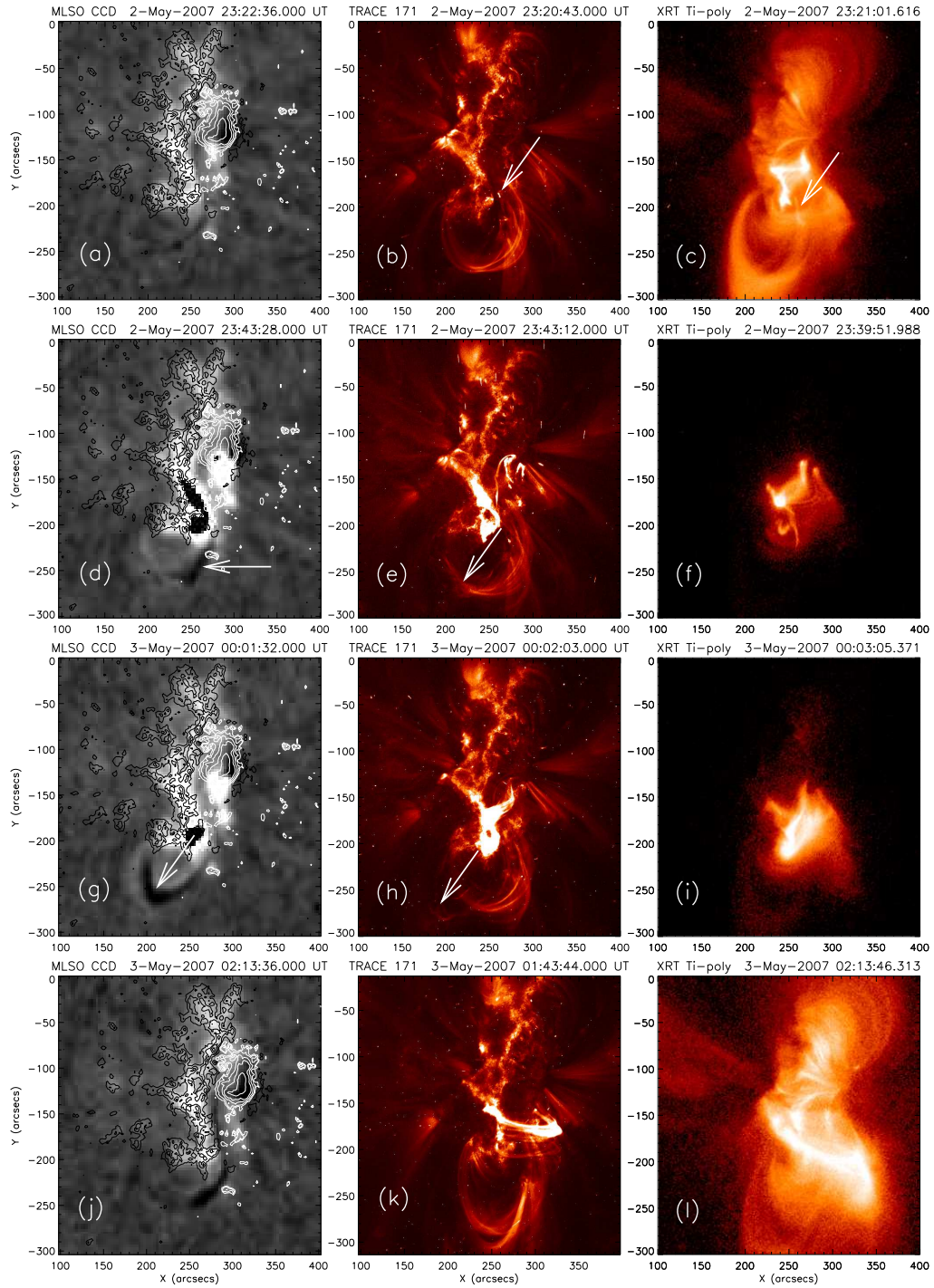


Figure 6-3 Evolution of the filament activation associated with the C8.5 flare. The left column shows the MLSO/PICS $H\alpha$ observations of this filament activation. The white and black contours refer to the negative and positive magnetic fields observed by SOHO/MDI. The corresponding closest in time TRACE EUV and *Hinode*/XRT observations are shown in the middle and right columns.

Evolution of the Filament Activation

The GOES soft X-ray light curves for the C8.5 two-ribbon flare are shown in Figure 6-2, which shows that the flare started around 23:12 UT and peaked at 23:48 UT on 2007 May 2, and ended about 02:00 UT on 2007 May 3. Figure 6-3 shows the evolution of the filament activation associated with the C8.5 flare in H α (MLSO/PICS, *left column*), EUV (TRACE, *middle column*), and X-ray (XRT, *right column*).

The first row of Figure 6-3 shows the images at the onset of the filament activation. From Figure 6-3a we can see that the northern end of the filament is rooted in the sunspot with negative polarity (*white contours*), but the southern end of this filament is unclear. This end of the filament is very unstable, and many activations were observed at multi-wavelengths (i.e., H α , EUV, and X-ray) from April 30 to May 3. Some bright features (marked by white arrows) corresponding to the onset of the filament activation are seen in both TRACE and XRT images (Figures 6-3b and 6-3c).

After 23:20 UT, a large amount of filament material was ejected from the northern part of the filament to the southern part (*second row*), then streamed into the nearby positive polarity (*third row*). The ejected materials are marked by the white arrows in both H α and EUV images (Figures 6-3d, 6-3e, 6-3g, and 6-3h), while no clear evidence is seen in the X-ray images (Figures 6-3f and 6-3i). Two bright flare ribbons showed up in all three wavelengths after the filament activation. The images at about three hours after the onset of the filament activation are shown in the fourth row of Figure 6-3. A comparison of Figures 6-3a and 6-3j shows that the shapes of the filament before and after the activation are very similar, but the H α filament after the activation appears to be darker than before.

Pre-EUV Flare X-ray Brightenings

Figure 6-4 shows the XRT and TRACE EUV images prior to and during the C8.5 flare. The XRT data used in this figure are normalized to its maximum value (D_{\max} , in unit of counts/s), which is presented on the top of each panel. The logarithm of the normalized XRT data is plotted in the figure, and the maximum and minimum values of the data are -0.2 and -2.8 .

An XRT image prior to the flare is shown in Figure 6-4a. At 23:07 UT, XRT started to see two short ribbon-like brightenings connected by a nearly potential loop (Figure 6-4b). A gradual increase in the GOES light curve started at 23:12 UT as shown in Figure 6-2. At 23:16 UT, there are no counterparts of the X-ray brightenings in the EUV image as can be seen from Figures 6-4c and 6-4f. As presented in the previous section, the filament activation began around 23:20 UT, after which a rapid increase is seen in the GOES light curve, and the EUV flare footpoint brightenings became visible (Figures 6-4d and 6-4g). However, the EUV brightenings are much smaller than the X-ray brightenings at this time. Several minutes later, most of the EUV counterparts of the X-ray brightenings can be seen in the TRACE images (see Figures 6-4e and 6-4h)

Highly Sheared Loops before and after the C8.5 Flare

Several long and highly sheared loops before and after the C8.5 flare are shown in Figure 6-5. The white and black contours overlaid on these images refer to the positive and negative magnetic fields observed by SOHO/MDI at 00:00 UT on 2007 May 3. Figure 6-5a shows a long and highly sheared loop observed by XRT at 15:17 UT on May 2, which is about 8 hours prior to the C8.5 flare. This loop appeared in the XRT images at 15:05 UT on May 2, and it seems to be distorted by a partial filament eruption that occurred around 16:20 UT, then vanished in the XRT images after 16:40

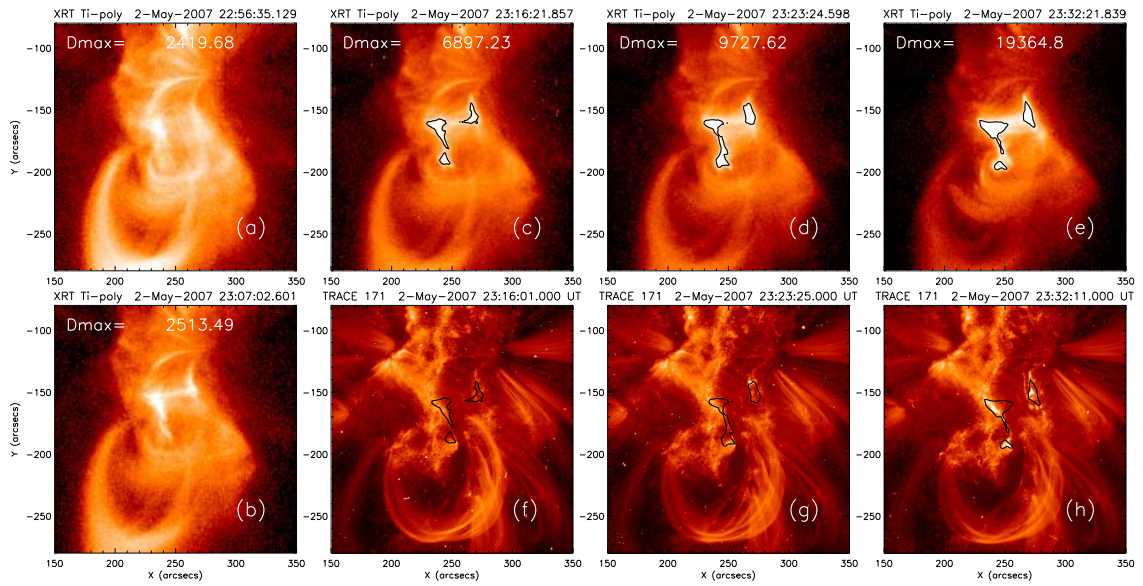


Figure 6-4 Pre-EUV X-ray footpoint brightenings during the C8.5 flare. The left column shows the X-ray observations prior to and at the early beginning phase of the C8.5 flare. The maximum intensity (D_{max}) of the XRT images is shown on the top of each panel. The X-ray and corresponding EUV observations during the flare are shown in (c)–(e) and (f)–(h), respectively. The black contours represent the brightenings in the XRT images at 23:16 UT (*second column*), 23:23 UT (*third column*), and 23:32 UT (*fourth column*), respectively.

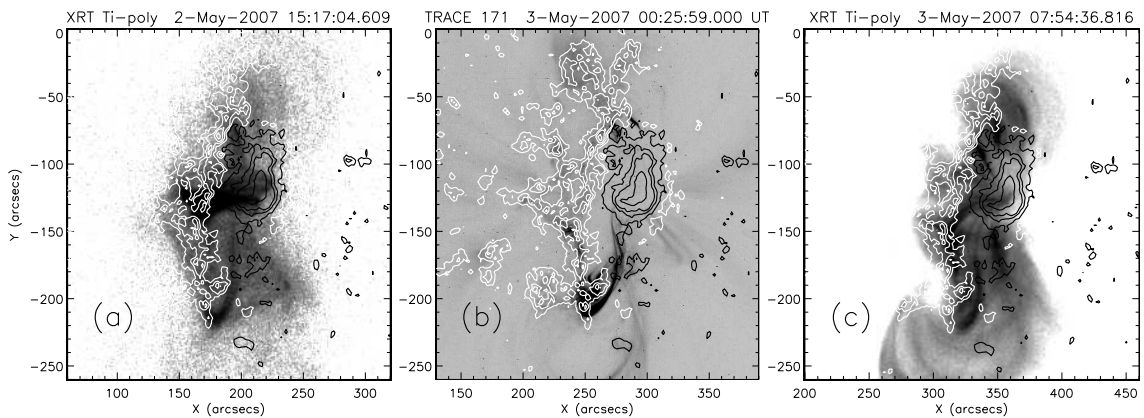


Figure 6-5 Highly sheared loops before and after the C8.5 flare. (a) and (c) X-ray observations of the highly sheared loops 8 hours before and 9 hours after the flare onset. (b) Highly sheared post-flare loops observed by TRACE. The white and black contours overlaid on these images refer to the positive and negative magnetic fields observed by SOHO/MDI at 00:00 UT on 2007 May 3.

UT. Figure 6-5b shows the longest and highly sheared EUV post-flare loops observed by TRACE around 00:25 UT on May 3. At around 07:54 UT, a highly sheared X-ray loop (Figure 6-5c) appeared associated with a small filament activation. About 20 minutes later, this loop vanished gradually in the XRT observations. The highly sheared loop in Figure 6-5a has almost the same shape as that in Figure 6-5c, but the loops in Figure 6-5b appears to be shorter. This result seems to suggest that the highly sheared loop in Figure 6-5a may not be disrupted by the filament eruption, and it is visible in XRT observations only when is heated up and becomes hotter than the overlying loops in this active region. However, we also cannot exclude the possibility that this loop was disrupted by the filament eruption, and the loop in Figure 6-5c is a newly reconnected loop at the same position.

6.3 Non-Linear Force Free Field Modeling of NOAA 10953

6.3.1 Flux -Rope Insertion Method

A flux rope insertion method has been developed by van Ballegoijen (2004) and van Ballegoijen et al. (2007) for constructing NLFFF models for solar active regions and filaments. The method involves inserting a magnetic flux rope into a potential-field model of an active region, then magneto-frictional relaxation is applied by solving the ideal MHD induction equation. The potential field represents the coronal arcade that overlies the flux rope and prevents it from erupting into the heliosphere. The flux rope has both axial and poloidal field components that are spatially separated from each other and distinct from the overlying arcade. The axial flux Φ_{axi} (in Mx) and the poloidal flux F_{pol} per unit length along the filament (in Mx/cm) are treated as free parameters. In this Chapter we use an improved version of this method. The detailed description of the new method can be found in Bobra et al. (2007); a brief summary is given below.

The computation domain is a wedge-shaped volume in the corona surrounding an observed active region and filament. The domain extends from the photosphere to a “source surface” at a radial distance of about $2 R_{\odot}$ from Sun center. The magnetic field $\mathbf{B}(\mathbf{r})$ in this volume is described using vector potentials in spherical geometry. The radial component of magnetic field at the photosphere, B_r , is derived from the observations. For the model presented in Chapter we use MDI magnetograms, which provide only the line-of-sight component of magnetic field, $B_{||}$. We approximate $B_r \approx B_{||}$, which is valid near solar disk center, but becomes increasingly inaccurate as we move away from disk center.

The first step in the model construction is selecting the path of the flux rope by manually tracing an H α filament. The curve starts in a region of positive polarity near the polarity inversion line (PIL), follows the path of the observed filament, and ends in a region with negative polarity on the opposite side of the PIL. The selected filament path on 2007 May 1 is shown in Figure 6-6a. The circles at the two ends of the path are sites where the flux rope can be anchored in the photosphere.

The next step is to compute the vector potential $\mathbf{A}(\mathbf{r})$ of the *potential* field based on the MDI magnetogram. The method for computing potential fields in a domain that is part of a spherical shell is described in Appendix B of van Ballegooijen et al. (2000). The gauge of \mathbf{A} is chosen such that $A_r = 0$. Then an elongated *cavity* is created along the selected filament path. Since the path is chosen to be along the PIL, the vertical fields in this volume are weak and the cavity is nearly field free.

The flux rope can now be inserted into this (nearly field-free) cavity. The rope consists of two spatially distinct components: a thin horizontal tube that represents the axial field of the flux rope, and a set of flux rings that are wrapped around the tube representing the poloidal field. At the two ends of the path the flux rope connects to the photosphere via two short vertical sections. The axial and poloidal fluxes of

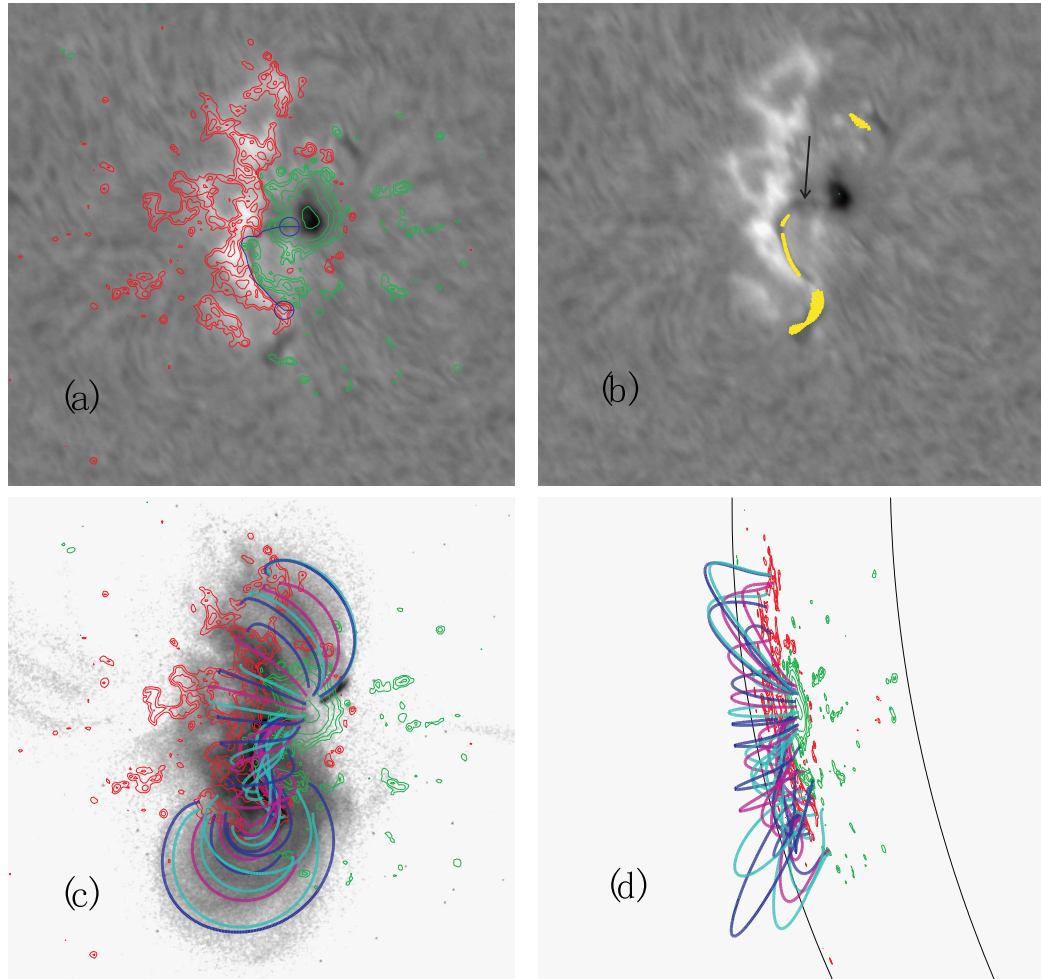


Figure 6-6 A NLFFF model for NOAA Active Region 10953 on 2007 May 1 at 06:27 UT. (a) H α image observed by Kanzelhöhe Solar Observatory at 07:51 UT overlaid with contours representing the positive (*red*) and negative (*green*) magnetic fields observed by SOHO/MDI at 06:27 UT. The blue line refers to the selected path for inserting the flux rope. (b) The same H α image overlaid with field-line dips (*yellow*) for Model 1. (c) Selected field lines from Model 1 and the same magnetic contours as shown in (a) overlay on an X-ray image at 05:56 UT. (d) The same field lines and contours rotated by 70° towards the east limb. The FOV of all panels is $0.4 R_{\odot}$. North is up, and West is to the right.

the flux rope are selected by trial and error, based on how well the final model fits the observations.

Finally, we use magneto-frictional relaxation (Yang et al. 1986; van Ballegooijen et al. 2000) in order to drive the magnetic field toward a force free state. The relaxation process causes the flux rope to expand and the surrounding arcade to contract, so the cavity quickly disappears, and the final results do not depend on the initial size of the cavity. The boundary conditions are such that the horizontal components of $\mathbf{A}(\mathbf{r})$ on the photosphere are held fixed during the relaxation process, so the radial magnetic field at the photosphere remains unchanged. We also use periodic boundary conditions in longitude, closed boundaries in latitude, and open boundary conditions at the top, where the field is assumed to be radial.

The end result of the relaxation is a 3D NLFFF model of the magnetic field $\mathbf{B}(\mathbf{r})$ with a magnetic flux rope located at the location of the filament. We then repeat the above process for different values of the axial flux Φ_{axi} and poloidal flux F_{pol} of the flux rope. The purpose is to find the solution that best fits the observed non-potential structure as revealed by comparison with XRT images.

6.3.2 Modeling Results

Figure 6-6 shows the results of a 3D NLFFF model ($\Phi_{axi} = 9 \times 10^{20}$ Mx, $F_{pol} = 15 \times 10^{10}$ Mx/cm) for AR 10953 on 2007 May 1 at 06:27 UT. The blue line in Figure 6-6a refers to the path that was selected along the H α filament for inserting the flux rope. Figure 6-6a shows that the filament originates in positive polarities (*red contours*) and ends in the sunspot with negative polarities (*green contours*). Therefore, the axial field of the filament is directed to the North, and has *sinistral* orientation with respect to the positive polarity (see Martin 1998). Figure 6-2b shows the location of dips in the field lines, i.e., sites where the field lines are horizontal and curved upward.

Table 6.1. The Average Deviations (dmavg) of the model field lines from the observed X-ray loops for various models of AR 10953

Time	Loop	F_{pol} (10^{10} Mx cm $^{-1}$)	Φ_{axi} (10^{20} Mx)				
			3.5	5	9	12	18
May 1 06:27 UT	Loop 1	5					2.0
		15	2.8	0.9	1.6	5.4	
		35					2.3
	Loop 2	5					4.8
		15	5.6	3.1	2.2	5.3	
		35					4.2
May 2 16:03 UT	Loop 3	5					7.8
		15	5.3	5.2	6.4	8.4	
		35					6.5
	Loop 4	5					2.9
		15	3.3	2.1	4.1	4.2	
		35					3.8
Loop 5	5					4.6	
	15	4.8	2.9	4.2	5.2		
	35					4.6	
May 3 07:59 UT	Loop 6	15	6.0	7.5	10.4	12.5	

It has long been suggested that filament plasma is located at such dips in the field lines (Aulanier & Démoulin 1998). However, others have argued that dips are not necessary for a filament to form (Antiochos et al. 2000; Karpen et al. 2001, 2005). Figure 6-6b shows that there are dips (*yellow*) along most parts of the filament except in the northern part (marked by black arrow). Some selected field lines of this model overlaid on an XRT image at 05:56 UT are shown in Figure 6-6c, and the green and red contours represent the negative and positive magnetic fields observed by MDI. The height of these field lines can be seen in Figure 6-6d, which shows the same field lines and contours rotated by 70° towards the east limb. This figure shows that this model is composed of a weakly twisted and highly sheared flux rope with overlying potential arcade, and it fits the observed XRT structures well. The model presented in this figure is one of the models that best fit the XRT observations. The process for selecting the best fits will be illustrated below.

For AR 10953 at three different times, we constructed a grid of models with

Table 6.2. Degree of Convergence for Various Models for AR 10953.

Time	Loop	F_{pol} (10^{10} Mx cm^{-1})	Φ_{axi} (10^{20} Mx)				
			3.5	5	9	12	18
May 1 06:27 UT	Loop 1	5				Y	
		15		Y	Y	?	N
		35				?	
	Loop 2	5				Y	
		15		Y	Y	?	N
		35				?	
May 2 16:03 UT	Loop 3	5				Y	
		15		Y	Y	?	N
		35				N	
	Loop 4	5				Y	
		15		Y	Y	?	N
		35				N	
Loop 5	5				Y		
	15		Y	Y	?	N	
	35				N		
May 3 07:59 UT	Loop 6	15	Y	Y	?	N	

different values of axial and poloidal fluxes of the flux rope. For each model, the computation domain is represented in spherical coordinates, which have been translated into average x and y values in arcseconds. The size of the computation domain is $384'' \times 384''$. We determine the best model for AR 10953 based on the following two criteria: (1) this model should best fit the observed highly sheared X-ray loops; (2) this model should converge to a stable solution.

In order to find the model that best fits the observations, we compared these models with the sheared loops observed by XRT. The ‘‘Average Deviation’’ between an observed loop and a model field line is defined by measuring the minimum angular distance between a point on the observed loop and any point on the projected field line, and then averaging these distances for various points along the observed loop. For each model we manually select the field line that minimize this Average Deviation; this is the 3D field line that best fits the observed coronal loop. Table 6.1 lists the Average Deviations of the best-fit model field lines from the observed X-ray loops for various models of AR 10953. The left three columns of Table 6.1 show the time,

loop number, and F_{pol} of the model, and models with different Φ_{axi} are listed in the other columns. Table 6.1 is composed of three main rows, corresponding to different times (see column 1). The first three rows of the first main row show the Average Deviations of model field lines from Loop 1 for models with different F_{pol} . Similar information for Loop 2 is shown in the second three rows. Similar to the first main row, information for Loop 3, Loop 4, and Loop 5 is listed in the second main row. The last main row of Table 6.1 shows information for Loop 6.

Some of the models we constructed converge toward to a NLFFF equilibrium state, while others do not converge and the flux ropes lift off. Such “lift-off” occurs when the axial and /or poloidal fluxes of the flux rope exceed certain limits and the overlying coronal arcade is unable to hold down the flux rope in an equilibrium state. Table 6.2 shows the degree of convergence of various models in a format similar to that of Table 6.1. Y indicates that the model is well converged to a NLFFF equilibrium state, N indicates lift-off, and a question mark indicates that after 30000 iterations it is still unclear whether the model is stable or not.

Modeling Results for AR 10953 on 2007 May 1 at 06:27 UT

We first consider results of NLFFF models for AR 10953 on May 1 at 06:27 UT, which is about 40 hours before the C8.5 flare. We chose this time because we see no significant changes in the highly sheared loops that are visible in XRT within at least three days before 07:30 UT on 2007 May 1, after which dramatic changes occurred in the highly sheared loop structure. To find which model best fits the observation, we selected two XRT images because: (1) they are close in time to the MDI magnetograms from which the models are constructed; (2) a single highly sheared loop is easily identified in these images. The two XRT images are shown in the left and right columns of Figure 6-7, respectively. The two selected sheared

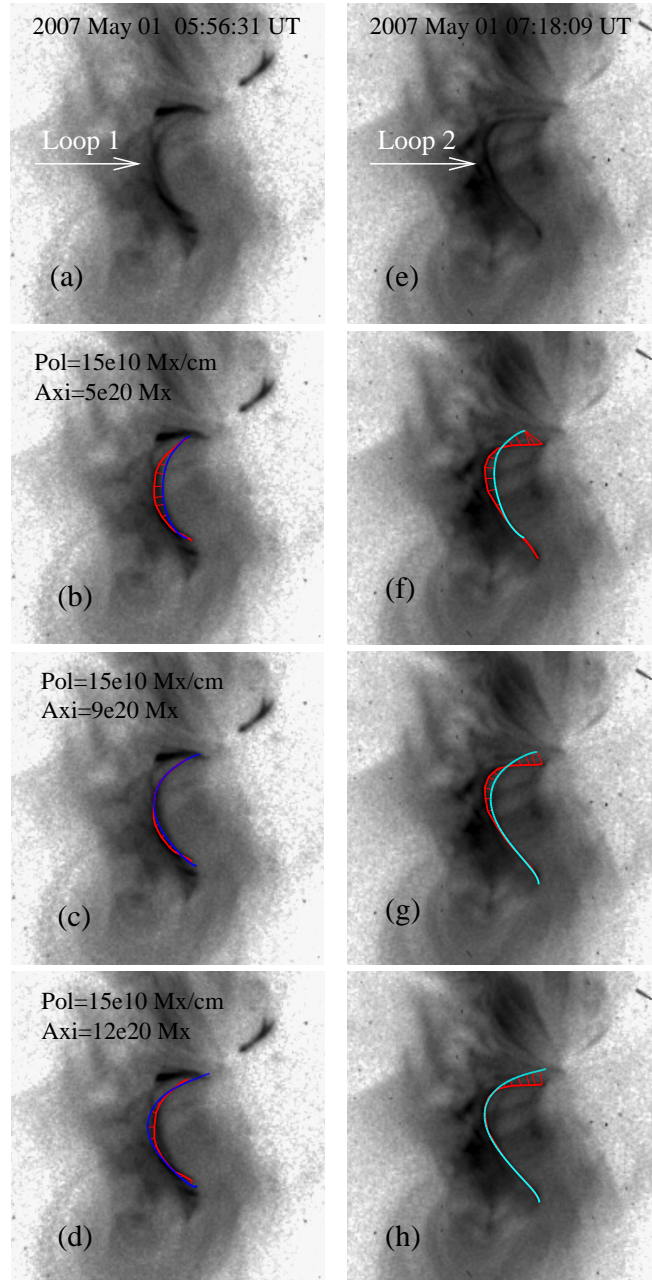


Figure 6-7 NLFFF models with different axial fluxes for AR 10953 on 2007 May 1 versus the observed X-ray loops. The first row shows the XRT images at 05:56 and 07:18 UT. The same X-ray observations of the highly sheared loops (*red*) overlaid with the best-fit field lines (*blue* and *light blue*) from models with different axial fluxes are shown in the second, third, and fourth rows. The FOV of all panels is $0.2 R_{\odot}$.

loops are marked by white arrows in the first row and represented by red lines (drawn manually by clicking different points along the observed loop) in the other rows of Figure 6-7. The blue and light blue lines in Figure 6-7, from the second to the fourth rows, are the projection of field lines from models with different axial fluxes of the flux rope. These field lines are the ones that best fit the observed loops.

Figure 6-7 shows models with different Φ_{axi} and fixed F_{pol} (i.e., 15×10^{10} Mx/cm). The first model (*second row*) shown in this figure has $\Phi_{axi} = 5 \times 10^{20}$ Mx. We see significant deviations of the best-fit model field lines from the two observed loops. We then increase Φ_{axi} to 9×10^{20} Mx to construct the second model, which is shown in the third row. This model shows very good fit to Loop 1, and it shows better fit to Loop 2 than the first model, but we still see some deviations of the model field line from Loop 2. The axial flux Φ_{axi} is then increased to 12×10^{20} Mx in the third model, which is shown in the fourth row of Figure 6-7. In comparison to the second model, this model shows worse fit to Loop 1, but a better fit to Loop 2. However, the model field line is still displaced from the northern part of Loop 2. In summary, this figure shows that the model with $\Phi_{axi} = 9 \times 10^{20}$ Mx is the best-fit model for Loop 1, while the best-fit model for Loop 2 has $\Phi_{axi} = 12 \times 10^{20}$ Mx. This result can also be seen in the Average Deviations listed in the first main row of Table 6.1.

The first main row of Table 6.2 shows that the model with $\Phi_{axi} = 9 \times 10^{20}$ Mx has converged, while the model with $\Phi_{axi} = 1.2 \times 10^{20}$ Mx is only marginally stable. If the axial flux is further increased, the magneto-frictional code will no longer reach an equilibrium state: the flux rope will keep expanding and moving radially outward. We also tried models with different poloidal fluxes (i.e., 5×10^{10} and 35×10^{10} Mx/cm), we found that the model with $F_{pol} = 15 \times 10^{10}$ Mx/cm shows best fit to the observed loop, which can be seen in Table 6.1. Moreover, models with $F_{pol} = 35 \times 10^{10}$ Mx/cm cannot produce a good NLFFF. Therefore, for AR 10953 on May 1 at 06:27 UT, the

model that produces a good NLFFF that best fits the XRT observations should be the model with $F_{pol} = 15 \times 10^{10}$ Mx/cm and $\Phi_{axi} = 5 \times 10^{20}$ Mx, which is named as Model 1 hereafter.

Modeling Results for AR 10953 on 2007 May 2 at 16:03 UT

In this subsection, we present modeling results for AR 10953 on May 2 at 16:03 UT, which is about 2 hours prior to the B3.8 flare and 7 hours before the C8.5 flare. Similar to the previous subsection, we also constructed a series of models with different combinations of Φ_{axi} and F_{pol} . To constrain the model, we select three non-potential X-ray loops, i.e., Loop 3, Loop 4, and Loop 5, which are shown in the left, middle, and right columns of Figure 6-8. These loops are marked by white and black arrows in the first row and represented by red lines in the other rows. Loop 3 shows a clear S-shaped structure, which first appeared in the XRT observations around 11:00 UT on May 2. Loop 4 is a long and highly sheared loop (also see Figure 6-5a), and showed up in XRT observations at 15:07 UT on May 2. Both Loop 3 and Loop 4 vanished associated with a partial filament eruption after 16:30 UT. Loop 5 appeared around 17:40 UT, and similar loops are visible in XRT images until the onset of the C8.5 flare. The blue, light blue, and magenta lines refer to the model field lines that best fit Loop 3, Loop 4, and Loop 5, respectively. The model field lines in Figure 6-8 are from models that have a fixed F_{pol} (i.e., 15×10^{10} Mx/cm) but different Φ_{axi} , i.e., 5×10^{20} Mx (*second row*), 9×10^{20} Mx (*third row*), and 12×10^{20} Mx (*fourth row*).

From Figure 6-8 we can see that the model with $\Phi_{axi} = 9 \times 10^{20}$ Mx shows much better fit to the observed Loop 4 and Loop 5, in comparison to the other two models. None of the model field lines shows very good fit to Loop 3 (especially the northern part), although the models with $\Phi_{axi} = 5 \times 10^{20}$ Mx and 9×10^{20} Mx appear to be better than the other model. These results can also be seen quantitatively in Table

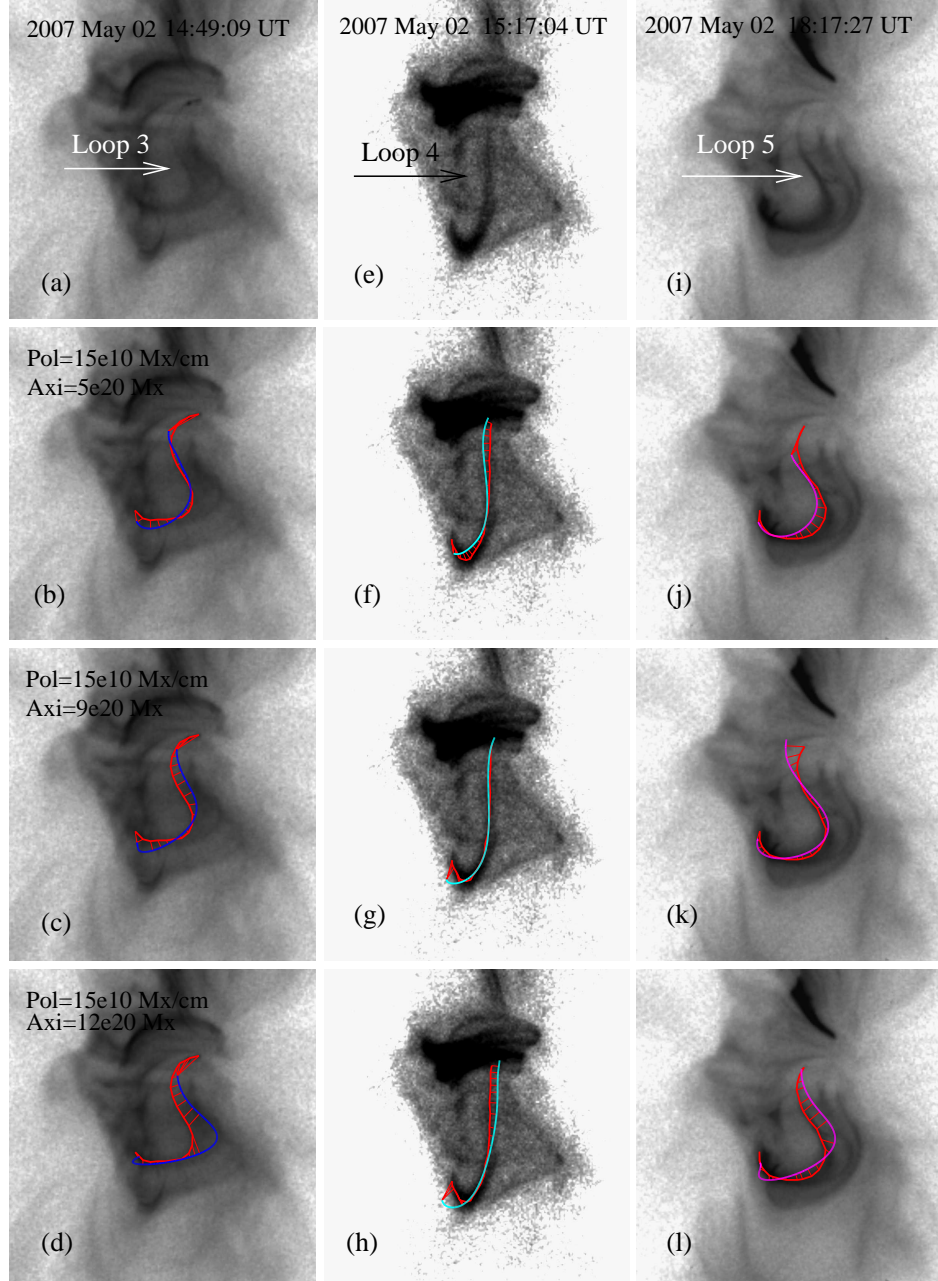


Figure 6-8 NLFFF models with different axial fluxes for AR 10953 on 2007 May 2 versus the observed X-ray loops. The first row shows the XRT images at 14:49, 15:17, and 18:17 UT. The same X-ray observations of the highly sheared loops (*red line*) overlaid with the best-fit model field lines (*blue, light blue, and magenta*) from models with different axial fluxes are shown in the second, third, and fourth rows. The FOV of all panels is $0.2 R_{\odot}$.

6.1. Similar to the previous subsection, models with $F_{pol} = 15 \times 10^{10}$ Mx/cm show the best fit to the observation, in comparison to the models with $F_{pol} = 5 \times 10^{10}$ and 35×10^{10} Mx/cm. Moreover, the model with $F_{pol} = 35 \times 10^{10}$ Mx/cm does not reach an equilibrium state (see Table 6.2). Therefore, the best model for AR 10953 on May 2 prior to the two flares is the model with $F_{pol} = 15 \times 10^{10}$ Mx/cm and $\Phi_{axi} = 9 \times 10^{20}$ Mx, which is named as Model 2 hereafter. Model 2 is stable as shown in Table 6.2. However, if the axial flux is increased to 12×10^{20} Mx, the flux rope will be only marginally stable. The magneto-frictional code no longer reaches an equilibrium state, if the axial flux is 18×10^{20} Mx. Therefore, the upper limit on the axial flux for this active region at 16:03 UT is between 12×10^{20} Mx and 18×10^{20} Mx, and the axial flux of Model 2 is close to the upper limit.

Modeling Results for AR 10953 on 2007 May 3 at 07:59 UT

A series of models are also constructed for AR 10953 on May 03 at 07:59 UT, which is 7 hours after the end of the C8.5 flare. To constrain the models, we selected one highly sheared X-ray loop (i.e., Loop 6), which appeared in XRT images associated with a small filament activation at 07:54 UT, then disappeared about 20 minutes later. This loop is marked by a white arrow in Figure 6-9a, and represented by red lines in the other panels of Figure 6-9. The magenta and light blue lines refer to the model field lines that best fit the northern and southern parts of Loop 6, respectively. The Φ_{axi} and F_{pol} of each model are presented in the corresponding panel.

None of the model shows good fit to the observed Loop 6, as shown in this figure. The right panels show better fit than that in the left panels. In the right panels, the model with $F_{pol} = 15 \times 10^{10}$ Mx/cm and $\Phi_{axi} = 3.5 \times 10^{20}$ Mx appears to show better fit than the other models. However, the model field line is still significantly displaced from most parts of the observed Loop. These results can also be seen from the average

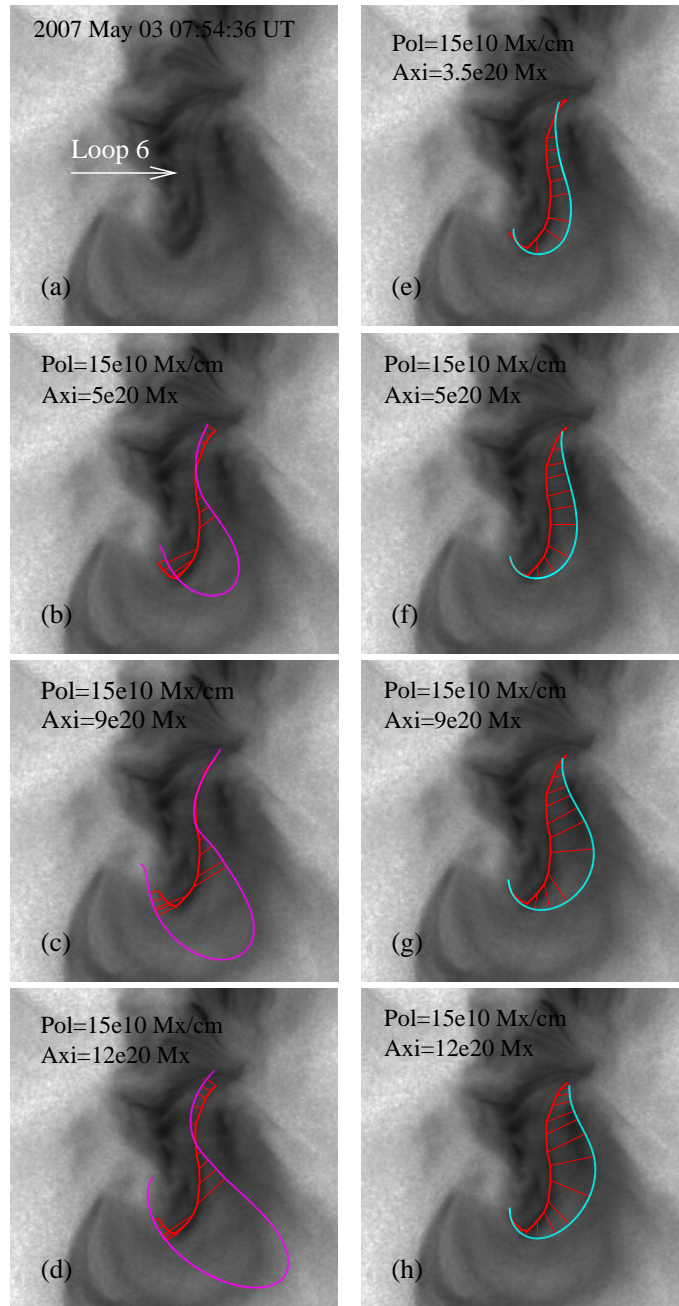


Figure 6-9 NLFFF models having different axial fluxes for AR 10953 on 2007 May 3 versus the observed X-ray loops. (a) XRT image at 07:54 UT. (b)–(h) The field lines from models with different axial fluxes overlaid with the X-ray image at 07:54 UT. The left panels show the field lines (*magenta*) that fit the upper part of the observed loop (*red*) the best. The field lines (*light blue*) that fit the lower part of the observed loop the best are shown in the right panels. The FOV of all panels is $0.2 R_{\odot}$. North is up, and West is to the right.

deviations of the model field lines and Loop 6, which are listed in Table 6.1. We also find that the model with $\Phi_{axi} = 9 \times 10^{20}$ Mx is only marginally stable. If the axial fluxes is increased to 12×10^{20} Mx, the magneto-frictional code no longer reaches an equilibrium state. Therefore, the upper limit of the axial flux of the flux rope is between 9×10^{20} and 12×10^{20} Mx.

Comparison of Various Parameters before and after the Flare

Table 6.3 shows various parameters of the best-fit model for AR 10953 at different times. The first two rows show the parameters for the two models before the C8.5 flare, and the last row shows the parameters after the flare. Since we did not find a good model that fits the observed loop after the flare, only potential energy and the length of the inserted flux rope are listed in the last row. Table 6.3 shows that the axial and poloidal fluxes of the best-fit models are the same, i.e., $F_{pol} = 15 \times 10^{10}$ Mx/cm and $\Phi_{axi} = 9 \times 10^{20}$ Mx, for the two cases before the C8.5 flare. The other parameters, such as magnetic potential energy (E_p) and magnetic free energy (E_f) of AR 10953 decreased. This decrease may be caused by the small filament activations triggered by the flux cancellations in the region close to the PIL. The magnetic free energy ($0.6\text{--}0.7 \times 10^{32}$ erg, 15% of the potential energy) stored in AR 10953 prior to the flare is sufficient for a C8.5 flare. The relative magnetic helicity (H_R) that also decreased before the flare is about 5×10^{42} Mx². The relative helicity is a measure of the linkage of magnetic flux tubes in the system (Berger & Field 1984; Bobra et al. 2007). The length of the inserted flux rope is about $3\text{--}4 \times 10^4$ km. The magnetic potential energy is decreased again after the flare, which appears to correspond to the strong flux cancellations.

Table 6.3. Model parameters for NOAA AR 10953 in 2007.

Date	Time (UT)	Model	Φ_{axi} (10^{20} Mx)	F_{pol} (10^{10} Mx cm^{-1})	E_p (10^{32} erg)	E_f (10^{32} erg)	H_R (10^{42} Mx ²)	L (10^4 km)	θ (radians)
May 1	06:27	1	9	15	4.81	0.75	5.19	4.04	4.23
May 2	16:03	2	9	15	4.50	0.62	4.78	3.27	3.42
May 3	07:59				4.25			4.14	

6.4 Summary and Discussion

In this study, we investigate the activity and magnetic configuration of a simple bipolar active region (NOAA 10953), which produced several small flares (mostly B class and one C8.5 class) and filament activations from April 30 to May 3 in 2007. The MLSO H α observations show that one end of the filament is rooted in the leading sunspot (negative polarity), while conditions at the other end of the filament are unclear. Many activations occurred at this end of the filament, which was located in the positive polarities on May 1, then moved to somewhere between the positive and negative polarities. Most of the filament activations and flares in this active region may be triggered by the flux cancellations that frequently occurred in the region close to the polarity inversion line (PIL), which were observed by SOHO/MDI.

A detailed analysis was carried out on a C8.5 flare associated with a filament activation that occurred in this active region on May 2. At around 23:20 UT, a large amount of material was ejected from the northern part of the filament to the southern part, then streamed into the nearby positive polarity. At least two similar filament activations were observed before the C8.5 flare on May 2. After the onset of the filament activation, a rapid increase in the flare intensity (GOES light curve) associated with EUV (TRACE) and X-ray (*Hinode*/XRT) flare footpoint brightenings was observed. At least 15 minutes prior to the filament activation, two short ribbon-like footpoint brightenings (close to the PIL) connected by a nearly potential loop

were already seen in XRT, while no counterparts of the X-ray brightenings were observed in EUV by TRACE. These pre-EUV flare brightenings are associated with a weak and gradual increase of the intensity in GOES light curve.

The two short ribbons that brightened in XRT about 15 minutes before the EUV flare brightenings were visible in XRT most of the time. The reason that XRT sees brightenings well before TRACE may be due to the fact that TRACE 171 Å images are sensitive only to plasmas in a narrow temperature range near 1 MK, while XRT is sensitive to a much broader range of temperatures. The footpoint brightenings in this flare started from a nearly unsheared geometry and close to the PIL, then evolved into highly sheared, and ended at unsheared, and a small increase in ribbon separation was also observed. The fact that we see no evidence of the outward eruption of the filament (i.e., breaking of the overlying field) appears to suggest that it is a confined flare. But the ribbon separation in this flare is in contradiction with the definition of a confined flare. This flare seems to be a case between confined and eruptive. This flare is different from most of the two-ribbon flares that we studied previously (Su et al. 2007b), in which we first see highly sheared footpoint brightenings close to the PIL, later evolving into unsheared brightenings further away from the PIL. More work needs to be done to understand how this flare occurred.

To study the magnetic configuration of this active region, we constructed NLFFF models at three different times (i.e., two before the C8.5 flare and one after the flare) and compared the results with XRT observations of highly sheared loops. The modeling used the flux-rope insertion method, which was based on the line of sight MDI magnetogram (i.e., vector magnetograms are not required). This method does not provide a unique solution for the 3D magnetic field. In general, a range of NLFFF models with different flux rope parameters (e.g., axial flux and poloidal flux) are compatible with observations, although the allowable range may be relatively

narrow. We find that AR 10953 contains a *sinistral* coronal flux rope, i.e., highly sheared, weakly twisted fields that are held down by an overlying arcade (Bobra et al. 2007). Such a flux rope is needed in order to fit the highly sheared loops observed by XRT.

Models with different axial fluxes and fixed poloidal flux (15×10^{10} Mx/cm) were constructed in order to constrain the axial flux of the flux rope and determine the conditions for which the flux rope can be stably held down by the overlying coronal arcade. For the two cases before the C8.5 flare, the models show a good fit to the observed non-potential loops. The axial magnetic flux in the flux rope of the best-fit model is about 9×10^{20} Mx, which is close to the upper limit (between 12×10^{20} Mx and 18×10^{20} Mx) of the axial flux that can be stably contained by the active region. This suggests that injection of additional axial flux may result in a “catastrophic loss of equilibrium” (Lin & Forbes 2000), in which the flux ropes pushes through the overlying coronal arcade and erupts. This may be the case for a partial filament eruption that occurred about 16:00 UT on May 2. Models with the same axial flux (9×10^{20} Mx) but different poloidal fluxes (i.e., 5×10^{10} and 35×10^{10} Mx/cm) are also constructed. We find that the model with poloidal flux of 15×10^{10} Mx/cm shows a much better fit to the observations than the other two models. Moreover, the model with poloidal flux of 35×10^{10} Mx/cm cannot be stably held down by the overlying arcade. However, for AR 10953 after the C8.5 flare, we did not find a good model that fits the observed highly sheared loop. The significant displacement of the model field line from the observed loop is due to the fact that on May 3 the photospheric magnetic fields on the western side of PIL are weaker than those on the eastern side, causing the flux rope to be pushed to the western side. We also find that the upper limit of the axial flux in the flux rope is between 9×10^{20} Mx and 12×10^{20} Mx, which is lower than that before the flare.

The potential energy of AR 10953 is about 4.5×10^{32} erg, and the relative magnetic helicity is 4.78×10^{32} Mx² on May 2 before the C8.5 flare. The magnetic free energy in this active region is 0.62×10^{32} erg, which is about 15% of the potential energy. The available free energy is sufficient to produce a large flare (such as M class), but no such event was observed. The fact that only several smaller events (B and C class) occurred suggest that this active region tends to release energy gradually.

Our current modeling is based on the original MDI data, which systematically underestimate magnetic field strength and saturate at high magnetic field strength values (Berger & Lites 2003). Therefore, the magnetic potential energy, free energy, and relative magnetic helicity listed in the present study are underestimated. Another problem left in this study is that there are some (either small or large) deviations of the model field line from the observed loop (e.g., the northern part of the loop), especially for the case after the flare. Our next step is to address these problems by improving the code with corrected magnetic field strength and flux imbalance.

Chapter 7

Summary and Outlook

7.1 Brief Summary

The main theme of this thesis is studying the evolution of the highly sheared magnetic fields before, during, and after solar flares, in order to address the question: how does the magnetic free energy stored and released? The work primarily focuses on the analysis of multi-wavelength data, while non-linear force free field (NLFFF) modeling of one active region is also explored.

We started from a detailed analysis of an X17 class (GOES soft X-ray) two-ribbon solar flare on 2003 October 28. EUV observations made by TRACE show a clear decrease in the shear of the flare footpoints during the flare. The shear change stopped in the middle of the impulsive phase. The observations are interpreted in terms of the splitting of the sheared envelope field of the greatly sheared core rope during the early phase of the flare. The good temporal correlation between the TRACE EUV and SPI/ACS hard X-ray emissions from the flare brightenings is favorable to the explanation that the EUV brightenings mainly result from direct bombardment of the atmosphere by the energetic particles accelerated at the reconnection site, as does the HXR emission. However, if there is a high temperature ($T > 20$ MK) HXR source close to the loop top, a contribution of thermal conduction to the EUV brightenings cannot be ruled out.

The research is then expanded to a statistical investigation of shear motion of the

UV/EUV footpoints in two-ribbon flares observed by TRACE in 1998–2005. We have selected 50 well-observed (X- and M- class) two-ribbon flares. We found that 86% (43 out of 50) of these flares show both strong-to-weak shear change of footpoints and ribbon separation (type I flares), and 14% of the flares show no measurable shear change of conjugate footpoints, including 2 flares with very small ribbon separation (type II flares) and 5 flares having no ribbon separation at all through the entire flare process (type III flares). Shear motion of footpoints is thus a common feature in two-ribbon flares. A detailed analysis of the type I flares shows: 1) for a subset of 24 flares, the initial and final shear angles of the footpoints are mainly in the range from 50° to 80° and 15° to 55° , respectively; 2) in 10 of the 14 flares having both measured shear angle and corresponding hard X-ray observations, the cessation of shear change is 0–2 minutes earlier than the end of the impulsive phase, which may suggest that the change from impulsive to gradual phase is related to magnetic shear change.

We then made a comprehensive statistical study addressing the question of what determines the intensity of a solar flare and associated coronal mass ejection (CME). For a sample of 18 two-ribbon flares associated with CMEs, we have examined the correlations between the *GOES* soft X-ray peak flare flux (*PFF*), the CME speed (V_{CME}) obtained from SOHO LASCO observations, and six magnetic parameters of the flaring active region. Among these six parameters, Φ and θ_{12} show the most significant correlations with $\log_{10}(\text{PFF})$ and V_{CME} . The fact that both $\log_{10}(\text{PFF})$ and V_{CME} are highly correlated with θ_{12} rather than with θ_1 indicates that the intensity of flare/CME events may depend on the *released* magnetic free energy rather than the *total* free energy stored prior to the flare. We also found that a linear combination of a subset of these six parameters shows a much better correlation with the intensity of flare/CME events than each parameter itself, and the combination of $\log_{10}\Phi$, θ_1 , and θ_{12} is the top-ranked combination.

Two X-class flares occurred in 2006 December were observed by XRT aboard *Hinode*, which was launched in 2006 September. Observations made with XRT and SOT aboard *Hinode* suggest that the gradual formation of the sheared magnetic fields in this active region is caused by the rotation and west-to-east motion of an emerging sunspot. In the pre-flare phase of the two flares, XRT shows several highly sheared X-ray loops in the core field region, corresponding to a filament seen in the TRACE EUV observations. XRT observations also show that part of the sheared core field erupted, and another part of the sheared core field stayed behind during the flares, which may explain why a large part of the filament is still seen by TRACE after the flare. About 2–3 hours after the peak of each flare, the core field becomes visible in XRT again, and shows a highly sheared inner and less sheared outer structure. We also find that the post-flare core field is clearly less sheared than the pre-flare core field, which is consistent with the idea that the energy released during the flares is stored in the highly sheared fields prior to the flare.

At last, we explored the NLFFF modeling of a simple bipolar active region (NOAA 10953), which produced several small flares (mostly B class and one C8.5 class) and filament activations from April 30 to May 3 in 2007. These events appear to be associated with the frequent flux cancellations (observed by SOHO/MDI) occurred in the region close to the polarity inversion line. We constructed non-linear force free field (NLFFF) models for this active region at three times, using the flux-rope insertion method. The models are constructed based on MDI magnetograms, and constrained by H α filaments observed at KSO and highly sheared loops observed by XRT. We find good NLFFF models that fit the observations before the C8.5 flare, but not for the case after the flare. The axial flux of the flux rope is better constrained by the observations in comparison to the poloidal flux. The flux rope contains highly sheared but weakly twisted magnetic fields. Before the C8.5 flare, this active region

is close to an eruptive state: the axial flux in the flux rope is close to the upper limit for eruption. We also find that the upper limit of the axial flux after the flare is lower than that before the flare.

7.2 Future Work

Although we have learned a great deal on the shear motion of flare footpoints and the important role of highly sheared fields during solar flares in this thesis, there are still many questions remain to be answered. In the following we discuss some of these questions and future works.

7.2.1 Further Study on Shear Motion of Footpoints

We have found that, like ribbon separations, the shear motion of flare footpoints is a common (86% of 50 flares) feature in two-ribbon flares. The distribution of the shear angles of the footpoints suggests that the post-flare magnetic fields are still sheared, which indicates a splitting of the flux rope (or the envelope) occurs in a large fraction of flares. This refers to the fact that some of the axial flux will be erupted outward associated with the CME, but some of the axial flux will be left behind. One important question is: what is the relative fraction of the erupted axial flux versus the ones that left behind and what determines the relative fraction? As mentioned in Chapter 3, this shear motion of the footpoints can also be found in the numerical simulation of several different CME models, e.g., the flux rope model (Gibson & Fan 2006), and the sheared arcades model (Manchester 2003). To determine which model is more realistic and get better understanding of the physics behind the observations, detailed comparisons between the model with observations and detailed modeling of real flare events is needed.

For a sample of 15 flares, we found that the cessation of shear change is 0–2

minutes earlier than the end of the impulsive phase in most of the events. This observation suggests that the transition of impulsive phase to gradual phase seems to be related to the transition of the reconnection from sheared field to unsheared field. The detailed interpretation is given by Lynch et al. 2004, who believe that the leading candidate for the acceleration of particles (primarily electrons) that give rise to the hard X-rays is the generation of fast shocks or strong turbulence by the Alfvénic outflows from the reconnection region. When the reconnection involves the highly sheared flux, the outflows carry a large quasi-perpendicular field component, but when the reconnection occurs in the unsheared field, the outflows are primarily field aligned. It is well known that quasi-perpendicular shocks or turbulence are much more efficient for electron acceleration than quasi-parallel shocks or turbulence (Giacalone 2003). If this interpretation is correct, why do we see a 0–2 minutes delay for the end of the impulsive phase? One possibility of this time difference may be due to the measurement uncertainties in the cessation time of the shear change. To get a more conclusive answer to this question, a statistical study using $H\alpha$ observations, for example from Hinode/SOT, should provide a better answer to this question. Because numerous observations have shown that the shear is invariably concentrated in the filament channel near the polarity inversion line (e.g., Martin 1998; DeVore & Antiochos 2000). The transition time of the reconnection from sheared to unsheared fields can be determined by the time when the flare footpoints propagate out of the filament channel, which can be seen in $H\alpha$ observations.

7.2.2 Evolution of Sheared Fields in Solar Flares: Observation

In Chapter 5, we presented XRT observations of evolution of sheared fields in two active regions (NOAA 10930 and NOAA 10953). These two active regions show very different characteristics. Active region 10930 is a newly developed and complex

(multi-polar) region, and a lot of motions (e.g., rotation and right-to-left motion) occurred in the emerging sunspot. The highly sheared fields are formed by these motions. It produced four X-class and numerous smaller flares. However, active region 10930 is a simple (decaying) bipolar region with frequent flux cancellations. This region only produced several smaller flares ($< M$ -class). The common feature in these two regions is that XRT can only see the highly sheared loops (near the polarity inversion line) where the flare started, prior to the flare. Although this may be helpful on determining the trigger mechanism of solar flares, the question of what is the pre-flare magnetic configuration still remains to be answered. How is the shear distributed in the fields from close to the polarity inversion line to the outer unsheared region? Is there an abrupt shear change from the sheared fields to the unsheared fields? Is there a flux rope prior to the eruption? All of these questions require a further detailed study of XRT observations with a much larger data sample.

7.2.3 Evolution of Sheared Fields in Solar Flares: Modeling

For active region 10953, we can make good NLFFF models for the highly sheared loops before the flare, but not for the case after the flare. we also found that the axial flux in the flux ropes is close to the upper limit for eruption prior to the C8.5 flare. However, there are still several problems. Such as, why we cannot make a good model for the loops after the flare? Why we see a lot filament activations, but the filament rarely erupts? Why the flare started from two short and nearly potential ribbons instead of the highly sheared footpoints which is often observed in two-ribbon flares? Further detailed modeling and analysis remain to be done.

In this thesis we only explored the NLFFF modeling for one active region. Since the modeling can provide very useful informations, such as the axial flux of the flux rope and the magnetic free energy, we plan to create models for more active regions

observed by XRT to create a statistically significant sample to address more important questions: for example, is there any relation between the magnetic free energy prior to the eruption and the intensity solar eruptions? Currently, our models are created based on the line-of-sight magnetograms. As a comparison, we also plan to make models using the high-resolution vector magnetograms from SOT.

Appendix A

Estimate of the Coronal Magnetic Field Strength

To estimate the coronal magnetic field strength in the flaring active region, we use a simple potential-field model. Let “P” be a point at height h above the magnetic inversion line and let “P₀” be the projection of “P” on the photosphere. We use a Cartesian coordinate system (x, y, z) with the origin at “P₀”; x and y are the horizontal coordinates along and perpendicular to the magnetic inversion line, respectively, and z is the height above the photosphere. The point “P” is located at $\mathbf{r} = (0, 0, h)$, and the potential field $B_{\text{cor}}(\mathbf{r})$ at this point can be estimated using the following formula:

$$\mathbf{B}_{\text{cor}}(\mathbf{r}) = \iint \frac{B_0(x_0, y_0)(\mathbf{r} - \mathbf{r}_0)}{2\pi|\mathbf{r} - \mathbf{r}_0|^3} dx_0 dy_0 \quad (7.1)$$

where $B_0(x_0, y_0)$ is the photospheric radial field strength at point $\mathbf{r} = (x_0, y_0, 0)$ in the selected subarea of the magnetogram. Equation (7.1) can be written as follows:

$$\begin{aligned} B_{\text{cor},x} &= - \sum_{ij} \frac{B_{0,ij}x_{0,i}}{2\pi(x_{0,i}^2 + y_{0,j}^2 + h^2)^{3/2}}, \\ B_{\text{cor},y} &= - \sum_{ij} \frac{B_{0,ij}y_{0,j}}{2\pi(x_{0,i}^2 + y_{0,j}^2 + h^2)^{3/2}}, \\ B_{\text{cor},z} &= \sum_{ij} \frac{B_{0,ij}h}{2\pi(x_{0,i}^2 + y_{0,j}^2 + h^2)^{3/2}}, \end{aligned} \quad (7.2)$$

and the field strength of the potential field is

$$B_{\text{cor}} = |\mathbf{B}_{\text{cor}}(\mathbf{r})| = \sqrt{B_{\text{cor},x}^2 + B_{\text{cor},y}^2 + B_{\text{cor},z}^2} \quad (7.3)$$

The height of h of point “P” is assumed to be 7250 km (10’). In this method, all points in the selected subarea of the magnetogram contribute to the coronal field strength at point “P”.

Appendix B

Multiple Linear Regression Fit

To study the relationship between the observed $\log_{10}(PFF)$ as well as V_{CME} and the observed magnetic parameters (i.e., $\log_{10}B$, $\log_{10}S$, $\log_{10}\Phi$, θ_1 , and θ_{12}) for our 18-event sample, we perform a multiple linear regression fit to the observed data by fitting a general linear equation. The fitting equation is expressed as:

$$Y_{fit,j} = a_0 + \sum_{i=1}^m a_i X_{ij}, \quad (7.4)$$

where X_{ij} is the measurement of the magnetic parameter i (e.g., $\log_{10}B_i$ or $\theta_{12,j}$, where $j=1, 2, \dots, n$); and $Y_{fit,j}$ refers to the fitted values of $\log_{10}(PFF)$ and V_{CME} . In this equation, a_0 is a constant, a_i is the coefficient of each magnetic parameter, m is the number of parameters used in the fit, and n is the flare events number. Let $Y_{obs,j}$ be the observed values of $\log_{10}(PFF)$ and V_{CME} . The mean value of $Y_{fit,j}$ is assumed to be equal to the mean value of $Y_{obs,j}$, so equation (7.4) yields:

$$Y_{fit,j} - \overline{Y_{obs}} = \sum_{i=1}^m a_i (X_{ij} - \overline{X_i}), \quad (7.5)$$

where $\overline{X_i}$ is the mean value of parameter X_{ij} .

The variance of $Y_{obs,j}$ due to a known magnetic parameter X_{ij} is defined as:

$$\sigma_i^2 = \frac{1}{n} \sum_{j=1}^n [a_i (X_{ij} - \overline{X_i})]^2, \quad (7.6)$$

and the variance due to other unknown parameters and/or measurement errors is defined as:

$$\sigma_o^2 = \frac{1}{n} \sum_{j=1}^n (Y_{obs,j} - Y_{fit,j})^2. \quad (7.7)$$

The total variance of $Y_{obs,j}$ is:

$$\begin{aligned} \sigma_{tot}^2 &= \frac{1}{n} \sum_{j=1}^n (Y_{obs,j} - \overline{Y_{obs}})^2 = \frac{1}{n} \sum_{j=1}^n [(Y_{obs,j} - Y_{fit,j}) + (Y_{fit,j} - \overline{Y_{obs}})]^2 \\ &= \frac{1}{n} \sum_{j=1}^n [(Y_{obs,j} - Y_{fit,j})^2 + 2(Y_{obs,j} - Y_{fit,j})(Y_{fit,j} - \overline{Y_{obs}}) + (Y_{fit,j} - \overline{Y_{obs}})^2] \end{aligned} \quad (7.8)$$

The last term on the right-hand side of equation (7.8) can be written as:

$$\begin{aligned} \frac{1}{n} \sum_{j=1}^n (Y_{fit,j} - \overline{Y_{obs}})^2 &= \frac{1}{n} \sum_{j=1}^n \left[\sum_{i=1}^m a_i (X_{ij} - \overline{X_i}) \right]^2 \\ &= \frac{1}{n} \sum_{j=1}^n \left\{ \sum_{i=1}^m [a_i (X_{ij} - \overline{X_i})]^2 + 2 \sum_{k \neq i} a_i a_k (X_{ij} - \overline{X_i})(X_{kj} - \overline{X_j}) \right\} \end{aligned} \quad (7.9)$$

The second terms on the right-hand side of equations (7.8) and (7.9) will be very small and can be neglected if there are no correlations between different magnetic parameters and the sample is big enough. After inserting equations (7.6) and (7.7) to equation (7.8), the total variance of $Y_{obs,j}$ can be approximated as:

$$\sigma_{tot}^2 \approx \sigma_o^2 + \sum_{i=1}^m \sigma_i^2 \quad (7.10)$$

Bibliography

- [1] Alexander, D., Liu, R., Gilbert, H. R. 2006, ApJ, 653, 719
- [2] Altschuler, M. D., & Newkirk, G. JR. 1969, Sol. Phys., 9, 131
- [3] Amari, T., & Luciani, J. F. 1999, ApJ, 515, L81
- [4] Amari, T., Luciani, J. F., Aly, J. J., & Tagger, M. 1996, ApJ, 466, L39
- [5] Amari, T., Luciani, J. F., Mikic, Z., & Linker, J. 2000, ApJ, 529, L49
- [6] Amari, T., Luciani, J. F., Aly, J. J., Mikic, Z., & Linker, J. 2003a, ApJ, 585, 1073
- [7] Amari, T., Luciani, J. F., Aly, J. J., Mikic, Z., & Linker, J. 2003b, ApJ, 595, 1231
- [8] Andrews, M. D. 2003, Sol. Phys., 218, 261
- [9] Andrews, M. D., & Howard, R. A., Space Sci. Rev., 95, 147
- [10] Antiochos, S. K., DeVore, C. R., & Klimchuk, J. A. 1999, ApJ, 510, 485
- [11] Antiochos, S. K., MacNiece, P. J., & Spicer, D. S. 2000, ApJ, 536, 494
- [12] Antiochos, S. K., & Sturrock, P. A. 1978, ApJ, 220, 1137
- [13] Asai, A., Ishii, T. T., Kurokawa, H., Yokoyama, T., & Shimojo, M. 2003, ApJ, 586, 624
- [14] Attié, D. et al. 2003, A&A, 411, L71
- [15] Aulanier, G., & Démoulin, P. 1998, A&A, 329, 1125
- [16] Aulanier, G., Srivastava, N., & Martin, S. F. 2000, ApJ, 543, 447
- [17] Bastian, T. S., Benz, A. O., & Gary, D. E. 1998, ARA&A, 36, 131
- [18] Berger, M. A., & Field, G. B. 1984, J. Fluid Mech., 147, 133
- [19] Berger, T., & Lites, B. W. 2003, Sol. Phys., 213, 213
- [20] Bleybel, A., Amari, T., van Driel-Gesztelyi, L., & Leka, K. D. 2002, A&A, 395, 685
- [21] Bobra, M. G., van Ballegoijen, A. A., Deluca, E. E. 2007, ApJ, in press
- [22] Bogachev, S. A., Somov, B. V., Kosugi, T., & Sakao, T. 2005, ApJ, 630, 561

- [23] Brueckner, G. E., Howard, R. A., Koomen, M. J., et al. 1995, *Sol. Phys.*, 162, 357
- [24] Bruzek, A. 1964, *ApJ*, 140, 746
- [25] Canfield, R. C., Hudson, H. S., & McKenzie, D. E. 1999, *Geophys. Res. Lett.*, 26 (No. 6), 627
- [26] Cargill, P. J., Mariska, J. T., & Antiochos, S. P. 1995, *ApJ*, 439, 1034
- [27] Carmichael, H. 1964, in W. N. Hess (ed.), *NASA Symposium on The Physics of Solar Flares*, NASA SP-50, p. 451
- [28] Carrington, R. C. 1859, *MNRAS*, 20, 13
- [29] Cheng, C.-C. et al. 1981, *ApJ*, 248, L39
- [30] Cheng, C.-C., Tandberg-Hanssen, E., & Orwig, L. E. 1984, *ApJ*, 278, 853
- [31] Chen, A. Q., Chen, P. F., & Fang, C. 2006, *A&A*, 456, 1153
- [32] Chen, P. F., & Shibata, K. 2000, *ApJ*, 545, 524
- [33] Chen, P. F., Fang, C., Shibata, K., & Tang, Y. H. 2002, *Adv. Space Res.*, 30, 535
- [34] Cheng, C. Z., Ren, Y., Choe, G. S., & Moon, Y. J. 2003, *ApJ*, 596, 1341
- [35] Choe, G. S., & Lee, L. C. 1996, *ApJ*, 472, 372
- [37] Cliver, E. W. 1989, *Sol. Phys.*, 122, 319
- [37] Cliver, E. W. 2000, in *Encyclopedia of Astronomy and Astrophysics*, P. Murdin (ed.), article 2285. (Bristol: Institute of Physics Publishing)
- [38] Cremades, H.; Bothmer, V. 2004, *A&A*, 422, 307
- [39] D’Azambuja, L. 1955, *Vistas in Astronomy*, 1, 695
- [40] Deluca, E. E., Weber, M. A., Sette, A. L., Golub, L., Shibasaki, K., Sakao, T., & Kano, R. 2005, *Adv. Space Res.*, 36, 1489
- [41] DeVore, C. R., & Antiochos, S. K. 2000, *ApJ*, 539, 954
- [42] Domingo, V., Fleck, B., & Poland, A. I. 1995, *Sol. Phys.*, 162, 1
- [43] Dryer, M. 1994, *Space Sci. Rev.*, 67, 363
- [44] Eddy, J. A., *A&A*, 34, 235
- [45] Emslie, A. G. et al. 2004, *J. Geophys. Res.*, 109, A10104
- [46] Falconer, D. A., Moore, R. L., & Gary, G. A. 2006, *ApJ*, 644, 1258
- [48] Fisher, R., Garcia, C. J., & Seagraves, P., *ApJ*, 246, L161
- [48] Fisher, R. R., & Poland, A. I., *ApJ*, 246, 1004
- [49] Fletcher, L., & Hudson, H. 2001, *Sol. Phys.*, 204, 69

- [50] Fletcher, L. 2002, in A. Wilson (ed.), *Solar Variability: From Core to Outer Frontiers*, ESA SP-506, ESA Publications Division, Noordwijk, The Netherlands, p. 223.
- [51] Fletcher, L., Pollock, J. A., & Potts, H. E. 2004, *Sol. Phys.*, 222, 279
- [52] Forbes, T. G. 1992, *Eruptive Solar Flares*, ed. Z. Švestka, B. V. Jackson, & M. E. Machado (Berlin: Springer), 79
- [53] Forbes, T. G. 1990, *J. Geophys. Res.*, 95, 11,919
- [54] Forbes, T. G. 2000, *J. Geophys. Res.*, 105 (A10), 23,153
- [55] Forbes, T. G., & Acton, L. W. 1996, *ApJ*, 459, 330
- [56] Forbes, T. G., & Isenberg, P. A. 1991, *ApJ*, 373, 294
- [57] Forbes, T. G., Malherbe, J. M., & Priest, E. R. 1989, *Sol. Phys.*, 120, 285
- [58] Foukal, P. 1971, *Sol. Phys.*, 19, 59
- [59] Gaizauskas, V. 1989, *Sol. Phys.*, 121, 135
- [60] Gaizauskas, V. 1998, in *ASP Conf. Ser. 150, New Perspectives on Solar Prominences*, ed. D. Webb, D. Rust, & B. Schmieder (IAU Colloq. 167; San Francisco: ASP), p. 257
- [61] Gaizauskas, V., Zirker, J. B., Sweetland, C., & Kovacs, A. 1997, *ApJ*, 479, 448
- [62] Gary, D. A., Moore, R. L., Hagyard, M. J., & Haisch, B. M. 1987, *ApJ*, 314, 782
- [63] Gerrard, C. L., & Hood, A. W. 2003, *Sol. Phys.*, 214, 151
- [64] Gesztelyi, L., Karlicky, M., Farnik, F., Gerlei, O., & Valnicsek, B. 1986, in *The Lower Atmosphere of Solar Flares*, ed. D. F. Neidig, Sacramento Peak, p. 163
- [65] Giacalone, J. 2003, *Planet. Space Sci.*, 51, 659
- [66] Gibson, S. E., & Low, B. C. 1998, *ApJ*, 493, 460
- [67] Gibson, S. E., & Fan, Y. 2006a, *ApJ*, 637, L65
- [68] Gibson, S. E., & Fan, Y. 2006b, *J. Geophys. Res.*, 111, A12103
- [69] Gibson, S. E., et al. 2002, *ApJ*, 574, 1021
- [70] Gilbert, H. R., Alexander, D., & Liu, R., to be submitted
- [71] Gilbert, H. R., Holzer, T. E., Burkepile, J., & Hundhausen, A. J. 2000, *ApJ*, 537, 503
- [72] Gilbert, H. R., Holzer, Low, B. C., & Burkepile, J. T. 2001, *ApJ*, 549, 1221
- [73] Golub, L., & Pasacoff, J. M. 1997, in *The Solar Corona*, Cambridge University Press, Cambridge, UK

- [74] Golub, L., Austin, G., Bookbinder, J., et al. 2007, *Sol. Phys.*, in press
- [75] Golub, L., Bookbinder, J., Deluca, E., et al. 1999, *Phys. Plasmas*, 6, 2205
- [76] Gopalswamy, N., 2006, *J. Astrophys. Astron.*, 27, 243
- [77] Gopalswamy, N., Shimojo, M., Lu, W., Yashiro, S., Shibasaki, K., & Howard, R. A. 2003, *ApJ*, 586, 562
- [78] Gopalswamy, N., Yashiro, S., Kaiser, M. L., Howard, R. A., & Bougeret, J.-L. 2001, *J. Geophys. Res.*, 106, 29219
- [79] Gopalswamy, N., Yashiro, S., Liu, Y., Michalek, G., Vourlidas, A., Kaiser, M. L., & Howard, R. A. 2005, *J. Geophys. Res.*, 110, A09S15
- [80] Gosling, J. T., Hildner, E., MacQueen, R. M., Munro, R. H., Poland, A. I., & Ross, C. L., *J. Geophys. Res.*, 79, 4581
- [81] Gosling, J. T., Hildner, E., MacQueen, R. M., Munro, R. H., Poland, A. I., & Ross, C. L. 1976, *Sol. Phys.*, 48, 389
- [82] Gosling, J. T., McComas, D. J., Phillips, J. L., & Bame, S. J. 1991, *J. Geophys. Res.*, 96, 7831
- [83] Green, L. M., Démoulin, P., Mandrini, C. H., & Van Driel-Gesztelyi, L. 2003, *Sol. Phys.*, 215, 307
- [84] Gros, M. et al. 2004, in V. Schönfelder, G. Lichti, & C. Winkler (eds.), *Proceedings of the 5th INTEGRAL Workshop on the INTEGRAL Universe*, ESA SP-552, p. 669
- [85] Guo, J., Zhang, H. Q., Chumak, O. V., & Liu, Y. 2006, *Sol. Phys.*, 237, 25
- [86] Guo, J., Zhang, H. Q., & Chumak, O. V. 2007, *A&A*, 462, 1121
- [87] Guo, W. P., Wu, S. T., & Tandberg-Hanssen, E. 1996, *ApJ*, 469, 944
- [88] Hagyard, M. J., Smith, J. B. Jr., Teuber, D., and West, E. A. 1984, *Sol. Phys.*, 91, 115
- [89] Handy, B. N., Acton, L. W., Kankelborg, C. C., et al. 1999, *Sol. Phys.*, 187, 229
- [90] Harrison, R. A. 1991, *Adv. Space Res.* 11(1), 25
- [91] Harrison, R. A. 1995, *A&A*, 304, 585
- [92] Harrison, R. A. 1996, *Sol. Phys.*, 166, 441
- [93] Harrison, R. A. 2006, in *Solar Eruptions and Energetic Particles*, eds. N. Gopalswamy, R. Mewaldt, & J. Torsti, the American Geophysical Union, Washington, DC, p. 73-88
- [94] Henoux, J. C. 1986, in *Solar Maximum Analysis*, eds. Stepanov, V. E., & Obridko, V. N., VNU Science Press, Utrecht, p. 109
- [95] Heyvaerts, J. 1974, *Sol. Phys.*, 38, 419

- [96] Heyvaerts, J., Priest, E. R., & Rust, D. M. 1977, *ApJ*, 216, 123
- [97] Hirayama, T. 1974, *Sol. Phys.*, 34, 323
- [98] Hodgson, R. C. 1859, *MNRAS*, 20, 15
- [99] Howard, R. A. 2006, in *Solar Eruptions and Energetic Particles*, eds. N. Gopalswamy, R. Mewaldt, & J. Torsti, the American Geophysical Union, Washington, DC, p. 7-14
- [100] Howard, R. A., Michels, D. J., Sheeley, N. R., Jr., & Koomen, M. J. 1982, *ApJ*, 263, L101
- [102] Hu, Y. Q. 2001, *Sol. Phys.*, 200, 115
- [102] Hu, Y. Q., & Jiang, Y. W. 2001, *Sol. Phys.*, 203, 309
- [103] Hu, Y. Q., Li, G. Q., & Xing, X. Y. 2003, *J. Geophys. Res.*, 108, 1072
- [104] Huang, G. L., & Ji, H. 2005, *Sol. Phys.*, 229, 227
- [105] Hundhausen, A. 1999, in *The Many Faces of the Sun*, K. T. Strong, J. L. R. Saba, B. M. Haisch, and J. T. Schmelz., New York : Springer, p.143-200
- [107] Hurford, G. J., Schwartz, R. A., Krucker, S., Lin, R. P., Smith, D. M., & Vilmer, N. 2003, *ApJ*, 595, L77
- [107] Hurford, G. J., Krucker, S., Lin, R. P., Schwartz, R. A., Share, G. H., & Smith, D. M. 2006, *ApJ*, 644, L93
- [108] Isenberg, P. A., Forbes, T. G., & Demoulin, P. 1993, *ApJ*, 417, 368
- [111] Ji, H. S., Wang, H., Schmahl, E. J., Moon, Y.-J., & Jiang, Y. 2003, *ApJ*, 595, L135
- [111] Ji, H., Wang, H., Goode, P. R., Jiang, Y., & Yurchyshyn, V. 2004a, *ApJ*, 607, L55
- [111] Ji, H., Wang, H., Schmahl, E. J., Qiu, J., & Zhang, Y. 2004b, *ApJ*, 605, 938
- [112] Ji, H. S. , Huang, G. L., Wang, H. M., Zhou T. H., Li, Y. P., Zhang, Y. A., & Song, M. T. 2006, *ApJ*, 636, L173
- [113] Ji, H. S., Huang, G. L., & Wang, H. M. 2007, *ApJ*, 660, 893
- [114] Jing, J., Song, H., Abramenko, V., Tan, C. Y., & Wang, H. M. 2006, *ApJ*, 644, 1273
- [115] Jing, Ju, Yurchyshyn, Vasyl B., Yang, Guo, Xu, Yan, & Wang, Haimin, *ApJ*, 614, 1054
- [116] Kan, J. R., Akasofu, S. I., Lee, L. C. 1983, *Sol. Phys.*, 84, 153
- [117] Kane, S. R., Frost, K.J. & Donnelly, R. F. 1979, *ApJ*, 234, 669
- [118] Kano, K. R., Deluca, E., Austin, G., et al. 2007, *Sol. Phys.*, in press

- [119] Karpen, J. T., Antiochos, S. K., Hohensee, M., Klimchuk, J. A., & MacNiece, P. J. 2001, *ApJ*, 553, L85
- [120] Karpen, J. T., Tanner, S. E. M., Antiochos, S. K., & DeVore, C. R. 2005, *ApJ*, 635, 1319
- [121] Khan, J. I., & Hudson, H. S. 2000, *Geophys. Res. Lett.*, 27, 1083
- [122] Kopp, R. A., & Pneuman, G. W. 1976, *Sol. Phys.*, 50, 85
- [123] Kosugi, T., & Acton, L. W. 2002, in P. C.H. Martens, & D.P. Cauffman (eds.), *Multi-wavelength Observations of Coronal Structure and Dynamics*
- [124] Kosugi, T., et al. 1991, *Sol. Phys.*, 136, 17
- [125] Kosugi, T., Matsuzaki, K., Sakao, T., et al. 2007, *Sol. Phys.*, in press
- [126] Krall, J., Chen, J., & Santoro, R. 2000, *ApJ*, 539, 964
- [127] Kreplin, R. W., Chubb, T. A., & Friedman, H. 1962, *J. Geophys. Res.*, 67, 2231
- [128] Krucker, S., & Hudson, H. S. 2004, in R.W. Walsh, J. Ireland, D. Danesy, & B. Fleck. (eds.), *Proceedings of the SOHO 15 Workshop*, ESA SP-575, p. 247
- [129] Kundu, M.R., Schmahl, E.J., & Garaimmov, V.I. 2004, in A.V. Stepanov, E.E. Benevolenskaya, & A.G. Kosovichev (eds.), *Multi-Wavelength Investigations of Solar Activity*, IAU Symp., 223, 425
- [130] Kurokawa, H. 1989, *Space Sci. Rev.*, 51, 49
- [131] Kuznetsov, S. N., Kurt, V. G., Myagkova, I. N., Yushkov, B. Y., & Kudela, K. 2005, *Solar System Research*, 40, 104
- [132] Lara, A., Gopalswamy, N., Xie, H., Mendoza-Torres, E., Pérez-Eriquez, & Michalek, G. 2006, *J. Geophys. Res.*, 111, A06107
- [133] Leblanc, Y., Dulk, G. A., Vourlidas, A., & Bourgeret, J. L. 2001, *J. Geophys. Res.*, 106, 25301
- [144] Lin, A. C., Nightingale, R. W., & Tarbell, T. 2001, *Sol. Phys.*, 198, 385
- [135] Lin, H. S., Penn, M. J., & Kuhn J. R. 1998, *ApJ*, 493, 978
- [136] Lin, J. 2002, *Chinese J. Astron. Astrophys.*, 2, 539
- [137] Lin, J. 2004, *Sol. Phys.*, 219, 169
- [138] Lin, J., & Forbes, T. 2000, *J. Geophys. Res.*, 105, 2375
- [144] Lin, J., Forbes, T. G., & Isenberg, P. A. 2001, *J. Geophys. Res.*, 106, 25,053
- [140] Lin, J., Soon, W., & Baliunas, S. L. 2003, *NewA Rev.*, 47, 53
- [141] Lin, R. P., Dennis, B. R., Hurford, G. J., et al. 2002, *Sol. Phys.*, 210, 3

- [142] Lin, R. P., & Hudson, H. S. 1976, *Sol. Phys.*, 50, 153
- [143] Linker, J. A., & Mikic, Z. 1995, *ApJ*, 438, L45
- [144] Linker, J. A., Lionello, R., Mikic, Z., & Amari, Z. 2001, *J. Geophys. Res.*, 106, 25,165
- [145] Liu, Y. 2007, *ApJ*, 654, L171
- [146] Lockwood, M. 2003, *J. Geophys. Res.*, 108, 7
- [147] Low, B. C. 1996, *Sol. Phys.*, 167, 217
- [148] Low, B. C. 2001, *J. Geophys. Res.*, 106, 25,141
- [149] Low, B. C., & Hundhausen, J. R. 1995, *ApJ*, 443, 818
- [150] Low, B. C., Zhang, M. 2002, *ApJ*, 564, L53
- [151] Lynch, B. J., Antiochos, S. K., DeVore, C. R., & Zurbuchen, T. H. 2005, in “Connecting Sun and Heliosphere” Conference (ESA SP-592), eds. B. Fleck, T.H. Zurbuchen, H. Lacoste, Published on CDROM., p.44.1
- [152] Lynch, B. J., Antiochos, S. K., MacNeice, P. J., Zurbuchen, T. H., & Fisk, L. A. 2004, *ApJ*, 617, 589
- [153] Machado, M. E., Moore, R. L., Hernandez, A. M., Rovira, M. G., Hagyard, M. J., & Smith, J. B. 1988, *ApJ*, 326, 425
- [154] Mackay, D. H., & Lockwood, M. 2002, *Sol. Phys.*, 207, 291
- [155] Mackay, D. H., & van Ballegooijen, A. 2006, *ApJ*, 641, 577
- [156] MacQueen, R. M. 1980, *Philosophical Transactions, Series A*, 297, 605
- [157] MacQueen, R. M., Eddy, J. A., Gosling, J. T., Hildner, E., Munro, R. H., Newkirk, G. A., Jr., Poland, A. I., & Ross, C. L., *ApJ*, 187, L85
- [158] MacQueen, R. M., & Fisher, A. A. 1983, *Sol. Phys.*, 89, 89
- [159] Manchester, W. 2003, *J. Geophys. Res.*, 108, 1162
- [160] Martin, S. F. 1990, in *IAU Colloq. 117, Dynamics of Quiescent Prominences*, ed. V. Ruzdjak & E. Tandberg-Hanssen (Berlin: Springer), 1
- [161] Martin, S. F. 1998, *Sol. Phys.*, 182, 107
- [162] Martin, S. F., Bilimoria, R., & Tracadas, P. W. 1994, in *Solar Surface Magnetism*, ed. R. J. Rutten & C. J. Schrijver (Dordrecht: Kluwer), p. 303
- [163] Martin, S. F., Livi, S. H. B., & Wang, J. 1985, *Australian J. Phys.*, 38, 929
- [164] Martin, S. F., & Ramsey, H. E. 1972, in *Solar Activity Observations and Predictions*, eds. P. S. McIntosh & M. Dryer, MIT press, Cambridge, MA
- [165] Masuda, S., Kosugi, T., & Hudson, H. S. 2001, *Sol. Phys.*, 204, 57

- [166] Maxwell, A., Dryer, M., & McIntosh, P. 1985, *Sol. Phys.*, 97, 401
- [167] McClymont, A. N., Jiao, L., & Mikic., Z. 1997, *Sol. Phys.*, 174, 191
- [168] McIntosh, P. S. 1972, in P. S. McIntosh & M. Dryer (eds.), *Solar Activity Observations and Predictions*, MIT press, Cambridge, p. 65
- [169] McAteer, R. T. J., Gallagher, P. T., Ireland, J., & Young, C. A. 2005, *Sol. Phys.*, 228, 55
- [170] Michels, D. J., Howard, R. A., Koomen, M. J., Sheeley, N. R., Jr. 1980, in *Radio physics of the sun*, eds. M. R. Kundu & T. Gergely, Dordrecht, D. Reidel Publishing Co., p. 439-442.
bibitem[Mikic & Linker (1994)]Mik94Mikić, Z., Linker, J. A. 1994, *ApJ*, 430, 898
- [171] Mikić, Z., & McClymont, A. N. 1994, in *Solar Active Region Evolution: Comparing Models with Observations*, eds. K. S. Balasubramaniam & G. W. Simon, ASP Conf. Ser., 68, 225
- [172] Mikić, Z., Barnes, D. C., & Schnack, D. D. 1988, *ApJ*, 328, 830
- [173] Moon, Y.-J., Choe, G. S., Wang, Haimin, Park, Y. D., Gopalswamy, N., Yang, Guo, & Yashiro, S. 2002, *ApJ*, 581, 694
- [174] Moore, R. L., et al. 1980, *Solar Flares: A Monograph from Skylab Solar Workshop II*, Ed. P. Sturrock (Boulder: Colorado Assoc. Univ. Press), 341
- [175] Moore, R. L. 1988, *ApJ*, 324, 1132
- [176] Moore, R. L., LaRosa, T. N., & Orwig, L. E. 1995, *ApJ*, 438, 935
- [177] Moore, R. L., Sterling, A. C., Hudson, H. S., & Lemen, J. R. 2001, *ApJ*, 552, 833
- [178] Munro, R. H., et al. 1979, *Sol. Phys.*, 61, 201
- [179] Nagai, F. 1980, *Sol. Phys.*, 68, 351
- [180] Nakagawa, Y., & Raadu, M. A. 1972, *Sol. Phys.*, 25, 127
- [181] Nakagawa, Y., Wu, S. T., & Tandberg-Hanssen, E. 1978, *A&A*, 69, 43
- [182] Ogawara, Y., Takano, T., Kato, T., et al. 1991, *Sol. Phys.*, 136, 10
- [183] Pevtsov, A. A. 2002, *Sol. Phys.*, 207, 111
- [184] Plunkett, S. P., et al., *Sol. Phys.*, 194, 371
- [185] Pneuman, G. W. 1981, in *Solar Flare Magnetohydrodynamics*, ed. E. R. Priest (New York: Gordon and Breach Science Publishers), p. 379-428
- [186] Priest, E. R. 1981, in *Solar Flare Magnetohydrodynamics*, ed. E. R. Priest (New York: Gordon and Breach Science Publishers), p. 2-46
- [187] Priest, E. R. 1982, *Solar Magneto-Hydrodynamics* (Dordrecht: Reidel)

- [188] Priest, E. R. 1989, in *Dynamic and Structure of Quiescent Solar Prominences*, ed. E. R. Priest, Kluwer Academic Publ., Dordrecht, The Netherlands, p. 1-14
- [189] Priest, E. R., & Forbes, T. G. 2002, *A&A Rev.*, 10, 313
- [190] Qiu, J., Lee, J., & Gary, D. E. 2004, *ApJ*, 603, 335
- [191] Qiu, J., & Yurchyshyn, V. B. 2005, *ApJ*, 634, L121
- [192] Reeves, K. K., & Forbes, T. G. 2005, *ApJ*, 630, 1133
- [193] Reeves, K. K. 2006a, *ApJ*, 644, 592
- [194] Reeves, K. K. 2006b, PhD Thesis
- [195] Reeves, K. K., Seaton, D. B., & Forbes, T. G. 2007, *ApJ*, submitted
- [196] Régnier, S., Amari, T., & Kersalé, E. 2002, *A&A*, 392, 1119
- [197] Roussev, I. I., Forbes, T. G., Gombosi, T. I., Sokolov, I. V., DeZeeuw, D. L., & Birn, J. 2003, *ApJ*, 588, L45
- [198] Roy, J. R. 1972, *Sol. Phys.*, 26, 418
- [199] Rust, D. M., Bar, V. 1973, *Sol. Phys.*, 33, 445
- [200] Rust, D. M., & Kumar, A. 1996, *ApJ*, 464, L199
- [201] Sakao, T. 1994, Ph.D. Thesis (University of Tokyo)
- [202] Sakurai, T. 1976, *PASJ*, 28, 177
- [203] Schatten, K. H., Wilcox, J. M., & Ness, N. F. 1969, 6, 442
- [204] Scherrer, P. H., Bogart, R. S., Bush, R. I., et al. 1995, *Sol. Phys.*, 162, 129
- [205] Schmieder, B., Forbes, T. G., Malherbe, J. M., & Machado, M. E. 1987, *ApJ*, 317, 956
- [206] Schmieder, B., Mandrini, C.H., Démoulin, Pariat, E., Berlicki, A., & Deluca, E. 2006, *Adv. Space Res.*, 37, 1313
- [207] Schmieder, B., & van Driel-Gesztelyi, L. 2005, in *Coronal and Stellar Mass Ejections*, eds. K. Dere, J. Wang, & Y. Yan. Cambridge: Cambridge University Press, p.149-160
- [208] Schrijver, C. J., Title, A. M., Berger, T. E., et al. 1999, *Sol. Phys.*, 187, 261
- [209] Schrijver, C. J., Derosa, M. L., Metcalf, Th. R., Liu, Y., McTiernan, J., Régnier, S., Valori, G., Wheatland, M. S., & Wiegmann, Th. 2006, *Sol. Phys.*, 235, 161
- [210] Sen, H. K., & White, M. L. 1972, *Sol. Phys.*, 23, 146
- [211] Sheeley, N. R., Jr., Bohlin, J. D., Brueckner, G. E., Purcell, J. D., Scherrer, V. E., Tousey, R., Smith, J. B., Jr., Speich, D. M., Tandberg-Hanssen, E., & Wilson, R. M. 1975, *Sol. Phys.*, 45, 377

- [212] Sheeley, N. R., Jr., Howard, R. A., Koomen, M. J., & Michels, D. J., *ApJ*, 272, 349
- [213] Sheeley, N. R., Walters, J. H., Wang, Y.-M., & Howard, R. A. 1999, *J. Geophys. Res.*, 104, 24739
- [214] Shibata, K. 1999, *AP&SS*, 264, 129
- [215] Shibata, K., Nozawa, S., & Matsumoto, R. 1992, *PASJ*, 44, 265
- [216] Shimizu, T. 2004, in *The Solar-B Mission and the Forefront of Solar Physics*, eds. Sakurai T. & Sekii T. (San Francisco: Astronomical Society of the Pacific), p.3
- [217] Smith, D. F., & Auer, L. H. 1980, *ApJ*, 238, 1126
- [218] Smith, D. F., & Lilliequist, C. G. 1979, *ApJ*, 232, 582
- [219] Smith, H. J., & Smith, E. v. P. 1963, in *Solar Flares*, The Macmillan Co., New York
- [220] St. Cyr, O. C., et al. 2000, *J. Geophys. Res.*, 105, 18,169
- [221] St. Cyr, O. C., Webb, D. F. 1991, *Sol. Phys.*, 136, 379
- [222] Steinegger, M., Denker, C., Goode, P. R., et al. 2000, in *the Solar Cycle and Terrestrial Climate, Proceedings 1st European SOLSPA Conf.*, ed. A. Wilson, (Noordwijk: ESA SP 463), p. 617
- [223] Sterling, A. C., Hudson, H. S., Thompson, B. J., & Zarro, D. M. 2000, *ApJ*, 532, 628
- [224] Sturrock, P. A. 1966, *Nature*, 211, 695
- [225] Sturrock, P. A. 1968, in *Structure and Development of Solar Active Regions*, IAU Symp., ed. Kiepenheuer, K. O., p. 471
- [226] Sturrock, P. A. 1973, in *High Energy Phenomena on the Sun*, NASA SP-342, p. 3
- [227] Sturrock, P. A. 1980, in P. A. Sturrock (ed.) *Solar Flares*, Co. 1980 Colorado Associated University Press, Boulder (Colorado)
- [228] Su, Y. N., Golub, L., Van Ballegooijen, A. A., & Gros, M. 2006, *Sol. Phys.*, 236, 325
- [229] Su, Y. N., Golub, L., & Van Ballegooijen, A. A. 2007a, *ApJ*, 655, 606
- [230] Su, Y. N., Golub, L., van Ballegooijen, A., Deluca, E., Reeves, K. K., Sakao, T., Kano, R., Narukage, N., & Shibata, K. 2007b, *PASJ*, accepted
- [231] Su, Y. N., Van Ballegooijen, A. A., McCaughey, J. , Deluca, E., Reeves, K. K., & Golub, L. 2007c, *ApJ*, 665, 1448
- [232] Su, Y. N., Van Ballegooijen, A. A., Golub, L., & Deluca, E. 2007d, *ApJ*, in preparation

- [233] Švestka, Z. 1976, *Solar Flares*, Co. by D. Reidel Publishing Company, Dordrecht, Holland
- [234] Švestka, Z. 1981, in *Solar Flare Magnetohydrodynamics*, ed. E. R. Priest (New York: Gordon and Breach Science Publishers)
- [235] Švestka, Z. 1986, *The Lower Atmosphere of Solar Flares*, ed. D. F. Neidig (Tucson: Univ. Arizona Press), p. 332
- [236] Švestka, Z. 1995, *Sol. Phys.*, 160, 53
- [237] Švestka, Z., & Cliver, E. W. 1992, in Z. Švestka, B.V. Jackson, & M.E. Machado (eds.), *Eruptive Solar Flares*, Springer-Verlag, New York, p. 1
- [238] Švestka, Z. 2001, *Space Sci. Rev.*, 95, 135
- [239] Tanaka, K., & Nakagawa, Y. 1973, *Sol. Phys.*, 33, 187
- [240] Tang, F. 1985, *Sol. Phys.*, 102, 131
- [241] Tang, F. 1986, *Sol. Phys.*, 105, 399
- [242] Tandberg-Hanssen, E., & Emslie, A. G. 1988, *The Physics of Solar Flares*, (Cambridge: Cambridge Univ. Press)
- [243] Török, T., & Kleim, B. 2005, *ApJ*, 630, L97
- [244] Tousey, R., in *Space Research XIII*, eds. M. J. Rycroft & S. K. Runcorn, Akademie-Verlag, Berlin, p. 713
- [245] Tsuneta, S., Hara, H., Shimizu, T., Action, L. W., Strong, K. T., Hudson, H. S., & Ogawara, Y. 1992, *PASJ*, 44, L63
- [246] Tsuneta, S., Suematsu, Y., Ichimoto, K., et al. 2007, *Sol. Phys.*, submitted
- [247] van Ballegooijen, A. A. 2004, *ApJ*, 612, 519
- [248] van Ballegooijen, A. A., & Mackay, D. H. 2007, *ApJ*, 659, 1713
- [249] van Ballegooijen, A. A., Priest, E. R., & Mackay, D. H. 2000, *ApJ*, 539, 983
- [250] Vedrenne, G. et al. 2003, *A&A*, 411, L63
- [251] Venkatakrisnan, P., & Ravindra, B. 2003, *Geophys. Res. Lett.*, 30 (No. 23), 2181
- [252] Vourlidas, A., Subramanian, P., Dere, K. P., & Howard, R. A. 2000, *ApJ*, 534, 456
- [253] Vourlidas, A., Buzasi, D., Howard, R. A., & Esfandiari, E. 2002, in *Solar variability: from core to outer frontiers*, ESA SP-506, Vol. 1. Noordwijk: ESA Publications Division, p. 91-94
- [254] Vršnak, B.; Sudar, D.; Ruzdjak, D. 2005, *A&A*, 435, 1149
- [255] Wang, Y. M., Sheeley, N. R., Jr. 1992, *ApJ*, 392, 310

- [256] Wang, Y. M., Sheeley, N. R., Jr., & Lean, J. 2000, *Geophys. Res. Lett.*, 27, 621
- [257] Wang, Y. M., Ye, P. Z., Zhou, G. P., Wang, S. J., Wang, S., Yan, Y. H., & Wang, J. X. 2005, *Sol. Phys.*, 226, 337
- [258] Warren, H. P. & Warshall, A. D. 2001, *ApJ*, 560, L87
- [259] Webb, D. F., & Hundhausen, A. J. 1987, *Sol. Phys.*, 108, 383
- [260] Wheatland, M. S. 2006, *Sol. Phys.*, 238, 29
- [261] Wheatland, M. S., Sturrock, P. A., & Roumeliotis, G. 2000, *ApJ*, 540, 1150
- [262] Wiegelmann, T. 2004, *Sol. Phys.*, 219, 87
- [263] Wiegelmann, T., Inhester, B., & Sakurai, T. 2006, *Sol. Phys.*, 233, 215
- [264] Woodgate, B. E., Shine, R. A., Poland, A. I., & Orwig, L. E. 1983, *ApJ*, 265, 530
- [265] Wu, S. T., Guo, W. P., & Wang, J. F. 1995, *Sol. Phys.*, 157, 325
- [266] Wu, S. T., Guo, W. P., Michels, D. J., & Burlaga, L. F. 1999, *J. Geophys. Res.*, 104, 14,789
- [267] Wu, S. T., Guo, W. P., Andrews, M. D., & Brueckner, G. E., Howard, R. A. et al. 1997, *Sol. Phys.*, 175, 719
- [268] Yang, W. H., Sturrock, P. A., & Antiochos, S. K. 1986, *ApJ*, 309, 383
- [269] Yokoyama, T. & Shibata, K. 1997, *ApJ*, 474, L61
- [270] Yurchyshyn, V., Yashiro, S., Abramenko, V., Wang, H., & Gopalswamy, N. 2005, *ApJ*, 619, 599
- [271] Zhang, J., Dere, K. P., Howard, R. A., Kundu, M. R., & White, S. M. 2001, *ApJ*, 559, 452
- [272] Zhang, M., Golub, L., Deluca, E., & Burkepile, J. 2002, *ApJ*, 574, L97
- [273] Zhang, M., & Golub, L. 2003, *ApJ*, 595, 1251
- [274] Zhang, M., & Low, B. C. 2005, *ARA&A*, 43, 103
- [275] Zirin, H., 1983, *ApJ*, 274, 900

Curriculum Vitae

Name	Yingna Su
Date of Birth	May 27, 1979
Place of Birth	Hebei, China
Nationality	China

Education History

9/1997-7/2001	B.S. in Physics, Hebei Normal University
9/2001-7/2004	M.S. in Astrophysics, Purple Mountain Observatory <i>Analysis of Loop-top and Footpoint Sources in Solar Microwave Bursts</i> Thesis advisor: Guangli Huang
9/2004-12/2007	Ph.D. in Astrophysics, Purple Mountain Observatory
1/2005-12/2007	Pre-doctoral Fellow at Harvard-Smithsonian Center for Astrophysics Thesis: <i>Magnetic Shear in Two-ribbon Flares</i> Thesis advisor: Guangli Huang and Leon Golub

Professional Association and Awards

2007-now	American Astronomical Society
2002-2003	Scholarship of the director of Purple Mountain Observatory
2003-2004	Scholarship of the director of Purple Mountain Observatory
6/2006	The Solar Physics Division of the American Astronomical Society Studentship Awards

List of Publications

Publications in Refereed Journals

- **Su, Y. N.**, van Ballegoijen, A. A., Golub, L., & Deluca, E. E. 2007, ApJ, in preparation
- **Su, Y. N.**, Golub, L., van Ballegoijen, A. A., Deluca, E. E., Reeves, K. K., Sakao, T., Kano, R., Narukage, N., Shibasaki, K. 2007, “Evolution of the Sheared Magnetic Fields of Two X-class Flares Observed by *Hinode*/XRT”, PASJ, in press
- **Su, Y. N.**, van Ballegoijen, A. A., McCaughey, J., Deluca, E. E., Reeves, K. K., & Golub, L. 2007, “What Determines the Intensity of Solar Flare/CME Events”, ApJ, 665, 1448
- **Su, Y. N.**, Golub, L., & van Ballegoijen, A. A. 2007, “A Statistical Study of Shear Motion of the Footpoints in Two-ribbon Flares”, ApJ, 655, 606
- **Su, Y. N.**, Golub, L., van Ballegoijen, A. A., & Gros, M. 2006, “Analysis of Magnetic Shear in an X17 Solar Flare on October 28, 2003”, Sol. Phys., 236, 325
- **Su, Y. N.**, & Huang G. L. 2004, “Polarization of Loop-top and Footpoint Sources in Microwave Bursts”, Sol. Phys., 219, 159

Coauthored Publications in Refereed Journals

- Liu, R., Gilbert, H. R., Alexander, D., & **Su, Y. N.** 2007, “A Partial Filament Eruption Driven by Kink Instability”, ApJ, to be submitted

- Sakao, T., Kano, R., Narukage, N., Kotoku, J., Bando, T., Deluca, E. E., Lundquist, L., Tsuneta, S., Harra, L. K., Katsukawa, Y., Kubo, M., Hara, H., Matsuzaki, K., Shimojo, M., Bookbinder, J. A., Golub, L., Korreck, K. E., **Su, Y. N.**, Shibasaki, K., Shimizu, T., & Nakatani, I. 2007, *Science*, accepted
- Reznikova, V. E., Melnikov, V. F., **Su, Y. N.**, & Huang, G. L. 2007, “Pulsations of Microwave Flaring Emission at Low and High Frequencies”, *Astronomy Reports*, 51, 588
- Huang, G. L., Zhou, A. H., **Su, Y. N.**, & Zhang, J. 2005, “Calculations of the Low-cutoff Energy of Non-thermal Electrons in Solar Microwave and Hard X-ray Bursts”, *New Astronomy*, 10, 219
- Zhou, A. H., **Su, Y. N.**, & Huang, G. L. 2005, “Energetic Electrons in Loop Top and Footpoint Microwave Sources”, *Sol. Phys.*, 226, 327
- Zhou A. H., **Su Y. N.**, & Huang G. L. 2004, “Effects of the Gyroresonance Absorption and self Absorption on the Gyrosynchrotron Radiation Spectrum”, *Chinese Physics letters*, 21, 2067

Selected Conference Proceedings

- **Su, Y. N.**, Golub, L., Van Ballegooijen, A., & Huang, G. L. 2006, “A Statistical Study of Shear Motion of EUV Footpoints in Two-ribbon Flares”, in V. Bothmer and A. A. Hady (eds.), *Proc. of the IAU Symposium 233, ‘Solar Activity and its Magnetic Origin’*, p. 409
- **Su, Y. N.**, & Huang, G. L. 2003, “Analysis of Loop-top and Foot-point Sources in Microwave Bursts”, in *Proc. of the IAU Symposium 219, ‘Stars as Suns: Activity, Evolution and Planets’*, p. 246

- **Su, Y. N.**, & Huang, G. L. 2003, “Analysis of Loop-top and Foot-point Sources in Microwave Bursts”, in A. Wilson (ed.), Proc. of the International Solar Cycle Studies (ISCS) Symposium, ‘Solar variability as an input to the Earth’s environment’, ESA SP-535, p. 695